PNL-3700 PT4
UC-48

Pacific Northwest Laboratory Annual Report for 1980 to the DOE Assistant Secretary for Environment

Part 4 Physical Sciences February 1981

Prepared for the U.S. Department of Energy
under Contract DE-AC06-76RLO 1830

Pacific Northwest Laboratory
Operated for the U.S. Department of Energy
by Battelle Memorial Institute

Battelle

PACIFIC NORTHWEST LABORATORY
operated by
BATTELLE
for the
UNITED STATES DEPARTMENT OF ENERGY
Under Contract DE-AC06-76RLO 1830

Printed in the United States of America
Available from
National Technical Information Service
United States Department of Commerce
5285 Port Royal Road
Springfield, Virginia 22151

Price: Printed Copy $_____*; Microfiche $3.00

*Pages	NTIS Selling Price
001-025	$4.00
026-050	$4.50
051-075	$5.25
076-100	$6.00
101-125	$6.50
126-150	$7.25
151-175	$8.00
176-200	$9.00
201-225	$9.25
226-250	$9.50
251-275	$10.75
276-300	$11.00

PNL-3700 PT4
UC-48

Pacific Northwest Laboratory Annual Report for 1980 to the DOE Assistant Secretary for Environment

Part 4 Physical Sciences

J. M. Nielsen and Staff Members
of Pacific Northwest Laboratory

February 1981

Prepared for
the U.S. Department of Energy
under Contract DE-AC06-76RLO 1830

Pacific Northwest Laboratory
Richland, Washington 99352

PREFACE

Pacific Northwest Laboratory's (PNL) 1980 Annual Report to the Department of Energy (DOE) Assistant Secretary for Environment describes research in environment, health, and safety conducted during fiscal year 1980. The report again consists of five parts, each in a separate volume.

The five parts of the report are oriented to particular segments of our program. Parts 1 to 4 report on research performed for the DOE Office of Health and Environmental Research. Part 5 reports progress on all other research performed for the Assistant Secretary for Environment, including the Office of Environmental Assessment and the Office of Environmental Compliance and Overview. Each part consists of project reports authored by scientists from several PNL research departments, reflecting the interdisciplinary nature of the research effort. Parts 1 to 4 are organized primarily by energy technology.

The parts of the 1980 Annual Report are:

Part 1:	Biomedical Sciences Program Manager - H. Drucker	D. L. Felton, Editor
Part 2:	Ecological Sciences Program Manager - B. E. Vaughan	B. E. Vaughan, Report Coordinator C. M. Novich, Editor
Part 3:	Atmospheric Sciences Program Manager - C. E. Elderkin	R. L. Drake, Report Coordinator M. F. Johnson, Editor
Part 4:	Physical Sciences Program Manager - J. M. Nielsen	J. M. Nielsen, Report Coordinator I. D. Hays, J. L. Baer, Editors
Part 5:	Environmental Assessment, Control, Health and Safety Program Managers - D. L. Hessel S. Marks W. A .Glass	W. J. Bair, Report Coordinator R. W. Baalman, I. D. Hays, Editors

Activities of the scientists whose work is described in this annual report are broader in scope than the articles indicate. PNL staff have responded to numerous requests from DOE during the year for planning, for service on various task groups, and for special assistance.

Credit for this annual report goes to many scientists who performed the research and wrote the individual project reports, to the program managers who directed the research and coordinated the technical progress reports, to the editors who edited the individual project reports and assembled the five parts, and to Ray Baalman and Irene D. Hays, editors in chief, who directed the total effort.

W. J. Bair, Manager
S. Marks, Associate Manager
Environment, Health, and Safety Research Program

Previous Reports in this series:

Annual Report for

1951	W-25021, HW-25709
1952	HW-27814, HW-28636
1953	HW-30437, HW-30464
1954	HW-30306, HW-33128, HW-35905, HW-35917
1955	HW-39558, HW-41315, HW-41500
1956	HW-47500
1957	HW-53500
1958	HW-59500
1959	HW-63824, HW-65500
1960	HW-69500, HW-70050
1961	HW-72500, HW-73337
1962	HW-76000, HW-77609
1963	HW-80500, HW-81746
1964	BNWL-122
1965	BNWL-280, BNWL-235, Vol. 1-4, BNWL-361
1966	BNWL-480, Vol. 1, BNWL-481, Vol. 2, Pt. 1-4
1967	BNWL-714, Vol. 1, BNWL-715, Vol. 2, Pt. 1-4
1968	BNWL-1050, Vol. 1, Pt. 1-2, VNWL-1051, Vol. 2, Pt. 1-3
1969	BNWL-1306, Vol. 1, Pt. 1-2, BNWL-1307, Vol. 2, Pt. 1-3
1970	BNWL-1550, Vol. 1, Pt. 1-2, BNWL-1551, Vol. 2, Pt. 1-2
1971	BNWL-1650, Vol. 1, Pt. 1-2, BNWL-1651, Vol. 2, Pt. 1-2
1972	BNWL-1750, Vol. 1, Pt. 1-2, BNWL-1751, Vol. 2, Pt. 1-2
1973	BNWL-1850, Pt. 1-4
1974	BNWL-1950, Pt. 1-4
1975	BNWL-2000, Pt. 1-4
1976	BNWL-2100, Pt. 1-5
1977	PNL-2500, Pt. 1-5
1978	PNL-2850, Pt. 1-5
1979	PNL-3300, Pt. 1-5

FOREWORD

Part 4 of the Pacific Northwest Laboratory Annual Report for 1980 to the Assistant Secretary for Environment, DOE, includes those programs funded under the title "Physical and Technological Programs". The Field Task Program Studies reports are grouped under the most directly applicable energy technology heading. Each energy technology section is introduced by a divider page which indicates the Field Task Agreement reported in that section. These reports only briefly indicate progress made during 1980. The reader should contact the principal investigators named or examine the publications cited for more details.

CONTENTS

1 Coal

• Reaction Kinetics of Combustion Products

The goal of the Reaction Kinetics of Combustion Products program is to determine the conditions, mechanisms, and chemical reactions that control the identity and concentrations of emissions from coal combustion processes. Presently, the major emphasis of the program is on the investigation of the mechanism of formation of organic pollutants during combustion. Mass spectrometric techniques have been developed for the study of the high-temperature kinetics relevant to coal combustion, with specific emphasis on techniques that will allow investigation of the mechanisms and rates of formation for toxic and carcinogenic organic compounds. The chemistry of certain model compounds at combustion temperatures is being investigated. Our studies have begun to unravel the complex interactions between organic species in the combustion zone and the kinetic parameters relevant to pollutant release into the environment.

Kinetics and Mechanisms for the Formation of Organic Pollutants During Pyrolysis and Combustion

Richard D. Smith and A. L. Johnson

The potential toxicity and mutagenicity of emissions from coal-fired plants continue to be of concern. Of these emissions, the aromatic pollutants probably represent the major source of the mutagenically active constituents. Aromatic compounds, soot and related compounds are known to be produced efficiently under many combustion conditions but their formation mechanisms have not been clearly established.

A fundamental understanding of the kinetics and mechanisms for formation of aromatic pollutants is necessary for a number of reasons. An understanding of the high-temperature chemistry can facilitate the development of effective control strategies based upon manipulation of combustion parameters. Similarly, information supplied from these fundamental studies provides necessary thermochemical data for equilibrium calculations or kinetic data for modeling studies. Other practical problems related to soot formation, heat transfer and combustion efficiency will also benefit from these data.

Studies of the polycyclic organic emissions from flames and various combustion facilities have shown that the emissions are qualitatively similar. Most aromatic compounds (or their precursors) ultimately emitted from coal combustion will result from the highly fuel rich local conditions resulting from coal pyrolysis during the initial stages of combustion. An initial working assumption is that after formation the rates of the various oxidation and destruction pathways govern the emission concentrations. Thus, our initial approach has involved the study of simple aromatic model compounds (e.g., benzene, toluene, ethyl benzene, phenylacetylene, etc.) which may be formed during coal devolatilization. Our goal is to determine representative primary unimolecular and bimolecular rate data and to identify important reaction pathways for the formation and destruction of representative species. Measurements of rate constants as a function of temperature are also used to derive valuable thermochemical information and input for modeling calculations while mechanistic data provide a perhaps even more useful qualitative understanding of pollutant formation.

Part of the experimental equipment used in these studies has been described previously (Smith 1979a, and 1979b). Modulated molecular beam mass spectrometry, and related techniques such as phase angle spectroscopy, are used to analyze the products from high-temperature reaction cells or flow tubes. The major advantage of this approach is the near universal nature of the detector; nearly equal sensitivities are obtained for both radicals and stable molecules. To obtain reliable quantitative or qualitative data from these studies, one

must correct for, or avoid, thermal effects, e.g., the dependences of the mass spectral fragmentation pattern upon temperature and more subtle effects related to changes in molecular velocity. Our initial studies have examined the pyrolysis of a number of model compounds as a function of pressure and temperature. Figures 1.1 and 1.2 give typical data obtained from the pyrolysis of a model compound as a function of temperature using the computer-controlled mass spectrometer. In this case, the major species involved in the pyrolysis of phenylacetylene are given in Figure 1.1 and two of the major higher molecular weight product profiles are given in Figure 1.2. Mechanistic studies involving a number of additives (O_2, N_2, NO, SO_2) have also been carried out. Rate constants for the initial unimolecular pyrolysis processes have been determined as a function of temperature at low pressures; similar experiments are planned at elevated pressures. Figure 1.3 gives typical rate data obtained from the pyrolysis of benzene using the computer controlled system. In addition, initial heterogeneous processes involving surface reactions and condensation processes are being used to identify important high temperature intermediate species (e.g., CH_3, C_2H_2, C_3H_3, C_4H_2, C_5H_3, etc.) in the formation of specific aromatic species obtained by quenching the molecular beam on surfaces at controlled temperatures and analyzed by gas chromatography-mass spectrometry (GC/MS). Experiments with more complex heteroatomic species are also planned to study the chemistry of systems incorporating S, N, or O atoms.

Our results indicate that the formation of higher molecular weight products has a maximum, as a function of temperature, in the 1200°C to 1400°C range, for all aromatic systems studied thus far. This maximum is apparently nearly independent of pressure below about 10 torr. Initial results of the gas phase pyrolysis have supported the suggestion of two distinct routes for the formation of polycyclic aromatic hydrocarbons and soot. Below approximately 1450°C direct condensation of aromatic precursors leads to higher molecular weight compounds and ultimately some soot formation. At higher temperatures, initial pyrolysis reactions result in the formation of reactive lower molecular fragments (CH_3, C_2H_2, C_3H_3, C_4H_2, etc.) which are highly efficient in forming soot by heterogeneous processes. They are, however, less efficient in forming aromatic species although the reaction does apparently increase

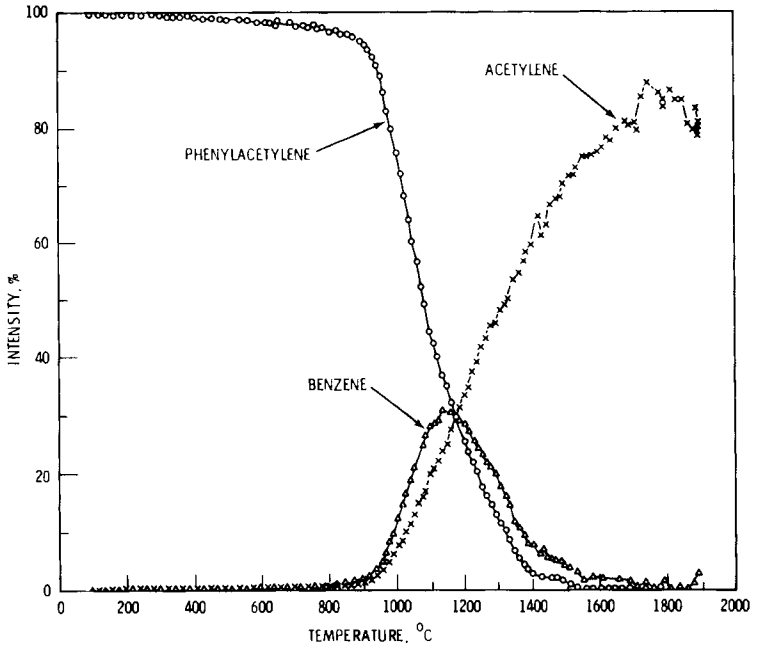

Figure 1.1. Profiles for the Major Species Involved in the Pyrolysis of Phenylacetylene. (Note that benzene is clearly an intermediate in acetylene formation.)

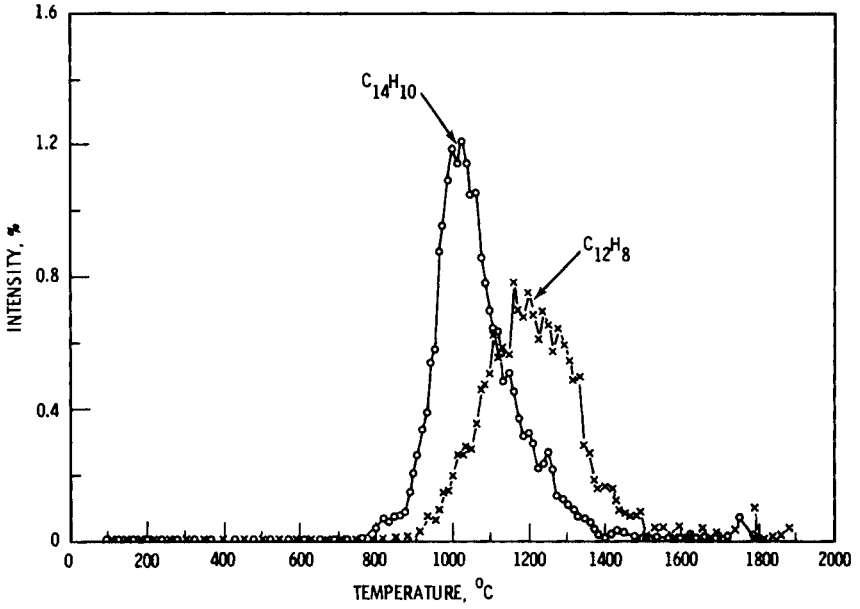

Figure 1.2. Profiles for Two of the Higher Molecular Weight Polycyclic Aromatic Products from the Pyrolysis of Phenylacetylene

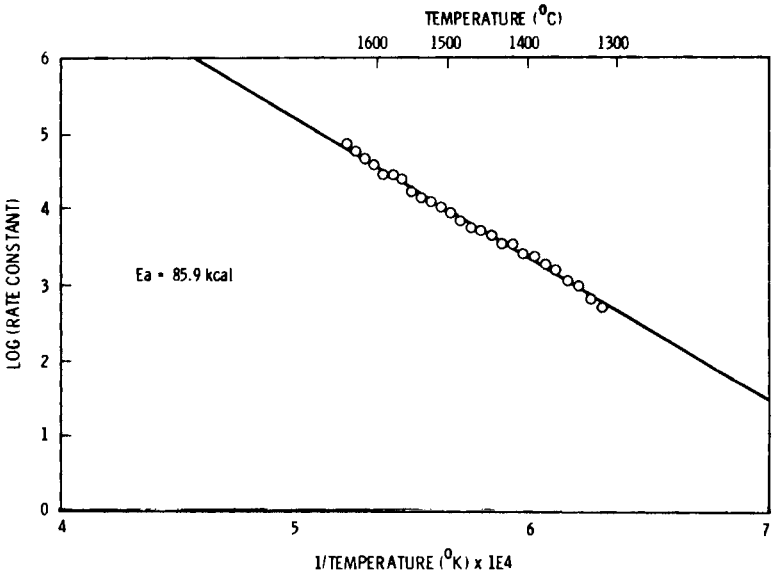

Figure 1.3. Typical Rate Data Obtained in a Study of the Decomposition of Benzene at 10^{-3} Torr and Approximately 3 ms Reaction Time

greatly upon cooling. Our gas phase studies have also identified a number of highly reactive intermediate hydrocarbons for the formation of higher molecular weight compounds (e.g., C_3H_3, C_4H_3, C_5H_3, and C_7H_7). Experiments are being planned to better define the heterogeneous chemistry of these high-temperature aromatic systems, to relate experimental results to actual combustion experiments and to explore equilibrium calculations for estimating the concentrations of important species at high temperatures.

Development of New Methods and Instrumentation for Liquid Chromatography/Mass Spectrometry

Richard D. Smith

A novel approach to liquid chromatography/mass spectrometry (LC/MS) combining a number of new concepts has been developed. The new approach uses a moving ribbon interface for transfer of material to the high vacuum region for analysis using secondary ion mass spectrometry (SIMS) as well as laser desorption (LD). The new moving ribbon interface also allows temporary storage of the separated sample for reanalysis of selected portions of the ribbon surface. Other novel features of the instrument include a silver vapor deposition unit for ribbon cleaning and surface preparation, and a triple quadrupole mass spectrometer for enhanced selectivity in many cases. While development of this technique is still in an early stage, initial results suggest extremely high sensitivities for many classes of unstable or nonvolatile compounds.

The need for a LC/MS interface which can efficiently handle nonvolatile and thermally unstable molecules is well recognized. Field desorption (FD) mass spectrometry is effective for the analysis of many such compounds, but a direct interface between the chromatograph and the mass spectrometer has not been constructed due to the high voltages and precise mechanical alignment required. Existing commercial LC/MS interfaces use either (1) introduction of a small flow of the LC effluent directly into a heated chemical ionization (CI) source; or (2) deposition of the effluent on a moving ribbon with evaporation of the volatile mobile phase and progression through a series of vacuum locks, and volatilization or pyrolysis of the material in or adjacent to a conventional CI or electron impact ion source. These and related interfaces have been demonstrated to be effective for a wide range of compounds, but their application for the analysis of nonvolatile and thermally labile compounds is limited at best. Recently, it has been recognized that a variety of alternate ionization methods produce mass spectra which are remarkably similar to those obtained by FD. These techniques include "in-beam" chemical ionization on Teflon® probes or special surfaces, secondary ion mass spectrometry (SIMS), ^{252}Cf plasma desorption, and laser desorption.

We have constructed a moving ribbon LC/MS interface for operation with either SIMS, LD, or conventional heating-electron impact ionization methods, and have begun to explore the various approaches. Figure 1.4 is a schematic diagram of the

® Registered trademark of E. I. duPont de Nemours and Co.

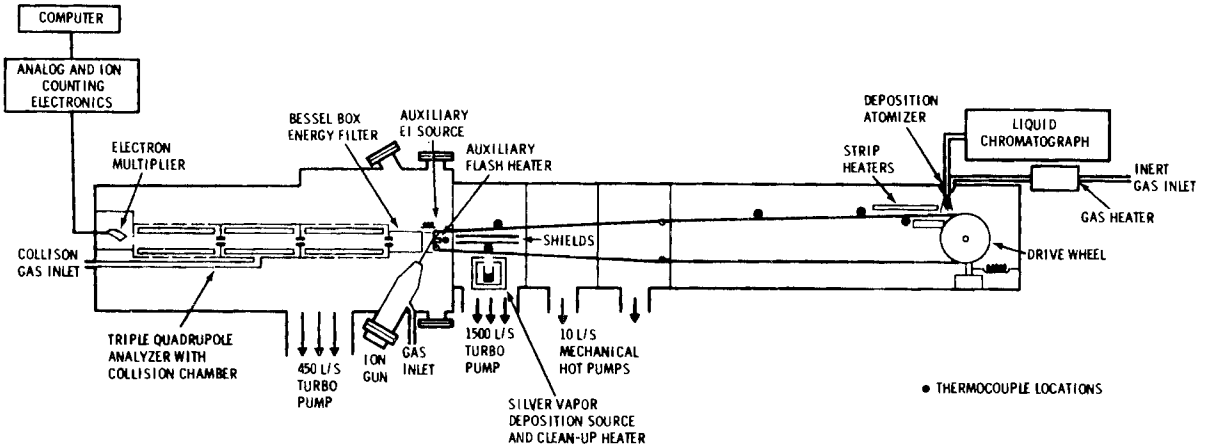

Figure 1.4. Schematic Diagram of the Liquid Chromatograph/Mass Spectrometer Designed and Constructed at PNL

LC/MS instrument constructed at Pacific Northwest Laboratory (PNL). The LC effluent is deposited on a slowly moving (5-60 cm/min) continuous ribbon (0.63 cm wide, 0.008 cm thick, 320 cm long). A unique feature of the interface is the inclusion of a 120-cm long evaporation region for the LC mobile phase before the first vacuum slit. This also allows the semipermanent storage of material. Evaporation is assisted by gentle heating (with the temperature of the ribbon maintained below the boiling point of the liquid) from strip heaters located just above and below the ribbon, a continuous flow of preheated argon, preheating of the liquid effluent, and the relatively slow speed of the ribbon. Three regions of differential pumping are employed prior to the high vacuum surface. The first two regions are pumped by "hot pumps" to limit the effects of condensable vapors during long-term pump operation, and the third by a 1500 ℓ/sec turbomolecular pump. The main drive wheel is also used to adjust ribbon tension and is motor driven through three universal joints; at no point does the sample surface of the ribbon contact another surface. The pressure in the high vacuum chamber ranges from 10^{-8} to 10^{-6} torr depending upon the required gas flow for the ion gun and mass spectrometer collision chamber.

Ions formed at the surface pass through an energy filter and are analyzed using either a single or a new triple quadrupole mass spectrometer which incorporates a chamber for collision-induced dissociation (CID) in the middle quadrupole of the triple quadrupole analyzer. The use of CID in conjunction with the LC/MS interface should greatly increase chemical specificity and the deconvolution of complex chromatograms. (The CID complements SIMS or LD ionization modes since these processes often produce spectra with intense molecular or quasi-molecular ion peaks and limited fragmentation.) We have demonstrated detection limits of <0.10 ngrams for an easily ionized material (arginine) while scanning the mass spectrometer. A significant "background" in such spectra is clearly associated with material on the ribbon; improved ribbon-cleaning techniques suggest the possibility of greatly enhanced detection limits. The recent incorporation of a silver vapor deposition unit for ribbon cleaning and surface preparation promises to considerably lower the practical detection limits by reducing the "background" of nonvolatile surface contaminants. Figure 1.5 illustrates the use of the ribbon storage system which allows use of different heating conditions, ion bombardment conditions or the triple quadrupole analyzer. The results show the LC/MS total ion reconstructed chromatogram for a biomass product for several passes through the ionization region.

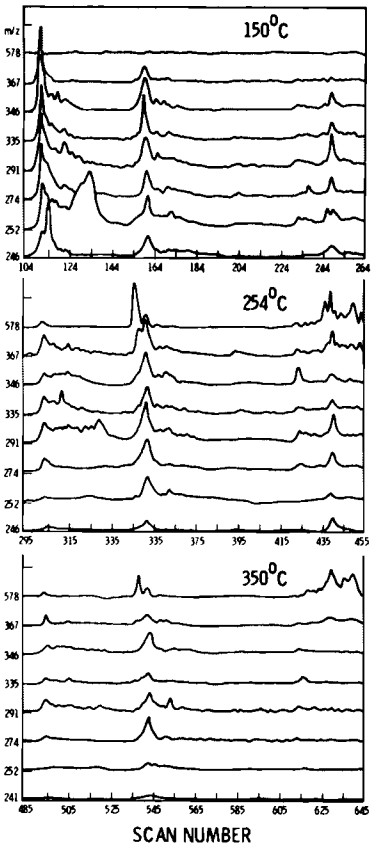

Figure 1.5. Reconstructed Total Ion Chromatogram of Biomass Bottom Material Using an NH_2LC Column and Three Different Heater Temperatures

The moving ribbon interface has several potential advantages when used with SIMS or LD ionization modes, and with CID in a triple quadrupole analyzer. First, the long evaporation region at atmospheric pressure easily allows complete evaporation of the LC mobile phase prior to the first vacuum slit; this reduces sample loss and degradation of chromatographic resolution without splashing and atomization of liquid. Second, the SIMS or LD ionization modes are highly localized processes; this allows the use of slower ribbon speeds than are allowed by "flash" heating for volatilization without loss of chromatographic resolution. Thus, ribbon temperature is no longer an important variable in determining sensitivity. Third, the ribbon

length and slow ribbon speed allow temporary storage of the separated materials for LC runs of 10-60 min, depending upon ribbon speed and required resolution; this is an important advantage since the SIMS or LD technique will consume only a minute amount of sample during the normal analysis. Thus, temporary storage allows selected portions of the separated materials stored on the ribbon to be reanalyzed after completion of the separation and initial analysis. Selected ribbon locations can be analyzed for extended periods to increase the signal/noise ratio and detection limits. More important, however, the subsequent analysis allows one to completely use the CID capability of the triple quadrupole mass spectrometer, which can only be applied during the initial separation to a limited extent due to mass spectrometer scan speed limitations. Thus, the SIMS ionization mode uniquely complements the storage capability of the interface. We are continuing to explore these analytical techniques using both the SIMS and LD ionization modes.

Characterization of Materials from the Solvent Refined Coal Processes

W. C. Weimer, B. W. Wilson, M. R. Petersen, D. M. Schoengold, D. S. Sklarew, B. A. Vieux, J. E. Burger, A. P. Toste, J. C. Kutt, R. D. Smith and D. R. Kalkwarf

Samples of products, effluents, and solid waste materials are being obtained from the solvent refined coal (SRC) II facilities in Fort Lewis, Washington, and Harmerville, Pennsylvania, and from the SRC-I facility in Wilsonville, Alabama. Samples have also been obtained from the Fort Lewis, Washington, pilot plant when operating in the SRC-I mode. (The SRC-II research is funded by the Office of Health and Environmental Research, while Fossil Energy is funding the research with SRC-I materials.) These samples have been collected during a variety of operating conditions including those which are considered to be representative of demonstration-scale or commercial-scale conditions. We have three objectives in obtaining these samples: (1) to obtain quantities of representative materials to be stored in a repository and subsampled as required for chemical, biological, and ecological testing; (2) to obtain general chemical composition data for all materials; and (3) to obtain very detailed compositional data for those samples, or fractions of samples, that have a demonstrated biological activity. The ultimate goal of this third objective is to identify the compounds responsible for the biological activity.

We are required to prepare, on a regular basis, status reports regarding specific areas of our SRC research. Summaries of two recently prepared status reports are listed at the end of this report. Additional areas of significant research activities which are not discussed in these two status reports are summarized briefly below.

All sample materials from the SRC-I and SRC-II processes are maintained in a repository and are tracked by a computerized materials accounting system. The samples are stored in the dark at a temperature of 4°C and are kept under an N_2 blanket. The purpose of this storage technique is to prevent or retard changes in chemical composition that may occur during storage. Several characterization analysis techniques that provide a fingerprint of sample composition are used when samples are first received and at six to twelve month intervals thereafter. These provide necessary documentation of sample stability. The computerized accounting system is used to track the quantity of each material remaining in the repository and to identify the principal investigators to whom subsamples of these materials have been released.

The very complex chemical make-up of the SRC materials often requires the modification of existing methods or the development of new methodologies for the chemical and biological analyses of these materials. There are several areas of continued methodology development. One of these is the comparison of different methods of chemical fractionation to prepare samples for subsequent biological assay. The purpose of this investigation is to develop a methodology that is capable of (1) providing sample purification to simplify the biological and chemical analyses, (2) isolating compound classes of greatest biological interest, (3) concurrently obtaining general chemical class distribution data for characterization, and (4) eliminating possible synergistic or antagonistic effects that may be present in the complex mixtures. High performance liquid chromatography and partition chromatography on Sephadex LH-20 followed by high performance liquid chromatography of the Sephadex fractions are the most useful of the methodologies examined. An additional area of research on methodology development is related to the examination of several solid substrates for the collection of organic vapors. This research is directed particularly at the

monitoring of laboratory environments, and those pilot plant and demonstration plant environments where significant worker exposure is likely.

Several new instrumental techniques are being developed for analysis of these complex SRC materials. A new approach to liquid chromatography/mass spectrometry (LC/MS) is being developed to analyze the less volatile and thermally unstable compounds in SRC liquids. This new approach uses a "soft" ionization technique at the MS inlet and a semipermanent storage of the separated LC materials to allow multidimensional mass spectral analysis. The development of this technique and the initial results obtained are described elsewhere in this annual report. Specialized detector systems for liquid chromatography that are sensitive principally to aromatic amines are being developed. These include both electrochemical detection systems and post-column chemical derivatization/fluorescence detectors. High resolution probe mass spectrometry coupled with metastable ion analysis is being used for the direct identification of higher molecular weight N-containing compounds. This approach provides a differentiation between aza compounds and primary amine compounds having identical masses. This differentiation is extremely important in characterizing the actual biologically active components of the SRC materials.

Initial Chemical and Biological Characterization of Hydrotreated Solvent Refined Coal (SRC-II) Liquids: A Status Report, PNL-3464

This status report compiles the results of chemical and biomedical studies of a hydrotreated refined coal liquid. Analyses of both feedstock and hydrotreated materials showed that concentrations of multiring aromatic and heteroatomic aromatic compounds decreased with commensurate increase in hydroaromatic species as a function of the extent of hydrogenation. A decrease in positive responses by the Ames assay of selected fractions was consistent with the decrease in nitrogen-containing compounds during hydrogenation. For example, primary aromatic amines which were detected in the feedstock were reduced to undetectable levels after hydrotreating.

Chemical, Biomedical, and Ecological Studies of SRC-I Materials from the Fort Lewis Pilot Plant, PNL-3474

SRC-I materials obtained from the Fort Lewis, Washington pilot plant have been analyzed using both chemical and biological assays. Inorganic analysis indicates decreased concentrations of most mineral elementsin the SRC-I product as compared to the feed coal. Bromine, titanium, and mercury, however, were not decreased. Among the organic components identified in SRC-I process streams were phenols, polynuclear aromatics, and nitrogen bases, including primary aromatic amines, which may be of biological or environmental concern. Additional chemical fractionation studies suggest that primary aromatic amines are major determinants of mutagenic activity expressed in the Ames assay. The report also discusses further biological and ecological assays, including toxicity, fetal development, tissue distribution, and plant germination.

• Modeling Cellular Effects of Coal Pollutants

Increasing interest in coal and in coal-derived fossil fuels as energy sources has prompted renewed concern over the environmental and health impacts resulting from coal refinement and combustion. The goal of this project is to develop and test models for the dose and dose-rate dependence of biological effects of coal pollutants on mammalian cells in tissue culture. Particular attention is given to the interaction of pollutants with the genetic material (deoxyribonucleic acid, or DNA) in the cell because the work of McCann and Ames (1975) has demonstrated a strong correlation between mutagenesis and cancer induction. Unlike radiation, which can interact directly with chromatin, chemical pollutants undergo numerous changes before the ultimate carcinogen becomes covalently bound to the DNA. Synthetic vesicles formed from a phospholipid bilayer are being used to investigate chemical transformations that may occur during the transport of pollutants across cellular membranes. The initial damage to DNA is rapidly modified by enzymatic repair systems in most living organisms. Increased cancer incidence among humans with hereditary repair deficiencies suggests that repair processes are important in reducing the risk to the normal population from chronic exposure to low levels of carcinogens. A model has been developed for predicting the effects of excision repair (the removal of carcinogen residues from DNA) on the survival of human cells exposed to chemical carcinogens. In addition to the excision system, normal human cells also have tolerance mechanisms that permit continued growth and division of cells without removal of the damage. We are investigating the biological effect of damage passed to daughter cells by these tolerance mechanisms. Chinese hamster ovary cells are being used for these studies because they tolerate a larger degree of carcinogenic damage than human cells. We feel that these cellular studies are a valuable complement to whole-animal and epidemiological studies in assessing the health effects of coal-related pollutants.

Modeling the Dose-Response Relationship for Survival of Human Cells Exposed to Chemical Carcinogens

J. H. Miller

The ability of cells to repair damage to deoxyribonucleic acid (DNA) molecules is an important factor in determining the cytotoxic and mutagenic effect of chemical carcinogens at a given dose. This fact is consistently demonstrated by the differential cytotoxicity between normal human cells and cells from patients with the disease xeroderma pigmentosum (XP). Because of a genetic deficiency, XP cells have a greatly reduced ability to excise some carcinogen adducts from their DNA. An analogous situation exists in the repair of damage induced by ultraviolet (UV) irradiation in the excision-repair-deficient bacteria *Escherichia coli* UVr^-.

For the bacteria case, Haynes (1975) demonstrated that the survival of normal cells after UV irradiation can be predicted if the sensitivity of the repair-deficient mutant and the kinetics of excision in the normal cell are known. We have applied the same type of model to the cytotoxicity induced in normal and XP human fibroblasts by the carcinogen N-acetoxy-2-acetylaminofluorene (N-AcO-AAF). Compounds of this type may result from the in-vivo reduction of nitrate derivatives of benzo-[a]pyrene. A paper on this work, which is being done in collaboration with Dr. R. H. Heflich at the National Center for Toxicology Research, has been accepted for publication in the proceedings of the 20th Hanford Life Sciences Symposium.

Little is known about the mechanism of reproductive death in cells exposed to chemical carcinogen. Although bonding to

molecules other than DNA may play a role in the biological response, the data of Heflich et al. (1980) suggest that potentially lethal damage and residues bound to DNA are removed at the same rate. Our model assumes that the mechanism of reproductive death involves an expression time during which potentially lethal damage is removed from the DNA of cells capable of excision repair. This leads to the relationship

$$\ln S = \ln S_{XPA} (1 - f) \qquad (1)$$

between the survival S of cells that excise a fraction f of the damage and the survival of XP cells from complementation group A, which do not exhibit any excision of AAF residues.

Figure 1.6 compares the survival of cloning ability in fibroblasts from normal humans with that from XP patients from several complementation groups (Maher et al. 1975; Heflich et al. 1980). Both the concentration of N-AcO-AAF in the growth medium and the initial number of residues bound to DNA are shown on the horizontal axis. From the dose that results in 37% survival of XPA cells, we estimate that about 10^5 residues are required to produce an average of one potentially lethal event per cell. The small probability that a residue will cause reproductive death may be due to nonessential genes in the human chromosome and to repair phenomena other than excision that permit replication of DNA on a damaged template. (The possibility of subsequent biological effects

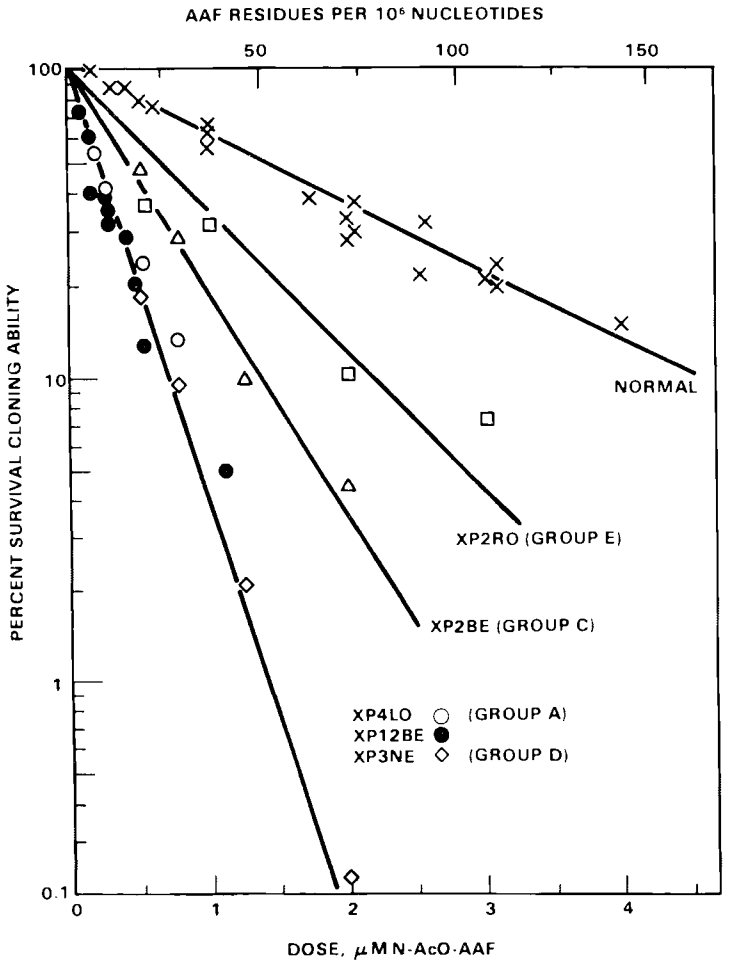

Figure 1.6. Survival of Normal and Xeroderma Pigmentosum (XP) Fibroblasts After Exposure to N-Acetoxy-2-Acelytaminofluorene (N-AcO-AAF)

resulting from damage passed to daughter cells is discussed in the following article in this report.)

The principal objective of our model is to obtain a quantitative correlation between survival data, such as those shown in Figure 1.6, and data derived from biochemical repair studies. If the excision of residues obeys classical enzyme kinetics, then the rate of excision is given by the Michaelis-Menton equation

$$\frac{d[P]}{dt} = \frac{V[R]}{K + [R]} \qquad (2)$$

where R is the concentration of carcinogen residues, P is the concentration of excised product, V is the high-dose limit of the removal velocity, and K is the dose at which the rate of removal is half its maximum value. When $[R] \ll K$, Equation 2 reduces to a first-order rate equation, and the number of residues decays exponentially with a lifetime $t = K/V$.

Levinson et al. (1979) have proposed a procession model of excision repair in which the repair enzymes travel unidirectionally along the DNA strand, rather than randomly attaching and detaching as is assumed in the classical model. In the processive model, the rate of excision does not decrease as residues are removed but maintains a constant value that is a function of the initial number of adducts on DNA. If k_t is the rate of travel of the repair complex along the DNA strand and K_e is the rate of excision and resynthesis at the damage site, then the rate of removal is related to the initial number of bound residues by a Michaelis-Menton equation with $V = k_e E$ and $K = k_e/k_t$.

Figure 1.7 shows the time course for removal of AAF residues at a dose less than 5 μM. The solid line shows a fit assuming a constant rate of removal over the first 18 h after treatment. The dashed curve illustrates the predictions of the classical first-order model with an initial removal rate equal to that of the processive model. The scatter in the data is too large to allow the two models to be distinguished on the basis of accuracy of fit.

Figure 1.8 shows the initial removal rate as a function of the initial number of bound residues. In most cases, the initial velocity was estimated from measurement of the number of adducts present 18 h after treatment. This procedure slightly underestimates the initial velocity if the number of residues decays exponentially instead of linearly. The data shown in Figure 1.8 cannot be used to distinguish between processive and classical kinetics because both models predict a Michaelis-Menton type of relation for the dose dependence of the initial removal velocity. Hence we conclude that the biochemical repair data currently available are consistent with either model. The data in Figure 1.8 show that if the classical model is valid, then 1) first-order kinetics are a good approximation in the dose range of the survival data shown in Figure 1.6, and 2) the mean lifetime of AAF residues on DNA in the normal human fibroblast is about 70 h.

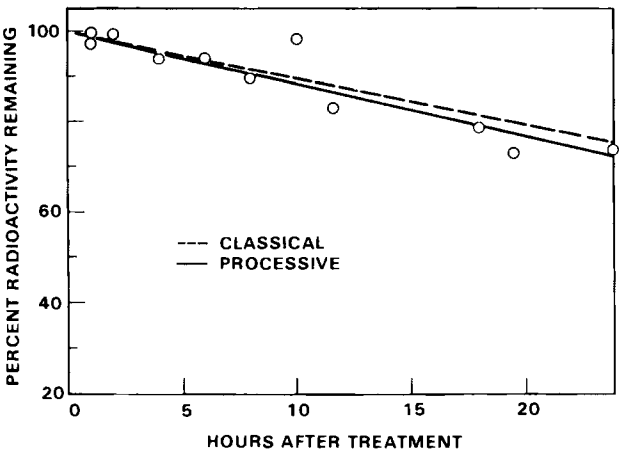

Figure 1.7. Fraction of AAF Residues Bonded to DNA as a Function of Time After Treatment

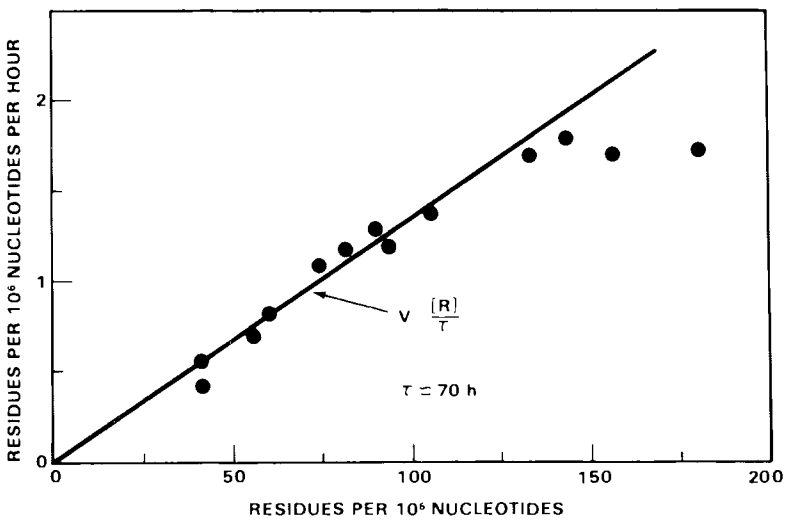

Figure 1.8. Initial Rate of Excision of AAF Residues in Confluent Human Fibroblasts as a Function of Initial Number of Bond Adducts

If the excision of AAF residues obeys classical first-order kinetics, then our model predicts a dose-response relationship of

$$\ln S = \ln S_{XPA}\, e^{-T/\tau} \qquad (3)$$

If the processive model is correct, the survival should be given by

$$\ln S = \ln S_{XPA}\,(1 - T/\tau) \qquad (4)$$

Equations (3) and (4) both predict an exponential survival curve, since the survival response of XP cells from complementation group A is exponential. Excision repair modifies the slope of the plot of ln S versus dose, making it less negative as a larger fraction of the damage is excised. Hence these simple models cannot account for shoulder effects such as that shown in Figure 1.6 for normal cells.

One way to explain this shoulder is to assume that excision of AAF residues is predominantly a first-order process but has a processive component that saturates at low dose and a maximum velocity that is small compared to the data in Figure 1.8. Other possible explanations for the shoulder on the dose-response curve for normal cells include 1) effects related to the kinetics of bonding and/or nonrandom bonding, 2) biological effects of damage passed to daughter cells by tolerance mechanisms, and 3) interactions between carcinogen residues.

More data at low dose are needed to develop and test models for the shoulder region of the dose-response relationship. We are testing the prediction of Equations (3) and (4) regarding the slope of the exponential part of the survival curve. One experiment in progress concerns the survival of partially repair-deficient XP cells. Figure 1.6 suggests that the fraction of AAF residues excised by XP cells from complementation groups C and E is substantially less than the fraction excised by normal cells. One way to account for this difference is to assume that under the same experimental conditions, all three cell lines have the same time available to excise AAF residues before the damage can be expressed as reproductive death. The difference in the extent of repair is then due to the difference in the rate of excision. If excision is a first-order process, then the ratio of the repair rates in normal, XP2RO, and XP2BE cells would be 1:0.6:0.4. These ratios would be 1:0.8:0.6 for processive repair kinetics. More survival and repair studies are planned with the cells XP2RO and XP2BE to test these predictions.

Figure 1.9 shows the results of another experiment designed to test our model of the dose-response relationship. Normal human cells in a confluent state were treated with N-AcO-AAF and then held at confluence to recover from the damage. They were then replated at low density to score survivors. At a given dose, survival increases with

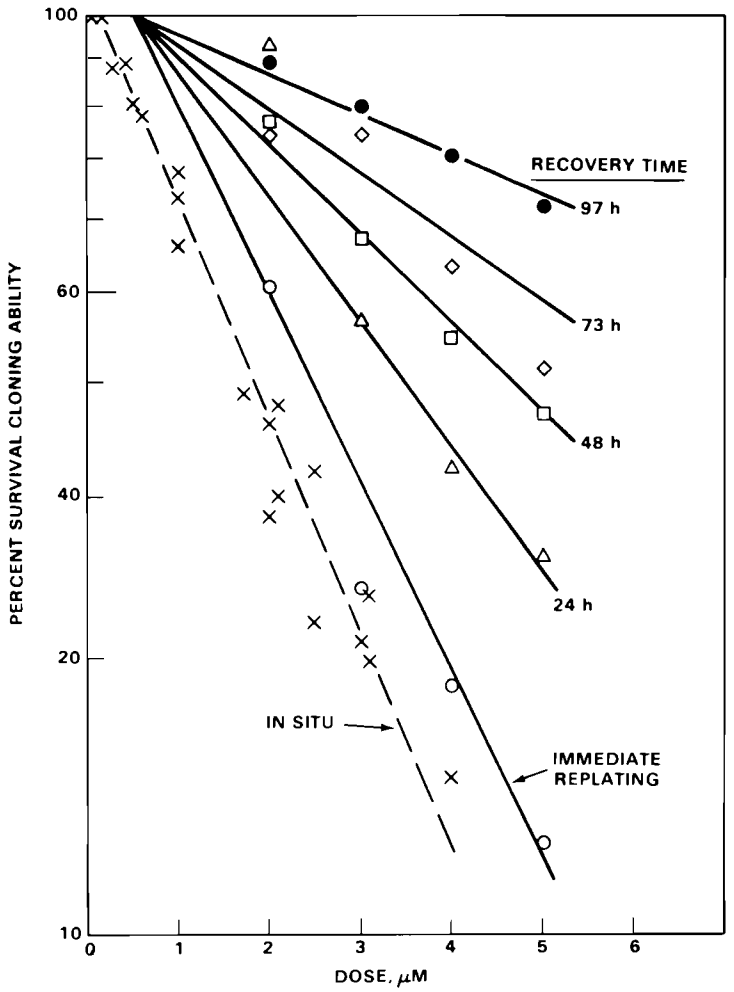

Figure 1.9. Survival of Normal Human Fibroblasts Treated with N-AcO-AAF and Held in a Nonproliferating State Before Replating to Measure Cloning Efficiency

recovery time, as would be expected if the time spent in the nonproliferating state increased the time available for repair. The survival data for normal human fibroblasts treated with N-AcO-AAF when the cells were growing at low density are also shown in Figure 1.9 (replotted from Figure 1.6). The slope of the exponential part of these survival data is nearly the same as the slope of the data for cells treated at confluence and immediately replated. However, the shoulder on the in-situ data is substantially smaller than that obtained when cells were treated at confluence. This suggests that the position of cells in the growth cycle may be an important consideration in modeling the shoulder on survival curves.

Estimates of the effect of recovery on the fraction of potentially lethal damage excised are given in Table 1.1. The fraction of damage excised is nearly independent of dose for a given recovery time. The slight tendency for the fraction to decrease with increasing dose is probably due to the shoulder on the survival response for normal cells treated at confluence. The fraction of damage excised at a dose of 5 μM when cells were immediately replated is used to estimate the time available for repair without recovery. This estimate is 142 h if the kinetics of excision are first order and 61 h if repair kinetics are processive. Given the time available for repair when cells are immediately replated, we predict the fraction of damage

Table 1.1. Effect of Recovery on the Fraction[a] of AAF Residues Excised by Normal Human Fibroblasts

Dose, μM	f_0	f_{24}	f_{48}	f_{73}	f_{97}
2	0.90	0.99	0.96	0.95	0.98
3	0.86	0.92	0.94	0.97	0.98
4	0.88	0.92	0.94	0.95	0.97
5	0.88	0.92	0.94	0.95	0.97
first-order[b]	—	0.91	0.94	0.96	0.97
processive[c]	—	1.0	1.0	1.0	1.0

[a] $f_\triangle = 1 - \ln S_\triangle / \ln S_{XPA}$ where $S_\triangle$ is the survival of normal cells held in confluence for $\triangle$ hours between treatment and replating, and S_{XPA} is the survival of XP12BE cells.

[b] Model prediction assuming first-order excision kinetics.

[c] Model prediction assuming processive excision kinetics.

excised when the cells are held at confluence between treatment and replating. These results are shown in Table 1.1, where it can be seen that the increase in the extent of repair with recovery is predicted very well by our model when classical first-order kinetics are used. If the kinetics of excision repair are processive, the increase in time available for repair in the recovery experiments should be sufficient to remove all the damage. This is not observed in the experiments. The success of our model in explaining the effects of recovery on survival encourages us to investigate the mechanism of reproductive death in cells exposed to chemical carcinogens. This mechanism should be consistent with the time available for repair that is suggested by our analysis of the survival data.

Biological and Biochemical Experimentation with Coal-Related Carcinogens

C. N. Newman

In this project, active forms of polynuclear aromatic hydrocarbon pollutants generated during the utilization of coal are being studied so that their effects on mammalian cells can be modeled in tissue culture. The presumptive consequences of radiologically and chemically induced chromosome damage on cell survival, induced mutation, and repair processes are similar, and mathematical approaches to one type of damage have been applied to the other (Lawley 1979; Munson and Goodhead 1977). In general, both show a dose-dependent survival and mutation response, and the damaged chromosomes appear to share common repair pathways (Maher and McCormick 1978).

Little information is available on the formation of carcinogen-induced damage at low concentrations of pollutants and on the corresponding significance of cellular repair processes other than error-free excision repair. Excision repair seems to predominate at high doses in human fibroblasts, but even so some lesions remain unexcised in viable cells (Maher and McCormick 1978). We do not know the consequences of residual damage, which may be cumulative at low doses. Because few if any lesions are excised from Chinese hamster ovary (CHO) cells, this cell system has been chosen to examine the fate of unexcised chemical lesions and to study other repair pathways that may be error-prone and may therefore bear more significantly on carcinogenesis.

Experiments in progress are designed to provide information on 1) the relationship between pollutant dose and cellular inactivation, mutation, and biochemical repair processes; 2) the kinetics of induction and repair of damage to deoxyribonucleic acid (DNA), and 3) the development of mutants with altered repair abilities. Repair-deficient CHO mutants have already been isolated (Stamato and Hohman 1975). We have approached this problem from a unique perspective by selecting repair-proficient mutants, cell lines with a repair ability more efficient than that of the parent cell line. For simplicity, we used ultraviolet (UV) light to induce lesions in cells because some of the enzymes that repair these lesions also repair some chemical-DNA adducts (Maher and McCormick 1978). Approximately 50 isolates have already been selected and are now being characterized with respect to enhanced repair abilities.

Figure 1.10 shows the survival of CHO cells after exposure to low concentrations of benzo[a]pyrene-4,5-epoxide. These data are consistent with the results obtained at higher doses by Huberman et al. (1976) using Chinese hamster V-79 cells. Even at low carcinogen concentrations, cellular inactivation is a simple exponential function, that is, there is no shouldered response. Figure 1.11 shows the corresponding alkaline CsCl density-gradient assay for replication repair of damaged DNA in cells treated with 0.8 μM of carcinogen. There is no detectable increase in the amount of ^{3}H-thymidine incorporated in parental DNA over a 45-h period, indicating

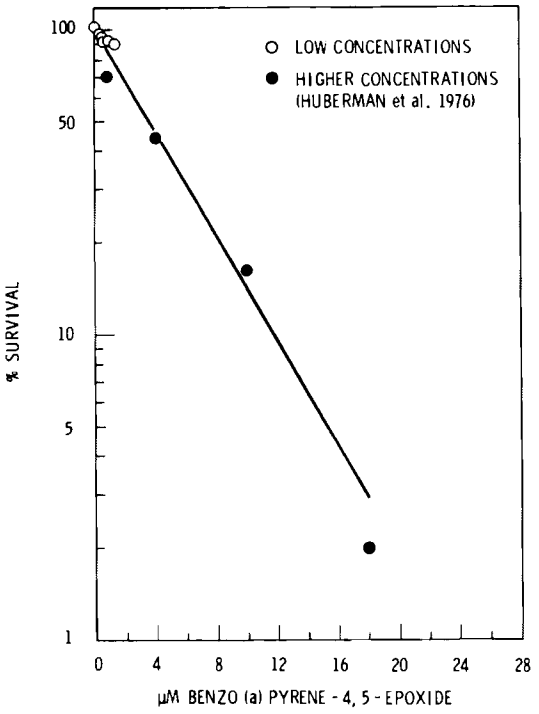

Figure 1.10. Survival of CHO Cells After Exposure to Benzo[a]pyrene-4,5-Epoxide

that little or no repair has occurred. Interestingly, preliminary data (not shown) failed to demonstrate the induction of mutants at doses up to 1.2 μM. This result contrasts with data shown in Figures 1.12 and 1.13 for cells treated with UV light. Low fluences of UV irradiation (<50 ergs/mm^2) proved relatively inefficient at killing cells (in the shouldered region of the survival curve); however, the frequency of mutation induction appears to be a linear fluence-dependent function, extrapolating approximately through the origin. These findings are being examined further.

To study genetic damage in CHO cells treated with carcinogens, the hypoxanthine-guanine phosphoribosyl transferase (HGPRT) mutation system, as described by Hsie et al. (1975), was selected. The HGPRT enzyme is normally a component of a purine salvage pathway. When challenged with the purine analogue, 6-thioguanine (TG), wild-type cells with functional enzyme incorporate lethal quantities of this substance in their DNA while mutant cells, unable to synthesize HGPRT, survive. Expression of the mutant phenotype usually requires continuous growth and division for 7 to 9 days after treatment before cells can be

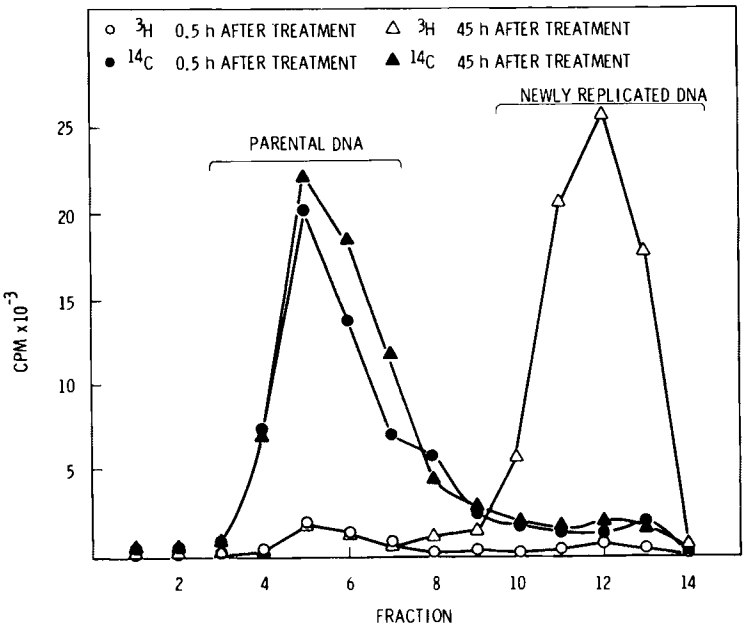

Figure 1.11. Replication Repair of CHO Cells Following Treatment with 0.8 μM of Benzo[a]pyrene-4,5-Epoxide. Cultures were grown for about five generations in medium containing ^{14}C-thymidine. After treatment with carcinogen, cells were grown in the presence of ^{3}H-TdR, BUdR, and FUdR and DNA was periodically analyzed on alkaline CsCl gradients.

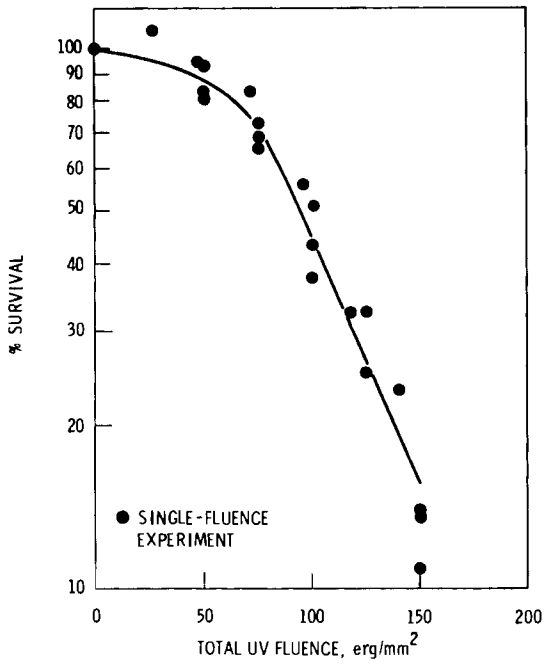

Figure 1.12. Inactivation of CHO Cells by Ultraviolet Light

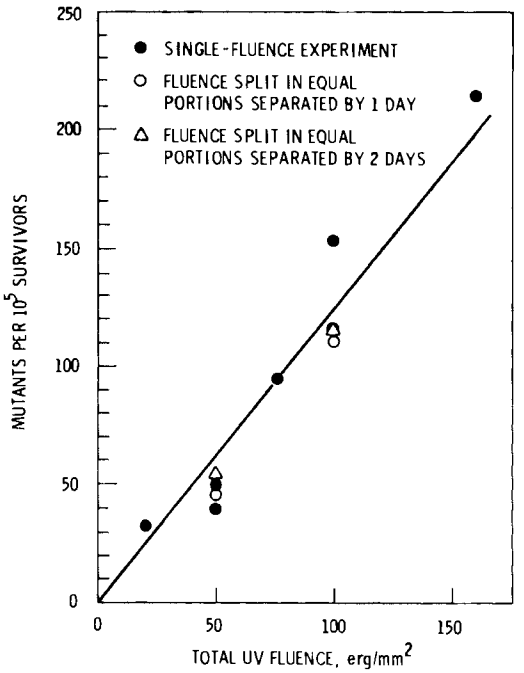

Figure 1.13. HGPRT Mutation Induction in CHO Cells by UV Light

challenged with TG. This expression period allows pre-existing HGPRT protein molecules to be diluted to low concentrations in mutant cells. Circumvention of the phenotypic expression period for HGPRT, one goal of this project, would greatly facilitate determination of the biological effect of residual damage, as will be discussed.

Figure 1.14 illustrates schematically the configuration of chemically-induced chromosomal lesions, C, in the HGPRT locus immediately after treatment (G = 0) and at up to two generations (G = 2) thereafter. Following the first round of semiconservative DNA replication and segregation of sister DNA molecules to daughter cells (G = 1), chemical adducts are confined to only one strand of a duplex. (Recombination is insignificant in CHO cells.) The fraction of cells with residual damage decreases by one half each generation, beginning at G = 2. If the damage remains biologically effective, then the number of

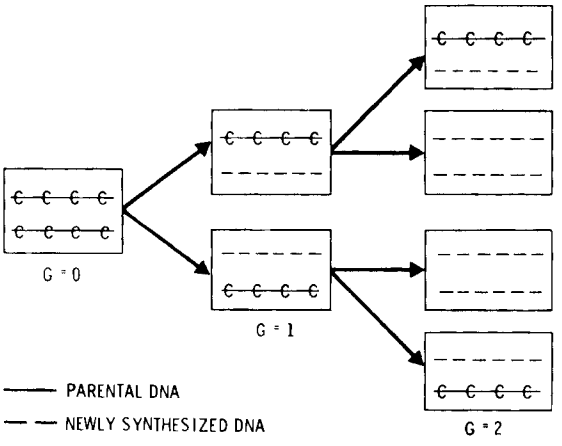

Figure 1.14. Schematic Representation of Carcinogen Residues, C, in HGPRT Locus of Cells at up to Two Generations, G, After Single Exposure to Chemical Carcinogen

HGPRT mutants per survivor after G generations of growth during the expression period is given by

$$M_G = p[C] + 1/2p[C] + \frac{1/2p[C]}{2} + \ldots + \frac{1/2p[C]}{2^{G-1}}$$

here p is the probability per adduct of a mutation in the HGPRT locus and [C] is the carcinogen dose. Each round of replication during the phenotypic expression period should increase the mutation frequncy by 50% of the number of mutants formed in the previous generation. If damage on both strands is required for mutation of the HGPRT locus, then no enhancement of the mutation frequency caused by growth and division should be observed.

To determine the mutation yield after each generation, we are attempting to bypass the required 7 to 9 days of cell division prior to the challenge with TG, while still permitting phenotypic expression in nongrowing cells. The rationale for this effort is that natural protein turnover is enhanced in arrested cells (O'Neill and Hsie 1979); thus, if growth could be arrested immediately or at specific times after treatment, HGPRT would decay to low concentrations in nondividing mutant cells, probably over a 7- to 10-day period.

We have tried several methods for arresting cell growth. 1) Cells were kept in a serum-free medium in agar-coated flasks (to prevent attachment). The survival of these cells was variable from experiment to experiment and among cells from different culture vessels in the same experiment, ranging from 100% to 2% of the survival of untreated cells. 2) Cells were allowed to attach in growth medium diluted to 1% fetal calf serum (FCS). The results of a typical experiment of this type are shown in Figures 1.15 and 1.16. Cells in 1% FCS stopped growing at 3 x 10^4 cells/cm^2, while fully supplemented cells (10% FCS) grew to a density five to six times higher (Figure 1.15). Figure 1.16 shows the results of labeling these cells with 15-min pulses of ^{3}H-thymidine to measure rates of DNA replication at various times after the medium shift. The rate of replication in serum-limited cells decreased continuously after 20 h to about 1% of the maximum rate in the control culture. Replication in the controls also declined after about 80 h when these cells entered the plateau phase. However, cells

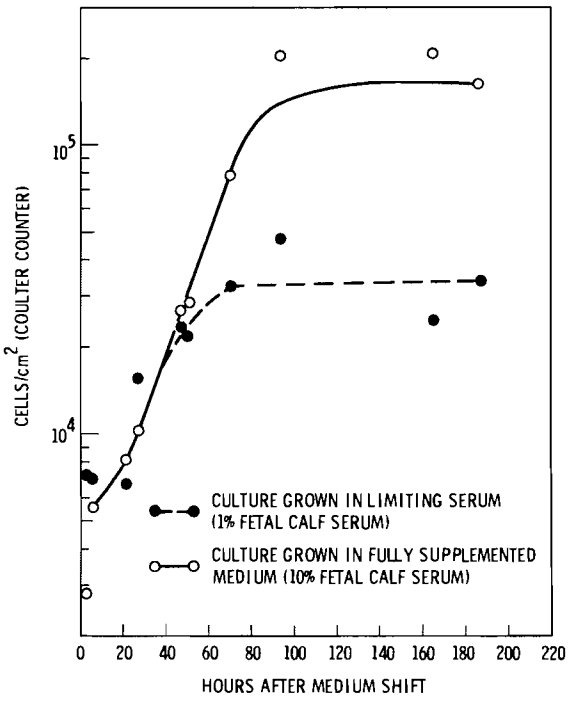

Figure 1.15. Inhibition of Cellular Growth by Serum Limitation

in the diluted medium remained viable (20% cloning efficiency), whereas the control culture did not. Experiments to improve the cloning efficiency of limited cells are directed toward maintaining culture pH within the physiological range over an extended time. The arresting of suspension cultures of CHO cells in 1% FCS is also being investigated, as suggested by R. Heflich of the National Center for Toxicology Research.

Experiments to examine the potential hazard of damage accumulated in DNA through tolerance mechanisms are also under way. If damage is effective only when it occurs on both DNA strands, then lesions on a single DNA strand may sensitize daughter cells to further exposure to the carcinogen. This effect should be observable in split-dose experiments. Figure 1.17 illustrates the configuration of lesions in the HGPRT locus that might result from equal fractions of a dose D separated by one generation. In this case we would expect the increase in mutation frequency caused by dose fractionation to be 25% of the single-dose value. The enhancement of the mutation frequency decreases rapidly as the interval

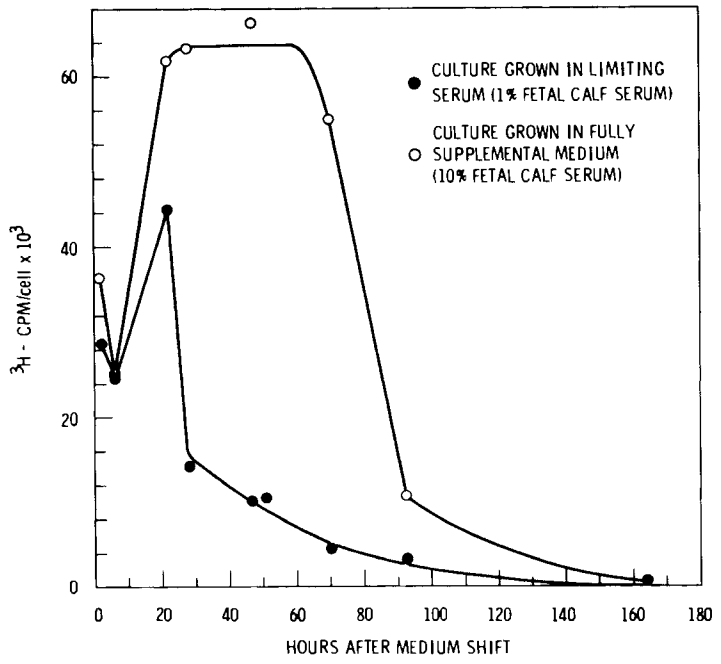

Figure 1.16. Rates of DNA Replication

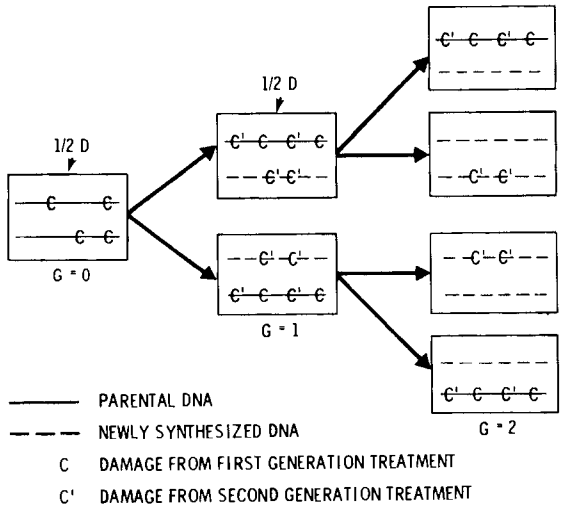

Figure 1.17. Schematic Representation of Carcinogen Residues in HGPRT Locus Resulting from Equal Fractions of a Dose, D, Separated by One Generation

between fractions increases because replication dilutes the population of cells that have been sensitized by the first fraction.

Figure 1.13 shows the results of a preliminary split-dose experiment using UV light as the carcinogen. Equal fluences were given 1 or 2 days apart (approximately 2 and 4 generations, respectively), followed by 8 days of growth for expression of HGPRT mutants. No significant increase in the mutation frequency was observed for the split-dose treatment relative to the single-dose treatment. The time interval between treatments may have been too large to give an enhancement greater than the usual statistical fluctuations. Control of DNA replication through growth arrest should increase the sensitivity of these split-dose experiments.

Permeabilities of Model Lung-Cell Membranes to Coal Pollutants

D. R. Kalkwarf

Sulfur dioxide and polycyclic aromatic hydrocarbons are pollutants common to stack emissions from all coal-fired power plants. Sulfur dioxide and its hydrolysis products, HSO_3^- and SO_3^{-2}, are known to be lung irritants; recent reports (Hayatsu 1976; Shapiro 1977) suggest that they could also exert mutagenic effects on lung cells. The probability of this occurring would depend

on the ability of the dominant species at physiological pH, HSO_3^-, to cross the cytoplasmic and nuclear membranes and react with deoxyribonucleic acid (DNA) before being oxidized to the relatively innocuous SO_4^{-2}. Similarly, some polycyclic aromatic hydrocarbons (PAHs) such as benzo[a] pyrene have been shown to be carcinogenic in skin-painting tests on mice, but the kinetics of PAH uptake by lung cells is not known in sufficient detail to predict rates of PAH diffusion into the cell nucleus or even to predict whether PAHs can diffuse across cell membranes at significant rates without chemical alteration of the PAH to a more polar derivative.

To estimate how rapidly HSO_3^- and representative PAHs diffuse across lung-cell membranes, we have evaluated the permeability coefficients of lung-phospholipid bilayer membranes to these pollutants in vitro. The results obtained to date indicate that HSO_3^- diffuses across these basic structural barriers in lung cells with its chemical reactivity intact as rapidly as Cl^-, but that the PAH, pyrene, does not enter these bilayers in unmodified form.

The phospholipid membranes were prepared in the form of residues by sonicating 2% suspensions of either dipalmitoylphosphatidylcholine or stearoyl sphingomyelin in $\mu = 0.20$ sodium phosphate buffer at pH 6.0. Multilayered residues were removed by centrifugation and the remaining vesicles, each bounded by a single phospholipid bilayer, were used in this investigation. These structures have an outer diameter of 25 nm and a membrane thickness of 6 nm, and are shown schematically in Figure 1.18.

Permeability evaluations for HSO_3^- were based on the bleaching rates of dye-loaded vesicles exposed to external HSO_3^-. Basic Violet 15 (C.I. 42510), a dye that is selectively bleached by HSO_3^-, was used for this purpose. Solutions of this dye in the above-mentioned buffer were incorporated inside the vesicles during sonication, and exterior dye solution was removed by passing the vesicle suspension through a Sephadex G-75 gel-filtration column. The absorbance of the dye-loaded vesicle suspension was then monitored at 539 nm with a spectrophotometer before and after the addition of a measured amount of HSO_3^- solution. Independent measurements showed negligible leakage of dye from the vesicles during this period. In suspensions where the vesicles contained no dye but were surrounded by dye, the bleaching rates were found to be much greater initially, as shown in Figure 1.19.

Permeability coefficients were calculated on the basis of the following mechanism:

$$(HSO_3^-)_{external} + \text{vesicle} \longrightarrow \text{reaction product}$$

$$(HSO_3^-)_{external} \xrightarrow{\text{diffusion}} (HSO_3)_{internal}$$

$$(HSO_3^-)_{internal} + \text{dye} \longrightarrow \text{bleached product}$$

Assuming that the reactions of HSO_3^- with dye or vesicles are all kinetically second

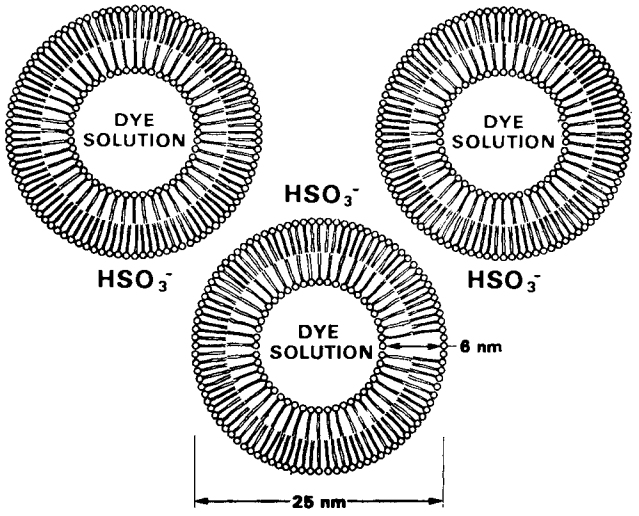

Figure 1.18. Cross Sectional View of Dye-Loaded Vesicles Exposed to External HSO_3^-

order, this mechanism predicts that the permeability coefficient, P, is given by

$$P = \left(\frac{V_i}{at}\right)\frac{(dA/dt)\ \text{dye inside}}{(dA/dt)\ \text{dye outside}}$$

for small values of time t, where A is the absorbance of the vesicle suspension at 539 nm and V_i/a is the ratio of the internal volume of a vesicle to its internal surface area, 2.2 x 10^{-7} cm.

Values obtained in this study are compared with those for other systems in Table 1.2. The assumed mechanism was considered to be verified by the constancy of P over a hundred-fold range of HSO_3^- concentration. These results demonstrate

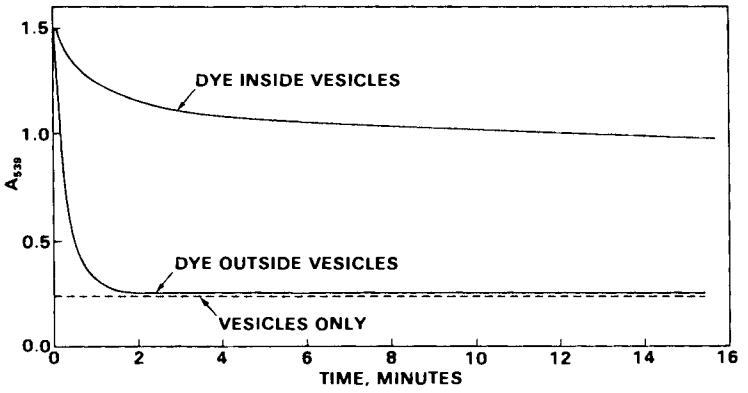

Figure 1.19. Bleaching of Dye-Loaded Vesicle Suspensions by Addition of External HSO_3^-

Table 1.2. Permeability Coefficients of Anions Through Phospholipid Bilayers

Bilayer and Temperature	Permeability Coefficient, cm/s	$[HSO_3^-]$, M	pH
Dipalmitoylphosphatidylcholine, 23°C[b]	$P_{HSO_3^-}$ = 1.8E-9[a]	4E-2	6.0
	1.9E-9	4E-3	6.0
	1.8E-9	4E-4	6.0
Stearoyl sphingomyelin, 23°C[b]	$P_{HSO_3^-}$ = 3.9E-9	1E-3	4.2
	4.6E-9	1E-4	6.0
	4.3E-9	1E-5	6.0
Egg phosphatidylcholine, 20°C	$P_{maleate}$ = 4E-9[c]		
	$P_{chloride}$ = 1.1E-10[d]		
Egg phosphatidylcholine/n-tetradecane, 20°C[e]	$P_{chloride}$ = 2.4E-7		
Diphytanoylphosphatidylcholine/n-decane, 20°C[d]	$P_{chloride}$ = 6.8E-8		

[a] 1.8E-9 = 1.8 x 10^{-9}
[b] Reference: This work
[c] Reference: Prestegard, Cramer and Viscio 1979
[d] Reference: Toyoshima and Thompson 1975
[e] Reference: Pagano and Thompson 1968

that HSO_3^- can cross the basic phospholipid bilayer structure in cell membranes about as fast as chloride ion. Since no extrinsic carriers or membrane pore-formers are present to facilitate this movement, it is estimated that cell membranes would be at least as permeable to HSO_3^- ions, and these species should be available for reaction with cellular DNA.

Permeability evaluations for pyrene were based on expected changes in the fluorescence intensity from vesicles whose interiors were filled with 0.1 M caffeine in aqueous solution and whose exteriors were suddenly exposed to solutions of pyrene in water. The solubility of pyrene was found to increase from 5×10^{-6} in water to 2×10^{-3} M in aqueous 0.1 M caffeine, and this solubility difference should act as a driving force for pyrene diffusion across the bilayer. On exposure of the vesicle exteriors to pyrene, their fluorescence emission was expected to rise as the pyrene diffused from a medium of high dielectric constant, the bilayer, and then to decrease as the pyrene diffused from the bilayer into the aqueous interior. Instead, the intensity of the 380-nm fluorescence from pyrene remained constant, indicating that no pyrene diffusion was occurring.

A similar constancy in 380-nm fluorescence intensity was observed when pyrene-saturated water was added to CHO cells suspended in nutrient solution. These results suggest that PAHs cannot enter phospholipid bilayers without being chemically altered to more polar derivatives.

REFERENCES

Hayatsu, H. 1976. "Bisulfite Modification of Nucleic Acids and Their Constituents." In Progress in Nucleic Acid Research and Molecular Biology, ed. W. Cohn, Vol. 16, pp. 75-124. Academic Press, New York.

Haynes, Robert H. 1975. "The Influence of Repair Processes on Radiobiological Survival Curves." In Cell Survival After Low Doses of Radiation: Theoretical and Clinical Implication, pp. 197-208. The Institute of Physics and John Wiley & Sons, London.

Heflich, R. H., R. M. Hazard, L. Lommel, L. D. Scribner, V. M. Maher and J. J. McCormick. 1980. "A Comparison of the DNA Binding, Cytotoxicity and Repair Synthesis Induced in Human Fibroblasts by Reactive Derivatives of Aromatic Amide Carcinogens." Chemical-Biological Interactions 29:43-56.

Hsie, A. W., P. A. Brimer, T. J. Mitchell and D. G. Gosslee. 1975. "A Dose-Response Relationship for Ultraviolet-Light-Induced Mutations at the Hypoxanthine-Guanine Phosphoribosyltransferase Locus in Chinese Hamster Cells." Som. Cell Genet. 1:383-389.

Huberman, E., L. Sachs, S. K. Yang and H. U. Gelboin. 1976. "Identification of Mutagenic Metabolites of Benzo(a)pyrene in Mammalian Cells." Proc. Nat. Acad. Sci. 73:607-611.

Lawley, P. D. 1979. "Approaches to Chemical Dosimetry in Mutagenesis and Carcinogenesis: Relevance of Reactions of Chemical Mutagens with DNA." In Chemical Carcinogens and DNA, ed. P. L. Grover, Vol. I, pp. 1-36. CRC Press, Inc., Boca Raton, Florida.

Levinson, J. W., B. Konze-Thomas, V. M. Maher and J. J. McCormick. 1979. "Evidence for a Common Rate Limiting Step in the Repair Process of Ultraviolet Light (UV) and N-Acetoxyacetamino Fluorene (N-AcO-AAF) Induced Damage in the DNA of Human Fibroblasts." Proceedings of the 17th Annual Meeting of the American Association for Cancer Research, New Orleans, May 16-19, 1979, p. 105.

Maher, V. M., N. Birch, J. R. Otto and J. J. McCormick. 1975. "Cytotoxicity of Carcinogenic Aromatic Amides in Normal and Xeroderma Pigmentosum Fibroblasts with Different DNA Repair Capabilities." Journal of the National Cancer Institute 54:1287-1293.

Maher, V. M., and J. J. McCormick. 1978. "Mammalian Cell Mutagenesis by Polycyclic Aromatic Hydrocarbons and Their Derivatives." In Polycyclic Hydrocarbons and Cancer, Vol. 2, pp. 137-160. Academic Press, New York.

McCann, J., and B. N. Ames. 1976. "Detection of Carcinogens as Mutagens in the Salmonella/Microsome Test: Assay of 300 Chemicals: Discussion." Proc. Nat. Acad. Sci. 73:950-954.

Munson, R. J., and D. T. Goodhead. 1977. "The Relation Between Induced Mutation Frequency and Cell Survival--A Theoretical Approach and an Examination of Experimental Data for Eukaryotes." Mut. Res. 42:145-159.

O'Neill, J. P., and A. W. Hsie. 1979. "Phenotypic Expression Time of Mutagen-Induced 6-Thyoguanine Resistance in Chinese Hamster Ovary Cells." Mut. Res. 59:109-118.

Pagano, R., and T. E. Thompson. 1968. "Spherical Lipid Bilayer Membranes: Electrical and Isotopic Studies of Ion Permeability." J. Mol. Biol. 38:41-52.

Prestegard, J. H., J. A. Cramer and D. B. Viscio. 1979. "Nuclear Magnetic Resonance Determinations of Permeation Coefficients for Maleic Acid in Phospholipid Vesicles." Biophys. J. 26:575-584.

Shapiro, R. 1977. "Genetic Effects of Bisulfite (Sulfur Dioxide)." Mut. Res. 39:159-176.

R. D. Smith. 1979a. "A Direct Mass Spectrometric Study of the Mechanism of Toluene Pyrolysis at High Temperatures." J. Phys. Chem., 83:1553.

R. D. Smith. 1979b. "Formation of Radicals and Complex Organic Compounds by High-Temeperature Pyrolysis: The Pyrolysis of Toluene." Combust. Flame, 35:179-190.

Stamato, T. D., and L. K. Hohman. 1975. "A Method for Replica Plating CHO Cells using Nylon Cloth." Cytogenet. Cell Genet. 15:372-379.

Toyoshima, Y., and T. E. Thompson. 1975. "Chloride Flux in Bilayer Membranes: Chloride Permeability in Aqueous Dispersons of Single-Walled Bilayer Vesicles." Biochem. 14:1525-1531.

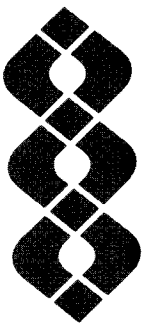

2 Fission

• Radiation Physics

A fundamental knowledge of the mechanisms by which radiation interacts with matter is essential for understanding dose-response relationships in terms of quantifiable chemical and physical processes. The Radiation Physics Program is directed toward investigation of the fundamental processes of energy deposition by fast charged particles and the subsequent transport and degradation of that energy as it leads to the formation of chemically active molecular species. The initial deposition of energy is studied through the measurements of differential ionization cross sections for fast charged particles which, when coupled with theoretical calculations, provide insight into the mechanisms of energy deposition in biologically significant matter. These measurements also provide the necessary data base for energy transport studies. Our effort in energy transport and degradation combines the use of Monte Carlo calculations and theoretical investigation of condensed-phase chemical kinetics. Monte Carlo calculations provide detailed information on the initial structure of the particle track, and the theoretical investigation of energy transport provides the link between initial energy deposition and the final observation of chemically active molecular species. Time-resolved measurements of fluorescence from liquid systems excited by irradiation with pulsed beams of fast charged particles and ultraviolet light provide definitive tests of the theoretical results. This integrated program of experimental and theoretical investigation results in a unified approach to understanding the mechanisms by which chemically active species are formed as a result of energy deposition via exposure in a radiation field.

• Initial Interaction Process

In our study of the initial interaction processes in the absorption of energy from a radiation field by biologically significant material, we have continued to concentrate on the measurement and interpretation of differential ionization cross sections for fast charged particles. Of particular interest is the determination of cross section systematics and interaction mechanisms, which will enable extrapolation of experimental results into regions where experiments are either impractical or not feasible. Understanding these processes is important in assessing the reliability of condensed-phase structure calculations based on interaction cross sections obtained from collisions with free atoms and molecules. During the past year, we have investigated interaction mechanisms for proton impact by taking measurements and performing Born approximation calculations for the ionization of neon, krypton, and xenon by 2.0- to 4.2-MeV protons. We have also begun a systematic study of the hard-collisions component of single differential ionization cross sections. Our investigation of collisions involving ions that have bound electrons has been extended by measurements of differential ionization cross sections for C^+ with energies from 0.8 to 4.2 MeV and by a theoretical investigation of screening in heavy-ion collisions. A study of interaction mechanisms contributing to autoionizing spectra in heavy-ion collisions was also completed.

Differential Ionization Cross Sections for Fast Protons

L. H. Toburen, W. E. Wilson, and
S. T. Manson[a]

Differential ionization cross sections for fast protons (differential in ejected electron energy and emission angle) provide the primary source term for detailed calculations of charged-particle track structure. Calculations of the distribution of energy density provide information needed to relate the effects of linear energy transfer (LET) to induced chemical and biological processes. Because of the short range and scattering properties of electrons in condensed media, it is necessary to make direct measurements of cross sections using gas-phase targets. A detailed knowledge of the interaction mechanisms is therefore required to assess the effects of the projectile and the target structure on the collision cross sections. Information on interaction mechanisms is obtained by comparing experimental cross sections with theoretical values and by analyzing cross sections for a wide selection of atomic and molecular target species. During the past year, additional data have been accumulated for the ionization of neon, krypton, xenon, and numerous molecular species by 2.0- to 4.2-MeV protons. These data are now being analyzed.

Our analysis of double differential ionization cross sections for the ionization of neon by protons indicates a substantially smaller contribution to the spectra attributable to continuum-charge-transfer (CCT) than was observed for the ionization of helium. If one assumes that the difference between the calculated and measured cross sections in the spectral region near $v_i \approx v_e$ (where v_i is the energy of the proton and v_e is the energy of the ejected electron) is due to CCT, then the ratio of measured to calculated cross sections becomes a measure of the relative importance of CCT. In Figure 2.1, the ratio of measured to calculated double differential cross sections is shown for electron emission at 15° and 30°; the insert illustrates similar results for the ionization of helium (Manson et al. 1975). The ratio is a factor of two greater for helium targets than for neon targets. We have no theoretical explanation for this difference. Further work will be required to determine the relative contribution of CCT for various atomic and molecular targets in order to provide more insight into this ionization process.

(a) Consultant, Georgia State University, Atlanta, Georgia.

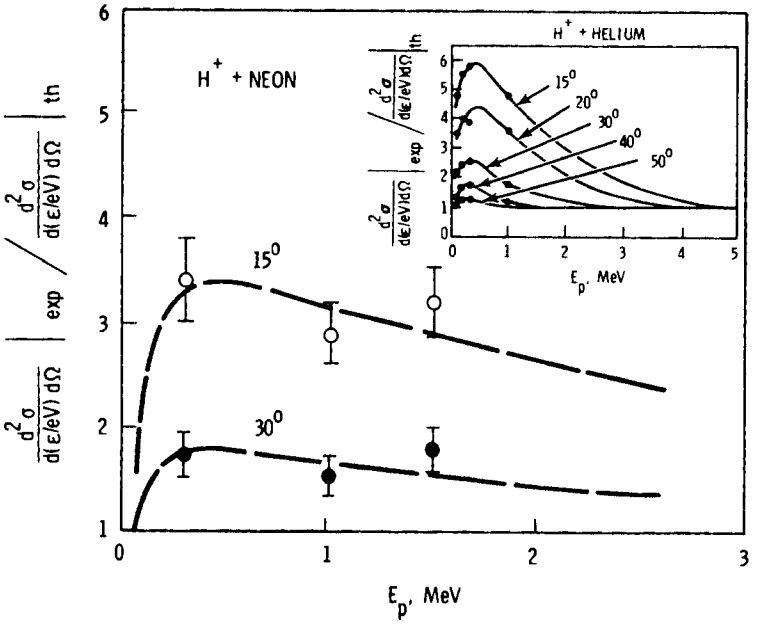

Figure 2.1. Ratio of Experimental to Theoretical Double Differential Cross Sections for Proton Ionization of Neon for Equal-Velocity Protons and Ejected Electrons, Versus Proton Energy for Different Emission Angles. Insert in upper right is similar data for ionization of helium from Manson et al. 1975.

Bethe-Born Approximation for the Energy Distribution of Secondary Electrons

J. H. Miller, L. H. Toburen, S. T. Manson,(a) and W. E. Wilson

The Bethe theory suggests that the single differential cross section (SDCS) for ionization by high-velocity ions can be approximated by the sum of a dipole component and a hard-collisions component (Kim 1975). This approximation is very attractive because the dipole component can be obtained from optical oscillator strengths, which are known for many species of radiological interest. We have initiated a project to study the systematics of the hard-collisions component. This component, which is similar to the Rutherford cross section (Toburen, Manson and Kim 1978), is expected to be independent of the ion energy at high ion velocities and to be dependent on the energy ϵ of the ejected electron.

We define the hard-collisions component, $B(\epsilon)$, of the SDCS as

$$B(\epsilon) = \frac{T}{4\pi a_0^2}\frac{d\sigma}{d\epsilon} - \ln\left(\frac{4T}{R}\right)\sum_j \frac{R^2}{\epsilon+I_j}\frac{df_j}{d\epsilon} \qquad (1)$$

where T is the kinetic energy of the incident ion in units of $1/2\ m_e v_i^2$ (m_e is the electron mass and v_i is the ion velocity), a_0 is the Bohr radius (0.529 Å), $d\sigma/d$ is the experimental SDCS, and R is the Rydberg energy (13.6 eV). The summation in Equation (1) is over subshells of the target. Each shell is characterized by a binding energy I_j and its optical oscillator strength $df_j/d\epsilon$.

Figure 2.2 shows the hard-collisions component for the ionization of neon by protons of several energies as a function of the kinetic energy of the ejected electron. This log-log plot emphasizes the ϵ^{-2} dependence characteristic of the Rutherford cross section for energy transfer to free electrons. From the intercept of the asymptote with the vertical axis, we can compute the effective number of target electrons participating in the collision. This number increases as the ion energy increases and reaches its maximum value of 10 for neon when the proton energy is about 4 MeV. Hence $B(\epsilon)$ for $\epsilon \gtrsim 500$ eV (at log

(a) Consultant, Georgia State University, Atlanta, Georgia.

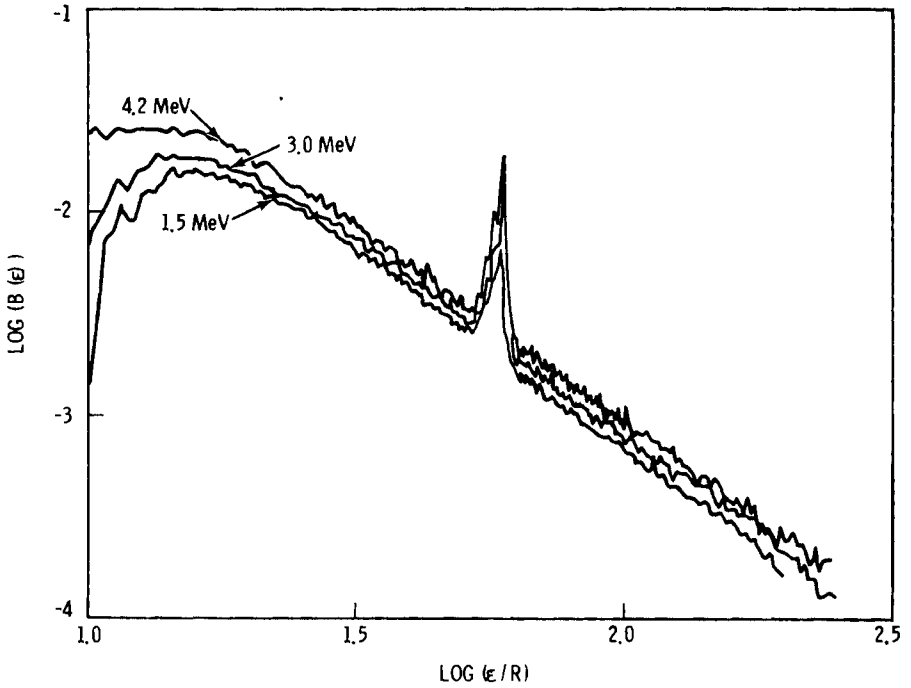

Figure 2.2. Log-log Plot of Hard-Collisions Component $B(\epsilon)$ of Single Differential Cross Section for Ionization of Neon by Proton Impact; ϵ is the kinetic energy of the ejected electron.

$\epsilon/R \simeq 1.5$) should not change when the proton energy is increased above 4 MeV.

Figure 2.3 shows $B(\epsilon)$ for low-energy electrons ejected from neon by proton impact. The results shown for 1.0- and 1.5-MeV protons are based on measurements including both electrostatic and time-of-flight energy analysis and are expected to be reliable for ejected-electron energies as low as 1 eV. A sharp minimum occurs at an electron energy of about half a Rydberg. The position of this minimum agrees well with calculations based on the Born approximation (Manson 1972) for the ionization of 2p electrons in aluminum. The depth of the minimum appears to decrease with increasing proton energy. The results shown for 4.2-MeV protons, where only electrostatic energy analysis was used, should be reliable for electron energies greater than two Rydbergs. The solid curve is a theoretical result for the ionization of 2p electrons in aluminum (Manson 1972).

The results obtained from experimental SDCS at 4.2 MeV together with the theoretical results at very low electron energy provide a good approximation to the high-velocity limit of the hard-collisions component. With this approximation for $B(\epsilon)$ and with optical oscillator strengths, we can predict the cross section for ionization of neon by ions with energies greater than 4 MeV/amu. These predictions will be tested by comparison with the Born approximation and with experimental results where available. We also plan to carry out a similar analysis of the hard-collisions component in the cross section for ionization of helium and water vapor by proton impact. We do not expect $B(\epsilon)$ to depend strongly on the electron structure of the target.

Ionization by Alpha Particles

L. H. Toburen, W. E. Wilson and S. T. Manson[a]

During the past year, we published two papers involving ionization by He^+ and He^{2+} ions of 0.3 to 2.0 MeV (Toburen, Wilson and Popowich 1980; Toburen and Wilson 1979). The experimental results described in these papers confirm the applicability of Z^2 scaling of differential ionization

(a) Consultant, Georgia State University, Atlanta, Georgia.

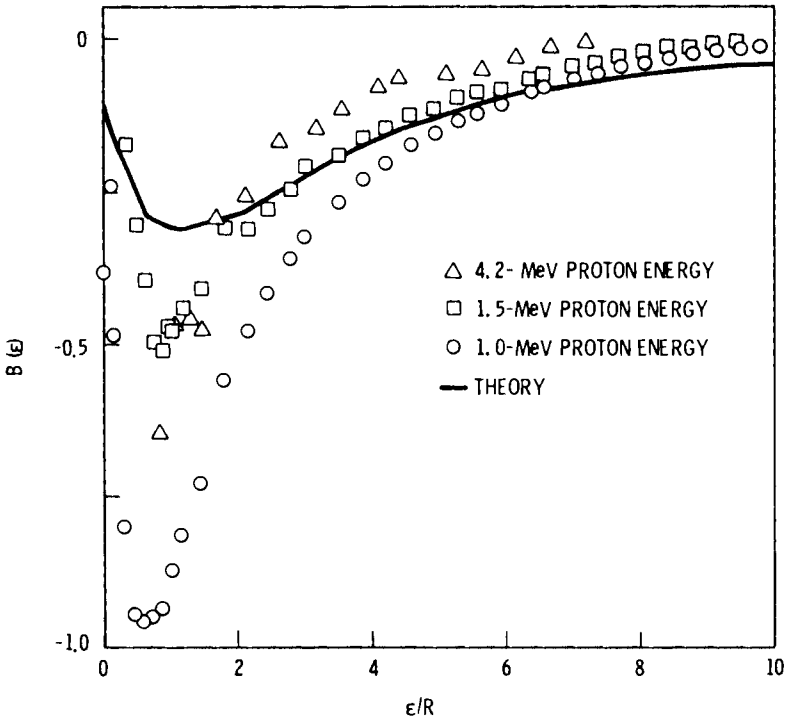

Figure 2.3. Hard-Collisions Component of Single Differential Cross Section for Ejection of Low-Energy Electrons from Neon by Proton Impact

cross sections for bare charged particles within this ion energy range, except in the ejected-electron energy range where continuum-charge-transfer (CCT) becomes important. Continuum-charge-transfer is expected to be important where the velocity of the incident ion is comparable to that of the outgoing electron and the emission angle is small. Here, our measurements support a Z^3 dependence for the cross sections.

Differential cross sections for ionization by He^+ ions clearly illustrate the effect of the bound projectile electron in screening the projectile's nuclear charge: for interactions involving a small energy transfer, the screening provided by the bound electrons is effective, whereas for a large energy transfer the screening is negligible. During the past year we have begun a theoretical investigation, via the Born approximation, of screening in He^+ - He collisions. Although considerable theoretical work has addressed ionization by bare charged particles, this is the first rigorous treatment of differential cross sections for collisions involving ions with bound electrons. Several features must be added to the description of ionization by structured projectiles relative to the bare charged particle. First, the screening of the projectile's nuclear charge by the projectile electron introduces a momentum-dependent interaction "strength." Second, the projectile electron may be stripped during the collision and contribute to the ionized electron spectra. Third, ionization of the target atom may occur simultaneously with excitation of the projectile electron. This is particularly important in conjunction with ionization of the projectile.

Calculations of the ionization of He by 1.2- and 2.0-MeV He^+ and He^{2+} ions have been made using the Born approximation for comparison with our measured double differential cross sections. The calculations use the theoretical technique previously developed for bare charged particles (Manson et al. 1975), with extensions for structured ions as discussed by Briggs and Taulbjerg (1978) and the incorporation of projectile ionization using the transformation of Drepper and Briggs (1976).

Within this framework, the double differential cross section for the ejection of an electron of energy ϵ is given by

$$\frac{d^2\sigma}{d\epsilon\, d\Omega} = \int_{k_{min}}^{k_{max}} \left[2 - \frac{1}{\left(1+\left(\frac{ka_0}{4}\right)^2\right)}\right]^2 I(k)\, dk \quad (2)$$

where k is the momentum transfer, a_0 is the Bohr radius, and I(k) is the momentum integrand obtained for a bare charged particle (Manson et al. 1975). The quantity in brackets is the screening function, which could be thought of as the projectile's effective nuclear charge. Note that this effective nuclear charge is a function of k; therefore, the differential cross section will exhibit screening effects that depend on both the energy and the emission angle of the ejected electron.

Preliminary results of the Born calculation of double differential cross sections for He^+ - He collisions at 2 MeV are shown in Figure 2.4. The calculated and measured cross sections agree well for emission angles greater than about 50°. Since electrons originating from projectile ionization will appear predominantly at small emission angles, the discrepancies observed at these angles may be attributed to an underestimation of the calculated projectile ionization cross section. This discrepancy may result because the Born approximation for the ionization of the projectile (He^+) by a neutral particle (He°) at this energy is inadequate, or because the Hartree-Slater wave functions used for He° are not accurate enough to properly describe the screening. Work is in progress to try to resolve these questions.

Ionization by Fast Carbon Ions

L. H. Toburen and W. E. Wilson

Differential ionization cross sections for low-Z low-energy heavy ions are important in radiological physics because of the need to understand interactions with tissue of both recoil ions produced in the stopping of fission and fusion neutrons in tissue, and heavy ion beams used for radiation therapy. The electronic structure of the ion itself makes evaluating collision cross sections for heavy ions particularly difficult, and no theoretical techniques presently available can provide reliable differential ionization cross sections for heavy-ion interactions.

We are investigating the systematics of differential cross sections over a wide range of collision energies and projectile charge states. Measurements to date have concentrated on ionization by singly charged carbon ions. During the past year, data were accumulated for the ionization of He, Ne, Ar, and CH_4 by 0.8-, 1.2-, 2.4-, 3.6-, and 4.2-MeV C^+ ions; electron spectra were recorded for 13 emission angles for each ion-energy gas-target combination. Preliminary analysis of the cross sections for methane has just begun.

Single differential cross sections for the ionization of methane by C^+ ions of several energies are shown in Figure 2.5. As the ion energy increases in this energy range, the cross sections for the ejection of low-energy electrons decrease whereas the cross sections for the ejection of high-energy electrons increase. Interpretation of the emission spectra is complicated by the combined effects of 1) the electronic screening of the projectile nucleus by bound electrons and 2) the ionization of both the projectile and the target. Cross sections for low-energy electron emissions, resulting predominantly from large-impact-parameter collisions, exhibit nearly a 1/T dependence on ion energy where T is the kinetic energy of the incident ion in units of $1/2\ m_e v_i^2$ (m_e is the electron mass and V_i is the ion velocity). This is illustrated more quantitatively in Figure 2.6, where the ratio of the measured single differential cross section to the corresponding Rutherford cross section is plotted as a function of energy loss (E = the kinetic energy of the ejected electrons plus the electron binding energy). Here the ratios for small values of energy loss tend to overlap for different ion energies, reflecting the 1/T dependence of the Rutherford cross sections. The structure observed in the spectra at about 250 eV results from ionization of the K-shell of the target molecule's carbon atom, followed by Auger electron emission. At higher electron energies, structure is introduced by Doppler-shifted Auger lines originating from the carbon projectile. These Auger lines contribute at different electron energies when the double differential cross sections are integrated to produce the single differential cross sections from which this graphical representation is derived. As the ion energy is increased,

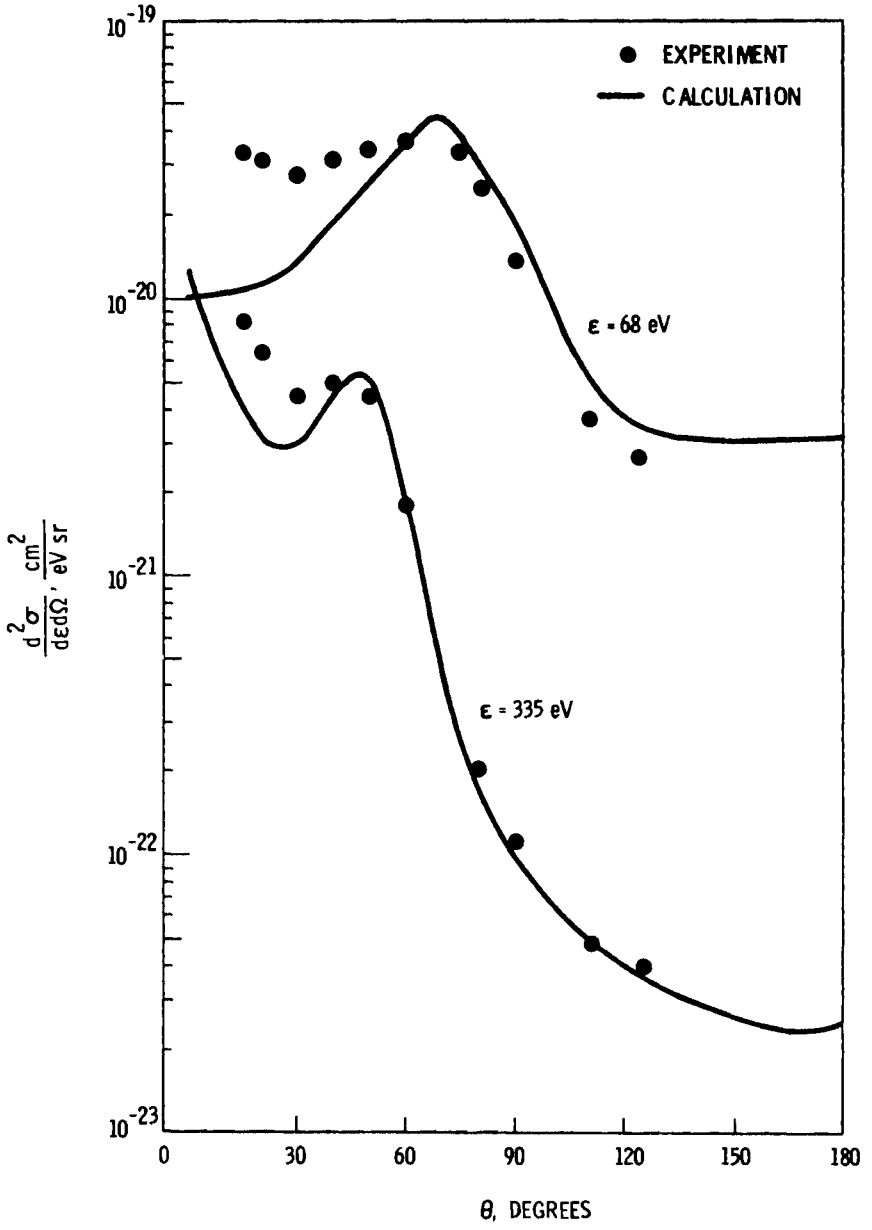

Figure 2.4. Angular Distributions for Calculated and Measured Double Differential Cross Sections for Electron Ejection in 2-MeV He^+ - He Collisions

the ratio for high-energy ejected electrons presented in Figure 2.6 increases. For ions and electrons with sufficiently high energy, one would expect this ratio to approach the number of electrons in the target molecule; these results indicate, as we expect, that these ion energies are well below the energies required for Rutherford-like cross sections. To provide a systematic interpretation of cross sections for ion impact in this velocity range, a detailed knowledge of projectile screening by bound electrons will be necessary. We anticipate that measurements involving simple targets such as helium and neon and measurements for other ion charge states will provide insight into details of the collisional ionization process.

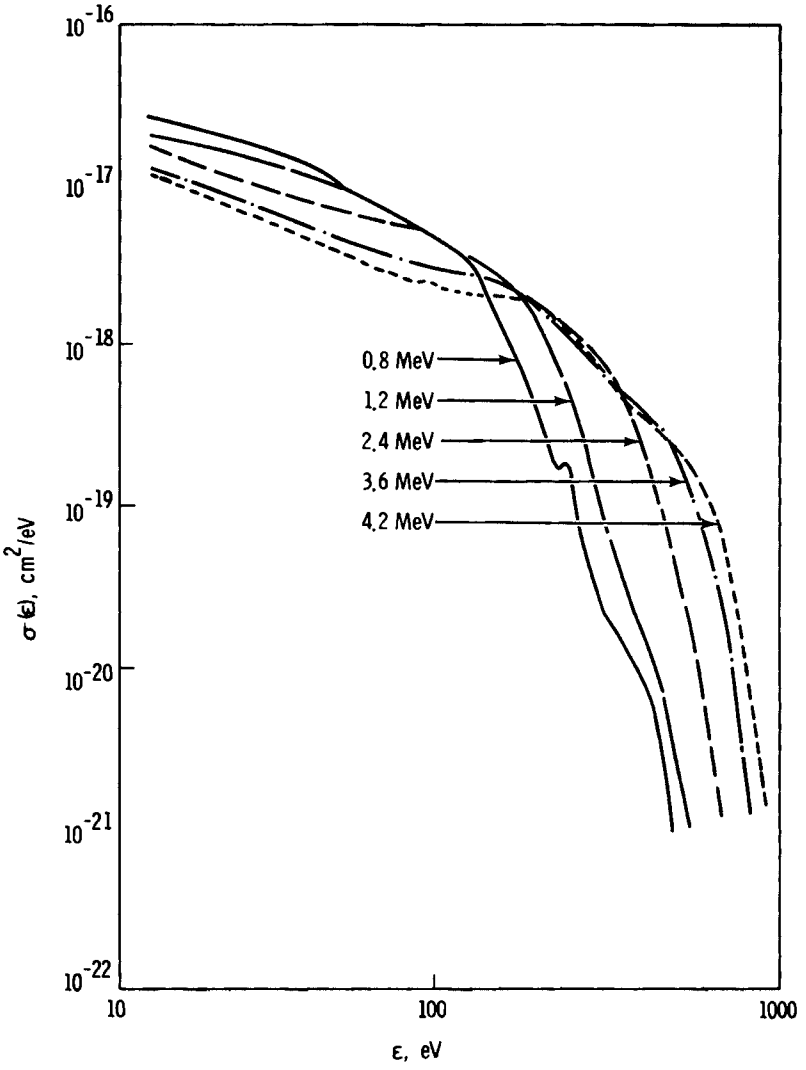

Figure 2.5. Single Differential Cross Sections for Ejection of Electrons in C^+ - CH_4 Collisions at Various Ion Energies

Screening in Heavy-Ion Collisions

L. H. Toburen(a)

Analysis of differential ionization cross sections for heavy-ion collisions illustrates that the effective nuclear charge of the projectile is a strong function of the collisional energy transfer. This has been discussed above ("Ionization by Alpha Particles") for He^+ impact and previously for carbon ions (Toburen 1979) and oxygen ions (Stolterfoht 1978; and Stolterfoht et al. 1974). While a guest of the Hahn-Meitner Institute in Berlin, this author worked with the atomic collisions group to develop a simple screening model that would enable differential ionization cross sections for structured ions to be estimated from results for bare charged particles.

A quantitative interpretation of the effective nuclear charge as a function of

(a) Work performed in collaboration with D. Schneider, N. Stolterfoht, P. Ziem, and M. Prost while a guest of the Hahn-Meitner Institute, Berlin (April 27-June 28, 1980).

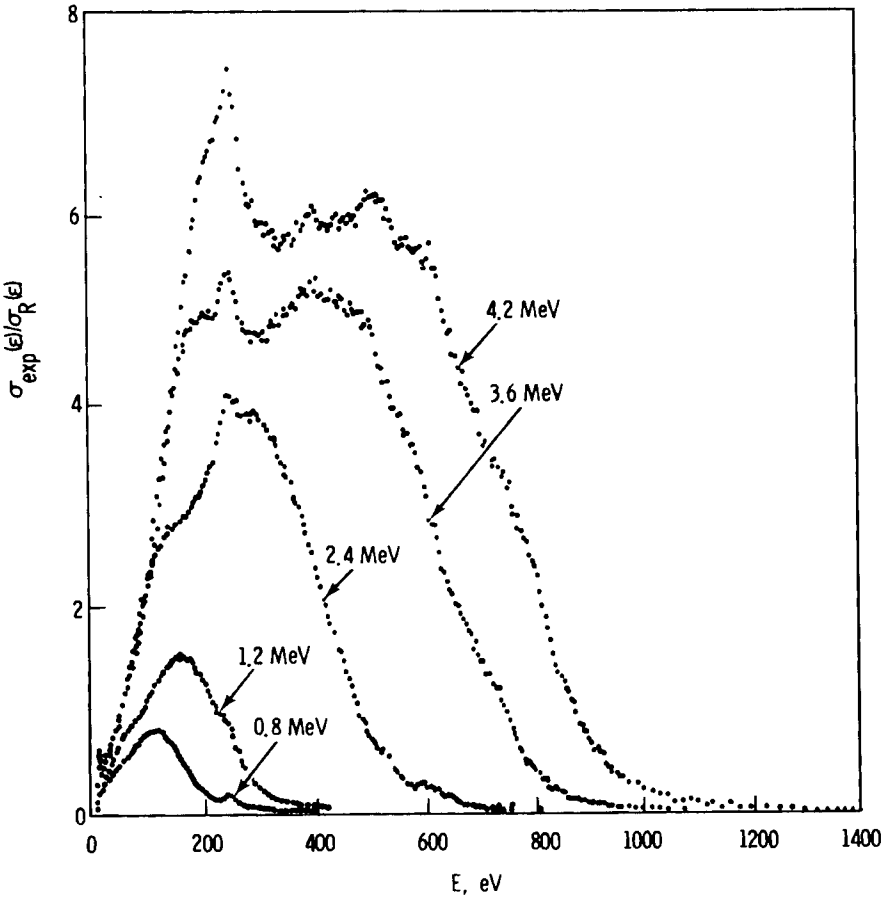

Figure 2.6. Ratio of Measured Single Differential Cross Section to Rutherford Cross Section for C^+ Ionization of CH_4 at Several Ion Energies

energy transfer was first discussed by Stolterfoht (1978) in his analysis of differential ionization cross sections for fast oxygen ions. The correlation of energy transfer with an effective impact parameter by means of the adiabatic radius $R_{ad} = v_i/\Delta E$, where v_i is the ion velocity and ΔE is the energy transfer, clearly illustrated the effects of the spatial distribution of projectile electrons in screening the nuclear charge. This application of the Massey criterion illustrates that collisions involving small energy transfers correlate with interactions at large internuclear distances where bound electrons provide effective screening, whereas large energy transfers occur when the projectile deeply penetrates the target atom and the effects of the projectile electrons are unimportant.

The correlation of the spatial distribution of effective charge with energy loss leads to a simple model for estimating the effective nuclear charge of the projectile. Within this model, the spatially dependent screening of the projectile charge is derived from the radial distribution of bound electrons. The effective nuclear charge is given by

$$Z_{eff}(R) = Z - S(R) \qquad (3)$$

where S(R) is the number of bound electrons screening the nuclear charge at a distance R from the nucleus. The screening function S(R) is derived from the spatial distribution of projectile electrons such that

$$S(R) = \sum_i N_i \int_0^R |\psi_i(r)|^2 \, r^2 dr \quad (4)$$

where $\psi_i(r)$ is the normalized radial wave function for the i^{th} bound electron and N_i is the number of electrons in the i^{th} subshell. The function S(R) may be evaluated by different methods; we have performed the integral analytically using hydrogenic wave functions and compared these results with numerical solutions using the Hartree-Fock program of Froese-Fisher (1972).

The reliability of this simple screening model in determining a projectile's effective nuclear charge can be tested by comparing estimates derived using the model with those derived by measurements of differential ionization cross sections. To estimate the effective nuclear charge of the incident ion from the measured cross sections, we assume that the cross sections are proportional to the square of the projectile charge, as predicted by first order collision theory (Inokuti 1971; Bonson and Vriens 1970). The effective nuclear charge can then be estimated from the differential cross sections as a function of energy transfer:

$$Z_{eff}(\Delta E) = Z \sqrt{\frac{d\sigma(q)/dE}{d\sigma(Z)/dE}} \quad (5)$$

where $d\sigma/dE$ (q) is the differential cross section for an incident ion with charge q and $d\sigma/dE$ (Z) is the differential cross section for the bare ion. To compare directly the effective nuclear charge as determined using the screening model and the experimentally determined effective nuclear charge Z_{eff}, we estimate that the effective interaction distance b_{eff} for a given energy transfer is equal to the adiabatic radius defined by the Massey criterion as described above and discussed previously by Stolterfoht (1978).

A comparison of the effective nuclear charge obtained from the model calculation with that derived from experimental results for helium ion impact is shown in Figure 2.7. The solid line is the result of our model calculation and the cross-hatched area represents the range of effective nuclear charge derived from measurements involving He^+ and He^{2+} ionization of H_2O for ion energies from 0.8 to 2 MeV (Toburen, Wilson and Popowich 1980). The screening model reflects accurately the shape of the experimentally derived curve. The shift of the experimental data to a somewhat larger impact parameter than is derived from the screening model may reflect an inappropriate use of the Massey criterion or an incomplete subtraction from the experimental data of the effect of electron loss on the cross sections. The left edge of the cross-hatched area coincides well with the model calculation. This edge represents the lowest-energy helium ions, where the effects of electron loss are expected to be minimal. A

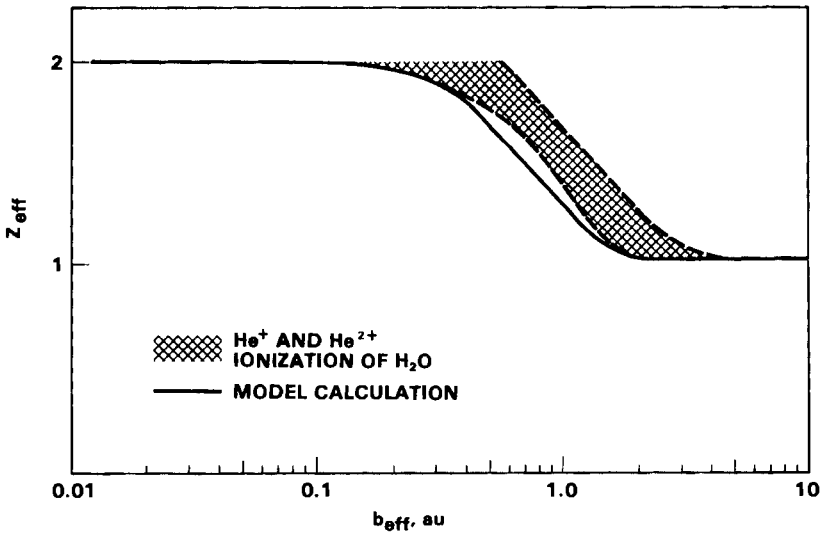

Figure 2.7. Effective Nuclear Charge of He^+ as a Function of Adiabatic Interaction Radius

description of the screening model and its application to He^+ and O^{n+} (n = 4 - 7) is being prepared for publication.

A screening model such as that discussed above can be used to extrapolate bare-ion results to structured ions. It can also be used in theoretical calculations such as the binary encounter approximation (BEA) to obtain cross sections for heavy-ion collisions. We have incorporated the model into the BEA formalism of Bonson and Vriens (1970) and have calculated single differential cross sections for the ionization of argon by helium ions. In Figure 2.8, calculated cross sections are compared with measured cross sections at three ion energies. The 0.3- and 2.0-MeV data are from our work and the 10-MeV data are from the work of Burch et al. (1975). The BEA results for He^{2+} impact agree well with the measured values for all ion and ejected electron energies except the lowest electron energies for 0.3-MeV ions. The BEA calculations for He^+, which incorporate the screening model, appear to provide a reliable estimate of target ionization, but the electron loss contribution is overestimated.

Cross sections for target ionization, designated by T in the 0.3-MeV data, agree very well with the measured spectrum. One would expect electron loss to be negligible for 0.3-MeV He^+ ions, based on knowledge of charge-exchange cross sections (Allison 1958); however, the BEA calculation gives a relatively large contribution attributable to projectile ionization. The 2-MeV data also agree well with the BEA calculation for electron energies above and below the spectral region containing electron loss. The 10-MeV results show excellent agreement between the BEA and measured cross sections for high-energy ejected electrons, but poorer agreement at the lower electron energies. The discrepancy for low-energy electrons may be due to contributions to the measured spectrum from Auger transitions; these are not included in the calculated cross sections. An ion energy of 10 MeV is near the maximum in the cross section for L-shell ionization of argon; thus a large L-Auger contribution is observed in the measured spectrum.

The single differential cross sections shown in Figure 2.8 indicate that the screened BEA provides a good representation of target ionization by He^+ ions. The contribution from electron loss is overestimated substantially, but the agreement improves significantly as the ion energy increases. A more detailed description of the BEA calculations for He^+ and preliminary results for O^{5+} was presented at the Small Accelerator Conference in Denton, Texas, in November 1980 and will appear in the published proceedings.

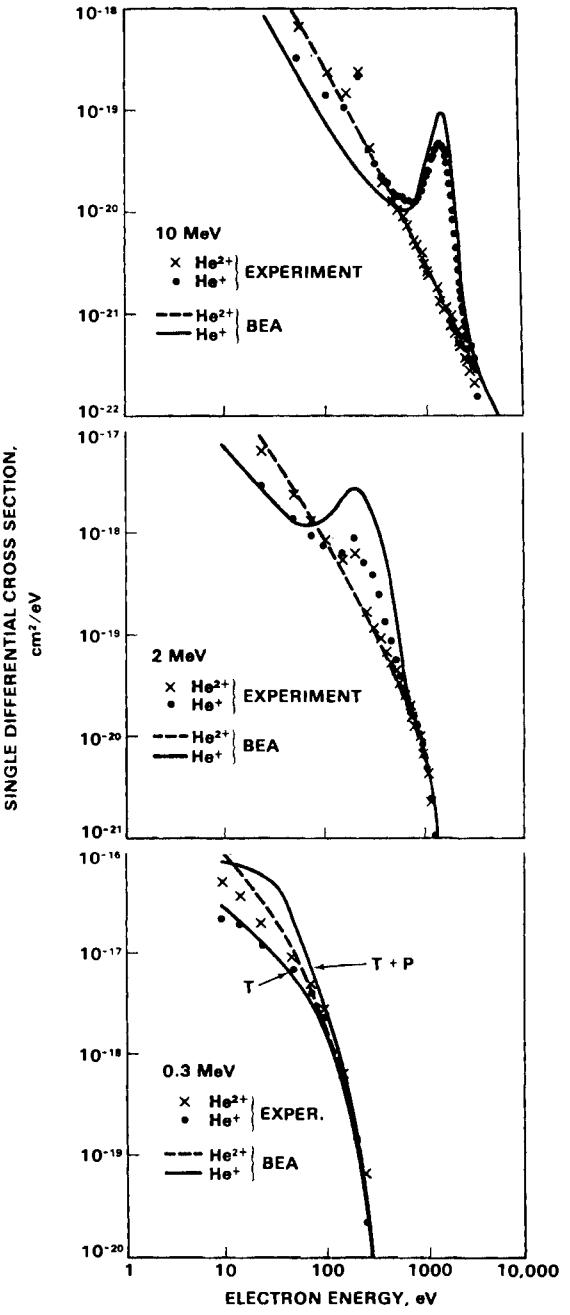

Figure 2.8. Calculated and Measured Single Differential Ionization Cross Sections for He^+ and He^{2+} Collisions with Ar. T refers to target ionization only; T+P refers to ionization of both projectile and target.

Autoionization in Heavy-Ion Collisions

L. H. Toburen[a]

Interaction mechanisms leading to electron production in heavy-ion collisions can be investigated through study of structure in the ejected-electron spectra. In particular, autoionization spectra can give information on the excitation of target states, the mixing of these states in the projectile-target coulomb field, and the interaction of the target with the final states of the projectile. In last year's report, we presented preliminary data on the energy and angular distributions of autoionization electrons ejected from helium in collisions with Cu^{3+} and I^{3+} ions that have velocities from 0.96 to 2 atomic units (Toburen, Manson and Schneider 1980). These data showed strong variations in line intensities with changes in ion velocities and electron-ejection angles. Our preliminary interpretation of these variations was that the autoionizing states were undergoing perturbations attributable to the coulomb field of the slow-moving projectile.

During the past year, additional data were accumulated to improve the statistical accuracy of the results and the data were extended to include iodine ions with charge states of +2 and +4 at the highest and lowest energies, respectively. These data were then analyzed at the Hahn-Meitner Institute using computer programs previously developed in their atomic collisions work. Careful analysis of the spectra indicated that the enhancement of autoionization lines for small emission angles (50°) was due to contributions to the spectra from autoionization of the projectile, rather than to stark mixing of states as was speculated earlier (Toburen and Schneider 1979). The autoionization spectra observed at 50° for iodine ions of various energies and charge states are shown in Figure 2.9. The dashed lines indicate the continuum electron distribution assumed in preliminary analysis. A more consistent interpretation of the spectra is obtained, however, if one considers the shaded area to represent autoionization of the iodine projectile. The lines connecting spectra for different ion energies indicate the

(a) Work performed in collaboration with D. Schneider and D. Brandt while a guest at the Hahn-Meitner Institute, Berlin (April 27-June 28, 1980).

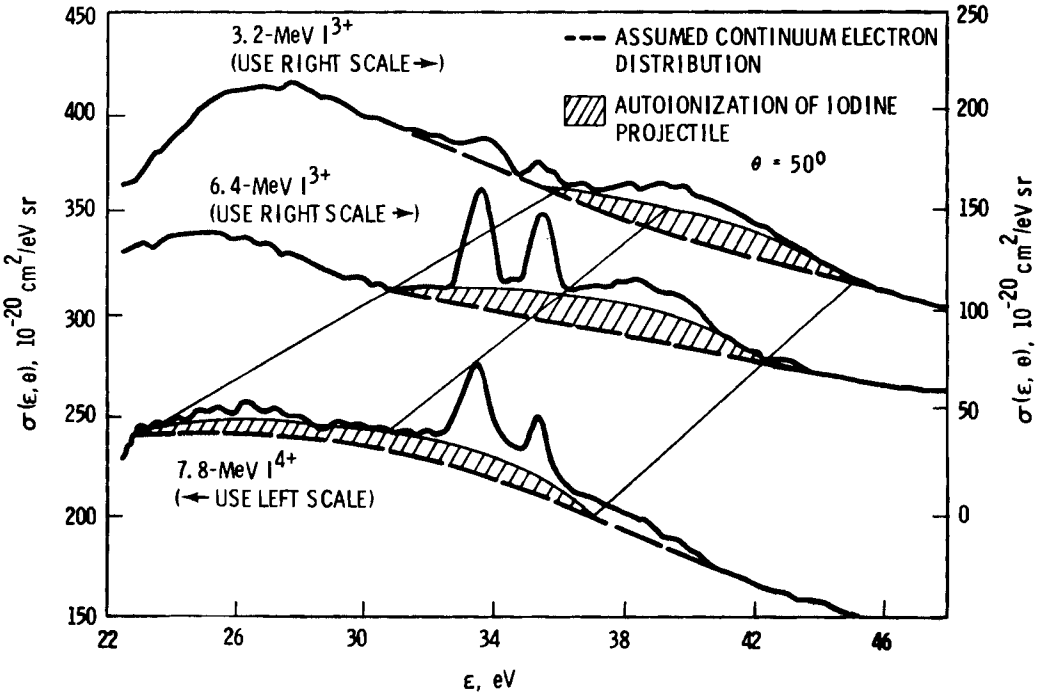

Figure 2.9. Autoionization Spectra at 50° for Ionization of Helium by Iodine Ions

variation in ejected-electron energy resulting from the Doppler shift associated with the ion velocity. After subtraction of the Doppler-shifted iodine-autoionization contribution, the helium autoionization spectra are nearly independent of electron-emission angle. Relative line intensities and excitation functions for each of the three major line groups in the autoionization spectra were presented in a paper given at the inner shell ionization conference held in Glasgow in August 1980.

• Track Structure

Experimental determination of radiation interactions in small absorber sites is limited to volumes greater than about 0.1 μm. This restriction has encouraged the development of computational methods to obtain the desired information in sites of arbitrary size. We are developing a Monte Carlo code, MOCA13, to calculate ionization and energy imparted in submicron sites by MeV positive ions. This code draws on extensive data for electron production in ion-molecule collisions as the source term for energy degradation calculations. The systematics of molecular cross sections are being analyzed to provide information on how molecular structure affects energy deposition calculations. The calculational technique is being improved through the use of conditional probabilities. We are assessing the reliability of calculations that use gas-phase cross sections to determine energy transport in the condensed phase. To make this assessment, we are comparing calculated multicollision electron spectra with measurements of the corresponding electron spectra emitted from foil targets on proton impact.

Analytical Systematics of Secondary Electron Production in Ion-Atom Collisions

W. E. Wilson and L. H. Toburen

The energy and angular distributions of delta rays ejected when energetic ions undergo ionizing collisions with the molecules of an absorber are fundamental to a realistic model for the track structure of radiations with high linear energy transfer (LET).

A sizeable literature has been published over the past 10 years on the double differential cross sections for the ionization of atomic and molecular targets by protons of up to a few MeV. This literature is sufficiently complete to allow the formulation of some general conclusions that are germane to microdosimetric modeling and calculations. In a paper presented at the 7th Symposium on Microdosimetry, Oxford, September 8-12 (1980), we reviewed the literature and outlined these conclusions. The following are excerpts from that paper.

For microdosimetric calculations that are dependent on track structure, cross sections are required for materials, or at ion energies, for which specific measurements are often unavailable. In those cases, an analytic expression describing secondary electron emission for a wide range of projectile and target parameters, preferably an expression derived from reliable theory, would be useful. An assessment of the variations in yields of secondary electrons for various molecules will provide guidance on how complex such an analytic expression must be. Also, the systematics of emission cross sections as a function of molecular weight may provide insight into what emission behavior can be expected in the condensed phase.

Angular distributions for delta rays of selected energies are convenient for illustrating the systematics of the emission cross sections for various molecular targets. The angular distributions in Figure 2.10 summarize the data for the ionization of low-Z molecules by 0.3- to 2-MeV protons. The differential cross section $\sigma(w,\theta)$ for electrons ejected with low energy is nearly isotropic, especially for high-energy proton impact. For energetic secondary electrons, the angular distributions become peaked. As the electron energy increases, this binary-encounter peak shifts to smaller angles, indicating that in collisions that have a small impact parameter and are therefore associated with large energy transfers, the delta rays are preferentially ejected forward. This point is important for ion track structure.

In a study of simple hydrocarbon molecules (Wilson and Toburen 1975) and a subsequent study of NH_3 and simple amines (molecules containing both carbon and nitrogen) (Lynch, Toburen and Wilson 1976), we found that the cross sections can be

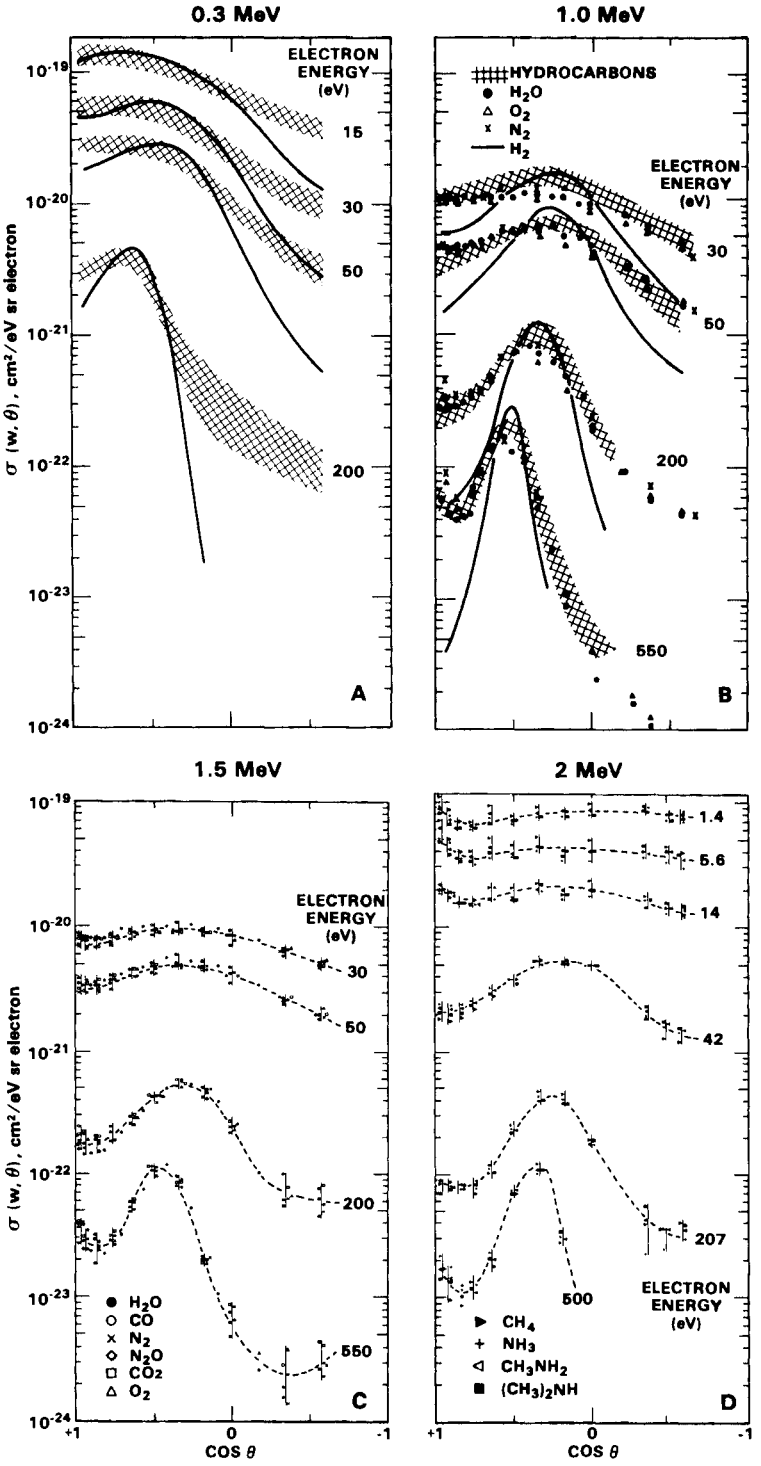

Figure 2.10. Angular Distributions for Delta Rays Ejected from Molecules by Protons. Cross sections are given per valence electron, i.e., K-shell electrons are not counted. Symbol legend for A is same as in B. Dashed lines in C and D are to aid the eye.

scaled in terms of the number of weakly bound electrons in the molecule; that is, the K-shell electrons of the carbon and the nitrogen atoms may be ignored when considering the magnitude of the ionization yield. This scalability of the yields is illustrated by dividing the double differential cross section per molecule by the number of valence electrons per molecule; a nearly universal angular distribution results, regardless of the atomic constituents (Figure 2.10).

The angular distributions for all of the molecules except H_2 fall into one of two almost identical groups. One group, indicated by the shaded bands in Figure 2.10(A) and (B), encompasses the data for the group of hydrocarbon molecules (including CH_4, C_2H_6, C_2H_2, and C_6H_6); the amine and NH_3 data also belong to this group [Figure 2.10(D)]. Not only are the yields for this group proportional to the number of weakly bound electrons in the molecule, but the angular distribution of the emission is, within experimental uncertainty, independent of molecular detail within this group of molecules.

Molecular structure does affect the ionization process, however. Molecular effects become apparent when angular distributions for the second group of molecules (including N_2, O_2, H_2O, N_2O, CO, and CO_2) are compared with the distributions for the hydrocarbon group, especially when low-energy delta rays are considered [Figures 2.10(B) and (C)]. The angular distributions for low-energy delta rays are more isotropic for the nonhydrogenous molecules; that is, they exhibit a less distinct binary-encounter peak than do the distributions for the hydrocarbons. Somewhat surprisingly, the angular distributions for H_2O fit into the second, non-hydrogenous group of molecules. As the delta-ray energy increases (i.e., as the energy transfer becomes large compared with the binding energy), the scaled cross sections show less dependence on molecular origin.

As mentioned above, molecular hydrogen is the one exception we have found to this scalability of cross sections. The shape of the angular distributions for molecular hydrogen is distinctly different from that for the other molecules. The scaled hydrogen cross sections, although in essential agreement with other molecules near the binary-encounter peak, may differ by more than a factor of 10 at large and small emission angles. The significance of this large difference for hydrogen is that most simple theoretical calculations, such as the Born approximation, which uses hydrogen wave functions, or the semiclassical binary encounter approximation, predict angular distributions that are similar to the distributions for hydrogen [Figures 2.10(A) and (B)] but that do not agree with the distributions for any other molecular target.

The systematics of delta-ray emission from low-Z targets are further revealed by considering the single differential cross section obtained by integrating the double differential cross section over solid angle (Figure 2.11). The energy spectrum of delta rays emitted at all angles is, within experimental uncertainty, independent of molecular type for delta rays with energy, w, greater than about 30 eV. Below 30 eV, the yield $\sigma(w)$ appears to depend in a systematic way on the amount of hydrogen in the molecule.

The curves in Figure 2.11 indicate the extremes in yields of low-energy delta rays that we have observed for molecules, CH_4 having the highest and O_2 the lowest yield. (Neon has a still lower yield for low-energy electrons.) This implies that the initial energy of the secondary electrons that produce the track "penumbra" or periphery does not depend to any significant degree on the chemical form of the medium. This result is not surprising; we should be suspicious of any other conclusion. The majority of the energetic secondary electrons are produced in hard, close (i.e., small impact parameter), and therefore essentially binary collisions. We expect such interactions to be influenced little by the proximity of neighbors. Indeed, that is what is meant by a "binary collision": all other influencing forces (scattering centers, particles) are sufficiently removed so as not to influence the interaction.

Figure 2.11 also shows that the curves do not diverge for decreasing w until ~30 eV, only 2 or 3 times the ionization potential of the medium. This experimental evidence indicates that in numerical methods for simulating ion tracks, it is not necessary for the high-energy delta-ray source term to be specific to the chemistry of the low-Z medium. The spectrum of inital delta-ray energies depends on the chemical composition of the medium only through the electron density. The situation may be somewhat different for He^{2+} and He^{+} ions, however; see Toburen, Wilson and Popowich 1980.

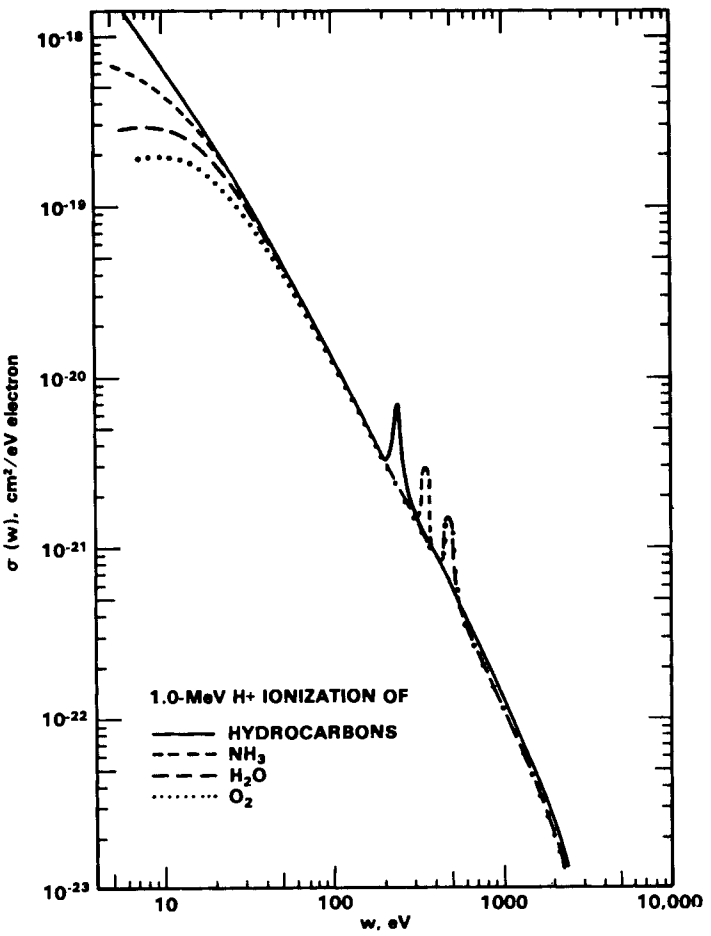

Figure 2.11. Single Differential Cross Section, $\sigma(w)$, for Delta-Ray Ejection from Molecules by Protons. The peaks arise from monoenergetic Auger electron emission following inner shell ionization of carbon, nitrogen, or oxygen atoms in the molecule.

Analytical Model for Primary Ionization by Positive Ions

W. E. Wilson and H. G. Paretzke[a]

Computational methods for track structure theories require extensive input that can be either taken from experimental data or derived from reliable physical theory. Of particular importance for positive ion track structure are accurate cross sections for the energy and angular dependence of secondary electron ejection following ionizing collisions.

For computational ease, we developed a phenomenological analytical representation of the initial ionization process from which we obtained the desired cross sections (Wilson 1978). This empirical model is based on the double differential cross sections for electron ejection from H_2O by 0.3- to 1.5-MeV H^+ ions (Toburen and Wilson 1977).

So that track structure calculations can be extended to ion energies beyond 1.5 MeV, we have begun to put our analytical representation of the input data on a

(a) GSF-Institut für Strahlenschutz, Neuherberg, Federal Republic of Germany.

theoretical basis.[a] We have extended and modified the previous representation to the following form:

$$Y(W,\theta,E_p) = \frac{G_1(W,E_p)}{G_2(W,E_p)} \text{Exp } (-Z(\theta)) + \sum C_L P_L \text{ (Cos } \theta) + CCT \qquad (6)$$

where $Y(W,\theta,E_p)$ is the ratio of the double differential cross section to the Rutherford cross section and, as before,

$$Z(\theta) = \left(\frac{\text{Cos } \theta - G_3}{G_2}\right)^2 \qquad (7)$$

The first term in Equation (6) is Gaussian shaped in Cos θ and represents hard collisions; the second term represents the distant or glancing collisions by a finite series of Legendre polynomials; and the term CCT (as yet undefined) will represent the continuum-charge-transfer interactions.

The coefficients G_2 and G_3 are identical with those in the previous representation and can be simply related to the kinematics of the hard, binary collisions. The ratio G_1/G_2 in Equation (6) is essentially A_1 in our previous representation. The inclusion of G_2 in the amplitude coefficient permits the integral of this Gaussian term over solid angle to be set to an arbitrary constant, thus allowing G_1 to become the single differential cross section for hard collisions.

We are investigating the applicability of various forms of binary encounter theory to represent the single differential cross section. The three coefficients in the hard collisions term are all related to the kinematics of the interaction or are theoretically based, hence this portion of the analytical representation extrapolates well with ion energy. In this preliminary effort, we were able to find coefficients for the glancing collisions, C_L, (by least-squares fitting of Equation (6), with CCT = 0) that were well-behaved functions of total energy transfer and ion energy, and that will therefore be at least extrapolable to higher ion energies, if not theoretically predictable.

Ionization Distributions in Condensed Phase

W. E. Wilson, L. H. Toburen and H. G. Paretzke[b]

The development and application of Monte Carlo codes for energy transport studies depend heavily on experiments to assess the reliability of the calculations. In particular, codes that use gas-phase data as input need careful testing to affirm their validity for use in condensed-phase calculations. The study of Auger electron emission from foils excited by heavy-ion beams provides an opportunity to investigate the reliability of our Monte Carlo codes as well as to obtain new information on a common background process in beam-foil spectroscopy.

The Monte Carlo code MOCA13 was used to calculate the spectral shape for both scattered and degraded Auger electrons leaving a foil after excitation by a 1-MeV proton. A free-molecule Auger spectrum, represented by the benzene Auger spectrum, was used as the initial probability distribution for primary Auger electrons generated within the foil from inner-shell excitation of the carbon atom. To expedite the computation time, only Augers arising from K-shell vacancies were generated, and they and their secondaries were followed as they multiply scatter until eventually escaping the foil or stopping within it. Thus moderated Auger electron spectra were obtained without the continuum background of electrons arising from the more abundant outer-shell ionization processes. The energy of each electron leaving the foil was recorded, along with its ejection angle with respect to the proton path. Energy bin widths of 5 eV and cosine bin widths between 0.002 and 0.1 were used. Four million Auger electron histories were followed during the calculation, which corresponds to about 2.35×10^7 protons penetrating a 3-$\mu g/cm^2$ carbon foil. An average of about 0.17 inner-shell ionizations are produced per proton if a K-shell ionization cross section of 1.15×10^{18} cm^2/C-atom is assumed for a 1-MeV proton.

(a) This initial work was accomplished while W. E. Wilson was a guest at the GST-Institut für Strahlenschutz, Neuherberg, Federal Republic of Germany; the use of their computer facilities and their hospitality and collaboration on this project are gratefully acknowledged.

(b) GSF-Institut für Strahlenschutz, Neuherberg, Federal Republic of Germany.

The calculated electron distribution resulting from Auger electrons generated within a foil is shown in Figure 2.12, along with the nearly Gaussian shape expected for unmoderated Auger electrons from free-atom collisions. In comparison with the free-atom data, the calculated spectrum shows a large contribution attributable to low-energy electrons. The calculated shape is in excellent agreement with our measurements for a 3-$\mu g/cm^2$ foil when allowance is made for degraded Auger electron contributions to the continuum spectrum at low electron energies. This is illustrated in Figure 2.13, where the solid line represents the estimated continuum background from outer-shell ionization. The dashed line represents an arbitrary continuum background that might be acceptable if degraded Auger electrons were not taken into account in the low-energy portion of the spectrum. A detailed comparison of the Monte Carlo calculations and the foil measurements is in progress.

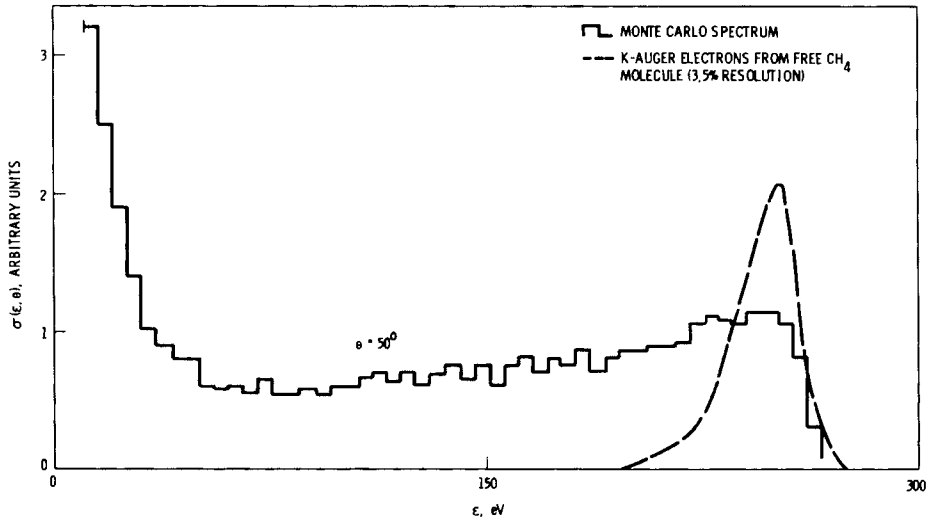

Figure 2.12. Monte-Carlo-Calculated Electron Emission Spectrum from Auger Electrons Produced by 1.0-MeV H^+ Impact on 3-$\mu g/cm^2$ Carbon Foil

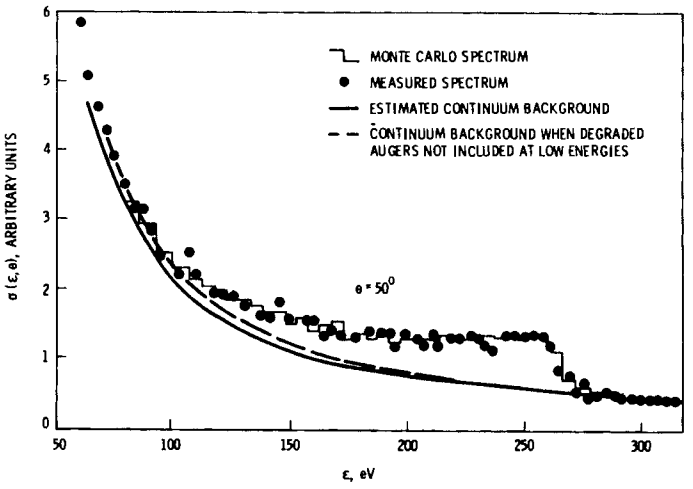

Figure 2.13. Comparison of Calculated and Measured Auger Spectra from Excitation of C-K Auger Transitions Produced by 1.0-MeV H^+ Impact on 3-$\mu g/cm^2$ Carbon Foil

• Energy Transport

The measurement of primary interaction cross sections and the incorporation of these data into Monte Carlo calculations provide detailed information about the initial spatial distribution of absorbed dose. As part of our theoretical energy transfer studies, we are attempting to use this information to predict the evolution of chemical species formed as a result of energy deposition. We have developed a stochastic model of diffusion kinetics. Our experimental program in time-resolved emission spectroscopy has played an integral part in the development of this model by providing a simple chemical system in which track structure effects can be measured on a nanosecond time scale. Linear energy transfer (LET) is probably the most important track structure parameter in radiation chemistry. Nevertheless, our stochastic model predicts different chemical yields for radiations with the same LET because of differences in the radial distribution of absorbed dose. These predictions are being tested through experiments with pulsed heavy-ion beams with the same stopping power but different velocity and charge. The studies suggest that the influence of track structure on fluorescence quenching is significantly greater than was predicted by the stochastic model. To resolve this discrepancy, we are improving our experimental technique and gaining more information about the quenching mechanism through measurements of total light emission and the dependence of the fluorescence decay on solute concentration.

Modeling Radiation Quality Effects in the Quenching of Benzene Fluorescence Excited by Proton and Alpha Particle Irradiation

J. H. Miller and M. L. West

The biological effectiveness of ionizing radiation depends upon quality factors such as the linear energy transfer (LET). We are investigating radiation quality effects in simple chemical systems to gain a better understanding of their mechanism in cells. The quenching of benzene fluorescences excited by pulsed heavy-ion irradiation (West 1976) has proved a useful system for studying radiation quality effects that are related to the initial spatial distribution of absorbed dose.

The first model of this system (Miller and West 1977) explained the dependence of the fluorescence decay on beam energy in terms of the LET of the radiation. Subsequent experiments (West and Miller 1980b) showed that this model was not adequate because the fluorescence excited by alpha particles was quenched less than the fluorescence excited by protons of the same LET. Analysis of the alpha-induced fluorescence decay based on the LET model suggested that if the initial yield of quenching species per unit of energy absorbed is the same for both types of radiation, then to explain the observed difference in quenching, the effective LET of the alpha irradiation must be about half the average stopping power.

To improve the fluorescence decay model, we have focused on incorporating the radial distribution of absorbed dose. Energy deposited by an alpha particle with the same LET as a proton has a more diffuse radial distribution, which should result in a reduction in quenching. The first attempt to calculate how the radial distribution of energy deposition affects fluorescence decay (Miller and West, in press) was based on Bohr's adiabatic criterion, which states that the maximum-impact parameter for transfer of energy ε to the medium is proportional to v/ε where v is the ion velocity. The predictions of this model can be expressed in terms of an effective LET, which approximately accounts for the radial distribution of absorbed dose. Unfortunately, this effective LET depends strongly on $\bar{\varepsilon}$, the mean energy transferred to the medium

in an energy loss event. Appleby and Schwarz (1968) recommend a value of $\bar{\epsilon}$ = 62.5 eV based on the yield of free radicals in an aqueous medium exposed to low-LET radiation. With this value of $\bar{\epsilon}$, the effective LET of alpha particles in the energy range used in the fluorescence study (West and Miller 1980b) is about two-thirds the average stopping power. Thus the reduction in quenching attributable to the radial distribution of energy deposition predicted by this model is somewhat less than the observed reduction.

A stochastic model of diffusion kinetics has been developed to obtain a more reliable estimate of the effect of track structure on the fluorescence decay. This model uses Monte Carlo techniques (Wilson and Paretzke 1980) to calculate the spatial distribution of energy-loss events. Figure 2.14 shows a plot of the mean number of energy-loss events that contribute to the quenching of an excited state as a function of time after irradiation. This number increases with time because the reactive species that result from an energy-loss event diffuse into the medium. The region containing these species is known as a spur. The radius of a spur at a given time is shown on the lower horizontal axis. If the radial displacement of energy-loss events in a track segment is neglected, the mean number of spurs that contribute to the quenching of an excited state in that segment increases linearly with spur radius, with a slope proportional to LET. This result is indicated by the dashed lines in Figure 2.14. When the Monte Carlo method is used to account for the radial distribution of spurs, the number of spurs contributing to quenching is approximately proportional to the spur radius, but with a smaller slope. Hence, from the slope of the solid lines in Figure 2.14, we obtain an effective LET for alpha particles that is about 75% of the stopping power.

Both the stochastic model and the simple model based on Bohr's adiabatic criterion predict that the reduction in quenching attributable to the radial distribution of absorbed energy is less than the observed reduction in the quenching of alpha-induced fluorescence relative to that of proton-induced fluorescence. From this we conclude that at least part of the observed reduction is not directly related to the spatial distribution of energy-loss events.

A number of alternative explanations are under consideration. Because the range of an alpha particle is much greater than the range of a proton of the same LET, any influence the entrance foil has on the fluorescence decay will be much less for alpha particles than for protons of the same LET. Experiments to vary the thickness of entrance foil or to eliminate it through the use of a jet sample are in progress. The initial yield of quenching species per unit of energy absorbed could also be a function of the radiation quality. Normally, the yield of primary species is assumed to be independent of the spatial distribution of energy-loss events because the initial separation of spurs makes the probability of their interaction small during the 10^{-11} sec in which primary products are formed. Nevertheless, some energy-loss events will give rise to clusters of ions closely correlated in space. Magee and Huang (1972) have proposed a mechanism by which the relative yield of singlets and triplets could be influenced by the spatial distribution of ion pairs. Modeling this type of radiation quality effect will require more information about the nature of the quenching species and the mechanism of their production.

Stochastic Model of Track Structure Effects in the Radiation Chemistry of Aqueous Solutions

J. H. Miller

Energy deposited by ionizing radiation gives rise to localized regions called "spurs" (Samuel and Magee 1953) that contain a high concentration of reactive species. The extent of interspur reaction as the medium relaxes to a state of thermodynamic equilibrium depends upon the linear energy transfer (LET) of the radiation. For low-LET radiation, spur overlap is small and a spherical symmetry is a good approximation for describing the concentration of reactants. For high-LET radiation, most spurs are near the trajectory of the primary ion, and their strong overlap makes a cylindrically symmetric concentration of reactants a good approximation. Intermediate cases have been treated by Mozumder and Magee (1966) through a combination of "spurs," "blobs," and "short tracks."

The stochastic model discussed in the preceding paper in regard to the quenching of radioluminescence provides a method for relating the concentration of reactants to the initial spatial distribution of energy-loss events determined by Monte Carlo techniques. For a system containing M species interacting through second-order processes,

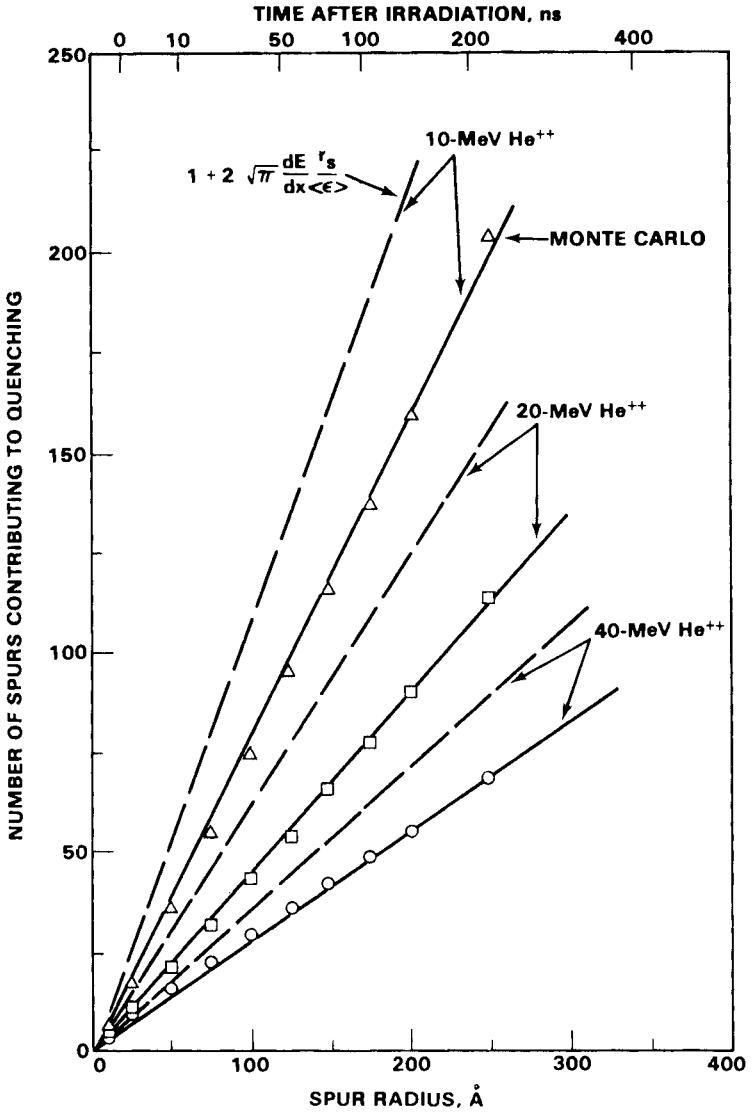

Figure 2.14. Mean Number of Energy-Loss Events (Spurs) Contributing to Quenching of an Excited State. Dashed lines show result obtained when radial displacement of spurs is neglected.

the time-dependent yields g(t) are obtained by solving coupled differential equations of the form

$$\frac{dg_\alpha}{dt} = \sum_{\beta,\gamma} P_{\beta\gamma}\, g_\beta g_\gamma \bar{d}_{\beta\gamma} - \sum_\beta A_{\alpha\beta} g_\alpha g_\beta \bar{d}_{\alpha\beta} \qquad (8)$$

where $P_{\beta\gamma}$ and $A_{\alpha\beta}$ are rate constants for the production and annihilation of species α, and $\bar{d}_{\beta\gamma}$ and $\bar{d}_{\alpha\beta}$ are time-dependent energy densities that account for the inhomogeneous distribution of the reactants. These track structure quantities are weighted averages of the energy density from all energy-loss events in the radiation field.

The Monte Carlo results discussed in the previous section suggest that the effect of the radial distribution of energy-loss events on the energy density in a track segment can be approximated by a time-dependent track structure factor, f_{TS}, that reduces the LET of the radiation.

Since f_{TS} does not depend upon time, solutions of Equation (8) for ions with the same stopping power but different velocities and charges can be related through the use of an effective LET equal to f_{TS} times the stopping power. Data from Sauer et al. (1977), on the yield of hydrated electrons in aqueous solutions irradiated with deuterons and alpha particles of the same LET, show that the yields would overlap if the stopping power of the He^{2+} ion were reduced by 0.7. This is consistent with our Monte Carlo results, which suggest that the track structure factor in this energy range is near unity for deuterons and about 0.75 for alpha particles.

Fluorescence in Binary Liquid Systems: Concentration Dependence

M. L. West and J. H. Miller

When solutions of benzene in cyclohexane are irradiated with subnanosecond bursts of protons, the time-resolved fluorescence emission is observed to change with a change in the benzene concentration. We have shown (West and Miller 1980a) that this concentration dependence cannot be attributed to excimer effects but is associated with a concentration dependence of the radiation-induced quenching. This dependence can be explained by either a direct involvement of benzene molecules in the quenching processes or an indirect effect of the concentration of benzene on the yield of quenchers from radiolysis of cyclohexane.

Figure 2.15 shows the concentration dependence of the fluorescence decay converted to a yield of quencher per 100 eV of energy absorbed for an assumed diffusion-limited quenching rate of 10^{10} 1/m·sec. The solid line of Figure 2.15 shows the average triplet yield for a number of aromatic solutes in cyclohexane as a function of solute concentration (Rzad 1972). The agreement in both shape and absolute magnitude suggests that triplet states of benzene may be responsible for the observed quenching.

Triplet states of benzene may be formed directly from the transfer of excitation energy or through the recombination of benzene ions formed by charge scavenging. The charge scavenging reactions are

$$C_6H_{12} \rightsquigarrow C_6H_{12}^{+} + e^{-} \qquad (9)$$

$$C_6H_{12}^{+} + C_6H_6 \rightarrow C_6H_6^{+} + C_6H_{12} \qquad (10)$$

$$C_6H_6^{+} + e^{-} \rightarrow C_6H_6^{*} \text{ (triplet)} \qquad (11)$$

Triplet yields formed through these ion scavenging reactions show a concentration dependence that agrees with our data where there is an initial square root dependence at low concentrations followed by a limiting value at higher concentrations. We plan to extend these measurements in order to confirm this square root dependence over a broader range of benzene concentrations. A more detailed analysis will also include measurements of steady-state fluorescence versus concentration, and competing charge scavenging experiments.

Fluorescence in Binary Liquid Systems: Dependence of Steady-State Emission on Beam Energy

M. L. West and J. H. Miller

When dilute solutions of benzene in cyclohexane are irradiated with subnanosecond bursts of protons and alpha particles, the initial rate of decay of benzene fluorescence is greater than the rate of decay observed with ultraviolet excitation, but approaches the ultraviolet decay rate as time increases (West 1976). This radiation-induced quenching is proportional to the mean stopping power of the incident ion.

To explain the decay of radiation-induced fluorescence, we proposed a model that involves a dynamic quenching of excited states by a time-dependent concentration of radiation-produced quenchers (Miller and West 1977). This model predicts a decrease in the intensity of the steady-state fluorescence with a decrease in beam energy. However, the observed reduction in the steady-state fluorescence with decreasing beam energy is greater than is predicted when we assume that the initial yield of excited states per unit of energy deposited is independent of the energy of the primary ion. We refer to the phenomenon that influences the initial yield of excited states as static quenching because these states are assumed to be quenched before they can participate in the fluorescence decay mode.

Steady-state fluorescence I_f for incident protons of energy E_i at beam current i_B can be expressed as

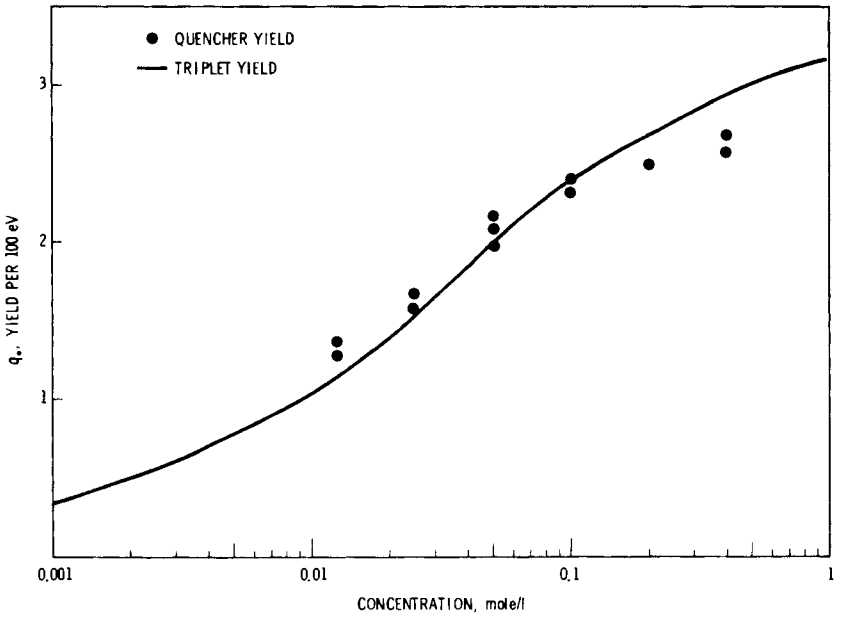

Figure 2.15. Yield of Radiation-Induced Quencher, q_*, as a Function of Benzene Concentration in Cyclohexane for an Assumed Diffusion-Limited Quenching Reaction

$$I_f(E_i) = i_B(E_i)\ \varepsilon \int_0^{E_i} dE\ g_*(E)\ P_f(E) \qquad (12)$$

where ε is the collection efficiency, g_* is the initial yield of excited states per unit of energy, and P_f is the probability of fluorescence (including dynamic quenching caused by radiation-induced quenchers). If we define

$$Q = \frac{I_f(E_i)}{i_B(E_i)} \qquad (13)$$

as the beam-normalized fluorescence, then from Equation 12

$$\frac{dQ}{dE_i} = \varepsilon\ g_*(E_i)\ P_f(E_i) \qquad (14)$$

This beam-normalized fluorescence intensity was measured for proton irradiation over the energy range 0.75 to 1.6 MeV and is shown in Figure 2.16 along with its derivative, which was obtained numerically. The proton energies shown in Figure 2.16 have been corrected for energy loss in the entrance foil.

In our first attempt to fit these data, we assumed that the yield of excited states $g_*(E)$ was independent of the proton energy. Values of $P_f(E)$ were then obtained from studies of proton-induced dynamic quenching. The dashed curve in Figure 2.16 shows the shape obtained for values of dynamic quenching parameters from our previous studies. These data suggest that dynamic quenching alone cannot explain the observed steady-state data and that additional quenching mechanisms are needed.

If we assume that the production of excited states is limited by the number of benzene molecules near the proton trajectory, then dN_*/dR is a constant where R is the particle range and N_* is the total number of excited states in the track. Under these conditions,

$$g_*(E) = \frac{dN_*}{dR}\frac{dR}{dE} = \frac{\text{constant}}{S(E)} \qquad (15)$$

where S(E) is the stopping power, and Equation (14) reduces to

$$\frac{dQ}{dE} = C\,\frac{P_f(E)}{S(E)} \qquad (16)$$

The solid line of Figure 2.16 shows the predicted energy variation of dQ/dE based on Equation (16).

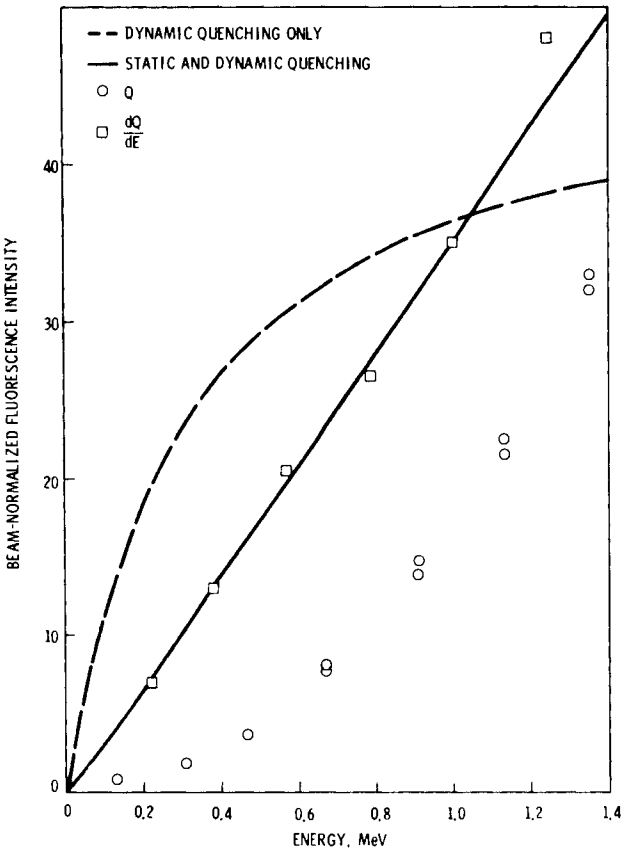

Figure 2.16. Beam Normalized Fluorescence Intensity Q and Its Energy Derivative dQ/dE as a Function of Proton Energy

The model based on a constant yield of excited states per unit track length gives a better fit to the data for steady-state emission than does the model based on a constant yield of excited states per unit of energy absorbed. More experiments are needed to test the hypothesis that this result is due to a saturation effect.

• Radiation Dosimetry and Radiation Biophysics

Radiation dosimetry and radiation biophysics are two closely integrated programs whose joint purpose is to explore the connections between the primary physical events produced by radiation and their biological consequences in cellular systems. The radiation dosimetry program includes the theoretical description of primary events and their connection with the observable biological effects. This program also is concerned with the design and measurement of physical parameters used in theory or to support biological experiments. The radiation biophysics program tests and uses the theoretical developments for experimental design, and provides information for further theoretical development through experiments on cellular systems.

Sublethal Damage Repair in Plateau-Phase Mammalian Cells

J. M. Nelson, L. A. Braby, and W. C. Roesch

The repair of sublethal damage produced by ionizing radiation is difficult if not impossible to quantify in exponentially growing cells because their radiosensitivity changes rapidly as a function of their age in the cell cycle. However, sublethal damage and its repair can be studied in noncycling, stationary-phase cells because their radiosensitivity is not expected to vary with time.

We have previously described techniques to stop exponential growth in Chinese hamster ovary (CHO) cells and to establish monolayer cultures of noncycling, stationary-phase populations (Nelson 1978, Nelson 1979). These cultures were induced by both density-contact inhibition (fed cells) and nutritional deprivation (starved cells). During the past few years, we have evaluated the resultant stationary-phase populations with respect to both cell viability (as defined by erythrosin-B dye exclusion techniques) and their ability to incorporate a labeled deoxyribonucleic acid (DNA) precursor. Labeling with tritiated thymidine (^{3}H-TdR) provides a means of determining both the duration of the DNA-synthetic phase and the fraction of cycling cells remaining in the plateau-phase population (Nelson 1979). We have also contrasted the radiosensitivity of each of these stationary-phase populations with that of exponentially growing cells in terms of their clonogenic cell survival as a function of dose (Nelson and Braby 1980). The survival curves for cells from the same CHO line maintained in these different metabolic states are surprisingly similar. They differ primarily in the magnitude of the shoulder that corresponds to different values for D_q (the width of the shoulder); the values of D_0 (the radiation sensitivity) in each case are not significantly different.

Split-dose experiments were performed using monolayers grown to plateau phase by the techniques described last year (Nelson 1979). The culture vessels in which cells were grown to plateau contain between 10^5 and 10^6 viable cells/cm^2 by the fourteenth day. Their DNA synthetic activity at this time has been suppressed about two orders of magnitude and no change in the numbers of viable cells or their metabolic activity is observable for at least the next seven days. Plates containing such noncycling stationary-phase populations were carefully removed from the incubator and inverted, so that the cells were suspended from the upper surface of the culture vessel. A 1.5-MeV electron beam scattered downward from a graphite block was used to irradiate these cells *in situ* through the polystyrene wall of the culture vessel. Immediately after this exposure, the plates were carefully turned upright, and medium was permitted to flow gently over the monolayer again. They were maintained at 37°C both during and between irradiations. At the time of the second exposure, the cells were treated in exactly the same manner. However, after this irradiation, they were suspended by trypsinization, and cell concentrations were determined using an electronic particle counter. The suspensions were diluted and distributed into additional flasks for the clonogenic cell assay. Throughout the experiment, plates were handled with extreme care so as not

to mechanically disturb the integrity of the dense but relatively fragile monolayers. Thermal shock was prevented by maintaining the temperature at 37°C throughout.

As with other studies of sublethal damage, survival data were analyzed according to our Accumulation-of-Damage Model (Nelson, Braby and Roesch 1979; Nelson, Braby and Roesch 1980). The details of this model, which considers exponential repair of the two-event or sublethal component of damage, have been described elsewhere (Roesch 1978; Braby and Roesch 1978b). The model predicts that when the survival data are plotted as the logarithm of $\ln S_1S_2/S$ against time between doses (where S_1 and S_2 are survivals after two doses given independently, and S is the net survival after both doses), the data will fall on a straight line (Braby and Roesch 1978b). The mean repair time is the negative reciprocal of the slope of this line. Furthermore, if more than one repair process exists simultaneously, data for each can be separated by subtraction in much the same manner as that used for separating mixed radioisotopes with different half-lives.

Since the presence of a shoulder on the survival curve suggests that plateau cells do accumulate sublethal damage (Nelson and Braby 1980), a systematic study of their repair capability was undertaken. Repair might proceed at the conventional rate (with a mean repair time of about 30 min as observed in exponentially growing cells) or might be either faster or slower.

The technique we used to study repair can be demonstrated using exponentially growing cells even though, because of changing radiosensitivity, they can be expected to give only a qualitative estimate of net repair for this mixed population. The results of such studies, using two equal radiation doses separated by intervals as long as 5 h, can be seen in Figure 2.17. The change in the logarithm of $\ln S_1S_2/S$, roughly one order of magnitude in 5 h, gives a mean repair time somewhere between 25 min and 2 h, which is consistent with our understanding of the conventional Elkind-Sutton repair. On the other hand, noncycling stationary-phase cells appear to repair sublethal damage somewhat differently.

Using very high dose rates and short interfraction intervals, we attempted to identifty repair processes in plateau-phase cells similar to those in exponentially growing cells. We found no evidence for such repair in stationary-phase CHO cells, even though Malcolm and Little (1979) described a 2-min process in plateau-phase 10-T1/2 cells (mammalian cells) and we have

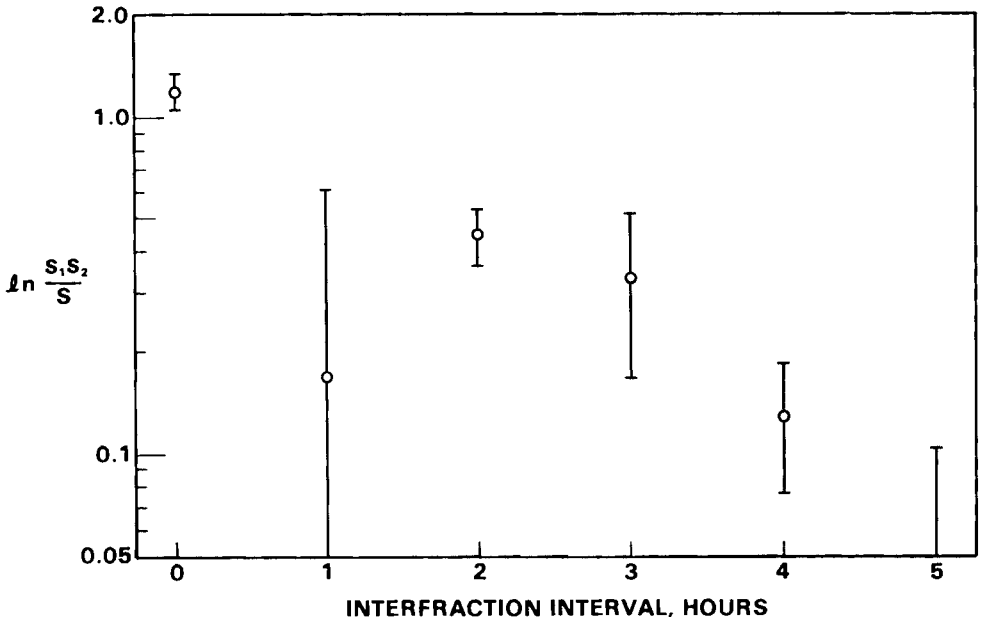

Figure 2.17. Split-Dose Survival Data for Asynchronous Exponentially Growing Chinese Hamster Ovary Cells

identified a similar process in Chlamydomonas reinhardi (Nelson, Braby and Roesch 1980). This difference in findings is probably a consequence of intrinsic differences between dissimilar eucaryotic cell lines, coupled with great variations in the kinetic status of two types of plateau mammalian cells maintained in different laboratories.

When longer intervals are used, as seen in Figure 2.18, the density-inhibited stationary-phase cells demonstrate a repair rate about the same as that in exponentially growing cells and perhaps analogous to that seen in Figure 2.17. However, not all of the damage produced is eliminated by this process. Damage remaining after 4 to 5 h persists for a considerable period of time or perhaps is not repaired at all. As seen in this figure, survival data for intervals greater than 5 h fall on a line with essentially no slope; if a very slow process were to effectively remove sublethal damage in this case, the mean repair time would be greater than 100 h. Similar experiments with nutritionally deprived cells (starved cells) suggest that a slower process (i.e., slower than Elkind-Sutton repair) does exist under these conditions. As seen in Figure 2.19, nearly all of the sublethal damage produced appears to be repaired by a process with a characteristic time of 15 to 20 h. Only a small fraction of the damage is removed by the conventional process.

The kinetic status of nutritionally deprived cultures has been found to be considerably different (see the following report) from that of the higher-density contact-inhibited cells, even though cellular viability and DNA synthetic activity are nearly the same. We are continuing our studies of slow repair processes in these cell systems to gain a better understanding of how sublethal radiation damage is produced and repaired in nonproliferating or nonrenewing cell systems.

Kinetics of Chinese Hamster Ovary (CHO) Cells After Release from Stationary Phase

J. M. Nelson and L. A. Braby

Recent studies with Chlamydomonas reinhardi (Nelson, Braby and Roesch 1980; Braby, Nelson and Roesch 1980b) have revealed unexpected results with respect to the rates at which cells repair sublethal damage from ionizing radiation and the dependence of the repair rate on the linear energy transfer of the radiation. To determine whether similar processes exist in mammalian cells and to extend studies of sublethal damage repair beyond

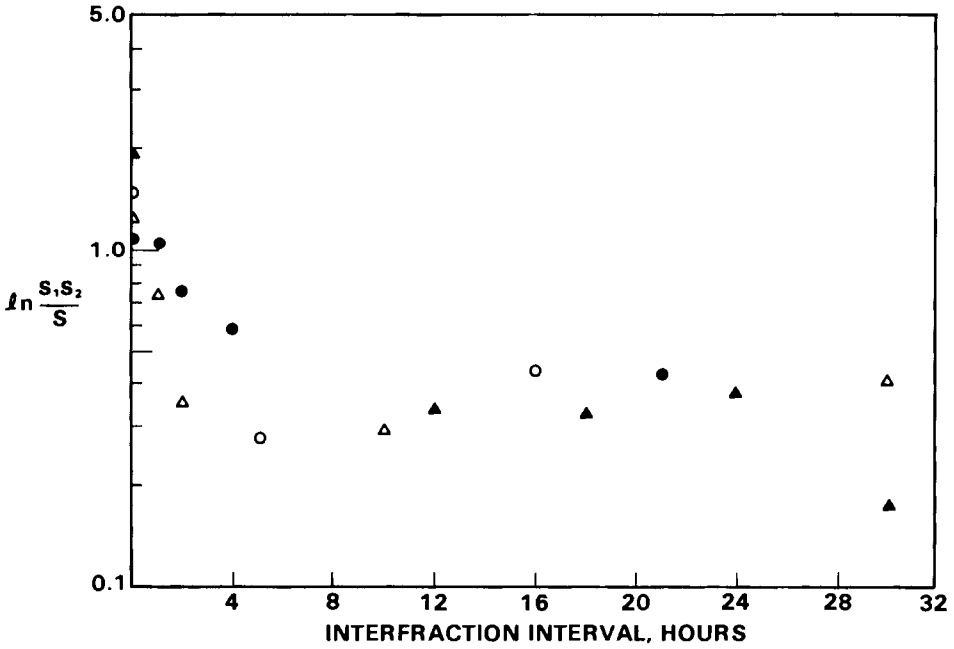

Figure 2.18. Split-Dose Survival Data for Density-Contact-Inhibited Stationary-Phase Chinese Hamster Ovary Cells

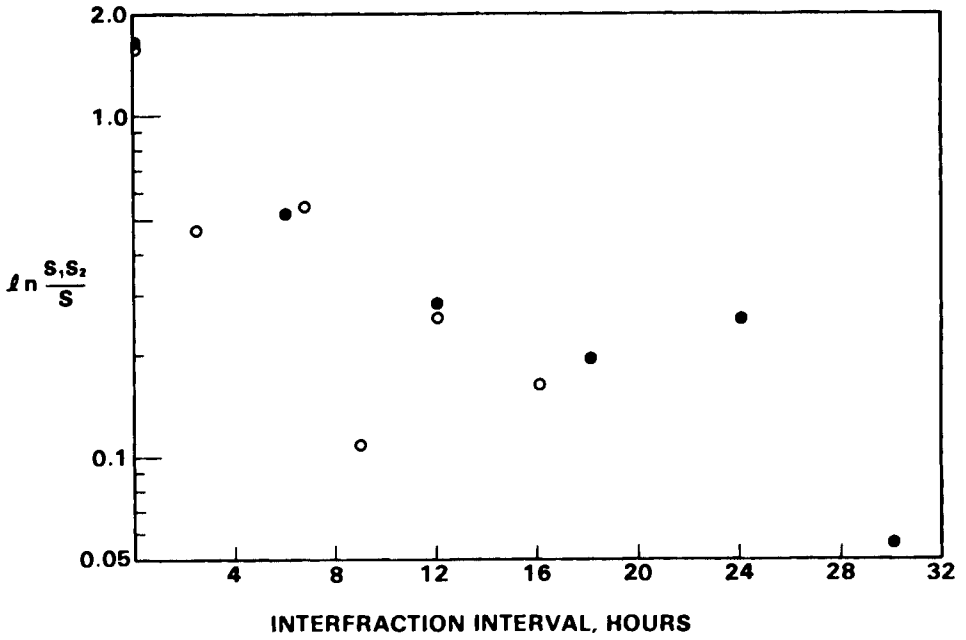

Figure 2.19. Split-Dose Survival Data for Nutritionally Deprived Stationary-Phase Chinese Hamster Ovary Cells

Chlamydomonas, a population of mammalian cells whose radiation sensitivity does not vary with time is needed. We believe that stationary-phase cells, that is, cells whose proliferative activity has virtually ceased, may satisfy this need.

The two types of noncycling, stationary-phase populations of Chinese hamster ovary (CHO) cells currently available in our laboratory are characterized by attenuated DNA-synthetic activity, relatively constant population density, and high cell viability (Nelson 1978). Although they are similar in these characteristics, they do not appear to repair sublethal radiation damage in the same manner or at the same rate (Nelson and Braby 1980).

To properly evaluate repair information for noncycling populations, we must clearly understand the physiology of these cells. Kinetic activity in noncycling cells is not directly measurable; we can determine cell age distributions and evaluate synchrony in such populations only indirectly, by studying the kinetic behavior of these cells as they enter the plateau phase and after they have been released from stationary phase.

Interest in plateau-phase cells grew out of the assumed correlations between these cells in vitro and the noncycling or slowly cycling populations in solid tissues that have low renewal rates. Several attempts have been made to describe their physiology and kinetic status. Hahn and Bagshaw (1966) presented evidence demonstrating a disproportionately large fraction of G_1 cells during periods of attenuated growth; this finding would help to explain the diminished radiosensitivity commonly observed after a period of serum deprivation. Chapman, Todd, and Sturrock (1970) found agreement with these earlier findings using 3- to 6-day starved monolayers. By autoradiographic methods, they observed that DNA-synthesis began at about 12 h after subculturing, following a very long G_1 phase. They also noted that a highly synchronous cohort of cells passed through mitosis at about 25 h. From these observations they concluded that resting cells, which represented the principal component of their plateau-phase populations, had ceased their proliferative activity (become noncycling) sometime after mitosis and were resident somewhere in the G_1 phase. Since then, it has been generally accepted that slowly cycling or noncycling plateau-phase cells, assumed by many to be analogous to Lajtha's G_0 cells (Lajtha 1963), were resting at a point in the cell cycle after mitosis but prior to DNA synthesis. These conclusions were reasonable, particularly considering

the experimental methods used and the instrumentation available at the time, although other explanations are also possible.

Thymidine labeling studies with plateau-phase cells in our laboratory do not support these findings. Rather, our data indicate that DNA synthesis begins almost immediately after a cell is released from the stationary phase and that no remarkable increase in activity is observed 12 h later. Our preliminary data were obtained from 18- to 19-day density-contact-inhibited monolayers that showed considerably less proliferative activity than the plateau cells used by other investigators.

We have used a relatively novel approach to characterize our stationary-phase cells and explain some of these discrepancies. Using a computer-controlled video-microscope coupled to both a video-disc and a tape recorder (Braby 1977), we selected large numbers of individual cells and followed them for periods of up to 36 h starting shortly after their release from the stationary phase. The microscope used differs from a conventional video-microscope only in that the specimen remains motionless while the optics move. Their motion is precisely controlled by a computer via stepping motors.

Populations of cells were released from the stationary phase by gentle trypsinization. They were then suspended, and replicate plated at low densities into plastic culture flasks. The flasks were placed into the microscope stage assembly where the cells were allowed to attach firmly. After a period of incubation, we selected and recorded the images of a number of individual microscope fields, each containing between 10 and 20 cells. We then instructed the computer to locate these same fields at specific intervals and automatically record the images onto the video-disc. When the entire set had been collected, they were transferred individually onto the video-tape, with the series of images for each individual field assembled together in chronological order. These series were then viewed as a progression of images in much the same manner as any other time-lapse series.

By following individual cells, we were able to determine which cells divide and when they do so; we have tabulated these mitoses for both the original cells and their progeny. Each mitosis was considered to have occurred when two daughter cells became clearly visible. The actual event had occurred sometime during the preceding interval, in this case a period of 1 h.

In Figure 2.20(A), the mitotic frequency in cells originating from starved-cell cultures has been plotted as a function of time after release from the stationary phase. A significant degree of synchrony is apparent. Most of these cells appear to pass through mitosis at or around 24 h after release; this would correspond to the wave of mitoses reported earlier. A large number of doublets were also clearly visible at the time of the first scan (3 h after release). Since they were observed then, they were included in the 3-h count, although there was no way of knowing then whether they represented artifacts (cells that had not been separated by the trypsinization and trituration processes) or the progeny of single cells that had divided in the first 3 h.

A substantial number of daughters or daughter pairs produced by early mitoses were found to undergo mitosis again 12 to 24 h later. On occasion, even a third generation could be observed within the experimental period. Since the age distributions and kinetic status of the first-generation daughters should not be affected by when later divisions occur, information relative to any mitosis other than the first was eliminated. These results, shown in Figure 2.20(B), indicate that most of the activity observed as a wave at around 24 h in Figure 2.20(A) represented mitoses after the first. For purposes of illustration, the curve showing frequency of first mitosis has been plotted as the fraction of total first mitoses observed against time; the frequency of all mitoses has been normalized to the frequency of first mitosis data and plotted on the same relative scale.

In Figure 2.21(A) and (B), density-contact-inhibited cells (fed cells) appear to behave in a manner similar to that of the nutritionally deprived cells. However, they fail to exhibit the dramatic wave of mitoses seen at 24 h in Figure 2.20(A) and the frequency of doublets found at the time of the initial scan is not nearly as remarkable as with the nutritionally deprived cells.

The presence of multiple-cell clusters, particularly doublets, seriously hampers our capability to assess mitosis in the early hours. However, cell-to-cell contact appears to be physiologically beneficial, and such clustering, or aggregation, whether by active or passive mechanisms, is

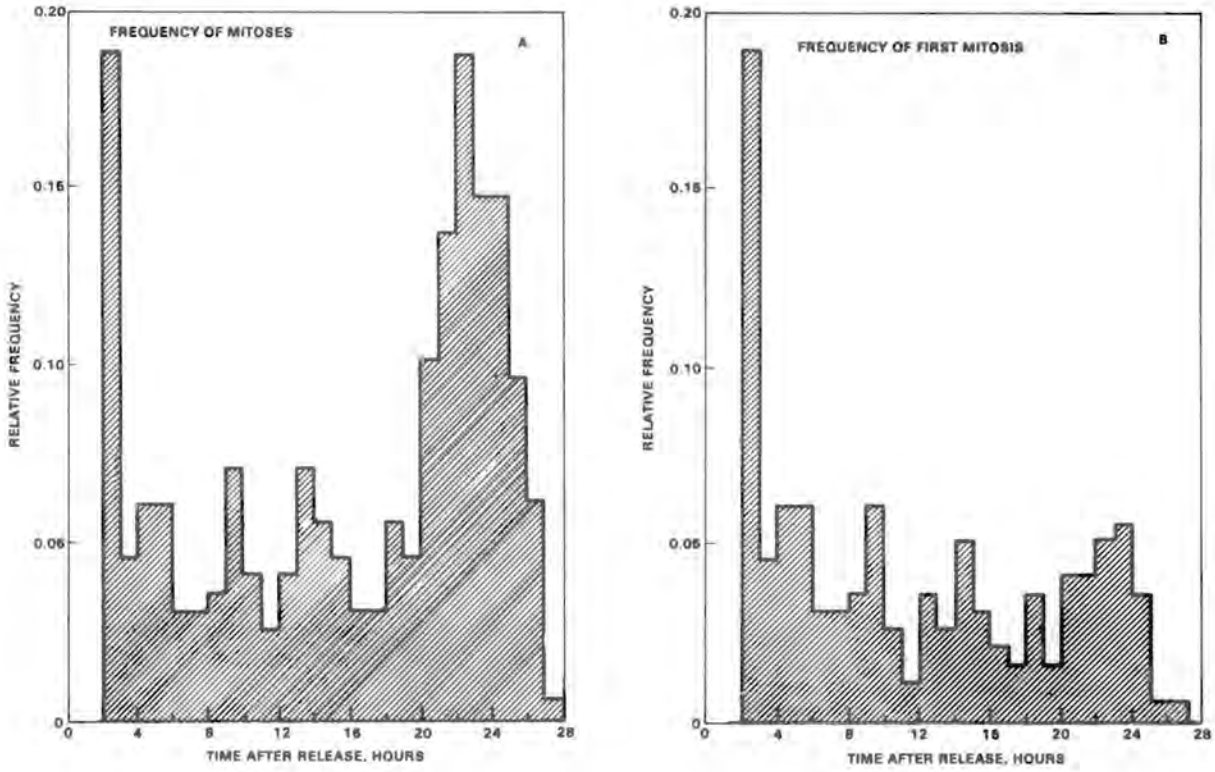

Figure 2.20. Relative Frequency of All Observed Mitoses (A) and of First Mitoses (B) Among Populations Derived from Nutritionally Deprived Plateau Cultures, Plotted Against Time After Release from Stationary Phase

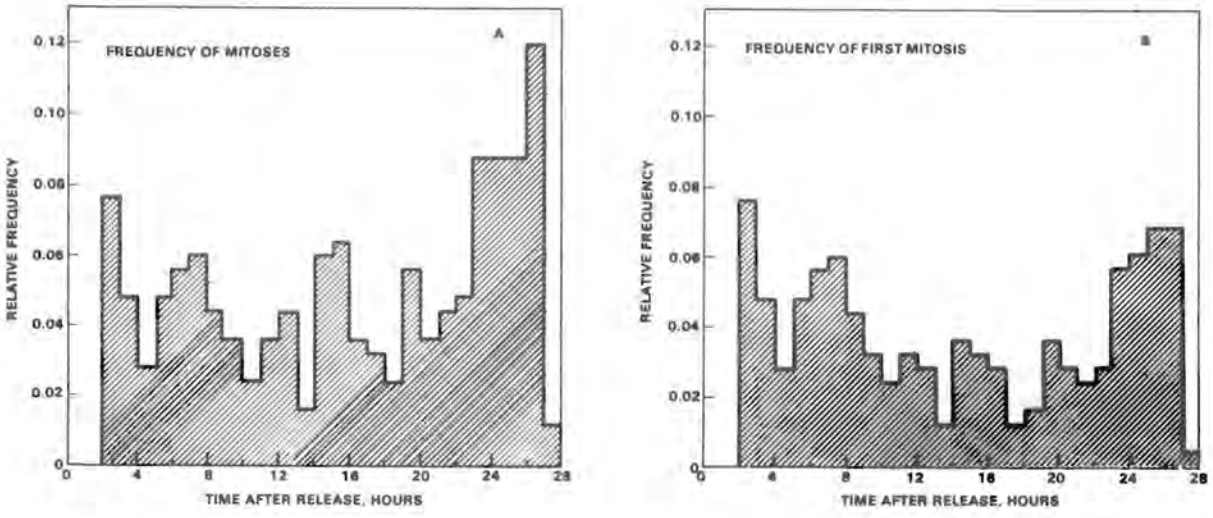

Figure 2.21. Relative Frequency of All Observed Mitoses (A) and of First Mitoses (B) Among Populations Derived from Density-Contact-Inhibited Plateau Cultures, Plotted Against Time After Release from Stationary Phase

generally present. Even in experiments using high-quality monocellular dispersions, clustering can occur after the fact.

In these experiments, cells are released from the stationary phase by conventional trypsinization procedures. They are transferred to new culture vessels at relatively low densities and permitted to attach prior to observation. This process involves separation by gravitational sedimentation, and mechanical attachment to the substrate. Only after such attachment can the plates be previewed and the images of cells in selected microscope fields be recorded. Under optimum conditions, this process requires a minimum of 90 min. However, if fewer microscope fields and consequently fewer cells are considered, it may be expedited somewhat. We have been able to assess mitotic activity in cells originating from both starved-cell and density-inhibited cultures beginning at about 2 h after release from the stationary phase. The mitotic frequency from each type has been plotted in Figure 2.22. The frequency of first mitoses rises from zero at the time of the first scan to a peak between 1 and 2 h later. The total absence of doublets at 2 h clearly shows that mitosis occurs between the 3rd and 5th h after release and confirms that the doublets observed at 3 h in the previous studies were indeed first mitoses.

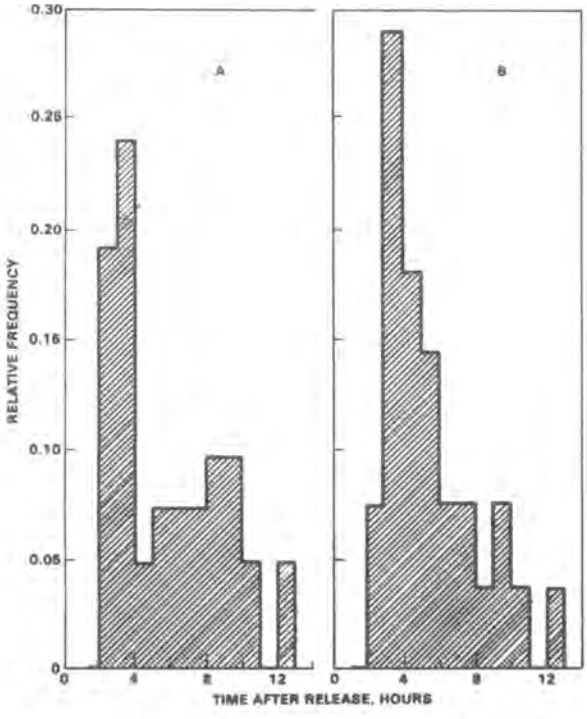

Figure 2.22. Relative Frequency of First Mitoses During the Early Hours Among Populations Derived from Nutritionally Deprived Cultures (A) and from Density-Contact-Inhibited Cultures (B) Plotted Against Time After Release from Stationary Phase

Recent autoradiographic data support these findings and demonstrate an even greater difference between these two types of cells. Although not yet complete, these studies suggest that, while density-contact-inhibited cells do not commence DNA-synthetic activity for several hours after release, a large number of the nutritionally deprived cells begin to synthesize immediately, indicating that a large fraction of these cells was arrested in S-phase. Both types of stationary-phase cells contain G_1 cells, but those derived from nutritionally deprived cultures have a major component of cells arrested in the premitotic G_2 phase. These cells pass through mitosis within 3 to 5 h after release. Investigations to determine the kinetic status of these cells, both during and after release from the stationary phase, are continuing with each of these types of cells.

Modeling the Radiation Response of Chlamydomonas reinhardi

W. C. Roesch, L. A. Braby, and J. M. Nelson

Experience has failed to show any way of evading the use of models for curve fitting and for extrapolating high-dose field and laboratory estimates of radiation risks to the low doses of concern in radiation protection. We are therefore studying Chlamydomonas reinhardi and Chinese hamster cells to develop and strengthen models of their radiation response for this use.

Several years ago, we reported a model that successfully described the protraction and fractionation effects in C. reinhardi (Braby and Roesch 1978b; Braby, Nelson and Roesch 1980b). Last year, however, we reported new experiments, at higher dose rates, that appeared inconsistent with the model (Roesch, Braby and Nelson 1980b). We proposed a revised model that seemed capable of explaining the new effects. Instead of inactivation resulting from cell damage caused by two charged radioactive particles, we postulated a series of steps requiring a total of more than two particles. Such multiple steps lead to strong dependence of the number of cells killed on the linear energy transfer of the radiation, such as we find experimentally. They

also provide opportunities for enough reactions at different rates to produce the effects we find experimentally.

This year we prepared a computer program for simulating experiments with the multistep models. Computer calculations are necessary because the mathematics of the models is too complex to permit analytical solutions in any except simple limiting cases. The program was written to be adaptable to a variety of similar multistep models. The only model studied much so far can be represented by:

$$\begin{array}{l} \overset{\sim\!\!\rightarrow}{\underset{\leftarrow\!\!\sim}{}}\,B \\ B + B \rightleftarrows C \\ C + C \rightarrow J \end{array} \qquad (17)$$

where B, C, and J represent biochemical products. B is the one product formed directly by the radiation. J is a product fatal to the cell. This model gives rise to five simultaneous differential equations, one each for individual Bs, Cs, and Js and one each for pairs of Bs and pairs of Cs.

Figures 2.23 and 2.24 show the nature of the solutions to this model and illustrate their complexity. The mean repair times for Bs and Cs were chosen to be 120 and 1200 s, respectively, to agree with experiment. (Other simulations indicate that the Bs are unlikely to recover slowly.) When the irradiation covers a period that is short compared with either repair time (Figure 2.23), the number of Bs and their pairs increases quickly and then falls relatively rapidly after the irradiation. The Cs, C pairs, and Js do not become observable until after the irradiation. They then build up at rates comparable to the disappearance rate of the Bs. Finally, the Cs slowly disappear. The Js do not, because they are fatal, leading to irreparable damage. When the irradiation covers a period comparable to the repair times for Bs and Cs (Figure 2.24), all of the products build up appreciably during the irradiation. The number of Cs and C pairs increases only slightly more during the postirradiation period before they start to disappear.

Figure 2.25 shows results from the model plotted in a way we popularized earlier (Braby and Roesch 1978b). According to our first model, survival data plotted as the quotient of the logarithm of the surviving fraction (S) by the square of the dose (D), versus the irradiation time, should lie on

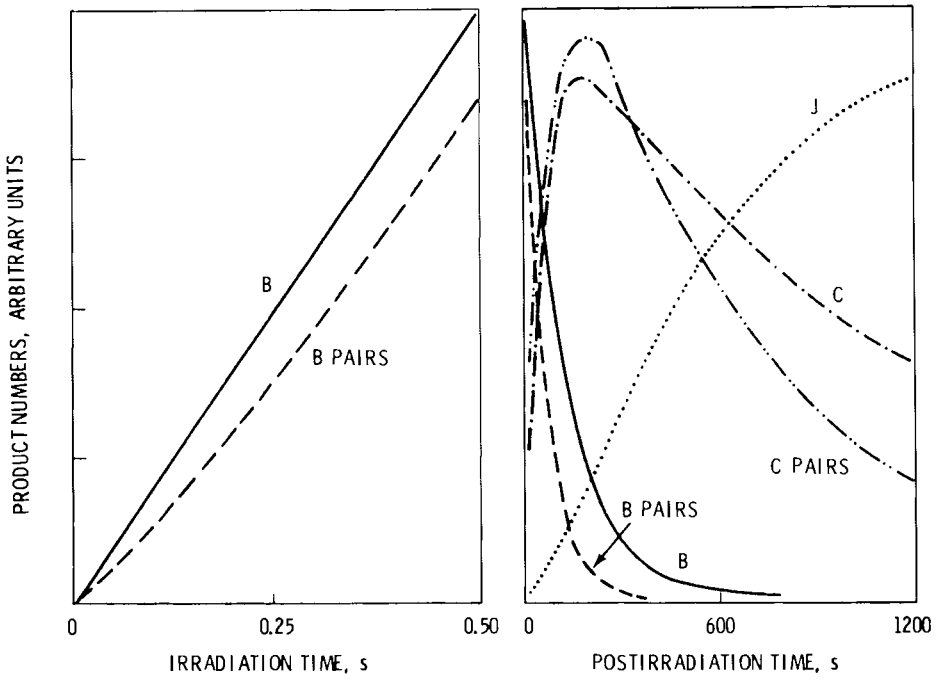

Figure 2.23. Number of Products in BCJ Model During and After Irradiation for an Irradiation Time Short Compared with the Recovery Times

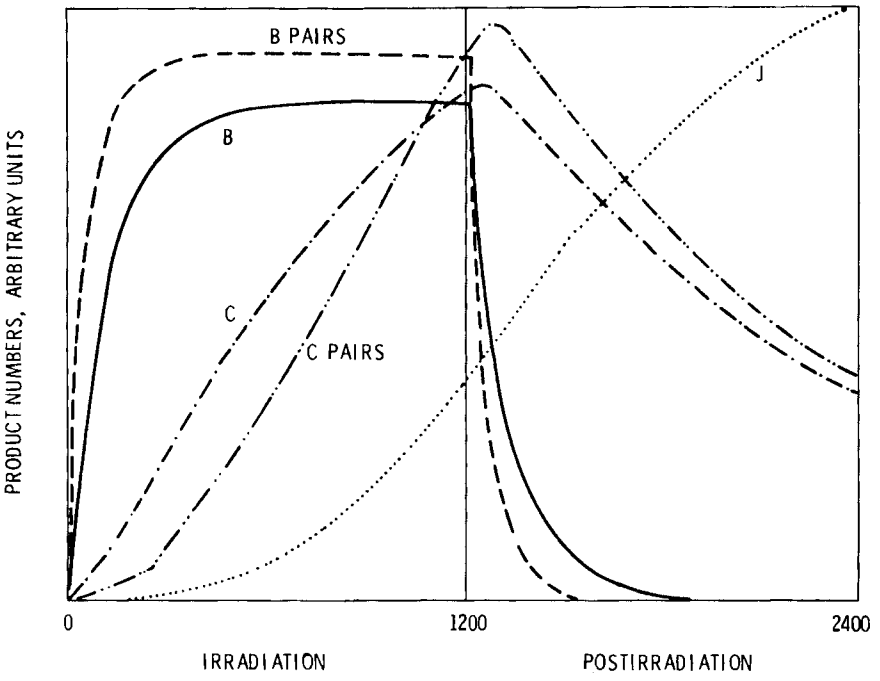

Figure 2.24. Number of Products in BCJ Model During and After a Long Irradiation

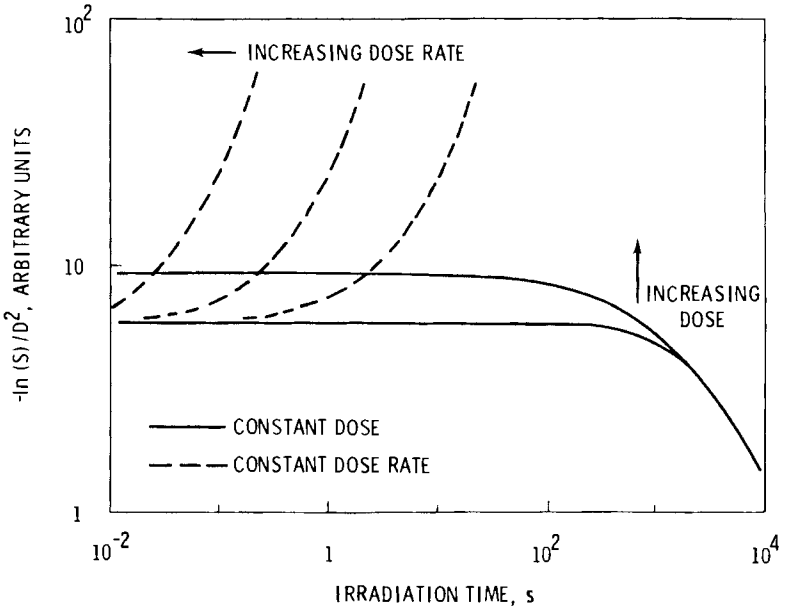

Figure 2.25. Analysis of Dose-Rate Effect for the BCJ Model

a single curve, regardless of the dose or dose rate. Because the new model does not predict a single curve, it is necessary to reconcile the theory with data that do seem to give a single curve. Part of the answer is that for long irradiation times, all of the curves for the new model converge into a single curve that is indistinguishable from the one curve of the old model. For short irradiation times, two kinds of curves are shown. One was made with the same dose at every point (changing the dose rate); the other with same dose rate at every point (changing the dose). Experimentally we use both methods: several points are obtained at a given dose rate over a range of doses. The data would thus lie on the dashed curves between the solid curves. The solid curves shown cover a larger range (about a factor of 1000) in survival than we ordinarily use. Thus the data may lie on different curves that are so close together as to be indistinguishable.

Figure 2.26 shows predictions of the model for split-dose experiments done at different doses (all for the same exposure time, 1 s). Surviving fractions (S) are plotted as the ratio of S to the fraction (Sm) surviving widely separated irradiations, a way that demonstrates the exponential recovery kinetics (Braby, Nelson and Roesch 1980a).

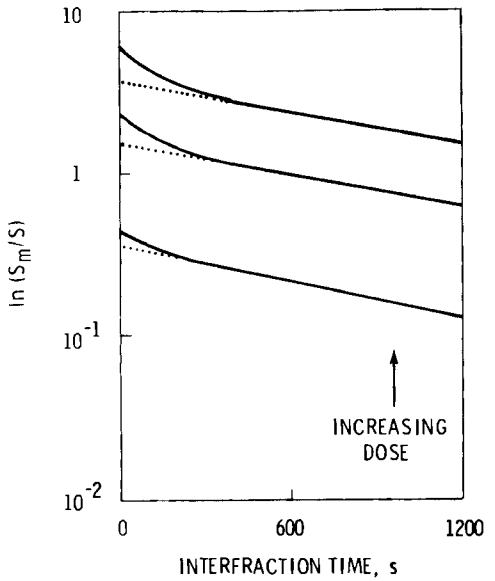

Figure 2.26. Analysis of Split-Dose Experiments for the BCJ Model

One of the objectives of our calculations is to find phenomena that can be compared with experimental results. Such a comparison is most effective when the model disagrees with experiment, because a faulty idea can thus be eliminated. The results in Figure 2.26 may lead us to reject the present model. The figure shows that the amount of fast recovery relative to the amount of slow recovery decreases with decreasing dose. Preliminary results from experiments to test this prediction show exactly the opposite.

Fast Processes in Chlamydomonas reinhardi

L. A. Braby, J. M. Nelson and W. C. Roesch

Last year we reported (Braby, Nelson and Roesch 1980b) a reversal of the radiation dose-rate effect in Chlamydomonas reinhardi for dose rates above 10^3 rad/s; that is, survival decreases with increasing dose rate up to 10^3 rad/s, but above that dose rate the survival again increases. One possible mode of radiation damage that would lead to this effect is outlined in Figure 2.27. A radiation product M' is not capable of interacting with other radiation products N* to produce lethal damage L until it has undergone some chemical change requiring the characteristic time τ_1. This model predicts a reverse dose-rate effect because at very high dose rates there is insufficient time for the chemical change to occur. At high dose rates, relatively less damage would be available for interaction than if the radiation time were long compared to τ_1. A mathematical version of this model leads to the curves of survival versus dose rate plotted in Figure 2.28.

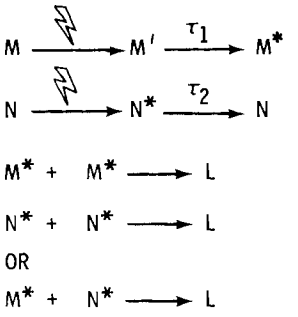

Figure 2.27. Schematic of Possible Sequence of Reactions Leading to a Reverse Dose-Rate Effect for Irradiation Times Short Compared with τ_1. Radiation product M' can not react with additional damage N*, but some product M* of M' can.

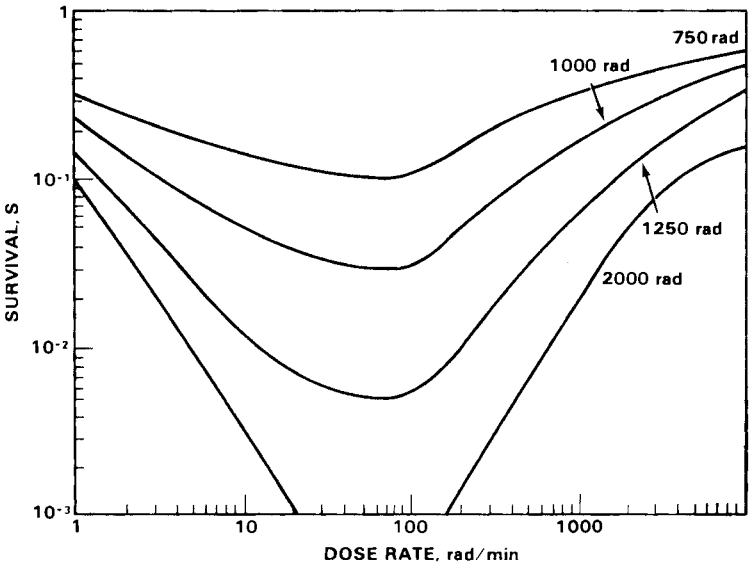

Figure 2.28. Survival as a Function of Dose and Dose Rate for the Model in Figure 2.27

To obtain an estimate of the characteristic time τ_1, one needs to measure survival out to very high dose rates where the reversal ceases. Experimental results at a single dose were shown last year. We now find that the survival curves for different dose rates also show the reverse effect, as shown in Figure 2.29. However, our experimental results do not show the expected leveling even to dose rates of 10^5 rad/s. Attempts to investigate the reverse dose-rate effect at still higher dose rates have been unsuccessful. Apparently the probability of producing this type of damage is strongly dependent on the radiation quality or the physical condition of the cells. In order to irradiate at higher dose rates, the cells must be concentrated so that a number of cells similar to the number used in previous experiments can be irradiated in a smaller space at a point closer to the electron exit window. When these changes are made, the two-event parameter becomes quite variable from one experiment to the next, indicating that unknown variables have a significant impact on cell survival. Adding a 0.25-mm polyethylene absorber between the electron exit window and the cells appears to increase the amount of reversal. It is possible, therefore, that this type of damage may be produced by low-energy electrons. Unfortunately, this plastic absorber reduces the dose rate, so it is still impossible to investigate survival at dose rates where cell survival is expected to level out.

Additional work will be necessary to clarify the effects of cellular physiology on these results and to understand the effect of radiation quality. An electrostatic ring lens, which is intended to flatten the electron beam distribution in order to produce higher dose rates in the center of the beam and a more homogeneous dose distribution, has been completed and will be tested soon. In addition, a scanning densitometer intended to read dose distributions that are measured with radiachromic film is nearly complete. It will allow more accurate control of the dose distribution in the cells and better estimation of dose reproducibility from one irradiation to the next.

Single-Event Distributions for Fast Electrons

L. A. Braby and W. C. Roesch

We reported last year (Braby, Nelson and Roesch 1980b) that when *Chlamydomonas reinhardi* cells are irradiated with an electron beam (initial energy of 1.5 MeV) through a 400-mg/cm^2 thickness of polymethylmethacrylate, slightly more than half as much dose is required for a given survival as for cells irradiated without the intervening material. Since these irradiations were identical in all other respects (temperature, dose rate, cell density, etc.), we believe the effect noted must be due to

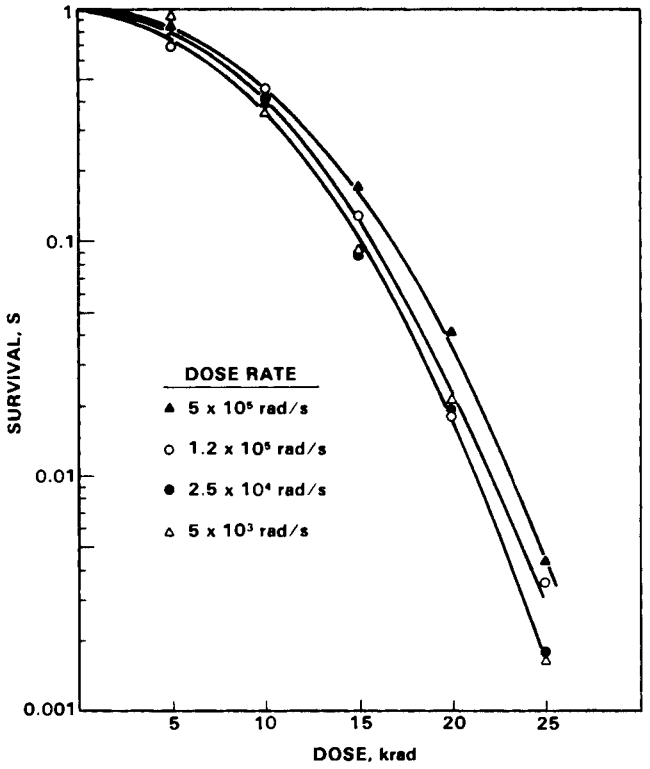

Figure 2.29. Measured Survival of *Chlamydomonas reinhardi* as a Function of Dose and Dose Rate when Exposed to a 1.5-MeV Electron Beam

differences in the spatial distribution of the energy deposited for different electron distributions.

In a preceding article in this report, "Modeling the Radiation Response of Chlamydomonas reinhardi," Roesch, Braby and Nelson described a model relating the response of C. reinhardi to the quality of the radiation (see also Roesch, Braby and Nelson 1980a). We have attempted to measure f(y), the probability density of single events, for electron beams that approximate those used in the biological experiment. Measuring the energy deposited by electrons is difficult, but the results may help clarify the dependence of relative biological effect (RBE) on ζ, the dose mean of the specific energy for single events, for radiations with low linear energy transfer.

To avoid wall-effect problems, a cylindrical grid-walled detector 2.5 cm in diameter and 2.5 cm high was used. The detector was operated in a plastic-lined tank approximately 30 times the dimensions of the detector, as described in conjunction with previous electron microdosimetry measurements (Braby and Roesch 1978a). The single-event spectrum was measured directly using a multichannel analyzer with dual analog-to-digital converters, as illustrated in Figure 2.30. The detector was calibrated using a ^{244}Cm-powered source of aluminum X-rays (1.487 keV).

An experimental geometry for a microdosimetry measurement must meet several requirements if it is to simulate the conditions of the biological measurements we have made. It must provide a means of reducing the count rate; bring the beam out of the lead cave in which the cells are irradiated; provide for changing the thickness of plastic between the detector and the source; and provide delta-ray equilibrium similar to that produced by the broad-beam geometry used for the cells. Two approaches to meeting this set of requirements have been used, with slightly different results. In each case, an evacuated beam line with a 0.0076-cm aluminum entrance window was placed against the exit window of the electron beam line. In one case, the beam intensity was reduced by

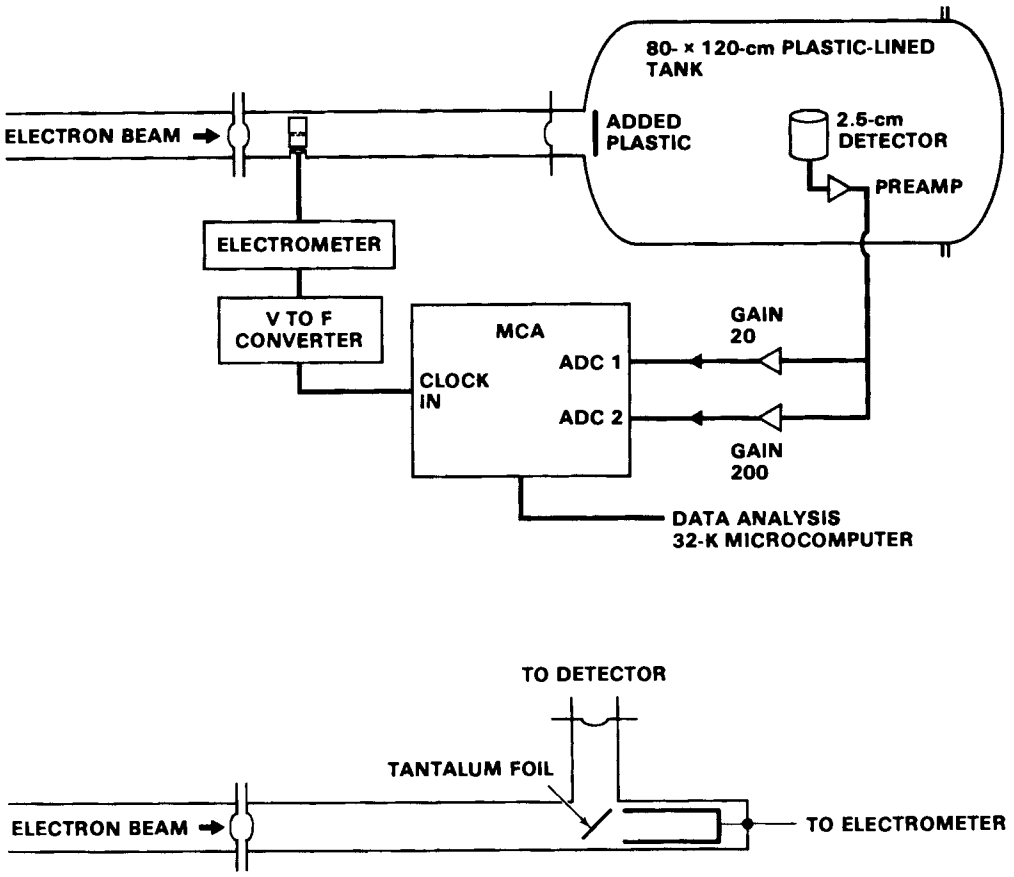

Figure 2.30. Schematic of Electron Beam Line and Electronics for Direct Measurement of f(y) for Electrons. The alternative beam line for scattering electrons from a thin foil is shown at bottom of figure.

passing it through a 0.033-cm-dia hole in a graphite beam stop near the entrance window. In the other case, the beam was scattered by a 0.0013-cm-thick tantalum foil placed at 45° to the beam axis about 75 cm from the entrance window. In both cases, the beam then entered the detector tank through a 1.4-mg/cm^2 aluminized mylar film and through a 0.05-cm polyethylene or a 0.15- or 0.3-cm methylmethacrylate absorber 60 cm from the detector.

Neither of these approaches provides a perfect simulation of the electron spectrum reaching cells irradiated in air 35 cm from the electron accelerator exit window, with or without 0.33 cm of methylmethacrylate covering that window. The collimator is limited to electrons of 1 MeV and less because higher-energy electrons penetrate the 0.25 cm of graphite and add a large component of low-energy electrons. Since the collimator hole's length-to-diameter ratio is 7.5, the spectrum may also contain excess low-energy electrons produced by multiple scattering in the wall of the hole. Scattering by the thin, high-Z foil should result in little energy loss, but Bremsstrahlung and fluorescent X-rays reaching the detector may increase. In both cases, to assure freedom from pulse coincidence problems, the average beam current was increased until a coincidence-induced shift in the spectrum could be detected, and then measurements were limited to less than one-half of that beam current.

The electron beam profile at the position of the detector is approximately Gaussian and about five detector diameters wide at the 50% points. To determine whether the requirement of delta-ray equilibrium is being met and whether the detector chamber is large enough to prevent wall effects, spectra were obtained at various positions between the beam axis and the

tank wall. The density f(y) was nearly indistinguishable ($\bar{y}$ varied ∿2.5%) for the detector centered in the beam and halfway between the beam and the wall, and approximately one event was recorded at the midpoint for every 20 recorded at the center of the beam. Thus, no correction of these results was needed for delta-ray escape or wall effect.

With a proportional counter gas gain limited to 1000 to avoid variations in gas gain with initial pulse size, the minimum energy deposition measured was approximately 170 eV. Below this energy, the spectrum must be extrapolated to determine the moments of the distribution. We used the method of directly measuring f(z), the density of specific energy for multiple events, and applying Fourier transforms to unfold the multiple-event spectrum (Roesch and Braby 1980) for data obtained with the same detector and similar electron spectra. Although the results are noisy, especially for the first few eV, they suggest that the distribution of energy deposition increases exponentially with decreasing energy imparted, at least down to a few eV. Also the exponentials for a given site size seem to have the same slope, independent of energy or depth. Consequently, the data presented here are the result of fitting an exponential function of fixed slope to the data starting at the same channel number for each site size. This approach may introduce some small errors in f(y) and $\bar{y}$. Differences in f(y) are used to illustrate the changes in patterns of energy deposition; however, it is d(y), the probability density of the absorbed dose in y, that is important in biophysics modeling. Fortunately $\bar{y}_D$ is relatively insensitive to differences in the small-event portion of the spectrum.

Typical single-event densities for 1-MeV electrons in a 0.94-μm-dia site at different depths are shown in Figure 2.31 for the collimated beam and Figure 2.32 for the scattered beam. Although only minor differences between these two electron distributions were expected, the distribution of energy deposition changes substantially with depth in plastic. The results for the collimated beam show a continuous increase in $\bar{y}$ with increasing depth, as one would expect. The scattered beam shows a decrease in $\bar{y}$ for the 0.05-cm depth and increases at depths of 0.15 and 0.3 cm. It is not clear at this point which result more nearly represents the geometry prevailing in the cell irradiation, because

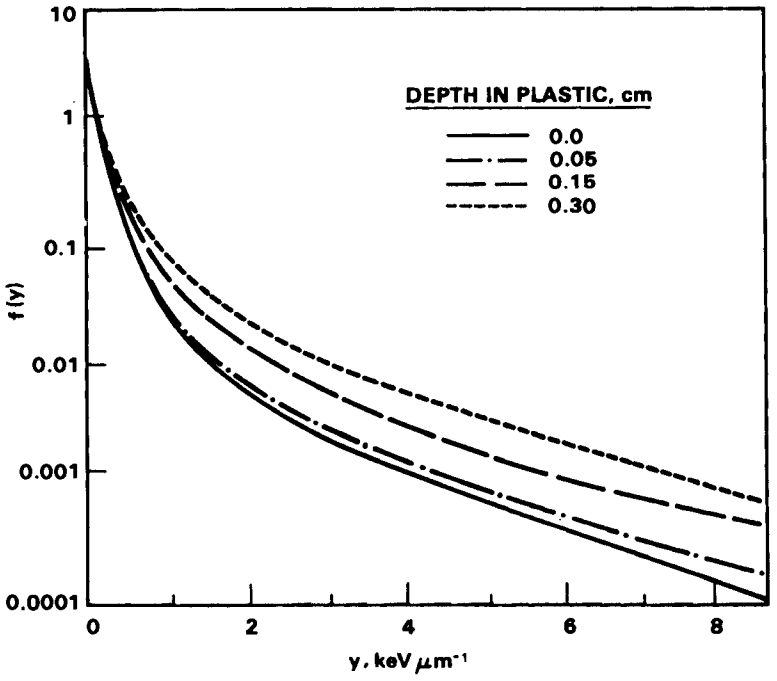

Figure 2.31. f(y) in a 0.94-μg/mm² Site for a Collimated Beam of 1.0-MeV Electrons at Various Depths in Plastic

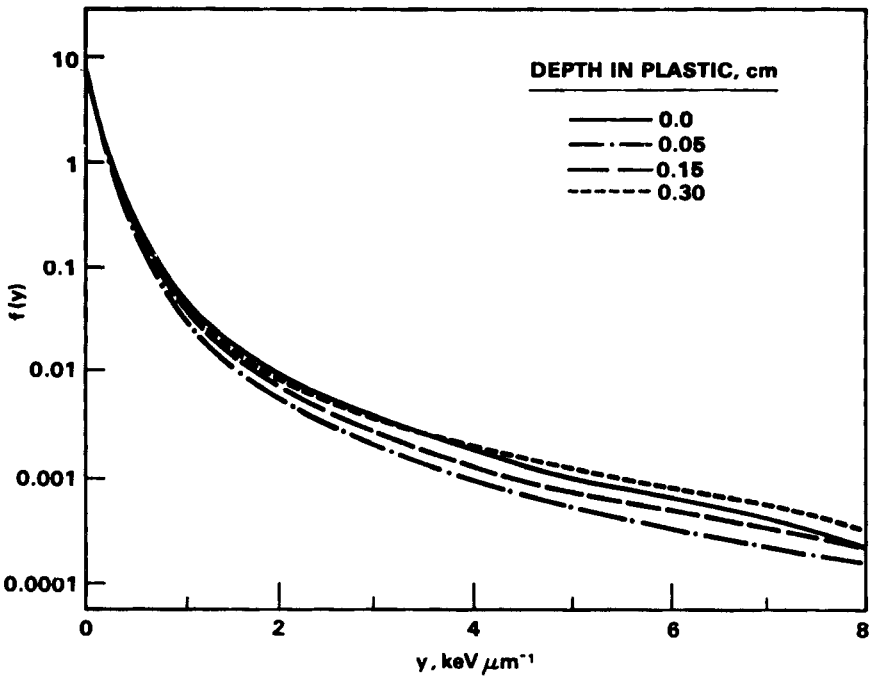

Figure 2.32. f(y) in a 0.94-$\mu g/mm^2$ Site for a Scattered Beam of 1.0-MeV Electrons at Various Depths in Plastic

the collimator may be adding scattered electrons and the foil may be adding soft X-rays.

The variations in ζ or $\bar{y}_D$ with depth in plastic can be compared with observed biological effects. Table 2.1 gives values of $\bar{y}_D$, using the mean chord length $\bar{l}$ for parallel chords perpendicular to the detector axis. A cell irradiation experiment that compared survival at a depth of 0.043 g/cm^2 in air with survival at a depth of 0.44 g/cm^2 of plastic and air resulted in an RBE of 1.6. We compared this with the ratio of $\bar{y}_D$'s for depths of 0.36 and 0.05 g/cm^2. For a 0.94-$\mu g/mm^2$ site and the scattered 1.5-MeV beam, this ratio is 1.3; for a 1.88-$\mu g/mm^2$ site, it is 1.2. Both numbers are substantially lower than the observed RBE. For the 1-MeV scattered beam and the 0.94-$\mu g/mm^2$ site, the ratio is 1.5 and for the 1-MeV collimated beam it is 1.8. The maximum absorber used in the microdosimetry measurements is only 80% of that used in the cell experiments and the additional absorber would probably raise $\bar{y}_D$. The ratio of $\bar{y}_D$'s for the 1.5-MeV beam scattered from a thick graphite absorber relative to $\bar{y}_D$'s for the scattered beam at 0.05-cm depth (for a 0.94-$\mu g/mm^2$ site) is 1.5. It is not clear at this point whether the beam scattered from the thin foil is giving the correct initial electron spectrum, but the results presented, though preliminary, indicate that the mean and dose mean of the single-event distribution increase significantly with depth in an absorber, and the magnitude of the effect is consistent with our understanding of the biological results.

Table 2.1. $\bar{y}_D$ at Various Depths in Plastic

Site Size, $\mu g/mm^2$	Beam Type and Energy, MeV	Depth in Plastic, $g/\mu m^2$			
		0	0.05	0.18	0.36
0.94	Collimated				
	0.5	1.10	1.44	2.22	2.82
	1.0	1.102	1.20	1.78	2.11
0.94	Scattered				
	1.0	1.21	0.93	1.02	1.38
	1.5	0.96	0.89	1.03	1.15
	2.0	1.17	1.14	1.53	1.58
1.88	Scattered				
	0.5	1.06	0.84	1.51	1.93
	1.0	0.85	0.70	0.80	1.15
	1.5	0.70	0.65	0.74	0.78
	2.0	0.67	1.39	1.51	1.57

Frequency Distributions for Ionization and Energy Imparted to Nanometer Volumes by Protons

W. E. Wilson and H. G. Paretzke[a]

The spatial dependence of the energy depositions and the number of interactions produced by a radiation field in macromolecular volumes is of continuing interest in radiation biology. Experimental methods for measuring the distribution of energy imparted by energetic heavy ions have concentrated on the use of proportional counters to magnify the microscopic site to experimentally realizable dimensions by lowering the density of molecules. It is not, however, technically feasible to use this approach to simulate volumes smaller than about 0.1 μm in diameter. Therefore, for very small sites it is necessary to calculate the statistical distributions of interactions.

At present, the most tractable method for solving particle transport problems in charged-particle track structure, and the only one that retains the inherent stochastics is the Monte Carlo method. A new Monte Carlo computer code (MOCA13) makes extensive use of the significant improvement in data on primary interactions, especially ionization cross sections, that have become available in recent years (see Wilson and Toburen, "Systematics of Secondary Electron Production in Ion-Atom Collisions," in this report). We are using this code to calculate single-event distributions, that is, frequency distributions for the stochastic quantity ε, the energy imparted in submicron spherical volumes that are centered a fixed distance b (the eccentricity) from individual fast proton tracks. Chord length is not a random variable in this first calculation but is controlled through b. Simultaneously and independently, we obtain the frequency distribution for the number of ionizations, ι, which is also a stochastic quantity and which generally correlates closely with the energy imparted. Proportional counters actually measure frequency distribution in ι rather than ε.

Representative frequency distributions for the number of ionizations and for the energy imparted are shown in Figures 2.33(A) and 2.33(B) for 1.0-MeV protons passing through spherical sites with diameters ranging from 1 to 100 nm. For the larger sites, the distributions exhibit the familiar skewed Gaussian shape similar to that of energy-loss straggling distributions. For the smaller sites, the distributions decrease monotonically and appear to be simple Poisson distributions. For the smallest sites, the ionization distributions become a sequence of delta functions at the integer values of the number of ionizations. All distributions in Figure 2.33 are normalized on a per track basis.

The shapes of the distributions for ionization and energy imparted in the larger sites correlate well; for small sites this correlation begins to fail. For site sizes of 5 nm and smaller, the frequency of zero ionization is significantly larger than the frequency of zero energy imparted. This difference occurs because the cross section for energy deposition includes the cross section for ionization. Hence, all ionizing events are also energy deposition events, but not all energy deposition events are ionizing ones. Therefore, under appropriate conditions of ion energy and site size, some tracks may deposit energy without producing ionization, and the proportionality between energy imparted and ionization changes.

For the distribution of energy imparted, $f(\varepsilon; d, b)$, for a proton passing through a site of diameter d at eccentricity b, we define a frequency mean event size as

$$\bar{y}(d,b) = \frac{1}{d} \int_0^\infty \varepsilon f(\varepsilon; d, b)\, d\varepsilon \qquad (18)$$

which is the expected value of the energy imparted divided by the site diameter, d. We use d for the characteristic length, rather than the mean chord length, for easier comparison with linear energy transfer (LET).

The calculated $\bar{y}$ for diametric tracks ($b = 0$) as a function of the LET for 0.25- to 3.0-MeV protons is shown in Figure 2.34. The curves for the various site sizes asymptotically approach the line $\bar{y} = L_\infty$ as the site size increases, as one would expect. For decreasing d, $\bar{y}(d,0)$ is a decreasing fraction of L_∞, which reflects greater transport of energy outside the smaller sites by energetic delta rays.

The frequency of zeros in the distribution for energy imparted [Figure 2.33(B)] affects the relationship between the dose absorbed at the site and the fluence of particles through it. The calculated

(a) GSF-Institut für Strahlenschutz, Neuherberg, Federal Republic of Germany.

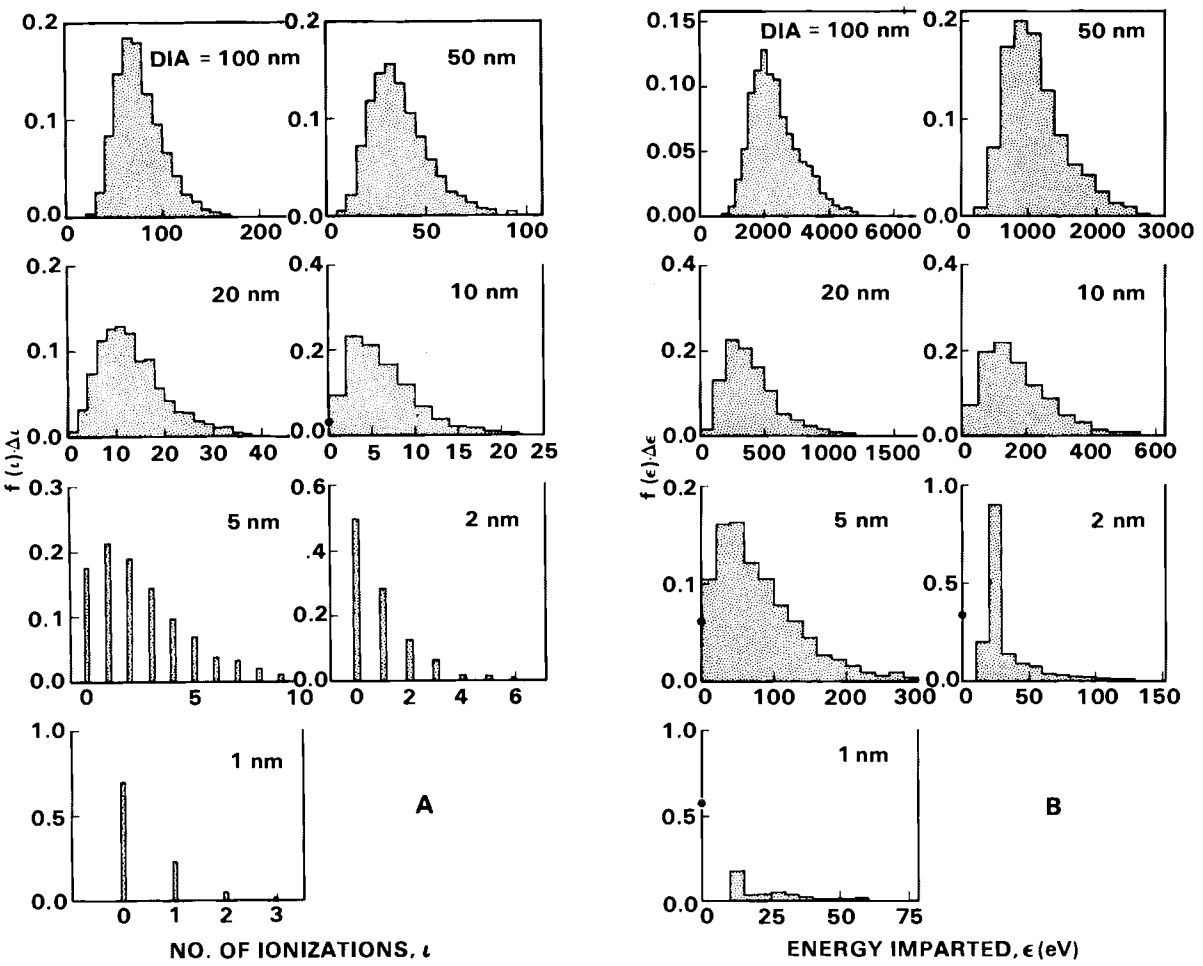

Figure 2.33. Single-Event Distributions for A) Ionization and B) Energy Imparted Produced by 1-MeV Protons Passing Diametrically Through Spherical Sites of the Indicated Diameters in Unit Density Matter. The solid points on the frequency axis indicate the frequency for zero ionization or energy imparted. Each distribution is normalized to unit area including the "zeros", i.e., frequency per track.

frequencies of zero ionization for diametric tracks are almost exponential functions of site size (Figure 2.35). This relationship is readily understood in terms of the total ionization cross section. The frequency of zero ionization for the small absorbers is essentially the probability that the ion will travel a distance x equal to or greater than the site diameter d between successive primary ionizations. This latter probability is given by:

$$p_x = \exp(-n \cdot Q_{ion} \cdot x) = \exp(-x/\bar{\lambda}) \quad (19)$$

where n is the number of molecules per unit volume, Q_{ion} is the ionization cross section, and $\bar{\lambda}$ is the corresponding mean free path. Then for $x = \bar{\lambda}$, $p_{\bar{\lambda}} = 1/e$. The values of $\bar{\lambda}$ for the respective proton energies are indicated by the vertical arrows in Figure 2.35.

These preliminary results indicate that with sophisticated algorithms describing the basic physical interactions, the Monte Carlo method can be an effective technique for obtaining quantitative energy and ionization distributions in and around positive ion tracks of a few MeV in volumes too small for direct experimental measurement. A comprehensive analysis of the ionization and energy imparted in very small sites by discrete tracks of high-LET radiation should make it possible to develop an analytical model for calculating single-event spectra, $f_1(\epsilon)$, for broad beams that produce tracks with random eccentricities.

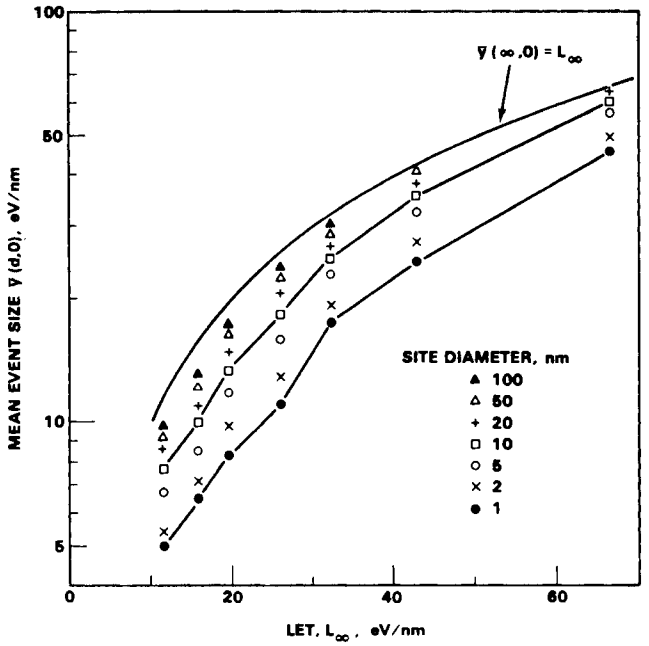

Figure 2.34. Mean Event Size as a Function of Linear Energy Transfer for 0.25- to 3.0-MeV Protons Passing Diametrically Through Spherical Sites of the Indicated Diameters in Unit Density Matter. Straight lines between successive data points are to aid the eye.

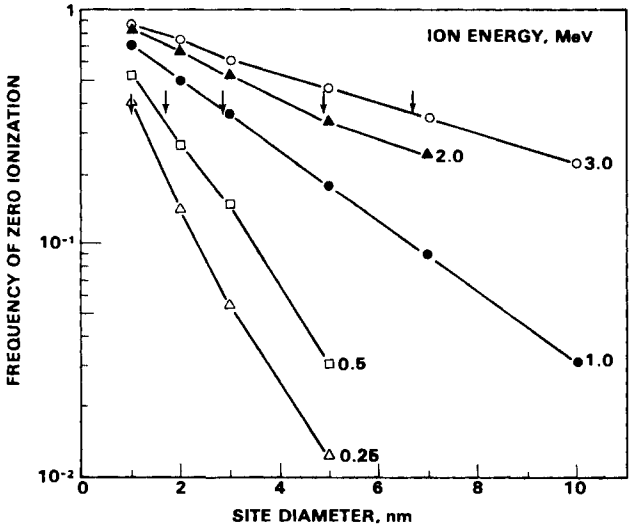

Figure 2.35. Frequency of Zero Ionization as a Function of Site Size for Protons of Indicated Energy Passing Diametrically Through Spherical Sites of Diameter d. Arrows indicate where the site diameter equals the mean free path for ionization for the respective proton energy.

• Microdosimetry of Internal Sources

The purpose of this study is to develop practical methods for calculating microdosimetric distributions of plutonium or other alpha-emitting elements that are deposited, especially as particulates, in soft tissue and lung tissue. This study will aid the correlation and extrapolation of radiation effects measured at different levels of exposure and in different species. Computational methods are being developed and tested in the Radiological Physics Section. Concurrently, the Dosimetry Technology Section is developing cell and tissue models in which those methods will be applied.

Computer Programs for Microdosimetry of Alpha Particles in the Lung

W. C. Roesch

Our computer program for calculating microdosimetric densities attributable to alpha-particle emitters in homogeneous tissue has been revised to work for lung tissue. Little that was conceptually new had to be added to the program, but wholesale changes were needed in the order of the computational steps because the computer memory was not large enough to permit us to handle lung tissue the way we handled other tissue.

To calculate a microdosimetric density for particulates randomly distributed in the lung, we first assume that a particulate is on the surface of an alveolar wall adjacent to a cell and calculate the density in specific energy allowing for the spread in distance from that wall to the nucleus. Then we assume that the particulate is on the next wall and correct for the distribution in distances across the first alveolar space. Then we go to the other side of the second wall and correct for the distribution in wall thicknesses; then to the other side of the next alveolar space; and so on. The probabilities for different distances from a nucleus to an alveolar wall, across alveolar spaces, and through alveolar walls were those for beagles and were obtained as described in the following article in this report. The calculation is greatly simplified by the stochastic independence we found to exist between the probabilities for adjacent structures.

Figure 2.36 presents one of the simpler consequences of the inhomogeneity of the lung. It shows the density, $f(z)$, in specific energy produced by two similar particulates, one of which is separated from a given site by 30 μm of tissue, while the other is the same distance away, but 27 μm of that distance is taken up by air space. Because they are at the same distance, their alpha particles have equal probabilities of traversing the site, but those that travel through air lose less energy and arrive at the site with lower stopping power. They thus deposit less energy in the site, with a resulting shift of the distribution toward lower specific energies. The computer program for the lung takes care of these differences as well as those attributable to stochastics in alpha-particle emission and in location of the alpha-emitting particulates.

The geometric effects produced by the lower density of the lung relative to other tissues are more dramatic than those caused by the stopping power changes. First, for comparison, Figure 2.37 shows for a solid, homogeneous tissue the mean probability density for all positions of a cell nucleus relative to a particulate. The particulate emitted 10,000 alpha particles on the average. Figure 2.38 shows the mean density for the same particulate in the beagle lung. Superficially it looks like that for the solid tissue; the dramatic difference is in the range of the abscissa. Much higher specific energies are produced in the solid tissue. The difference is due to the number of alpha particles that deposit energy in the sites. Examination of the details of the computation shows that, for the lung, typically just one alpha particle affects each site. For the solid tissue, a large number of alpha particles (typically 25) affect each site.

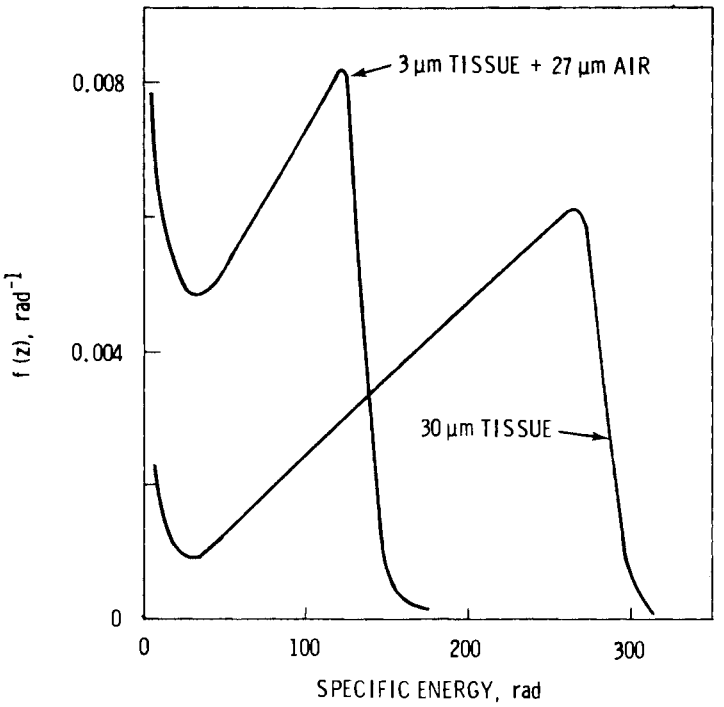

Figure 2.36. Effect of Air Spaces in Lung on Microdosimetric Densities

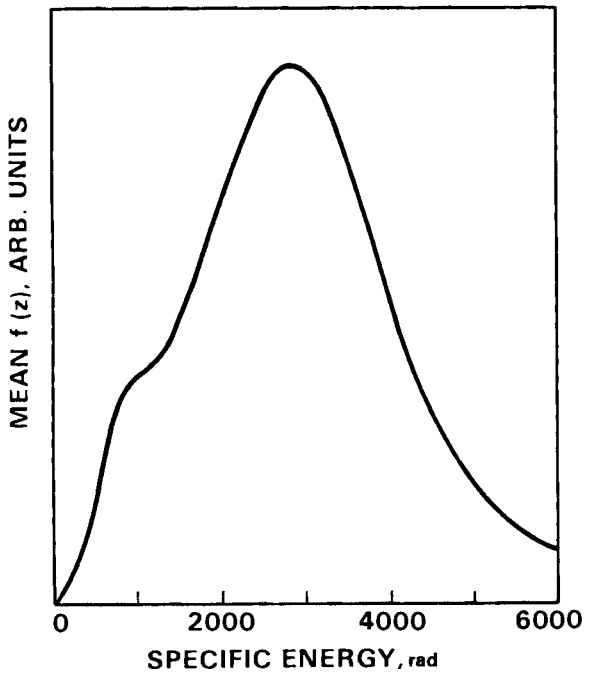

Figure 2.37. Mean Density in Specific Energy for Particulate Emitting 10,000 ^{239}Pu Alpha Particles in Solid Tissue Whose Cells have Sensitive Sites 4.66 μm in Diameter

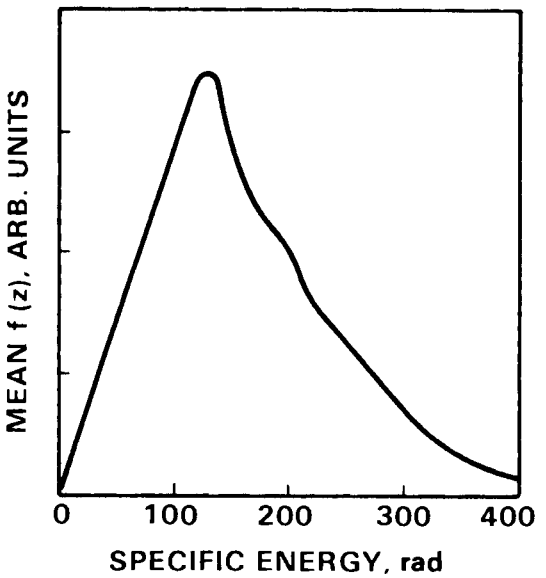

Figure 2.38. Mean Density in Specific Energy for Particulate Emitting 10,000 ^{239}Pu Alpha Particles in Beagle Lung Tissue Whose Cells have Sensitive Sites 4.66 μm in Diameter

Such a difference is expected. Because the lung is about 1/5 the density of solid tissue, the alpha particles travel about 5 times as far. The probability of traversing any particular site is thus about 1/25 (inverse-square attenuation) that in solid tissue, as observed.

While the probability of traversing any particular site goes down, the number of sites traversed goes up: the number of cells at a given distance is proportional to the square of the distance. Therefore, less energy is deposited per site, but the number of sites increases in proportion. The same total energy (the alpha-particle energy) is absorbed in both cases. In other words, in the solid tissue, relatively few sites are traversed many times and many sites are completely missed; in the lung tissue, few sites are traversed more than once, but few sites are completely missed.

Microdosimetry of Plutonium in Beagle Dog Lung

D. R. Fisher, W. C. Roesch, G. F. Piepel, J. L. Daniel, and W. M. Bowen

A better understanding of the microdosimetry of internally deposited radionuclides should provide new clues to the complex relationships between organ dose distribution and early or late biological effects. Our study focuses on the microdosimetry of plutonium oxides in the lungs of beagle dogs. For many years, this laboratory has been conducting long-term toxicological studies of the life-span effects of inhaled transuranic elements in beagles. The value of the data resulting from these animal studies will be greatly enhanced as the internal dosimetry is refined. The ultimate objective of the study is to improve dose-response correlations. This summary reports our recent progress in modeling the microstructure of pulmonary lung tissue and calculating microdosimetric quantitites for inhaled plutonium.

Last year we reported the development of analytical techniques to define probabilistic source-target parameters using image analysis of magnified lung-tissue fields (Fisher, Daniel and Piepel 1980). A randomized scheme was used to select specimens of lung tissue from three healthy adult male beagle dogs. The image analyzer was programmed to perform measurements along evenly spaced horizontal lines across the magnified field of view, simulating straight-line paths of alpha particles. Gray-level contrast was used to categorize intersected features such as tissue, nuclear material, or air space. The location coordinates of each feature were recorded, and the feature's chord length was calculated. A large data set resulted from these measurements. The dependability of the automated analysis was verified by hand measurements on a smaller set of enlarged photomicrographs.

It was then possible to construct hypothetical alpha particle tracks through lung tissue and to determine total track length, the widths of tissue or air segments encountered, and the number and widths of epithelial-cell nuclei traversed along each path.

Histograms of air-sac widths, tissue-chord lengths, and distances from tissue walls to cell nuclei were constructed. QQ-plotting of the lung morphometry data showed that the distribution of air-chamber-chord lengths closely resembled a gamma probability density function. The gamma probability density function is described by the equation

$$g(x) = \frac{x^{\alpha-1}\, e^{-x/\beta}}{\Gamma(\alpha)\beta^{\alpha}} \quad \text{for } x,\ \alpha,\ \beta > 0 \qquad (20)$$

where x is a variable representing the observed chord length, α and β are parameters of the function, and Γ is the gamma function, which is a constant obtained from tables when the parameter α has been determined. The distributions of tissue-chord lengths and of distances from nucleus to tissue wall were both found to approximate the Weibull probability density function

$$w(x) = \frac{\alpha x^{\alpha-1}\, e^{-x^{\alpha}/\beta}}{\beta} \quad \text{for } x,\ \alpha,\ \beta > 0 \qquad (21)$$

Mean estimates of the parameters for the probability density functions are given in Table 2.2. Taken together, these

Table 2.2. Estimated Probability Density Function (pdf) Parameters for Lung Model Distributions

Feature	pdf	α	β
Air chords	gamma	1.119	86.617
Tissue chords	Weibull	0.983	8.002
Nucleus-to-wall distance	Weibull	1.162	2.936

probability density functions constituted our model of the microstructure of beagle dog lung (Figure 2.39).

To calculate the microdosimetric probability density in specific energy (z, in rad or Gray), we 1) determined the specific energy densities at all distances in the lung from a single point source, 2) represented the activity as a distribution of point sources, and 3) convoluted the point-source densities from that distribution using Fourier transforms (Roesch 1977). The preceding article in this report describes the method used to calculate the microdosimetry of inhaled plutonium particulates in the pulmonary lung. The lung model (Figure 2.39) was used in these calculations (Roesch and Fisher 1980). For each calculation, we assumed that the plutonium particulates were located on the surfaces of alveolar walls.

The single-event density curve (Roesch 1977) for a $^{239}PuO_2$ particulate in the beagle dog pulmonary lung is shown in Figure 2.40. Probability densities in specific energy can be determined from the single-event density for various exposure conditions in the lung. Figure 2.41 shows the mean density in specific energy for cell nuclei of the pulmonary epithelium in the beagle, where the plutonium particulates were assumed to be randomly distributed on alveolar walls and each particulate had the same activity. For this example, the exposure period was 28 days, during which 29 alphas were emitted from each particulate. The absorbed dose was found to be 23 rad. The probability of no energy deposition in a site (given by the Dirac delta function δ) was 0.92. The curve in Figure 2.41 is similar to the single-event density curve because relatively few alpha decays were considered (in comparison with the next figure). Figure 2.42 resulted from extending the exposure time to 1400 days. The delta function dropped to δ = 0.02, indicating that most of the sites were traversed at least once. In addition, the absorbed dose (1140 rad) is more representative of the distribution of specific energies.

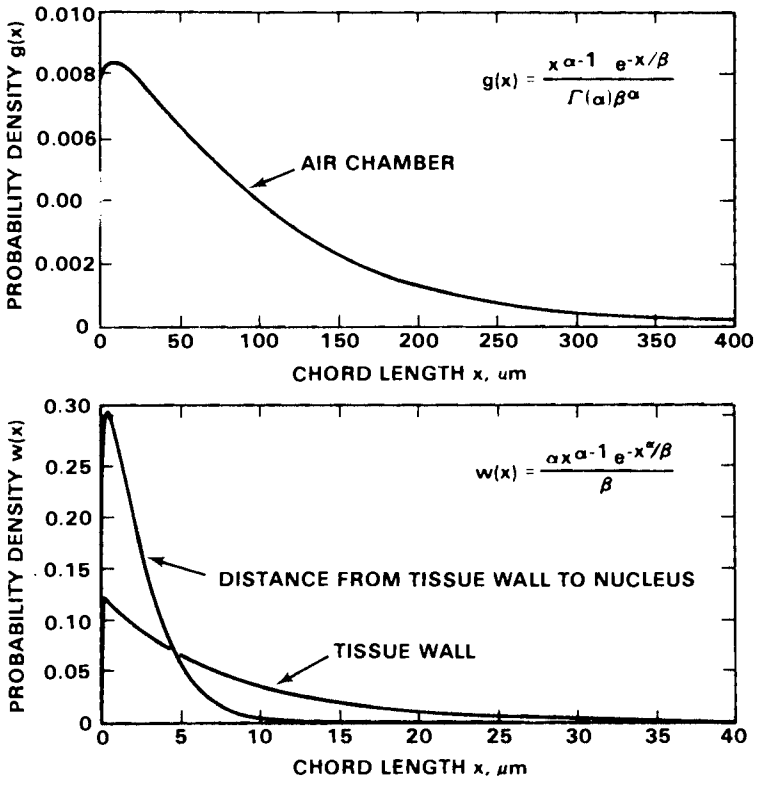

Figure 2.39. Lung Model for Microdosimetry: Estimated Probability Density Functions for Air-Chamber-Chord Lengths, Tissue-Wall Thicknesses, and Locations of Epithelial-Cell Nuclei Relative to Alveolar Walls

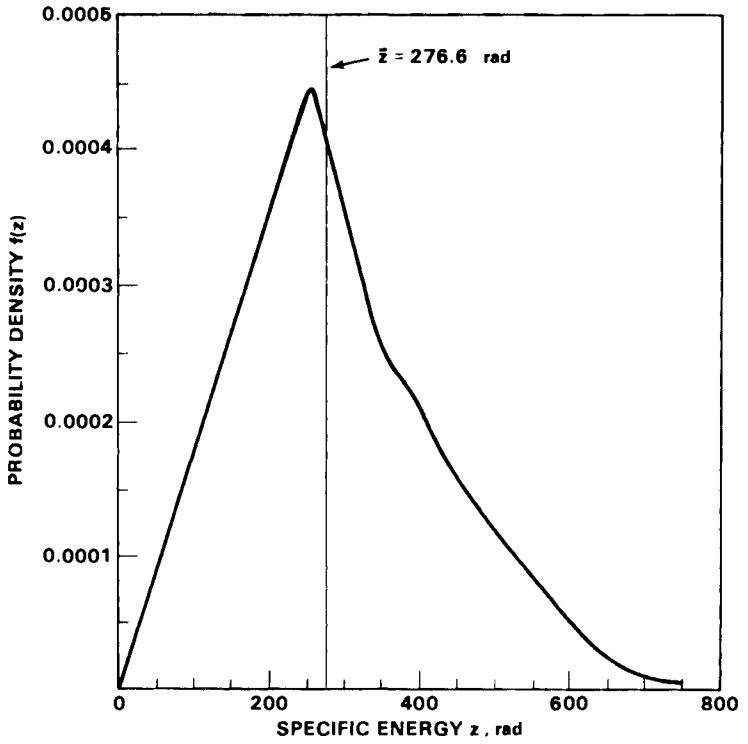

Figure 2.40. Single-Event Density for Epithelial-Cell Nuclei from a Point Source of ^{239}Pu in Beagle Dog Lung

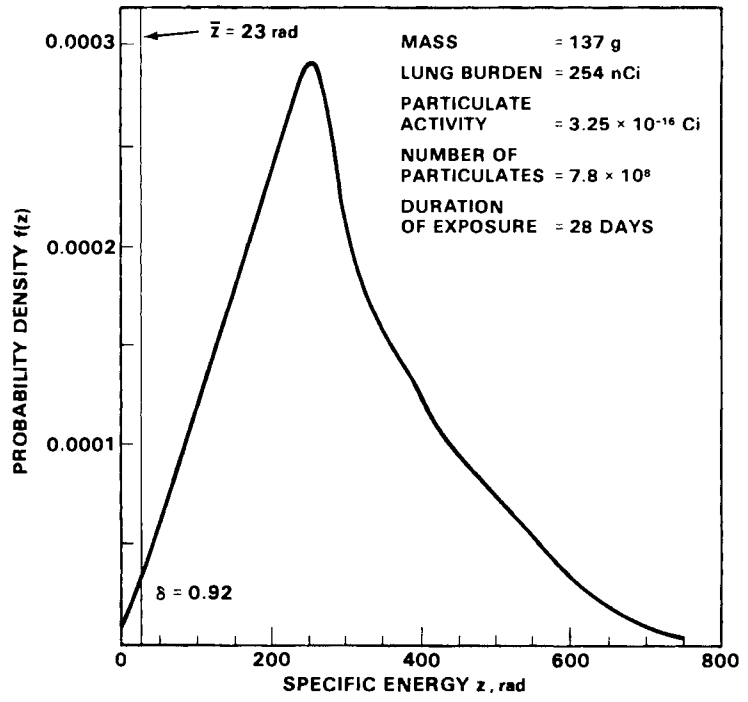

Figure 2.41. Dose to Epithelial-Cell Nuclei in Beagle Dog Lung from Inhaled $^{239}PuO_2$ for an Exposure Period of 28 Days

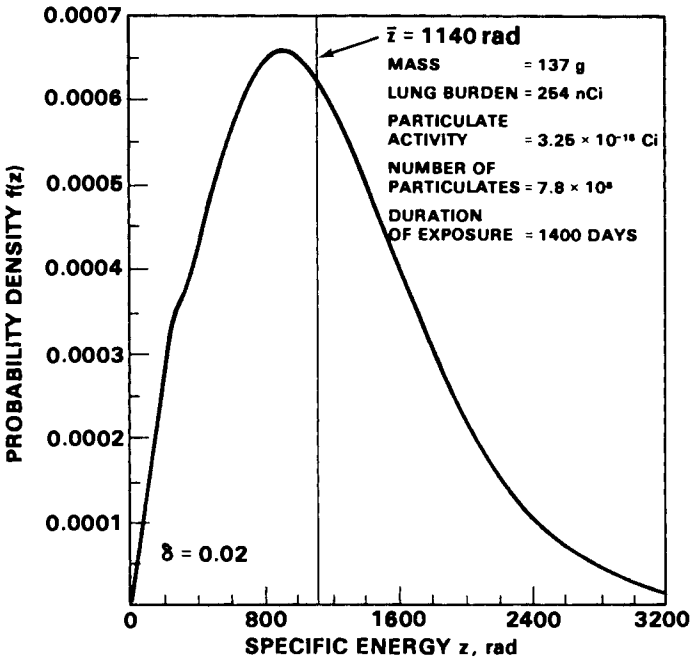

Figure 2.42. Dose to Epithelial-Cell Nuclei in Beagle Dog Lung from Inhaled $^{239}PuO_2$ for an Exposure Period of 1400 Days

Since the mean lifetimes of epithelial cells are relatively short (~28 days), Figure 2.41 may be more indicative of the microdosimetry for individual cells than is Figure 2.42. Some of the important factors in lung microdosimetry yet to be considered include the long-term migration and clearance of radioactive materials in the lung, changes in lung-tissue structure caused by fibrosis, and the size distribution (and possible agglomeration) of PuO_2 particulates. Also, a distinction must be made between Type I and Type II epithelial cells.

The density and geometry of the lung tend to have an effect on the microdosimetric densities similar to the dispersion of activity in a solid tissue. The methods discussed in this report for determining the microdosimetry in the lung make it possible to evaluate the differences in specific energy density for so-called "hot particles" versus uniformly distributed activity. Work is in progress to refine internal microdosimetry so that correlations with long-term biological effects can be established (Fisher and Roesch 1980). We expect that this improvement in dose-response information will eventually be used in predicting the relative toxicities of inhaled alpha emitters, and in improving and updating radiation protection standards.

• Dosimetry of Internal Emitters

The Dosimetry of Internal Emitters Program endeavors to refine the correlation between radiation dose and observed biological effects. The program is presently engaged in the development of studies that will test the microdosimetry models developed under the Microdosimetry of Internal Sources Program. The program also provides guidance and assistance to Pacific Northwest Laboratory's Biology Department in the dosimetric analysis of internally deposited radionuclides. The investigators work closely with the Biology Department staff and collaborate on the Microdosimetry of Internal Sources Program.

In-Vitro Alpha-Particle Microdosimetry

R. J. Traub, D. W. Murphy, D. R. Fisher, and R. Harty

An in-vitro method to correlate microdosimetry and the response of cells exposed to alpha radiation has been devised to help show how microdosimetry can be applied to radiobiology and radiation protection. Microdosimetry, which has been extended to the dosimetry of internal emitters at this laboratory (Roesch 1977), substitutes the stochastic quantity "specific energy (z)" (the value of the energy actually imparted divided by the mass of the site) for the nonstochastic quantity "absorbed dose" of conventional dosimetry. Absorbed dose is not a meaningful concept for small sites traversed by only a few charged particles because conventional dose averaging overlooks microscopic patterns of dose deposition.

Internal microdosimetry can be applied to cells in vivo or in vitro. We believe that in-vitro microdosimetry must be better understood before microdosimetry is extended to the study of how man or animals respond to radionuclides. Consider, for example, an agar medium containing randomly dispersed Chinese hamster ovary (CHO) cells and microspheres labeled with the alpha-particle-emitting nuclide ^{244}Cm. We can set up three experimental systems in which the number of alphas emitted per particulate ranges from 20 to 1000, and then vary inversely the number of particulates in the medium so that the total number of alpha particles emitted remains constant across all systems. Using microdosimetry, we calculate the probability that cells will be irradiated and compute the probable radiation dose to individual cells.

Table 2.3 summarizes the three cases. The delta function is the probability that a cell will not be hit by an alpha particle. In Figure 2.43, the probability densities f(z) in specific energy for the three cases are plotted. These curves show that as the activity of individual particulate sources is increased and the number of sources is correspondingly decreased, the probability of a cell being hit decreases. If a cell is hit, the amount of energy most likely deposited increases because the cells that are irradiated are traversed with greater frequency. This example shows how the specific energy deposition is influenced by point source activity and distribution.

We have recently begun a series of experiments to measure the correlations between microdosimetry and various biological endpoints of irradiation. The biological responses that will be measured include cell survival, mutation, production of primary deoxyribonucleic acid (DNA) damage, and repair of DNA damage. Cell

Table 2.3. Summary of Experimental Conditions

Curve[a]	Particulates per μm^3	Alphas per Particulate	Average Dose, rad	Delta Function
1	4.12×10^{-5}	20	72	0.11
2	2.35×10^{-6}	350	72	0.48
3	8.23×10^{-7}	1000	72	0.74

[a]Curve numbers correspond to those in Figure 2.43.

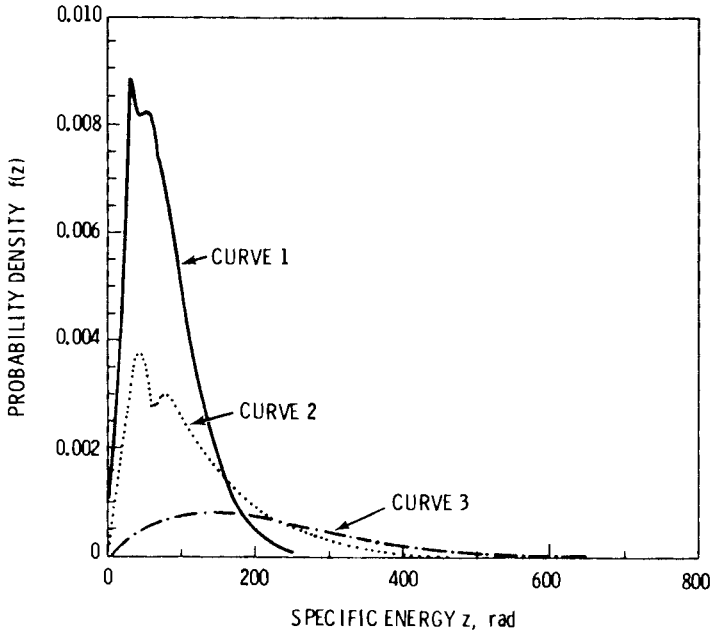

Figure 2.43. Dose to Cell Nuclei from ^{244}Cm *in Vitro*

survival will be determined by the ability of cells to produce colonies. Production of mutations will be measured by a reduction in the activity of the purine salvage enzyme hypoxanthine-guanine phosphoribosyl transferase (HGPRT), which allows the mutant cells to grow on a usually lethal medium. Primary DNA damage will be evaluated by the technique of sister chromatid exchange, and DNA repair will be quantified by ^{3}H-thymidine uptake. These experiments will help improve and refine the application of microdosimetric computations, resulting in improved dosimetry of internally deposited radionuclides.

^{85}Kr Infinite Cloud Exposure

D. W. Murphy, F. N. Eichner

Dosimetric analysis for the Toxicology of ^{85}Kr Program was continued from previous years. The final measurements were taken in August 1980. The external radiation doses measured by thermoluminescence dosimeters for FY80 were 3072 rad, 295 rad and 37 rad for groups of rats exposed to 3×10^{-3}, 3×10^{-4}, and 3×10^{-5} μCi ^{85}Kr/ml air, respectively. The animal exposures were terminated in August 1980. The external exposure and internal organ doses (primarily lung dose) are now being correlated with the observed biological effects.

Organ Dose Analysis of ^{232}U and Daughters in Rats

D. W. Murphy, D. L. Haggard, and J. E. Ballou

Radiation doses are being analyzed in conjunction with the Toxicity of Thorium Cycle Nuclides Program. Gamma spectra are being analyzed to determine the distribution of ^{232}U and its daughters following the endotracheal injection of $^{232}UO_2(NO_3)_2$ in rats. The uranium in the solution was in equilibrium with all its daughters prior to injection. The rat tissues (lung, liver, kidney, and femur) were counted with intrinsic germanium and two Ge(Li) detectors to identify the radionuclides present in each tissue and to quantify the initial amounts of each radionuclide. The results of the analyses performed to date are discussed under The Toxicity of Thorium Cycle Nuclides (Part 1 of this Annual Report). When the radionuclide concentrations have been determined for each organ, the radiation doses to the organs will be determined.

• Radiation Instrumentation — Radiological Chemistry

During the past year, major efforts in this program have concentrated on lowering the background for the measurement of small amounts of radioactivity by beta and gamma counting, on the design of specialized systems, on specific procedures for the measurement of certain radionuclides, on improved computer programs for the analysis of gamma-ray spectral data, and on the development of X-ray fluorescence techniques that permit concentrations to be measured without the weight of the sample being known.

Natural Contamination In Radionuclide Detection Systems

N. A. Wogman

Several sources contribute radioactivity to radionuclide detection systems. These sources are natural radioactivity from the earth's crust, cosmic rays, and radioactivity produced by humans. Thus, the potential exists for radioactive contamination of materials used for radionuclide detection.

In designing low-level gamma-ray counting systems, attempts are made to use the purest of materials as well as sophisticated electronic anticoincidence shields to eliminate the inherent radioactive background created within the system or contributed from radioactive sources external to the system.

In order to detect low levels of radioactivity in construction materials, the most sensitive technology available must be used to identify the radionuclide species in a sample. This study used a multidimensional gamma-ray spectrometer system (MDGRS) (Wogman, Perkins and Kaye 1969) which employs two 23-cm-dia x 20-cm-thick NaI(Tl) crystals as principal detectors. The detector system is coupled to a computer memory and uses the gamma-ray decay characteristics of each of the radionuclides to identify and measure radioactivity.

Through use of the MDGRS, the natural radioactivity in NaI(Tl) and Ge(Li) spectrometer construction materials has been measured and is shown in Table 2.4. In general, aluminum contains high quantities of ^{232}Th and ^{238}U with minimal quantities of ^{40}K. Stainless steels contain ^{60}Co, although, in general, they are becoming cleaner as the use of ^{60}Co in iron fabrication is eliminated. The radioactive content of foams, cements and light reflective material is variable. The magnesium oxide reflective material used in NaI(Tl) spectrometer construction contains ^{232}Th, ^{238}U, and ^{40}K; calcium carbonate does not. Molecular sieve material used in germanium spectrometers contains 4 to 9 dpm/g of sieve. As is illustrated in Table 2.4, many construction materials used for gamma-ray spectrometer systems contaminate these same systems. Only through a judicious choice of materials can systems with the lowest achievable background be assembled. It should be noted, however, that the lowest achievable background of a spectrometer allows for further study of radioactivity in construction materials that may be used in future generations of gamma-ray detection systems.

The degree of contamination can be reduced in various ways. Quartz light pipes can be placed between the NaI(Tl) gamma-ray detectors and glass phototubes. Ceramic phototubes may eliminate some ^{40}K background. Systems can be constructed of titanium metal using pure calcium carbonate reflective coating. In diode spectrometers, molecular sieve material can be placed at a 90° angle to the detector. Shielding can be placed between these two points. Pure charcoal can also be used as a vacuum pumping material. All of these techniques can be used to reduce the radioactive content or its inherent effect on the spectrometer system.

Table 2.4. Radioactivity in Alpha, Beta, and Gamma-Ray Detection Construction Materials (dpm per gram of sample)

Spectrometer Assembly

Material	^{232}Th	^{238}U	^{40}K
Al (25)	0.12	<0.07	1.0
Al (6061)	0.42	0.04	<0.05
Al (1100)	0.24	<0.017	<0.06
Al (1100)	0.08	<0.026	<0.11
Al (3003)	0.10	<0.026	0.56
Al (sheet)	<0.08	<0.1	<0.4
Al (sheet)	<0.1	<0.2	<0.5
Al (sheet)	0.9	<0.007	<0.09
Al (sheet)	0.3	<0.007	<0.09
Al	0.02	0.005	0.07
Al_2O_3 (reflector)	0.11	<0.07	<0.3
CdF_2 (light pipe)	<0.003	<0.003	<0.01
Cu (sheet)	<0.05	<0.006	<0.2
Cu (rod)	<0.02	<0.03	<0.09
Ge (ingot)	<0.02	<0.02	<0.05
Ge (ingot)	<0.02	<0.02	<0.04
Ge (cylinder)	<0.02	<0.02	<0.04
Ge (cylinder)	<0.01	<0.01	<0.02
Fe (plate-old)	<0.003	<0.005	<0.01
Fe (304 stainless)[a]	<0.006	0.007	0.06
Fe (304-L stainless)[a]	<0.005	<0.005	<0.02
Mg (rod)	0.06	<0.04	0.1
Mg (ingot)	<0.01	<0.002	<0.02
MgO (reflector)	0.088	0.14	<0.23
MgO (reflector)	<0.05	<0.05	<0.2
Pb (shavings)	<0.008	<0.01	<0.03
Pyrex (window)	0.45	0.27	3.8
Se (59S)	0.04	0.01	10.3
Quartz (window)	<0.018	<0.018	<0.07
Quartz (window)	<0.018	<0.018	<0.07
Polyvinyl chloride foam	1.0	0.9	1.6
Polyvinyl chloride foam	0.19	0.4	0.36
Polyvinyl chloride foam	<0.2	0.4	<0.7
Neoprene	<0.008	<0.01	0.36
Rubber	0.12	1.2	1.8
Rubber	0.12	1.0	2.0
Mattress Foam - U.S. Rubber	1.9	15.0	24.70
Apiezon Z	4.5	4.5	2.7
Electrical Tape -3M	<0.04	<0.06	<0.1
Cement - Portland	0.25	1.3	4.5
Molecular Sieve	4.5	3.0	9.0
Epoxy	0.006	0.01	0.19
Lacquer	<0.002	<0.005	<0.04
Vycor Lens			
$CaCo_4$	0.003	0.002	0.01
$CaCo_4$	0.003	0.003	0.01
MgO	0.01	0.05	0.2
MgO	0.02	0.07	0.2
MgO	0.02	0.07	<0.2
Millipore	<0.002	<0.009	<0.01
Ti	<0.003	<0.002	<0.01
Ti	0.002	0.04	<0.01
Lavite Clay[b]	4.0	3.0	10.0
Lead Solder[b]	0.4	0.5	<0.01
Charcoal	<0.003	<0.005	<0.02
Glass Tubes	0.5	0.3	5.0
Lucalox	0.6	0.4	1.0

[a]0.02 dpm/g ^{60}Co
[b]Old Style Gold Surface Barrier Detectors

Design of an Ultralow Background, High-Efficiency Intrinsic Germanium Gamma-Ray Spectrometer

N. A. Wogman

An ultralow background, high-efficiency intrinsic germanium gamma-ray spectrometer has been designed, constructed, and evaluated for environmental radiochemical measurements. The design of the system eliminates the major cause of background radioactivity (contaminated construction materials) and reduces through electronic means the background effects created by cosmic rays.

The spectrometer, shown in Figure 2.44, is constructed using an intrinsic germanium ingot (25%) placed geometrically inside a NaI(Tl) detector operating in anticoincidence so that the primordial radionuclides in the phototubes of the NaI(Tl) system and in the diode and liquid nitrogen cryostats contribute minimal background. This design achieves the lowest background yet reported in the literature for the energy range 60 to 10,000 keV. At 3.0 MeV, the background is 0.000058 counts per minute per keV (c/m/keV); at 1.0 MeV it is 0.00048 c/m/keV; and at 0.5 MeV it is 0.0045 c/m/keV. There are still traces of primordial species-creating backgrounds at 2.614 MeV [$^{232}Th(^{208}Tl)$] of 0.016 counts per minute (c/m); at 2.448 MeV (^{226}Ra) of 0.0058 c/m; and at 2.204 MeV [$^{238}U(^{214}Bi)$] of 0.023 c/m. Methods to eliminate the last vestiges of primordial and cosmic-ray backgrounds are presently being studied.

The detector design discussed in this report achieves efficiencies of 6% for a 1-cm thick x 5-cm dia environmental matrix and 12.5% for a point source geometry at 300 keV using an ingot of 25% efficiency. Various cryostat designs have also been evaluated using charcoal to maintain cryostat vacuum instead of using primordially contaminated molecular sieves. The present backgrounds were obtained using 15.2 cm of lead and 5.1 cm of iron in conjunction with shadow shielding of the germanium detector. Borated paraffin, which filled all remaining cave space, and electronic blocking techniques reduced backgrounds created by cosmic-ray neutrons. In the present design, electronic blocking of cosmic-ray events reduces by twofold the photon continuum in the 0.1 to 2.0 MeV range. The design also reduces the background tenfold below that normally achievable with typical diodes as they are delivered by detector manufacturers. The present design achieves peak-to-Compton edge ratios exceeding

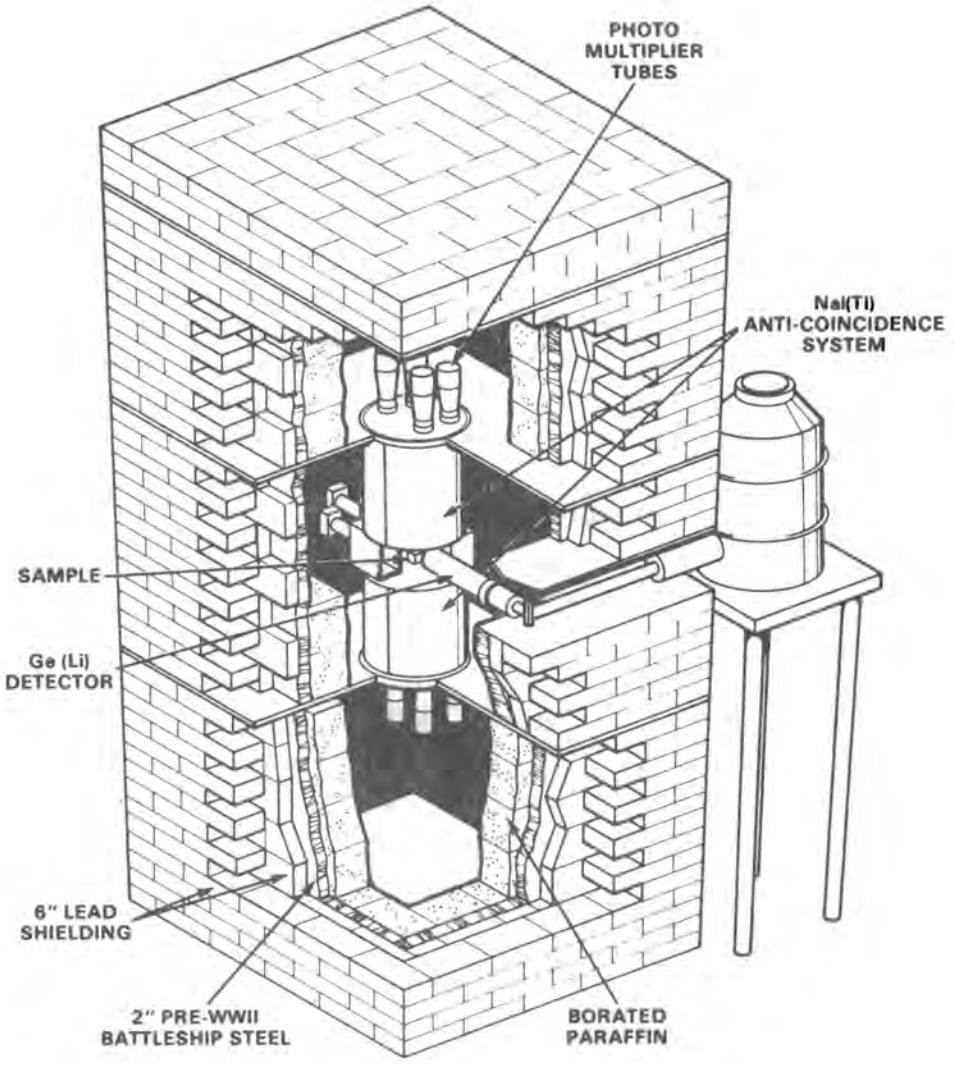

Figure 2.44. High-Efficiency, Low-Background Ge(Li) Gamma-Ray Spectrometer

1000:1 for ^{137}Cs. By electronically routing coincidence and single photon events to different areas within a data storage computer, no data are lost during the gamma-ray analysis.

The present detector design has backgrounds lower than those obtained in earlier studies (Wogman 1980a,b,c) using diode sizes from 24.4 to 31.5% and NaI(Tl) and plastic phosphor anticoincidence shields. In plastic shields, a background photon is produced by neutron interaction created by cosmic rays which yield a 2.225-MeV event. This event cannot be eliminated in surface counting room facilities.

Use of the new spectrometer allows environmental measurements at extremely low background levels. The system is being used to study the radioactivity present in radioanalytical detector construction materials such as titanium, aluminum, stainless steel, NaI(Tl), charcoal, MgO, $CaCO_3$, and quartz, as well as components like phototubes. This low-background spectrometer is being applied to problems in the fields of energy generation and fuel extraction. It is being used to measure plutonium, americium, and curium isotopes created in the nuclear fuel cycle through both their high- and low-energy photon emissions. The system is also being applied to neutron activation analysis in studies of trace

elements as pollutants or tracers of environmental pathways. The system has such a low background it is even allowing studies of the basic physics of double beta decay.

The Measurement of Long-Lived Radionuclides in the Nuclear Power Industry

C. W. Thomas

Over the next thirty years the nuclear power industry is expected to generate considerable amounts of radioactive material. The radionuclides of concern have been identified; next, it will be necessary to develop methods of separating and measuring them. A large number of these radionuclides (listed in Table 2.5) can be measured by direct counting and gamma-ray spectrometry. The isotopes have gamma rays whose energies are unique and/or can be corrected for interferring gamma energies. However, a large number of isotopes (also listed in Table 2.5) will require chemical separation before measurements can be made.

Tables 2.6 and 2.7 show the decay characteristics of the radionuclides that require chemical separation. The most notable characteristic for these radionuclides is that nearly all decay by emission of low-energy beta, low-energy photons, or an alpha particle. This characteristic makes the measurement and chemical separation of the isotopes difficult. Nearly all the heavy element isotopes decay by alpha emission and nearly all can be resolved by alpha spectrometry. Figures 2.45, 2.46, 2.47, and 2.48 show the separation of spectra from the isotopes obtained and the interference when using alpha spectrometry. Nearly all radionuclides of uranium can readily be measured by alpha spectrometry. The only interference is between ^{234}U and ^{233}U.

The isotopes of thorium can readily be measured by alpha spectrometry. All the

Table 2.5. Radionuclides in the Nuclear Power Industry and Methods of Measurement

Measurement and Separation by Gamma-Ray Spectroscopy		
^{22}Na		
^{144}Ce		
^{54}Mn		
^{228}Ac		
^{110m}Ag		
^{152}Eu		
^{154}Eu		
^{155}Eu		
^{60}Co		
^{106}Ru		
^{137}Cs		
^{65}Zn		
^{134}Cs		
^{125}Sb		
^{226}Ra		
Chemical Separation Required		
^{93}Zr	^{126}Sn	^{237}Np
^{93}Nb	^{126}Sb	^{90}Sr
^{59}Ni	^{79}Se	^{234}U
^{63}Ni	^{135}Cs	^{230}Th
^{99}Tc	^{244}Cm	^{232}U
^{55}Fe	^{241}Am	^{228}Th
^{151}Sm	^{239}Pu	^{243}Am
^{129}I	^{238}Pu	^{242}Cm

Table 2.6. Decay Characteristics of Fission and Activation Products Requiring Chemical Separation

Isotope	Half-life (Years)	Radiation	Energy (KeV)	Abundance (%)
^{59}Ni	8×10^4	X-ray (Co)	6.93, 7.65	
^{63}Ni	92	Beta	67	100
^{79}Se	6.5×10^4	Beta	160	100
^{93}Zr	1.5×10^6	Beta	60	95
^{93m}Nb	13.6	X-ray (Nb)	16.60, 18.62	
^{99}Tc	2.1×10^5	Beta	292	100
^{129}I	1.7×10^7	X-ray (Xe)	29.77, 33.62	
—	—	Gamma	39.7	4
^{90}Sr	28	Beta	2000 (Y^{90})	100

Table 2.7. Decay Characteristics of Heavy Elements Requiring Chemical Separation

Isotope	Half-life (Yr)	Radiation	Energy	Abundance (%)
^{238}Pu	86	Alpha	5.49	100
^{239}Pu	24000	Alpha	5.14	100
^{240}Pu	6600	Alpha	5.15	100
^{241}Pu	15	Beta	21 keV	100
^{242}Pu	8.8×10^5	Alpha	4.89	100
^{241}Am	458	Alpha	5.48	100
^{242m}Am	152	Beta	660 keV	82
^{243}Am	7370	Alpha	5.28	100
^{239}Np	2.3 days	Gamma	278 keV	12
^{242}Cm	0.45	Alpha	6.12	100
^{243}Cm	30	Alpha	5.78	85
^{244}Cm	11.9	Alpha	5.81	100
^{234}U	2.47×10^5	Alpha	4.77	100
^{232}U	72	Alpha	5.32	100
^{230}Th	8.0×10^4	Alpha	4.68	100
^{228}Th	1.91	Alpha	5.42	99

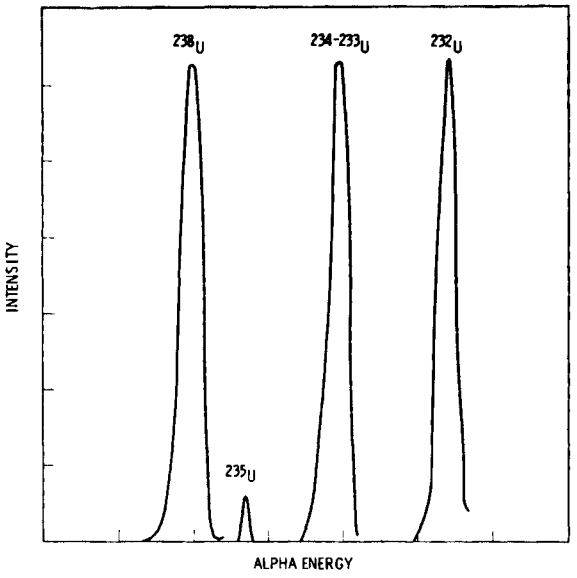

Figure 2.45. Alpha Spectrum of Uranium Isotopes

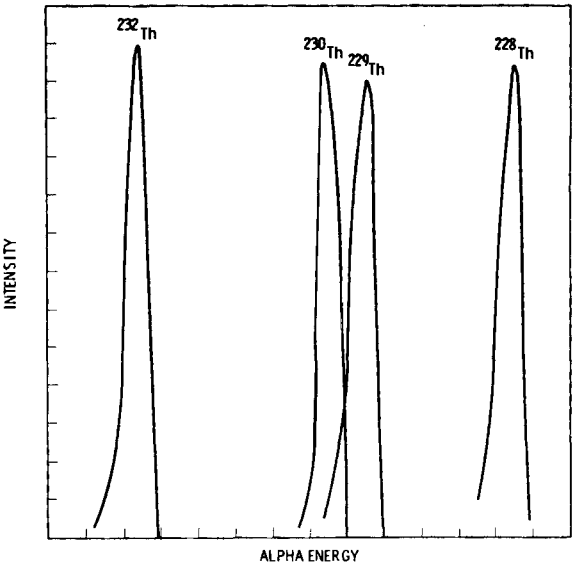

Figure 2.46. Alpha Spectrum of Thorium Isotopes

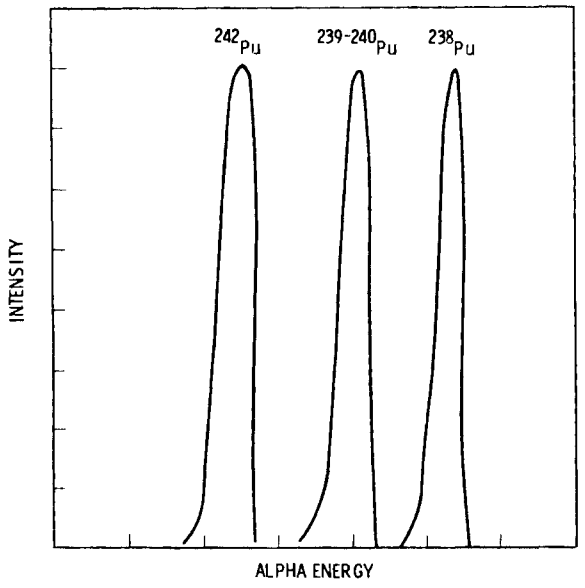

Figure 2.47. Alpha Spectrum of Plutonium Isotopes

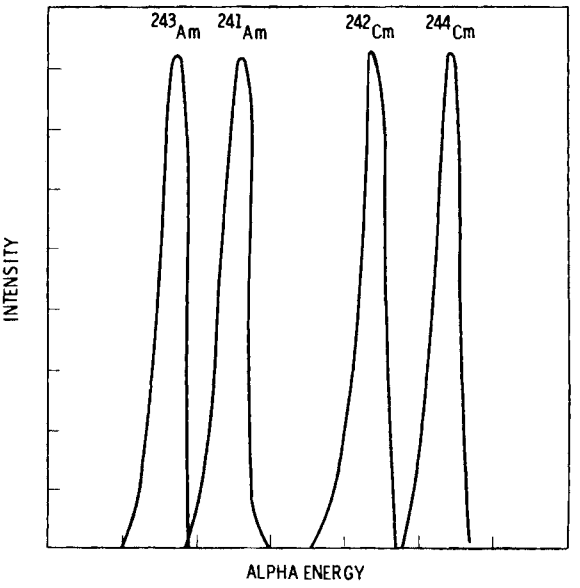

Figure 2.48. Alpha Spectrum of Americium and Curium Isotopes

alpha energies of plutonium isotopes are well separated except for ^{239}Pu and ^{240}Pu which are generally reported as a mixture. Americium and curium are extremely hard to separate chemically, but the various isotopes can be readily measured by alpha spectrometry.

To measure these heavy element isotopes, as well as the weak beta and weak photo-emitting radionuclides, a uniform, reproducible source mounting containing very little inert material is necessary. Generally, electrodeposition is the best method of preparing a source mount with these decay characteristics. Figure 2.49 shows the electroplating characteristics of several of the elements as measured at PNL. The electroplating method developed (Figure 2.50) uses a sulfate solution and electroplates at 1 amp/cm^2. The electroplating area was a circle with a 1-cm diameter. Thymol blue was used as the pH indicator. In the electroplating of technetium and selenium it was necessary to add sodium sulfite to the electroplating solution. In all cases a good uniform plate was readily obtainable.

In the measurement of americium and curium considerable inert material was present in the electroplate from samples containing large amounts of salt. It was found that anion exchange and thiocyanate did not thoroughly separate americium and curium from the rare earths, but did an excellent job removing yttrium from these heavy elements. Cation exchange from a concentrated hydrochloric acid media thoroughly separated americium-curium from rare earths; however, the separation from yttrium was poor. The combination of anion exchange from thiocyanate and cation exchange from concentrated HCl has resulted in uniform electroplates of americium-curium.

In the measurement of those radionuclides emitting soft beta particles, a recently designed windowless gas-flow proportional beta counter is used. Depending on the sensitivity needed, either an intrinsic germanium diode or the beta counter is used to measure the radionuclides emitting low-energy photons.

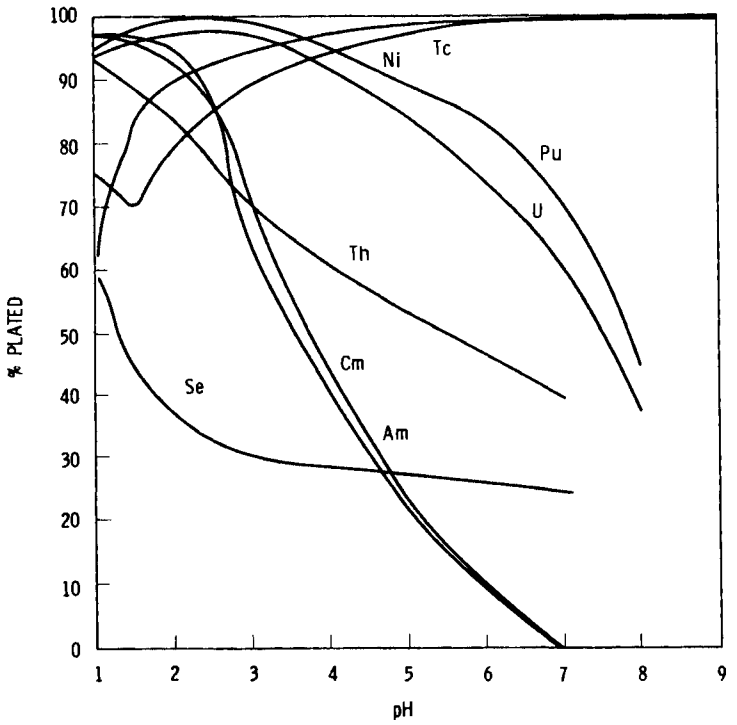

Figure 2.49. Electroplating Characteristics of Several Elements

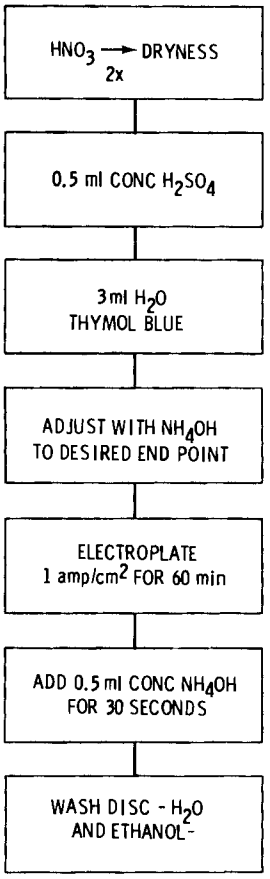

Figure 2.50. Electroplating Method Using a Sulfate Solution and a Current Density of 1 amp/cm^2

A Method for Operation of Anticoincidence Shielded Solid-State Detectors at High Count Rates

D. P. Brown and N. A. Wogman

To achieve the rated resolution of solid-state gamma-ray spectrometers operating at high count rates requires the use of a pulse pile-up rejector/live-time corrector. Typical germanium gamma-ray spectrometers use electronics such as the Canberra 1468A which has an output signal to the analog-to-digital converter delayed in time from the incoming pulse as determined by the amplifier time constant (typically 4 μsec). The analyzer stores the delayed pulse. Deciding in which half of the memory to store the coincidence or noncoincidence events must be done at the time of the coincidence determination in the detector. In application, the output of the 1468A preamplifier input discriminator (which triggers on all incoming pulses from the solid-state detector) is tested for coincidence with the output of a discriminator in the shield detection circuits. Coincidence between these two outputs generates a "store second half" signal to steer the output to the proper memory location. This pulse must then be delayed long enough so that it will be present when the delayed output pulse for storage occurs. Stretching the coincidence pulse long enough to equal the delay time would permit proper operation of the system at low count rates. However, solid-state detector signals at high count rates that normally would be in coincidence with correspondingly high count rate signals from the anticoincidence shield would be lost and would not generate the proper signals for direction of pulse location (steering circuit) during the pulse stretching time.

In order to accommodate high count rate situations, the input signals are thus differentiated (see Figure 2.51) to make them very short (minimizing chance coincidences). The discriminator and coincidence pulses are kept short, approximately 100 nsec, to again reduce the chance coincidence effect. The coincidence pulses are injected into a delay circuit which permits each pulse to propogate a pulse independent of any second pulse preceding it within the delayed time. In this manner, the pulses required to direct event location arrive in time coincidences with the 1468 delayed output. System operation is shown in block diagram in Figure 2.51.

Instrumentation for Using Multiple BF_3 Neutron Counters in High-Gamma Fields

D. P. Brown and R. L. Brodzinski

A large array of BF_3 neutron detectors has been designed to measure fissile material remaining in chopped-leached hulls of fuel elements. Because the gamma radiation from the hulls is high, precautions must be taken to minimize erroneous neutron counting due to gamma pile-up. The BF_3 tube array in the present detector consists of 80 tubes in eight groups of 10 tubes each. In this configuration the gamma noise in each group results from summing the noise from 10 tubes which then contributes to pile-up and limits the maximum gamma radiation level below which the rated neutron sensitivity can be achieved. This effect seriously limits the use of large arrays. Therefore, a method was devised to permit each tube to operate essentially independent of all the others. This was done by designing a preamplifier-discriminator

which could be attached directly to each BF_3 tube. The preamplifier amplifies the BF_3 tube signal and then uses a differentiator of very short time-constant (0.1 μsec) to reduce pile-up. The 0.1 μsec time-constant permits a BF_3 tube such as the one used (2-in. dia x 22-in. long) to operate in a gamma field of 250 roentgen/hr with no loss in sensitivity because of pile-up. In addition, the circuitry used amplifies the signal and differentiates it a second time for further use on the system. The signal is then passed to a pulse height discriminator where neutron pulses are separated from the noise. The discriminator places the output pulse on the high-voltage cable which delivers it to a standard preamplifier, which separates the pulse from the high voltage, amplifies it and passes it on to a counting circuit. Each BF_3 tube has its own preamplifier-discriminator and each group of 10 tubes is connected in parallel through the high-voltage bias line to a common proportional counter preamplifier. In this manner, the ability of each tube to operate separately in a high gamma field is preserved and the combination operates correctly. Figure 2.52 illustrates the implementation of this technique.

The preamplifier-discriminator is housed in a 2-in. dia x 3-in. long brass cylinder. This housing contains, in

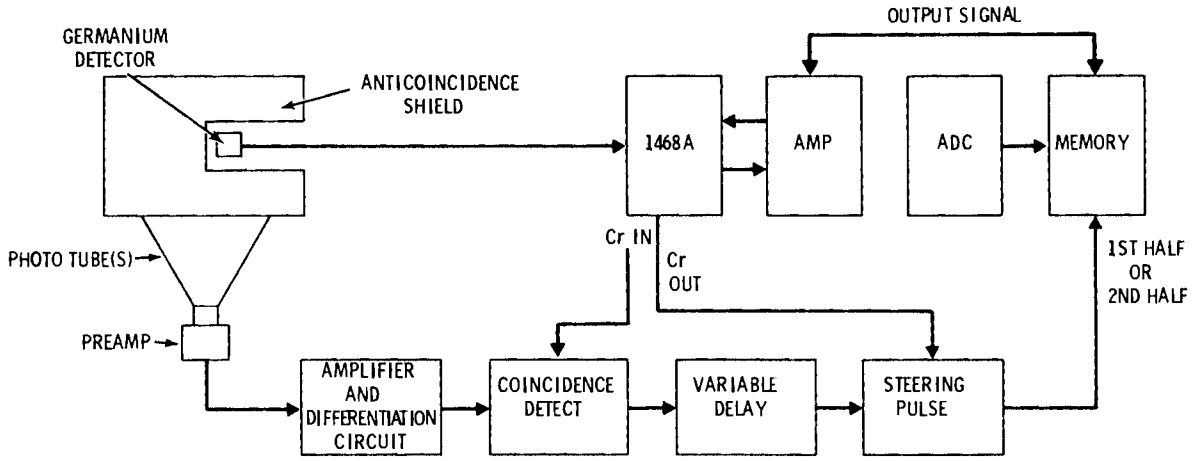

Figure 2.51. System Operation of Anticoincidence Shielded Solid-State Detectors at High-Count Rates

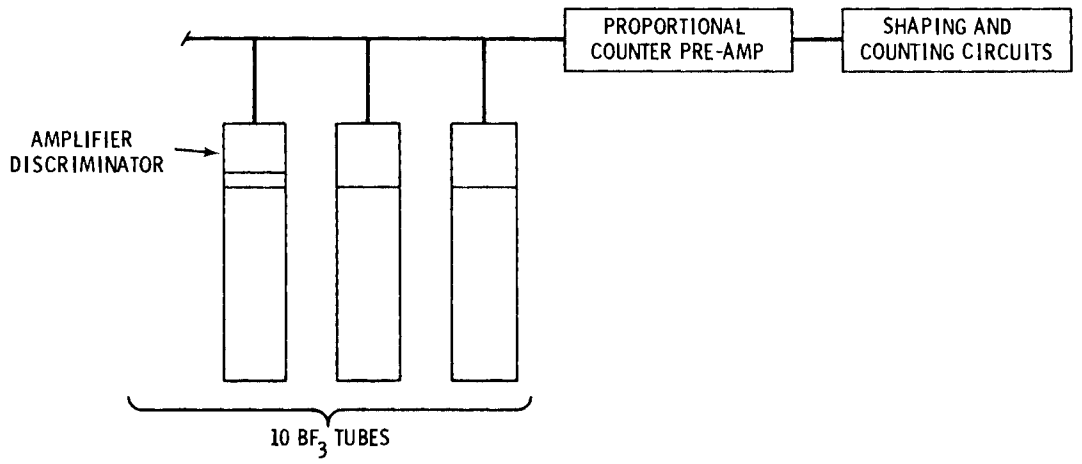

Figure 2.52. Implementation of BF_3 Tube Preamplifier Discriminator

addition to the preamplifier-discriminator circuits, the high voltage decoupling circuits which permit using the high voltage cable to carry the signal, and conditioning circuits for the power supply. The mechanical design of the device permits it to be attached directly to the BF_3 tube in place of the original HN connector. Figure 2.53 shows a block diagram of a BF_3 preamplifier-discriminator.

A Windowless Gas-Flow Proportional Beta Counter for Measuring ^{63}Ni And ^{59}Ni

C. W. Thomas and E. A. Lepel

Recent estimates of the amounts of activation radionuclides in nuclear wastes show the radionuclides that will be of greatest significance in the year 2000 are ^{63}Ni, ^{55}Fe, ^{54}Mn, ^{3}H, ^{60}Co, ^{14}C, and ^{99}Tc. After a 100-year decay, only the longer-lived radionuclides, ^{63}Ni, ^{3}H, ^{14}C, ^{59}Ni, ^{93}Zr, and ^{99}Tc, will be present in large amounts. Since most of these radionuclides decay with soft-beta emission and/or weak X-rays, a detector capable of measuring beta energies less that 100 keV would enhance the measurement of most of them. For this purpose a windowless 2 pi counter of thin-walled plastic was designed (Figure 2.54). It is coated with silver-conducting paint and uses a single loop electrode. The sample is electroplated on a stainless steel disc and mounted on the flat bottom surface of the detector. The measurement capability of this counter with respect to background and efficiency is compared to a thin window counter in Table 2.8. The background, as measured in a 4-in lead cave, is similar for both window and windowless counters (16.9 and 16.5 cpm); the

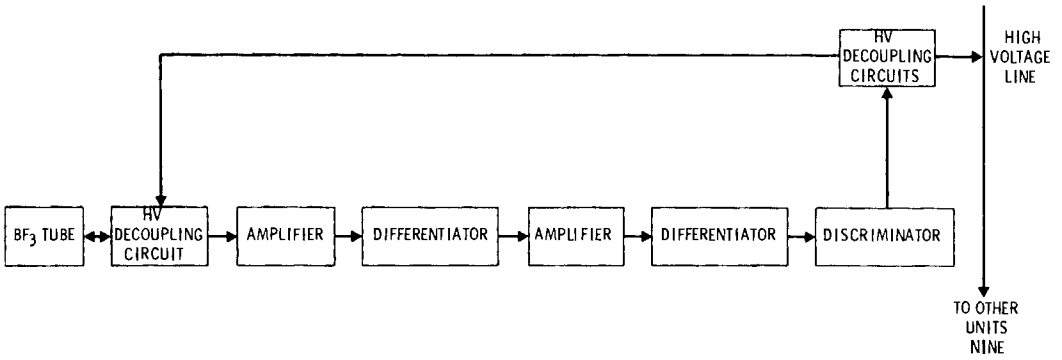

Figure 2.53. Block Diagram BF_3 Tube Preamplifier Discriminator

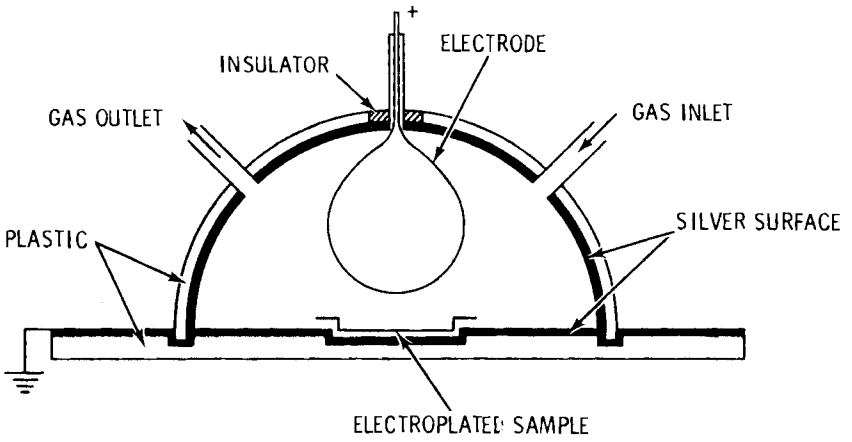

Figure 2.54. A Windowless Gas-Flow Proportional Beta Counter

Table 2.8. Counting Characteristics for Window and Windowless Gas-Flow Proportional Beta Counters

Characteristic	Window	Windowless
Detector with window	1.2 mg/cm²	—
Background with 4" Pb shielding	16.9 c/m	16.5 c/m
Background with 4" Pb, 125 mil plastic as shielding, 20 mil Cd, 40 mil Cu		12.9
Efficiency - ^{63}Ni (500 μg Ni)	2.9	22.5%
Efficiency - ^{59}Ni (500 μg Ni)	7.8%	33.2%

efficiency for counting ^{63}Ni increases when using the windowless counter (22.5%) as opposed to using a window counter (2.9%). Nickel-59 is a weak X-ray emitter similar to ^{55}Fe, and its detectability is also improved by using the windowless counter (33.2% efficiency for the windowless counter as compared to 7.8% for the window counter).

Figure 2.55 shows the response of the windowless counter as a function of voltage. The plateau is flat from 1650 to 2000 volts showing a rise of only 4.3% over this voltage span, or an increase of 1.22%/100 volts.

Since ^{63}Ni decays with the emission of a 67 keV beta particle, the response of any counter will be seriously affected by the amount of inert nickel in the sample aliquot. The effect of varying amounts of stable nickel is shown in Figure 2.56. The self-absorption/self-scatter for ^{63}Ni shows a rapid drop in efficiency and a realistic limit of about 1000 to 2000 μg of stable nickel allowable in a sample aliquot. About 10 times this amount could be tolerated in measuring ^{59}Ni (and ^{55}Fe) in this counter. The overall size of the counter allows it to be easily fitted between anticoincidence shields for reducing the background. A 100-fold reduction in background is expected when the counter is placed in

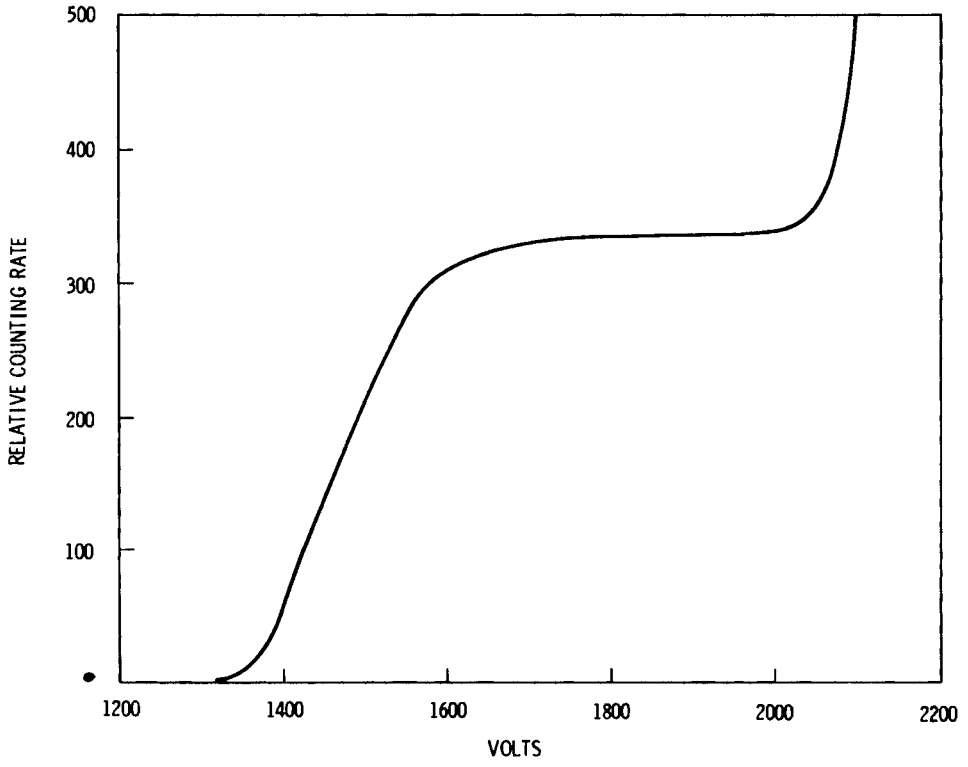

Figure 2.55. Windowless Counter Response as a Function of Applied Voltage

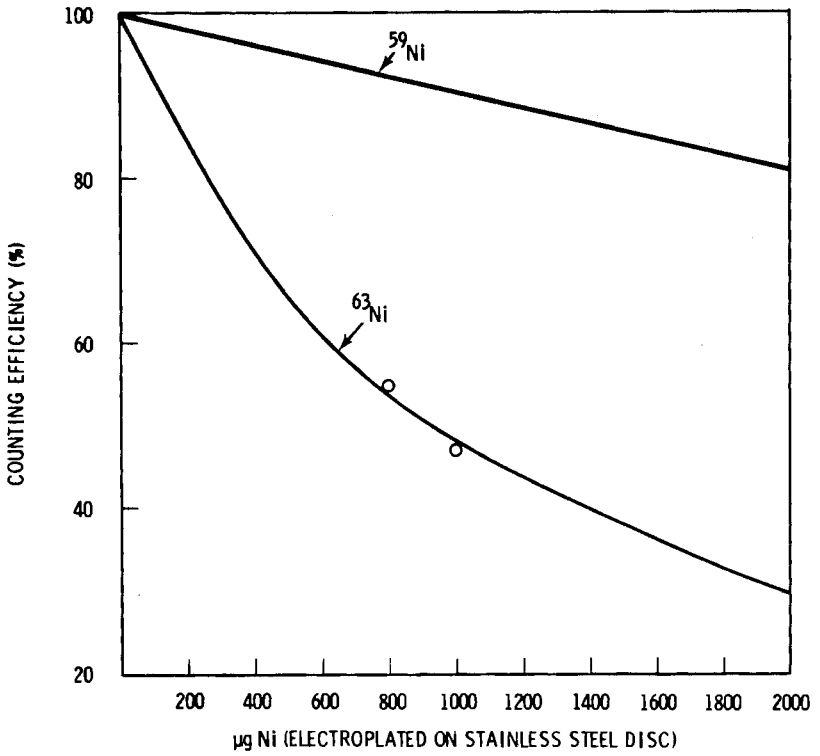

Figure 2.56. ^{63}Ni and ^{59}Ni Counting Efficiency as a Function of Self-Absorption

anticoincidence with a multidimensional gamma-ray detection system (Wogman and Brodzinski 1973).

Methods for Suppression of Cosmic Ray Effects in Anticoincidence Shielded Solid-State Detectors

D. P. Brown

Large anticoincidence NaI(Tl) and plastic phosphor shields are efficient in detecting cosmic rays. Cosmic-ray-induced count rates of 3000 count/min are common in these types of systems. Amplifiers with voltage gains used in the analyses of gamma-ray energies up to 2 MeV are driven far beyond rated saturation by large cosmic-ray pulses of up to 1 GeV in energy. The detection of GeV energies by the anticoincidence shield results in failure of the normal overload recovery circuits in the amplifiers. Under these circumstances, the recovering pulse often undershoots the baseline and then returns to the baseline in a period of time which can approach 500 µsec. The return to the baseline is often accompanied by some form of oscillation; thus, for up to 500 µsec following a cosmic-ray event in the shield, the shield circuitry operates incorrectly. Ordinarily the shield provides coincidence signals from detection of photons scattered from the solid-state detector. When the detector and shield see a pulse in coincidence, the circuitry normally directs the pulse storage to a specific location of a multichannel analyzer memory. By this procedure, a reduced Compton background is achieved for radionuclides not emitting coincidence photons. However, when the coincidence-directing circuitry becomes disabled following a cosmic event, those pulses which should be directed to coincidence locations are erroneously stored in the noncoincidence locations, and the suppression of Compton background suffers. To reduce this problem, two approaches have been evaluated: 1) total blocking, and 2) signal differentiation.

In the total blocking method, a discriminator is set to trigger on only the very large cosmic-induced pulse in the amplifier. The signal triggers an adjustable blocking system set to the time required for the amplifier to recover. This disables the analyzer ADC. During the time

the directing circuits are operating incorrectly, the ADC is prevented from storing any pulses. To correct for the lost pulses and the circuit dead time, the blocking pulse also disables the live-time clock. Use of this approach significantly reduces the noncoincidence background; however, the additional dead time introduced by the blocking signal adds to the total counting time required to analyze a sample.

In the signal differentiation method, RC circuit differentiation of rising pulses [typical of those produced by phototubes attached to the large NaI(Tl) or plastic phosphor anticoincidence shields] produces pulses which are reduced in amplitude and shortened in time. The very large pulses from cosmic-ray events in these shields can now be detected and used to generate a blocking signal as before; however, because of the action of the differentiation circuits, the blocking time required is greatly reduced. This improves the time required to count the sample. The normal-event pulses from the differentiation are further conditioned and used in circuitry to determine in which half of the memory to store the pulse from the solid-state detector.

Both of these methods reduce the Compton background; the second method gives an added advantage by permitting the use of higher count rates in the anticoincidence shields.

• Magnetic Field Dosimeter Development

Magnetic field dosimeters have been developed to measure the exposure of personnel who work in magnetic field environments. The battery-operated devices use Hall-effect sensors and microprocessors for data analysis. In the operation of a magnetic field dosimeter data recording system the magnetic field exposure data (dose) is transferred from the dosimeter to a readout console for final analysis and storage. These instruments demonstrate the feasibility of monitoring personnel exposure in magnetic field environments.

Magnetic Field Dosimeter Development

D. K. Lemon, J. R. Skorpik and J. L. Eick

There is increasing concern over potential health hazards related to exposure to magnetic fields. If realistic exposure standards are to be established and enforced, a dosimeter for magnetic fields must be available. This project was established to develop a means for obtaining data on exposure of personnel to magnetic fields. In this concluding year of the project, two working models of magnetic field dosimeters have been developed and delivered to the sponsor. The development of these instruments is an important step towards meeting the requirements in this area.

The basic sensors of the dosimeter are three Hall-effect sensors. They are attached to the body of the dosimeter with an umbilical cord (Figure 2.57). The Hall-effect sensors measure three components of the magnetic field, B_x, B_y, and B_z, thereby uniquely defining the field. The measurements obtained from these sensors are sampled cyclically by a microprocessor in the dosimeter. During an operation period the dosimeter stores the dose information for subsequent readout. At the end of a measurement period (e.g., one work-day), the dosimeter is connected to a data recording console. The worker's name is typed in and the dosimeter data are read out into the console. A microprocessor in the console then reduces the dose information and prints it out on the teletype unit. In actual field applications a cassette tape unit would also be used to permanently record the dose information for each individual. Through a cassette recording, data on a large number of individuals could be recorded and later retrieved for analysis.

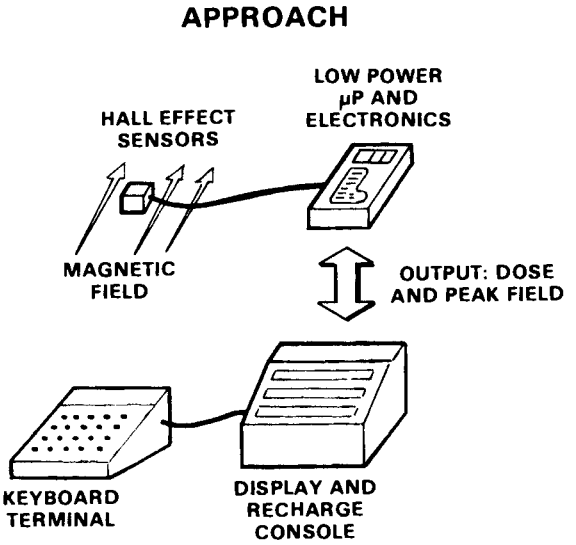

Figure 2.57. Diagram of the Approach Used in the Magnetic Field Dosimeter Data Recording System

We conclude from this project that the Hall-effect microprocessor design is feasible for dosimeters in field use. The working models have shown that the problems of temperature compensation, voltage drift and electronic storage of the data can be solved. During this project, we investigated alternative dosimeter designs, in particular, designs that would allow several weeks of continuous operation. Unfortunately, none were found that promised to

offer long-term, unattended operation. Therefore, we conclude that the Hall-effect microprocessor approach is the one that should be pursued in future development.

Based on the progress of this project and recent advances in low-power microprocessors, we make the following recommendations:

- The present dosimeters should have limited field testing to further determine changes that should be made in future models. In particular, "human engineering" factors should be considered.
- The dosimeters should be altered to employ one of the new, low-power microprocessors now on the market. Doing so would double the battery life (to 12 hours) and also allow greater flexibility in the computation of dose.
- A redesigned dosimeter should then be field-hardened through a series of field tests and design improvements.

After these design and testing tasks are completed, a limited number of the dosimeters (perhaps one hundred) could be produced and deployed in the field.

• Transuranic Chemical Species in Groundwaters

Groundwater transport of the transuranic radionuclides is a little understood problem of immediate concern to DOE and other regulatory agencies. At the Hanford N-Reactor site a unique groundwater microcosm exists which allows the study of the physicochemical processes that control the mobility of radionuclides in groundwaters. This system is being utilized as a natural laboratory to identify specific forms of the transuranic radionuclides that migrate in groundwater and to determine the rates and mechanisms that control this migration.

Transuranic Chemical Species in Groundwaters

D. E. Robertson and K. H. Abel

At the Hanford N-Reactor site, low-to-intermediate levels of radioactivity contained in aqueous effluents from the N-Reactor are continually discharged at a rate of approximately 3 million gal/day to a rock-lined crib and overflow seepage trench located on a bluff overlooking the Columbia River (Figure 2.58). The effluent water percolates by gravity through a soil bank and some of the water emerges to form seepage springs located along the bank of the Columbia River directly below the crib-trench. The spring area represents the shortest time path (typically four to six days) for the discharge water flow to the river. The remaining water seeps into the river below its water level.

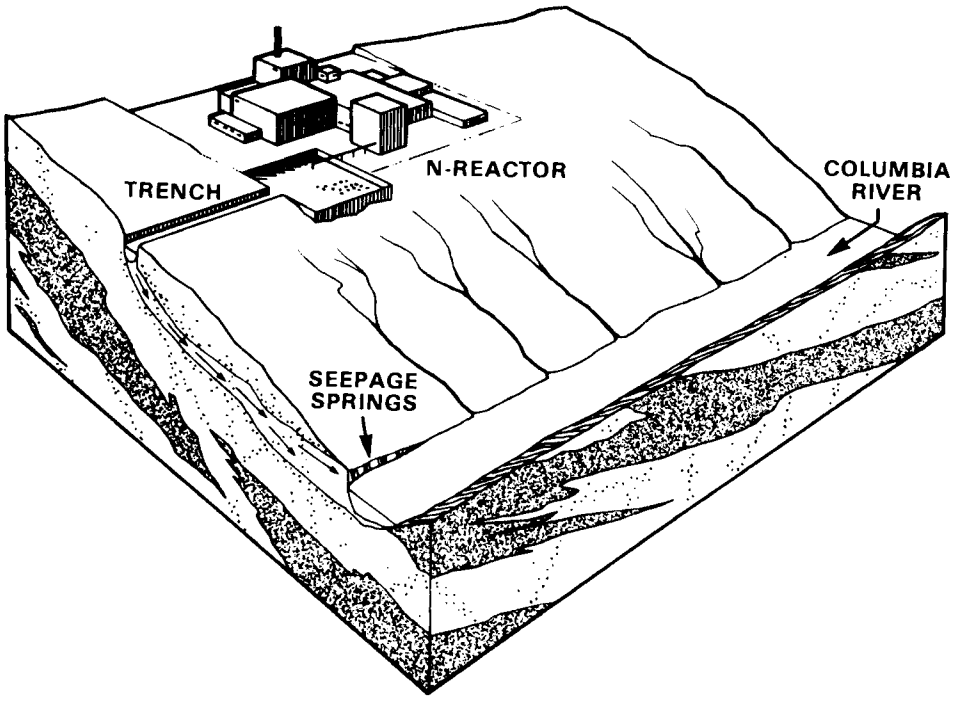

Figure 2.58. Schematic Cross-Sectional View of N-Reactor Liquid Effluent Disposal System

A total of 7167 Ci of long-lived fission and activation product radionuclides ($t_{1/2}$ - 27.7 days for ^{51}Cr) entered the crib-trench in 1978, and 3.32 Ci seeped through the soil bank and entered the Columbia River. A total of 0.26 Ci of ^{238}Pu and 1.3 Ci of $^{239-240}Pu$ entered the crib-trench in 1978, but only 0.00013 Ci of ^{238}Pu and 0.00030 Ci of $^{239-240}Pu$ entered the river from the seepage springs. Since the N-Reactor has been in operation fourteen years, the total inventory of plutonium in the soil bank probably amounts to several tens of curies. Plutonium concentrations in near-surface soils of the crib and trench range up to 2000 dpm/g, or roughly 40,000 times the fallout background in surface soils. Other transuranic radionuclides, $^{241-243}Am$, $^{242-244}Cm$, ^{239}Np and ^{237}Np, are also present in the crib-trench system although their absolute concentrations have not yet been measured. The 1301-N crib aqueous waste disposal site therefore offers a unique opportunity to study, under natural conditions, the rates and mechanisms of groundwater transport of the transuranic radionuclides.

A research program was initiated this past year to identify what specific physicochemical forms of the transuranic radionuclides are migrating with the groundwater and to determine the rates and mechanisms which govern the mobility of these radionuclides. Large-volume water sampling was conducted at the N-springs to determine the "total" plutonium concentrations in the spring water. This was accomplished by collecting 56ℓ of 0.4 μ Nuclepore filtered spring water, adding 2 dpm of ^{242}Pu tracer, and adjusting the oxidation state of all plutonium species to Pu(III) by the addition of HSO_3^- and HCl. Several hours later, 1000 mg of Fe^{++} carrier were added and the pH adjusted to 8.0. The water was allowed to stand overnight to complete the coprecipitation of the plutonium on the iron hydroxide. The iron hydroxide was then removed and the plutonium separated by ion exchange techniques and electroplated on stainless steel counting discs. The plutonium was then measured by counting for several thousand minutes on a silicon diode alpha spectrometer. The results of these analyses are compared in Table 2.9 with measurements obtained by United Nuclear Corporation Industries (UNC) who operate the N-Reactor.

The $^{239-240}Pu$ and ^{238}Pu concentrations measured in September 1979 were much lower than the UNC 1977-78 annual average concentration. However, UNC has reported considerable variation in plutonium concentrations in the spring water over a year's time. The difference between the PNL and UNC data may be due to temporal fluctuations in the discharge rates of plutonium in the springs.

Table 2.9. "Total" Plutonium Concentrations in N-Springs Water

	Concentration (femtocuries/liters)	
	$^{239-240}Pu$	^{238}Pu
PNL-Sept., 1979	1.85	0.56
UNC—1977-78 Annual Avg.	120	93

Following the "total" plutonium measurements, the oxidation states of plutonium were measured in the N-springs water to determine which forms were migrating. The procedure used by Nelson and Lovett for determining oxidation states of plutonium in Irish Sea water was employed. This method is based on the classical differentiation of Pu(III) and Pu(IV) from Pu(V) and Pu(VI) by coprecipiation of the former pair with NdF_3. Two 25ℓ samples of 0.4 μ Nuclepore filtered spring water were spiked with ^{238}Pu(IV) and ^{242}Pu(VI) tracers and the samples made 0.8 $\underline{M}$ in HNO_3, 0.25 $\underline{M}$ in H_2SO_4, 0.0005 $\underline{M}$ in $K_2Cr_2O_7$ and 0.0007 $\underline{M}$ in $Nd(NO_3)_3$. After standing for several hours, the water was made 0.25 $\underline{M}$ in HF and the resultant NdF_3 containing the Pu(III) and Pu(IV) was removed by filtration. Twenty-five grams of $(NH_4)_2SO_4 \cdot FeSO_4 \cdot 6H_2O$ were added to the filtrate and the water was allowed to stand overnight thus reducing the oxidized plutonium species to Pu(III) and Pu(IV). Another 500 mg of $Nd(NO_3)_3$ were added and the resulting NdF_3 was again removed by filtation. The plutonium in each NdF_3 precipitate was purified by routine ion exchange techniques and electrodeposited on stainless steel counting discs. The samples were counted on silicon diode alpha spectrometers for several thousand minutes.

The results of these measurements (Table 2.10) indicate that 80 to 89% of the plutonium in the spring water is in the Pu(V + VI) oxidation state. The total $^{239-240}Pu$ concentrations in these samples were much higher than our earlier measurements made by the iron hydroxide coprecipitation method. Also, Sample 1 contained approximately five times more $^{239-240}Pu$ than Sample 2 even though they were

Table 2.10. Oxidation States of $^{239-240}Pu$ Observed in N-Springs Water

Sample	Concentration (femtocurie/liter)		
	Pu(III + IV)	Pu(V +VI)	Total
1	11.6 ± 0.5 (11%)	90.3 ± 1.7 (89%)	101.9 ± 2.0
2	4.5 ± 1.1 (20%)	17.9 ± 1.0 (80%)	22.4 ± 1.3

collected only about one hour apart. The reason for this difference is not known, but further studies are in progress, including studies of the role of microparticulates which could act as carriers for plutonium in the groundwater.

REFERENCES

Allison, S. K. 1958. "Experimental Results in Charge-Changing Collisions of Hydrogen and Helium Atoms Ions at Kinetic Energies Above 0.3 keV." Rev. Mod. Phys. 30:1137-1168.

Appleby, A., and H. A. Schwarz. 1968. "Radical and Molecular Yields in Water Irradiated by γ-Rays and Heavy Ions." J. Phys. Chem. 73:1937-1941.

Bonson, T. F. M., and L. Vriens. 1970. "Angular Distribution of Electrons Ejected by Charged Particles. I. Ionization of He and H_2 by Protons." Physica 47:307-319.

Braby, L. A. 1977. "Experimental Methods for Use in Making Comparisons with Biophysical Models." In Part 4 of Pacific Northwest Laboratory Annual Report for 1976 to the ERDA Assistant Secretary for Environment, pp. 13-14. PNL-2100 PT4, Pacific Northwest Laboratory, Richland, Washington.

Braby, L. A., J. M. Nelson and W. C. Roesch. 1980a. "Comparison of Repair Rates Determined by Split-Dose and Dose-Rate Methods." Radiat. Res. 82:211-214.

Braby, L. A., J. M. Nelson and W. C. Roesch. 1980b. "Studies of Chlamydomonas reinhardi: Experimental." In Part 4 of Pacific Northwest Laboratory Annual Report for 1979 to the DOE Assistant Secretary for Enviroment, pp. 40-44. PNL-3300 PT4, Pacific Northwest Laboratory, Richland, Washington.

Braby, L. A., and W. C. Roesch. 1978a. "Direct Measurements of f(z) for Fast Electrons." In Sixth Symposium on Microdosimetry, eds. J. Booz and H. G. Ebert, pp. 251-260. Harwood Academic Publishers, London.

Braby, L. A., and W. C. Roesch. 1978b. "Testing of Dose-Rate Models with Chlamydomonas reinhardi." Radiat. Res. 76:259-270.

Briggs, J. S., and K. Taulbjerg. 1978. "Theory of Inelastic Atom-Atom Collisions." In Topics in Current Physics, Volume 5: Structure and Collisions of Ions and Atoms, ed. I. A. Sellin, pp. 105-154. Springer-Verlag, Berlin.

Burch, D., N. Stolterfoht, D. Schneider, H. Wieman and J. S. Risley. 1975. Nuclear Physics Laboratory Annual Report 1974. University of Washington, Seattle, Washington.

Chapman, J. D., P. Todd and J. Sturrock. 1970. "X-Ray Survival of Cultured Chinese Hamster Cells Resuming Growth After Plateau Phase." Radiat. Res. 42:590-600.

Drepper, F., and J. S. Briggs. 1976. "Double Differential Cross Sections for Electron-Loss in Ion-Atom Collisions." J. Phys. B 9:2063-2071.

Fisher, D. R., J. L. Daniel and G. F. Piepel. 1980. "Lung Tissue Modeling for Microdosimetry Application." In Part 4 of Pacific Northwest Laboratory Annual Report for 1979 to the DOE Assistant Secretary for Environment, p. 57. PNL-3300 PT4, Pacific Northwest Laboratory, Richland, Washington.

Fisher, D. R., and W. C. Roesch. 1980b. "The Microdosimetry of Plutonium in Beagle Dog Lung." In Seventh Symposium on Microdosimetry, Oxford, September 8-12, 1980.

Froese-Fisher, C. 1972. "A Multi-Configuration Hartree-Fock Program with Improved Stability." Comput. Phys. Commun. 4:107-116.

Hahn, G. M., and M. A. Bagshaw. 1966. "Serum Concentration: Effects on Cycle and X-Ray Sensitivity of Mammalian Cells." Science 151:459-461.

Inokuti, M. 1971. "Inelastic Collisions of Fast Charged Particles with Atoms and Molecules--The Bethe Theory Revisited." Rev. Mod. Phys. 43:297-347.

Kim, Y-K. 1975. "Energy Distribution of Secondary Electrons." Radiat. Res. 61:21-35.

Lajtha, L. G. 1963. "On the Concept of the Cell Cycle." J. Cell. Comp. Physiol. 62(supp. 1):143-145.

Lynch, D. J., L. H. Toburen and W. E. Wilson. 1976. "Electron Emission from Methane, Ammonia, Monomethylamine, and Dimethylamine by 0.25 to 2.0 MeV Protons." J. Chem. Phys. 64:4212-4221.

Magee, J. L., and J. J. Huang. 1972. "Triplet Formation in Ion Recombination in Spurs." J. Phys. Chem. 76:3801-3805.

Malcolm, A. W., and J. B. Little. 1979. "Rapid Recovery in Plateau Phase Mammalian Cells." Radiat. Res. 80:38-48.

Manson, S. T. 1972. "Inelastic Collisions of Fast Charged Particles with Atoms: Ionization of the Aluminum L Shell." Phys. Rev. 6:1013-1024.

Manson, S. T., L. H. Toburen, D. H. Madison and N. Stolterfoht. 1975. "Energy and Angular Distributions of Electrons Ejected from Helium by Fast Protons: Theory and Experiment." Phys. Rev. 12:60-78.

Miller, J. H., and M. L. West. 1977. "Quenching of Benzene Fluorescence in Pulsed Proton Irradiation: Dependence on Proton Energy." J. Chem. Phys. 67:2793-2797.

Miller, J. H., and M. L. West. 1980. "Inhomogeneous Kinetics in the Quenching of Prompt Radioluminescence: Analysis of Alpha Particle and Proton Induced Fluorescence Decay Curves." J. Chem. Phys. (In Press). PNL-SA-8263, Pacific Northwest Laboratory, Richland, Washington.

Mozumder, A., and J. L. Magee. 1966. "Model of the Tracks of Ionizing Radiation for Radical Reaction Mechanisms." Radiat. Res. 28:203-214.

Nelson, J. M. 1978. "Plateau Phase Chinese Hamster Ovary Cells." In Part 4 of Pacific Northwest Laboratory Annual Report for 1977 to the DOE Assistant Secretary for Environment, pp. 2.20-2.21. PNL-2500 PT4, Pacific Northwest Laboratory, Richland, Washington.

Nelson, J. M. 1979. "Noncycling Plateau Phase Mammalian Cells." In Part 4 of Pacific Northwest Laboratory Annual Report for 1978 to the DOE Assistant Secretary for Environment, pp. 2.29-2.31. PNL-2850 PT4, Pacific Northwest Laboratory, Richland, Washington.

Nelson, J. M., and L. A. Braby. 1980. "Induction and Repair of Radiation Injury in Plateau-Phase Mammalian Cells." In Part 4 of Pacific Northwest Laboratory Annual Report for 1979 to the DOE Assistant Secretary for Environment, pp. 39-42. PNL-3300 PT4, Pacific Northwest Laboratory, Richland, Washington.

Nelson, J. M., L. A. Braby and W. C. Roesch. 1979. "Rapid Repair Processes in Irradiated Chlamydomonas reinhardi." In Part 4 of Pacific Northwest Laboratory Annual Report for 1978 to the DOE Assistant Secretary for Environment, pp. 2.26-2.27. PNL-2850 PT4, Pacific Northwest Laboratory, Richland, Washington.

Nelson, J. M., L. A. Braby and W. C. Roesch. 1980. "Rapid Repair of Ionizing Radiation Injury in Chlamydomonas reinhardi." Radiat. Res. 83:279-289.

Roesch, W. C. 1977. "Microdosimetry of Internal Sources." Radiat. Res. 70:494-510.

Roesch, W. C. 1978. "Models of the Radiation Sensitivity of Mammalian Cells." In Third Symposium on Neutron Dosimetry in Biology and Medicine, eds. A. Burger and H. G. Ebert, pp. 1-27. Commission of the European Communities, Luxembourg.

Roesch, W. C., and L. A. Braby. 1980. "Microdosimetric Single-Event Densities." In Part 4 of Pacific Northwest Laboratory Annual Report for 1979 to the DOE Assistant Secretary for Environment, pp. 51-52. PNL-3300 PT4, Pacific Northwest Laboratory, Richland, Washington.

Roesch, W. C., L. A. Braby, and J. M. Nelson. 1980a. "Microdosimetry and Reproductive Survival of Cells." In Seventh Symposium on Microdosimetry, Oxford, September 8-12, 1980.

Roesch, W. C., L. A. Braby and J. M. Nelson. 1980b. "Studies of Chlamydomonas reinhardi: Theoretical." In Part 4 of Pacific Northwest Laboratory Annual Report for 1979 to the DOE Assistant Secretary for Environment, pp. 44-46. PNL-3300 PT4, Pacific Northwest Laboratory, Richland, Washington.

Roesch, W. C., and D. R. Fisher. 1980. "Microdosimetry of Alpha Particles in the Lung." Radiat. Res. 83:401.

Rzad, S. J. 1972. "Application of Charge Scavenging Kinetics to the Formation of Excited States in Irradiated Solutions of Aromatics in Cyclohexane." J. Phys. Chem. 76:3722-3729.

Samuel, A. H., and J. L. Magee. 1953. "Theory of Radiation Chemistry. II. Track Effects in the Radiolysis of Water." J. Chem. Phys. 20:1080-1087.

Sauer, M. C., K. H. Schmidt, E. J. Hart, C. A. Naleway and C. D. Jonah. 1977. "LET Dependence on Transient Yields in the Pulse Radiolysis of Aqueous Systems with Deuterons and Alpha Particles." Radiat. Res. 70:91-106.

Solterfoht, N. 1978. "Excitation in Energetic Ion-Atom Collisions Accompanied by Electron Emission." In Topics in Current Physics,Volume 5: Structure and Collisions of Ions and Atoms, ed. I. A. Sellin, pp. 158-199. Springer-Verlag, Berlin.

Stolterfoht, N., D. Schneider, D. Burch, H. Wieman and J. S. Risley. 1974. "Mechanisms for Electron Production in 30 MeV O^{n+} - O_2 Collisions." Phys. Rev. Lett. 33:59-62.

Toburen, L. H. 1979. "Differential Cross Sections for Electron Emission in Heavy Ion-Atom Collisions." IEEE Transactions on Nuclear Science NS-26:1056-1061.

Toburen, L. H., S. T. Manson and Y-K. Kim. 1978. "Energy Distribution of Secondary Electrons. III. Projectile Energy Dependence for Ionization of He, Ne, and Ar by Protons." Phys. Rev. A. 17:148-159.

Toburen, L. H., S. T. Manson and D. Schneider. 1980. "Autoionization in Heavy-Ion Collisions." In Part 4 of Pacific Northwest Laboratory Annual Report for 1979 to the DOE Assistant Secretary for Environment, p. 17. PNL-3300 PT4, Pacific Northwest Laboratory, Richland, Washington.

Toburen, L. H., and D. Schneider. 1979. "Angular Dependence of Autoionization Lines from Helium Excited by Cu^{3+} and I^{3+} Ion Impact." Bul. Am. Phys. Soc. 24:1179.

Toburen, L. H., and W. E. Wilson. 1977. "Energy and Angular Distributions of Electrons Ejected from Water Vapor by 0.3-1.5 MeV Protons." J. Chem. Phys. 66:5202-5213.

Toburen, L. H., and W. E. Wilson. 1979. "Differential Cross Sections for Ionization of Argon by 0.3-2 MeV He^{2+} and He^{+} Ions." Phys. Rev. A. 19:2214-2224.

Toburen, L. H., W. E. Wilson and R. J. Popowich. 1980. "Secondary Electron Emission and Ionization of Water Vapor by 0.3 to 2.0 MeV He^{+} and He^{2+} Ions." Radiat. Res. 82:27-44.

West, M. L. 1977. "Quenching of Benzene Fluorescence in Pulsed Proton Irradiation." J. Phys. Chem. 81:377-380.

West, M. L., and J. H. Miller. 1980a. "Quenching of Benzene Fluorescence in Pulsed Proton Irradiation: Concentration Dependence." Radiat. Res. 83:391.

West, M. L., and J. H. Miller. 1980b. "Radiation Quality Effects in the Quenching of Benzene Fluorescence in Pulsed Proton and Alpha Particle Irradiation." Chem. Phys. Lett. 71:110-112.

Wilson, W. E. 1978. "Analytical Expression for Cross Section Data." In Part 4 of Pacific Northwest Laboratory Annual Report for 1977 to the DOE Assistant Secretary for Environment, p. 2.7. PNL-2500 PT4, Pacific Northwest Laboratory, Richland, Washington.

Wilson, W. E., and H. G. Paretzke. 1980. "Calculation of Ionization Distributions in Small Sites." Radiat. Res 81:326-335.

Wilson, W. E., and L. H. Toburen. 1975. "Electron Emission from Proton-Hydrocarbon Molecule Collisions at 0.3-2.0 MeV." Phys. Rev. A. 11:1303-1308.

N. A. Wogman, R. W. Perkins, and J. H. Kaye. 1969. "An All Sodium-Iodide Anticoincidence Shielded Multidimensional Gamma-Ray Spectrometer for Low Activity Samples." Nucl. Instr. and Methods. 74:197-212.

N. A. Wogman. 1980a. "A Low-Background, Ge(Li) Gamma-Ray Spectrometer Shielded with a Multidimensional NaI(Tl) Crystal System." Physical Sciences. Part 4 of Pacific Northwest Laboratory Annual Report for 1979 to the DOE Assistant Secretary for Environment. PNL-3300 PT4, Pacific Northwest Laboratory, Richland, Washington.

N. A. Wogman. 1980b. "A Low-Background, Ge(Li) Gamma-Ray Spectrometer Shielded with a Low-Background, NaI(Tl) Anticoincidence Well Crystal." Physical Sciences. Part 4 of Pacific Northwest Laboratory Annual Report for 1979 to the DOE Assistant Secretary for Environment. PNL-3300 PT4, Pacific Northwest Laboratory, Richland, Washington.

N. A. Wogman. 1980c. "Design of an Intrinsic Germanium-Diode, Plastic-Phosphor, Anticoincidence-Shielded, Gamma-Ray Spectrometer Using Charoal Vacuum Pumping." Physical Sciences. Part 4 of Pacific Northwest Laboratory Annual Report for 1979 to the DOE Assistant Secretary for Environment. PNL-3300 PT4, Pacific Northwest Laboratory, Richland, Washington.

Wogman, N. A. and R. L. Brodzinski. 1973. "The Development of a High Sensitivity Beta-Gamma-Gamma Multidimensional Spectrometer." Nuclear Instr. and Methods. 109:277-283.

3 Geothermal

• Heavy-Metal and Noxious-Gas Emission from Geothermal Resource Development

Although geothermal energy is generally considered a relatively clean source of power, the high-temperature processes that create the hydrothermal provinces mobilize some undesirable constituents. In this section, we report on studies to characterize and compare effluents from a number of different geothermal sites and to determine pathways of constituents through geothermal power plants to the environs.

Characterization of Gases and Trace Elements in Lake County, California, Geothermal Well Effluents

D. E. Robertson, J. D. Ludwick, K. H. Abel, and C. L. Wilkerson

The Lake County, California side of The Geysers Known Geothermal Resource Area (KGRA) has shown great promise for extending the extractable energy resources from this unique area. Numerous dry steam wells have been drilled and several geothermal power plants are in construction or are on the drawing boards. Because the Lake County side of The Geysers KGRA is much more populated than the less developed Sonoma County side, the control of undesirable gases and trace elements in geothermal effluents is a critical issue. Since the steam from each individual geothermal well can have its unique chemical composition, it is imperative to carefully analyze in detail the gases and trace elements in effluents from each well.

To assist in the environmentally sound development of this resource, a cooperative study of two Lake County geothermal wells was conducted in January 1980. The Lake County Air Pollution Control District arranged with Aminoil USA and McCulloch Geothermal (now MCR Geothermal) for Pacific Northwest Laboratory (PNL) to sample during special flow tests at two of their steam wells for gases and trace elements of environmental concern. The results of these analyses are presented in Tables 3.1, 3.2 and 3.3. Table 3.1 presents the noncondensable gas concentrations measured by gas chromatography and mass spectrometry. As usual, carbon dioxide was the major noncondensable gas accounting for 70.4% to 74.7% by volume. The Francisco 1-5 well contained a relatively high concentration of hydrogen, averaging 17.8% by volume. Of special interest from an emissions concern is the detectable amounts of benzene present in the noncondensable gases, averaging 0.002% (20 ppm) by volume in the Francisco 1-5 well and occurring at 0.003% (30 ppm) by volume in the PDC-1 well. Further work should be conducted to verify the presence of benzene and to determine its partitioning between vapor and condensable phases.

Table 3.2 presents the concentrations of hydrogen sulfide, radon, mercury, and ammonia in the noncondensable gases. The hydrogen sulfide was measured on a real-time basis over periods of approximately 30 min by carefully diluting the noncondensable gases and passing the diluted gas through an Interscan H_2S analyzer at the optimum range for this instrument. The hydrogen sulfide concentrations were quite typical of levels measured in noncondensable gases from Sonoma County geothermal wells at The Geysers KGRA. Thus, careful abatement technology will be required to reduce the hydrogen sulfide emissions during the exploitation of this resource. The radon concentrations were also quite typical of other areas of The Geysers KGRA and should not represent any significant environmental concern. The mercury concentrations were likewise representative of the levels observed in noncondensable gases at the generating units in Sonoma County. Although the mercury concentrations were low, this toxic trace element has accumulated in soils around the generating units, and further research should be conducted to determine its environmental fate.

Table 3.1. Gas Chromatography-Mass Spectrometric Analysis of Noncondensable Gases in McCulloch's Francisco 1-5 and Aminoil's PDC-1 Geothermal Wells

January 22, 1980

	Francisco 1-5		PDC-1
	Percent (Volume)		
Constituent	Sample 1	Sample 2	Sample 1
Carbon dioxide	74.748	70.437	73.003
Hydrogen	17.429	18.173	7.739
Methane	5.314	5.652	11.536
Nitrogen	1.616	2.594	2.408
Hydrogen sulfide[a]	0.264[a]	2.462[a]	1.216[a]
Water	0.576	0.613	4.036
Argon	0.015	0.028	0.008
Oxygen	0.015	0.000	0.000
Benzene	0.001	0.003	0.003
	Parts-Per-Million (Volume)		
Carbon monoxide	ND (<10)	ND (<10)	ND (<10)
Ethane	270	277	296
Propane	75	77	136
Iso-Butane	3	2	5
n-Butane	22	21	52
Iso-Pentane	1	1	2
n-Pentane	1	1	2
C_6 Hydrocarbons and higher	4	5	16

[a]Hydrogen sulfide is not accurately measured by this technique due to degradation between sampling and storage. These values are residual amounts and are included only to give a volumetric balance. Separate accurate analyses of H_2S are provided elsewhere.

The gas/steam ratio is presented in Table 3.2. This is a very important measurement because it allows calculation of a total mass flow of constituents in the gaseous and condensable phases. The gas/steam ratios in these wells are very typical of the ratios observed in geothermal wells supplying steam to the generating units in Sonoma County.

Table 3.3 presents the concentrations of trace elements in the condensate phase from these two wells. Aside from moderate amounts of sulfide and ammonia, the steam condensates were rather pure solutions. A surprising observation was the very low (undetectable at <0.01 ppm) boron content of the PDC-1 condensate, which was atypical for The Geysers KGRA. However, boron was measured using two different plasma emission spectrometers on several different condensate samples collected throughout the flow test, so we are confident that the nondetectable boron was not due to analytical error. It is possible that some flow or temperature anomaly could have kept the boron from volatilizing with the steam.

In summary, the steam wells in Lake County appear to be quite typical of those in Sonoma County which supply steam to The Geysers generating units. Because Lake County is more populated, the developers will need to install effective hydrogen sulfide abatement systems and monitor the environment for the accumulation of mercury and boron.

Table 3.2. Noncondensable Gas Analyses of McCulloch's Francisco 1-5 and Aminoil's PDC-1 Geothermal Wells

January 22, 1980

	Francisco 1-5	PDC-1
Constituent	Concentration	
Hydrogen sulfide[a]	19900 ppm (volume)	14950 (volume)
Radon	3122 picocuries/liter	2790 picocuries/liter
Mercury	2.7 micrograms/liter	1.6 picocuries/liter
Ammonia	<0.7 micrograms/liter	<0.7 micrograms/liter
Gas/Steam Ratio (liters/kg)	4.84 liters/kg	5.18 liters/kg

[a]This concentration was measured on a real-time basis over a period of about 30 minutes and represents the average concentration for this period.

Table 3.3. Steam Condensate Analysis of McCulloch's Francisco 1-5 and Aminoil's PDC-1 Geothermal Wells

January 22, 1980

Constituent	Francisco 1-5	PDC-1
	Concentration	
pH	6.6	6.0
Eh	-19 mv.	+39 mw
	Parts-Per-Million (Weight)	
Sulfide	25.4	7.2
Ammonia	56.0	13.2
Fluoride	0.045	0.0063
Boron[a]	0.50; 0.53	<0.01; <0.1
Sulfate	1.0	<1.0
Chloride	<0.1	<0.1
Aluminum	<0.1	<0.1
Arsenic	<0.01	<0.01
Barium	<0.01	<0.01
Calcium	<0.1	<0.1
Iron	0.10	<0.1
Lithium	<0.05	<0.05
Magnesium	<0.05	<0.05
Mercury	0.0057	0.0011
Sodium	8.0	<5.0
Phosphorus	<0.05	<0.5
Silicon	5.3	<0.1
Strontium	<0.01	<0.01
Silver	<0.01	<0.01
Cadmium	<0.01	<0.01
Cobalt	<0.01	<0.01
Chromium	<0.01	<0.01
Copper	<0.01	<0.01
Manganese	<0.01	<0.01
Molybdenum	<0.1	<0.1
Nickel	<0.01	<0.01
Lead	<0.1	<0.1
Antimony	<0.05	<0.05
Selenium	<0.2	<0.2
Tin	<0.1	<0.1
Thorium	<0.1	<0.1
Titanium	<0.05	<0.05
Thallium	<0.1	<0.1
Uranium	<0.05	<0.05
Zinc	<0.05	0.07
Zirconium	<0.05	<0.05

[a] Boron was measured by plasma emission spectroscopy on two different instruments. The values are much lower than for other steam condensates we have measured at other locations at The Geysers.

Emissions Studies at The Geysers Unit 15 Geothermal Power Plant

D. E. Robertson, J. D. Ludwick, K. H. Abel, and C. L. Wilkerson

The Geysers, California, Unit 15, a new 100 MWe geothermal power plant, contains state-of-the-art technology for pollutant abatement which greatly reduces the emissions of hydrogen sulfide, mercury, and other geothermal pollutants. The principal abatement system at Unit 15 is the Stretford plant, which removes hydrogen sulfide from the noncondensable gases by catalytic oxidation to elemental sulfur. The Stretford plant also appears to be effective in removing other gaseous pollutants, such as mercury. Therefore, it is of interest to determine the pathways of geothermal steam constituents through such a modern facility and to identify the emission routes to the environment.

In June 1979 and January 1980, studies were conducted at Unit 15 to determine the flow pathways of steam impurities through the plant. The results of these investigations are summarized in Tables 3.4, 3.5, and 3.6.

Table 3.4 presents the noncondensable gas composition of incoming steam as measured by gas chromatography and mass spectrometry. A large difference in major gas constituents was observed between gas samples analyzed from the June 1979 and January 1980 collections. The difference is due to the unusually high concentrations of hydrogen and methane in the January 1980 samples, which are representative of the highest range for these gas constituents at The Geysers. This could be the result of using a different combination of steam supply wells or it could reflect changes in the reservoir degassing characteristics.

Hydrogen sulfide is not accurately measured in these samples by this technique because of degradation between sampling and storage. The values in Table 3.4 are residual amounts and are included only to give a volumetric balance. Accurate hydrogen sulfide measurements are presented in Table 3.5. The hydrogen sulfide measurements in the noncondensable gases entering and exiting the Stretford plant indicate that the plant is removing H_2S with a greater than 99.95% efficiency (Table 3.5). The mercury vapor is also being removed by the plant condensers. The mercury vapor concentrations in the incoming steam were 2.2 and 3.8 µg/ℓ in June 1979 and January 1980, respectively, but the gases exiting

Table 3.4. Gas Chromatographic and Mass Spectrometric Analysis of Noncondensable Gases in Incoming Steam at Unit 15, The Geysers

Constituent	June 15, 1979	January 21, 1980
	Percent (Volume)	
Carbon dioxide	61.216	36.972
Hydrogen	25.301	37.576
Methane	6.623	17.409
Nitrogen	0.187	7.212
Hydrogen sulfide[a]	4.238	0.000
Water	0.403	0.576
Oxygen	0.000	0.122
Argon	0.011	0.096
Benzene	0.004	<0.0005
Toluene	0.001	0.000
Carbon monoxide	<0.001	0.000
	ppm (Volume)	
Ethane	117	278
Propane	28	63
Isobutane	1	2
n-butane	6	15
Isopentane	1	1
n-pentane	1	1
C_6 hydrocarbons & higher	6	6
Gas/steam (liters/kg)	2.58	1.93

[a] Hydrogen sulfide is not accurately measured by this technique because of degradation between sampling and storage. This value is a residual amount and is included only to give a volumetric balance. Separate accurate hydrogen sulfide analyses are included in Table 3.2.

the plant condensers and going to the Stretford plant contained undetectable amounts (<0.1 to <0.01 µg/ℓ) of mercury. Much of the mercury is being lost somewhere in the turbine-condenser system since the mercury concentrations in condensate from the units' condensers are also relatively low.

The overall success of the hydrogen sulfide abatement at Unit 15 depends upon the degree of partitioning between noncondensable gas and condensate phases in the unit's surface condenser. The more hydrogen sulfide that can be kept in the noncondensable gas phase after the steam condensation process, the more is available for removal to the Stretford plant. The Unit 15 condensers have not operated up to expectations. In June 1979, 65% of the H_2S remained in the gas phase, and in January 1980, only 52% left the condensers as noncondensable gases.

Table 3.6 presents the concentrations of a number of constituents of environmental concern in steam condensate from Unit 15. The concentrations of these constituents changed very little between June 1979 and January 1980. The $S^=$ concentration in the cooling tower inlet water (1.17 mg/ℓ) was about tenfold higher than the cooling tower blowdown sampled at the bottom of the tower. This indicates that approximately 90% of the H_2S entering the cooling tower is volatilized and emitted in the cooling tower exhaust. The nonvolatile constituents F^-, B, and As have approximately the same concentrations in cooling tower inlet and blowdown waters. It was surprising

Table 3.5. Hydrogen Sulfide and Mercury Vapor in Noncondensable Gases at Unit 15, The Geysers

Constituent	June 15, 1979	January 21, 1980
Hydrogen sulfide (ppm_v) --incoming steam	49,700[a]	23,100[b]
Hydrogen sulfide (ppm_v) --after Unit 15 condenser	24,900	21,000
Hydrogen sulfide (ppm_v) --exit gas from Stretford plant	10.5 (99.96% removal)	10 (99.95% removal)
Mercury (µg/l) --incoming steam	2.20	3.8
Mercury (µg/l) --into Stretford plant	<0.01	<0.1

[a] PNL glass condenser.
[b] PG&E stainless steel sampling condenser at Unit 15.

Table 3.6. Elemental Constituents of Environmental Concern in Geothermal Steam Condensate and Cooling Tower Waters at The Geysers Unit 15

	Steam Condensate		Cooling Tower Inlet		Cooling Tower Blowdown	
	June, 1979	Jan., 1980	June, 1979	Jan., 1980	June, 1979	Jan., 1980
pH	8.6	8.9	----	8.25	8.0	8.1
Eh	-235	-113	----	+33	+140	+140
$S^=$ (ppm)	49.5	54.0	----	1.17	0.13	0.12
F^- (ppm)	<0.003	<0.1	----	0.030	0.06	0.032
As (ppm)	0.065	<0.1	----	0.20	0.53	0.30
B (ppm)	30	35.8	----	127	124	126
NH_3 (ppm)	118	122	----	51.9	37.8	50.4
Hg (ppm)	0.0147	0.0144	0.0128	0.0056	0.0041	0.0062

that the NH_3 and mercury concentrations in the January 1980 cooling tower inlet water were approximately the same as the blowdown, indicating little volatilization in the cooling tower. In June 1979, the mercury behaved normally and was threefold lower in blowdown compared to the inlet, indicating that approximately 68% of the mercury entering the tower was vaporized to the atmosphere.

Cooling Tower Emission Studies at The Geysers Unit 15 Geothermal Power Plant

D. E. Robertson, J. D. Ludwick, K. H. Abel
C. L. Wilkerson

In modern, well-abated geothermal power plants such as Unit 15 at The Geysers, California, the most important route to the environs for the emission of undesirable steam impurities is via the cooling tower exhaust. These emissions may leave the cooling tower stacks as a vapor or as liquid drift droplets which become entrained in the air flow. The quantification of these emissions is an extremely difficult task because of the nonuniform air flow and cross-sectional distribution of gases and trace elements contained in the exhaust air of each stack.

In January, 1980 a cooperative study was conducted with Pacific Gas and Electric Company (PG&E) at the Unit 15 cooling tower to study the emissions of hydrogen sufide, mercury and ammonia, and to characterize the air flow and temperature profiles across individual stacks. In addition, PG&E measured the drift droplet size using a laser droplet size instrument.

A special scaffolding and instrument support beam, developed by PG&E, was used to make sampling traverses across the top of several stacks in north-south and east-west directions. Twelve equal area measurement stations were located along each traverse, as shown in Figure 3.1. A schematic diagram of the instrument support beam and the location of monitoring instruments and sampling lines above the top of the fan stack is shown in Figure 3.2. Simultaneous real-time measurements of H_2S concentrations were made at each station by both PNL and PG&E using Interscan® H_2S analyzers. In addition, grab samples of exhaust air for mercury and ammonia measurements were taken by PNL, and PG&E monitored the drift droplet size and collected drift droplets for boron analyses. Because of space restrictions on the sampling beam, only the PG&E anemometer and temperature probes were used to monitor air velocity and wet/dry temperatures directly above the stack.

The results of measurements made above Stack #4 on the Unit 15 cooling tower are presented in Table 3.7. These data illustrate the large variability in cross-sectional distribution of the hydrogen sulfide concentrations, of the air velocity, and of the temperature. Normally, the highest hydrogen sulfide concentrations are found near the outside rim of each cooling tower stack where the upward air velocity is decreased. The hydrogen sulfide concentrations gradually decrease towards the center of the stack. Between 2 to 6 feet from the edge, the air velocity reaches a maximum and then becomes negative at the center because of down-drafting. Thus, in order to determine emission rates of volatile constituents or drift droplets from each stack, it is necessary to divide the

® Registered trademark of Interscan Corporation.

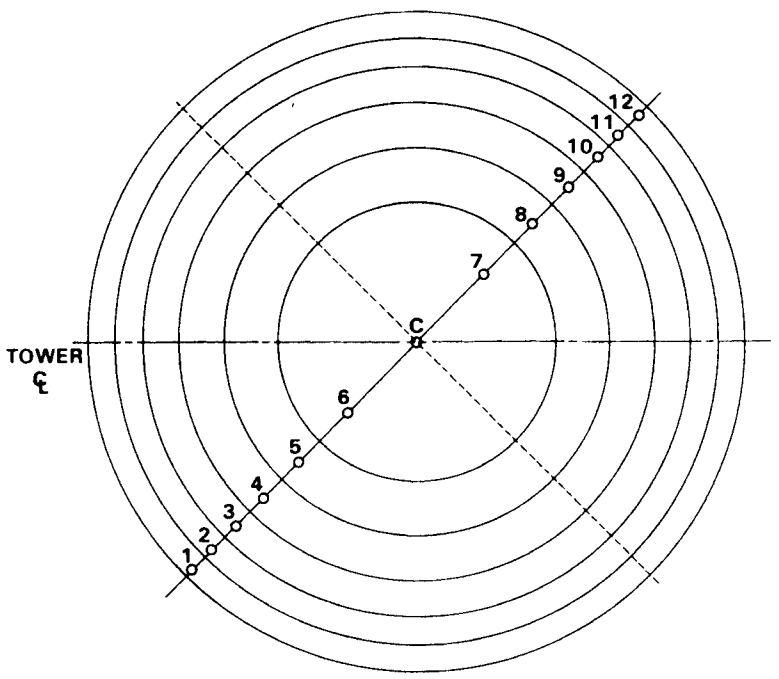

STATION	DISTANCE FROM RIM (FT)
1	0.67
2	2.10
3	3.71
4	5.57
5	7.85
6	11.17
CENTER	15.71
7	20.25
8	23.57
9	25.85
10	27.71
11	29.32
12	30.75

DIAMETER = 31.41 FEET

NOTE:
CENTER STATION IS NOT ONE OF THE EQUAL AREAS

Figure 3.1. Equal Area Measurement Stations for The Geysers Unit 15 Cooling Tower

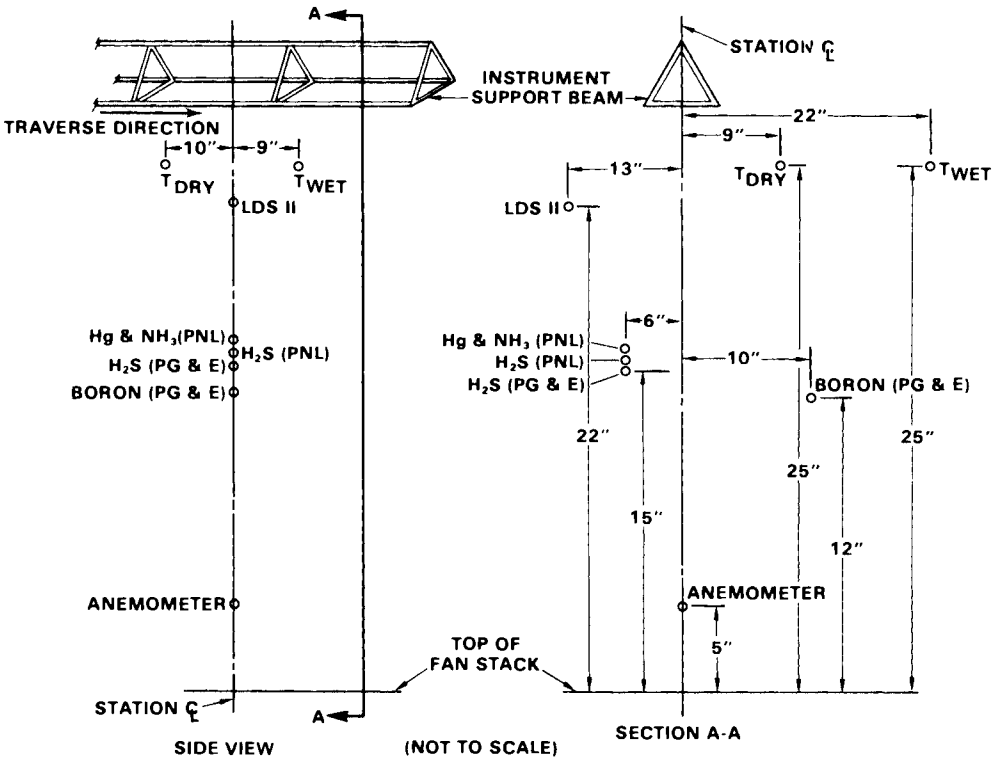

Figure 3.2. Instrument Support Beam and Location of Instruments and Sampling Lines Above the Top of the Fan Stack

Table 3.7. Unit 15 Cooling Tower Stack 4 Exit Air Measurements

Tested January 24, 1980

Traverse No. 1 (North to South)

Station	Time	PNL H_2S (ppm)	PG&E H_2S (ppm)	Hg (ng/1)	NH_3 (ug/1)	Air Velocity (m/s)	T_{Dry} (°C)	T/V Corr.	T_{Wet} (°C)
1	1328-1347	5.0	7.4	1.13		5.4	36.7	.88	36.6
2	1348-1357	3.7	5.6			10.2	36.8	.88	35.8
3	1358-1409	2.1	3.6		<60	10.5	36.0	.88	34.7
4	1409-1419	0.90	1.4		<60	10.8	33.8	.89	32.3
5	1424-1435	0.40	0.5			7.5	29.9	.90	29.7
6	1436-1442	0.25	0.2			0	28.2	---	28.2
Center	1443-1449	0.15	0.2			-2.4	27.9	---	27.9
7	1449-1455	0.10	0.1			-2.1	27.8	---	27.7
8	1456-1503	0.10	0.1			3.6	27.9	.90	27.9
9	1504-1518	0.20	0.2	0.16		9.0	29.8	.90	29.8
10	1518-1530	1.0	1.1			11.1	31.5	.90	31.5
11	1530-1540	3.0	3.0	0.033		10.8	35.9	.88	35.9
12	1540-1550	5.0	5.4			10.2	36.5	.88	36.5

Traverse No. 2 (West to East)

Station	Time	PNL H_2S (ppm)	PG&E H_2S (ppm)	Hg (ng/l)	NH_3 (ug/l)	Air Velocity (m/s)	T_{Dry} (°C)	T_{Wet} (°C)	STD. T. T/V Corr.
1	1009-1019	1.6	1.7			6.0	31.6	31.6	=.90
2	1021-1031	1.6	1.1			11.1	31.8	31.8	=.90
3	1032-1042	0.50	0.5	0.38	<60	10.8	30.5	29.5	=.90
4	1046-1056	0.10	0	0.35	<60	10.5	28.9	27.5	=.90
5	1100-1110	0.05	0			7.5	26.1	26.0	=.91
6	1111-1128	0.05	0			0	26.1	26.0	---
Center	1129-1135	0.10	0.1			-2.4	26.7	26.7	---
7	1136-1141	0.10	0			-2.4	26.9	26.9	---
8	1142-1153	0.10	0			3.6	26.4	26.1	=.91
9	1155-1208	0.05	0			9.6	26.8	26.3	=.91
10	1211-1225	0.10	0.2	0.39	<60	11.4	28.2	26.8	=.91
11	1225-1235	0.40	0.6	0.76		10.8	28.8	28.8	=.90
12	1235-1252	1.0	1.5			9.0	31.2	31.2	=.90

stack into a sufficient number of cross-sectional sectors to adequately characterize the total emission rates. When Stack 4 on the Unit 15 cooling tower is divided into four cross-sectional sectors (N, S, E and W) and each sector is divided into five equal-area stations where positive air velocities and hydrogen sulfide measurements are taken, then the stack can be divided into 20 separate areas each having its own characteristic emission rate. These areas can be integrated to give a total stack emission rate. This total amounted to 3.9 kg/hr of H_2S for Stack #4. Unit 15 has five stacks and if Stack #4 is fairly representative of the rest, then approximately 19.5 kg/hr of H_2S is emitted from the Unit 15 cooling tower stacks.

4 Oil Shale

• Oil Shale and Tar Sand Research

Oil shale and tar sand in the United States represent a potential supply of nearly one trillion barrels of crude oil for the country's future use. The renewed commercial interest in developing these reserves has increased the need for studies that would help developers assure that conversion processes are carried out in an environmentally acceptable manner. A vital part of this environmental research program is the physical and chemical characterization of the effluents from the various proposed conversion schemes. Characterization studies are important and should begin at an early stage of development, preferably at the pilot plant or semiworks stage. Because of the complex nature of the effluents, new sampling, analysis, and chemical separation procedures have had to be developed. In this section, new and improved techniques for organic, inorganic, and speciation analysis are presented with applications for oil shale research. Also reported is the progress of a program to provide representative and well-characterized fossil-fuel samples for environmental and health effects studies and for interlaboratory comparisons to ensure accuracy of the data.

Organic and Mutagenic Analyses of Shale Oil Waters

A. P. Toste, D. S. Sklarew and R. A. Pelroy

Contamination of natural groundwaters by the organic species in shale oil and/or the product waters associated with shale oil retorting constitutes a potential health and environmental hazard. The objective of this program is to identify potential environmental pollutants in product waters and aqueous extracts of shale oil.

Extracting organics from the shale oil product waters poses an analytical challenge. The waters are heterogeneous, both organically and inorganically. Three different methods for concentrating organics from aqueous samples have been compared:

1. solvent extraction with methylene chloride, chloroform, and hexane; with and without pH adjustment of the water to facilitate extraction of acidic and basic (pH 8.3 and pH 3) organics;
2. partition chromatography on XAD-4 resin followed by elution with methylene chloride; the water was chromatographed at its natural pH of ~8.3 and also adjusted to pH 3 to enhance the concentration of acidic species; and
3. partition chromatography on a C_{18}-reverse phase cartridge at pH 8.3 and pH 3 followed by elution with methanol and/or methylene chloride.

Specifically, each of these procedures was tested for concentrating the organics from Paraho product water separated from shale oil storage tanks.

The three concentration procedures have been chemically evaluated by normal phase, adsorption high-performance liquid chromatography (HPLC) using an NH_2 column with a 3-solvent, gradient mobile phase system (Figure 4.1). Hexane flows isocratically at 5 ml/min for the first 5 min followed by a linear gradient to 100% CH_2Cl_2 for 10 min; 100% CH_2Cl_2 isocratically for 5 min followed by a linear gradient to 100% iPrOH for 10 min; finally 100% iPrOH for 5 min. The NH_2 column is then reconditioned by cycling back to the first solvent, hexane. With the shale oils, three distinct regions of polarity are generally observed: nonpolar, moderately polar, and polar. Quite a variety of standards have been chromatographed on the NH_2 column (Figure 4.1). Hydrocarbon and polycyclic aromatic hydrocarbon (PAH) standards elute in the nonpolar region, as well as some nonpolar heterocyclics. The moderately polar region contains nitrogen heterocyclics, aromatic amines, and aza aromatic amines, as well as their alkylated analogs.

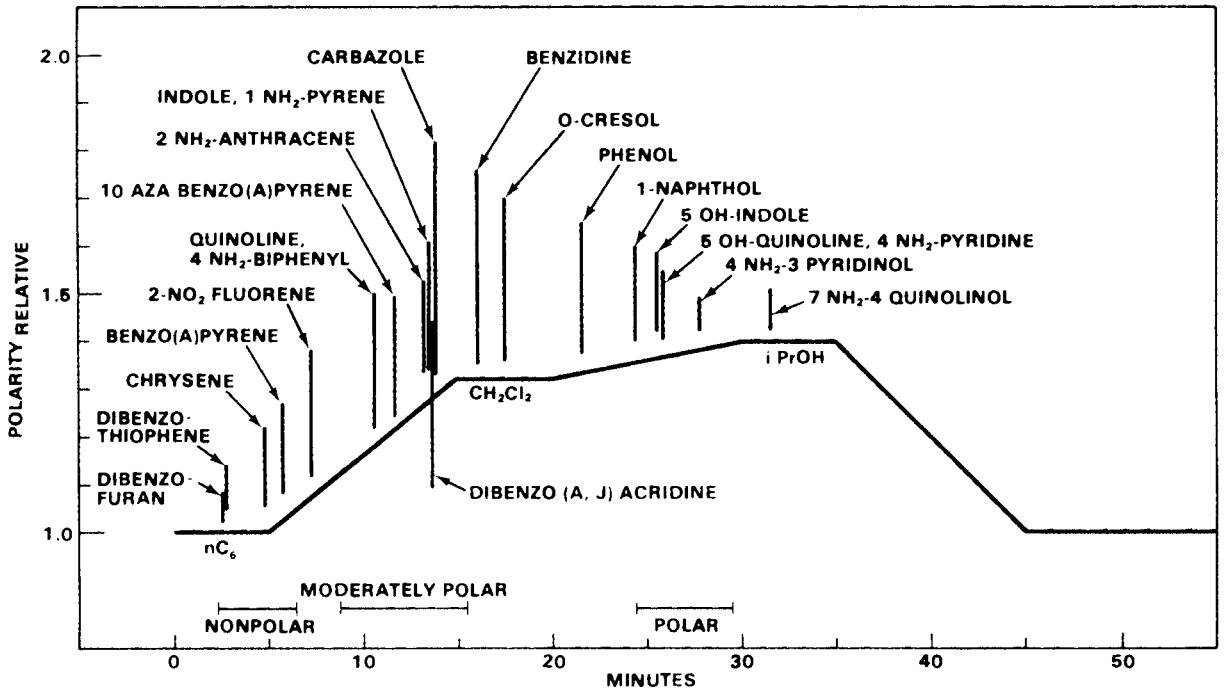

Figure 4.1. HPLC of Standards on a Normal Phase -NH_2 Column

The polar region contains phenols, and hydroxylated and mixed-function heterocyclics, such as amino pyridinol.

The HPLC chromatograms of the organic extracts for the Paraho product water were nearly identical for all three procedures, strongly suggesting that they yield chemically equivalent results. The only difference of any note is that methylene chloride solvent extraction of the water or the "organic-loaded" C_{18}-cartridge yields an extract enriched in moderately polar material, whereas methanol extraction yields more complete extraction with an extract containing moderately polar species but mainly enriched for polar species.

The three concentration procedures have also been evaluated biologically using the standard Ames bioassay with the TA98 strain of Salmonella typhimurium and the S9 fraction from rat liver for metabolic activation. Preliminary results of this study are listed in Table 4.1. The data suggest that basic solvent extraction and the C_{18}-partition chromatography concentrate organic fractions with similar mutagenicities. The acidic solvent extract (after basic solvent extraction of the sample) appeared to be nonmutagenic; the XAD-4 extract was only weakly mutagenic. The mildness and ease of the C_{18}-partition concentration, combined with the high recovery of mutagenic activity, make it the concentration procedure of choice for aqueous samples.

Paraho Product Water: The results of the HPLC analyses and Ames bioassay of the C_{18}-cartridge methanol extract of the Paraho product water are summarized in Figure 4.2. No chemical species appeared in the nonpolar region of the HPLC-UV chromatogram; a small amount appeared in the moderately polar region; and most of the sample chromatographed as a complex envelope in the polar region (HPLC fraction 9). Virtually all of the mutagenic activity appeared in the polar region (HPLC fraction 9) confirming that the mutagens of the Paraho product water are highly polar.

Aqueous Extract of Paraho Shale Oil: Contact of natural groundwaters with shale oil could lead to their extensive contamination by hazardous organic species. To test this possibility, the Paraho shale oil was extracted with deionized, filter-purified water in an attempt to assess any potential problems resulting from contact of natural groundwaters with shale oil. The yield of the water-extracted organic residue was ~1.4% by weight. Both the

Table 4.1. Mutagenic Activities of Organic Concentrates from Paraho Product Water

Material	Specific Activity (rev/μg)
Basic solvent extract	2.6
XAD-4 (acidic and basic combined)	0.68
C_{18} Cartridge	2-4

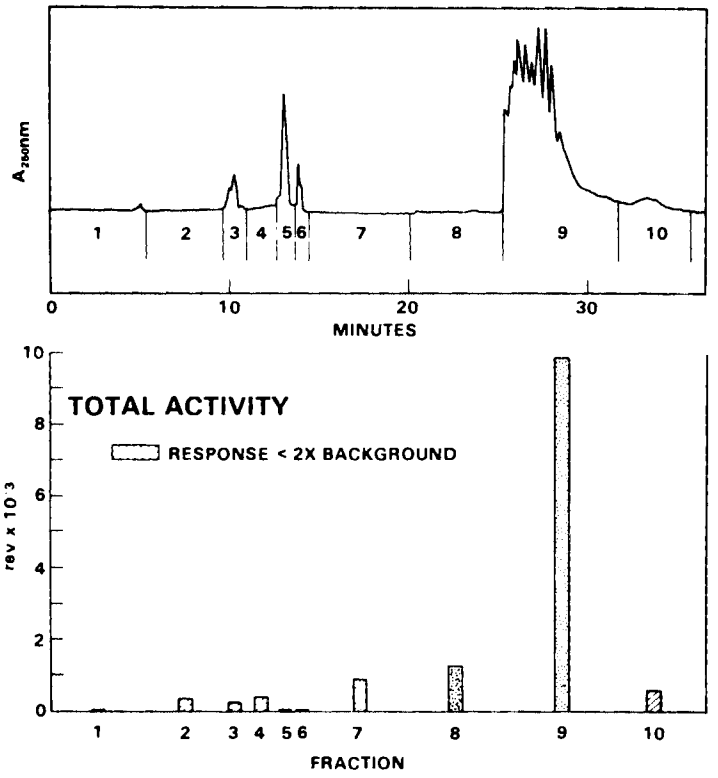

Figure 4.2. HPLC of Organics from Paraho Product Water on an NH_2 Column after C_{18}-partition Chromatography with Methanol

extracted shale oil and the concentrated aqueous extract were fractionated by Sephadex LH-20 chromatography followed by HPLC. Approximately half of the water extract eluted in the methanol fraction. Figure 4.3 illustrates the HPLC chromatograms of the LH-20 methanol fractions of the extracted shale oil, the aqueous extract, and the crude (unextracted) shale oil. The HPLC chromatograms of the two oil samples are quite similar; the aqueous extract is enriched in the polar region (22 to 30 min). Preliminary Ames assay data (Table 4.2) indicate that the mutagenic activity of the oil remains unchanged after water extraction (~11 rev/μg for the methanol fraction, 0.8 rev/μg for the toluene/hexane fraction). However, the water does accumulate mutagenic activity (2.4 rev/μg in the LH-20 methanol fraction) even during its limited contact time with the oil. Assuming additivity of mutagenic activities, the recovery of mutagens in the water-extracted organics residue was approximately 4% of the total mutagenic activity of the (unextracted) crude oil (Table 4.2). Finally, the specific activity of the aqueous extract is nearly identical to those of the organic extracts of the Paraho product water (Table 4.1).

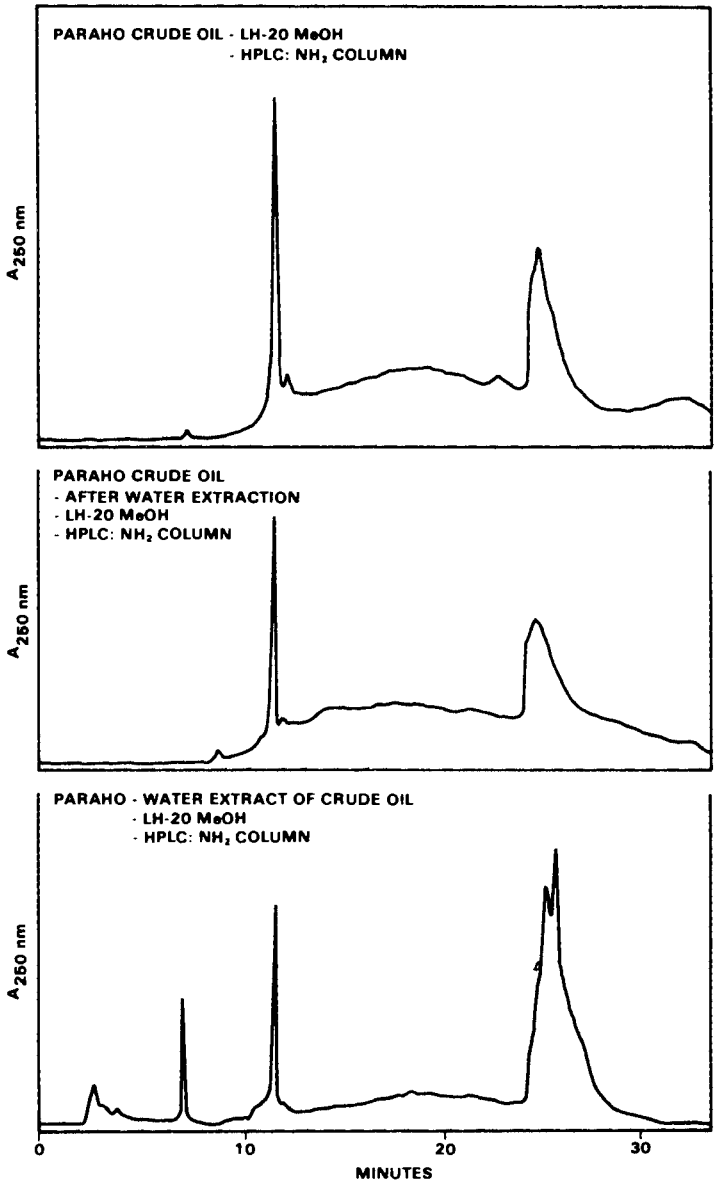

Figure 4.3. Aqueous Extraction of Paraho Shale Oil: HPLC Analysis of the Organics on an NH_2 Column

Table 4.2. Water Extraction of Paraho Shale Oil

LH-20 MeOH Fraction	Specific Activity[1]	Weight %[2]	Weighted Activity[3]	Recovery[4]
Crude Shale Oil	10.00	4.7	0.47	100
Extracted Shale Oil	11.56	3.7	0.43	91
Water Extract	2.36	0.7	0.02	4

[1]Rev/μg MeOH Fraction
[2]Weight % of Crude Shale Oil
[3]Specific Activity x Weight % (Rev/μg crude shale oil)
[4]Weighted Activity Material/Weighted Activity Crude

Trace Element Variations in Oil Shale Core Samples From Piceance Creek Basin

C. L. Wilkerson

It is important that major oil shale reserves be evaluated for trace element abundance variations as a function of location and depth. These source term evaluations can then be used to help assess the potential environmental implications of specific sites within the oil shale region.

To investigate elemental abundance variations in Colorado's Piceance Creek Basin, oil shale core samples were obtained from a peripheral and central basin location. The peripheral samples were obtained in Garfield County at Occidental Petroleum's Logan Wash facilities; the central basin samples were obtained in Rio Blanco County at the C-b federal lease tract.

Drill core samples were jaw crushed, split, and then ground with an Al_2O_3 jar-mill to pass a 140 mesh sieve. These procedures were carefully evaluated and found to be noncontaminating. The prepared samples were analyzed for 43 elements by a combination of instrumental neutron activation analysis (INAA) and energy dispersive x-ray fluorescence analysis (XRF). In addition, the element mercury was determined by a highly sensitive technique which employs thermal oxidation at 1000°C, gold-amalgamation, and cold-vapor atomic absorption spectrometry (CVAA). The possible loss of mercury by grinding was investigated by separately analyzing jar-mill ground, hand-ground, and orginal crushed samples from the peripheral LW-106 core. No mercury losses were observed for our laboratory grinding procedures.

The resulting abundance analyses for the various core samples are given in Table 4.3. The trace metals arsenic, cobalt, copper, mercury, molybdenum, iron, antimony, selenium, uranium, and zinc correlated with the oil yield and the sulfur content of the shale. Most of these elements are believed to be associated with sulfide mineral constituents. For core samples of equivalent oil yield, the elemental abundance concentrations are rather constant (within factors of 2 to 3) regardless of origin for a given technology, the increased levels of chalcophile elements

Table 4.3. Elemental Abundance of Colorado Oil Shale Core Samples

	Major Elements (%)									Trace Elements (ppm)					
Core Sample	Al	Ca	Fe	K	Mg	Na	S	Si	Ti	As	Ba	Br	Ce	Co	Cr
Rio Blanco Co., Tract C-b Core 33X-1, 1352.6-1352.8' 51.9 gal/ton[a]	2.93	6.0	2.39	1.0	1.7	1.37	1.91	11.8	0.17	116	360	1	38	13.1	36
Rio Blanco Co., Tract C-b Core 33X-1, 1189.0-1189.2' 15.1 gal/ton[b]	2.56	19.1	1.41	0.72	3.8	1.30	0.53	10.0	0.18	31	470	<1	26	5.3	24
Rio Blanco Co., Tract C-b Core 32X-12, 1891.8-1892.2' "Lean"	4.67	6.8	2.33	1.6	2.6	2.21	0.78	17.1	0.20	35	320	<1	41	11.0	45
Rio Blanco Co., Tract C-b Core 32X-12, 1452.6-1452.8' "Rich"	3.30	16.2	2.14	1.5	2.2	1.77	0.98	9.9	0.17	45	820	<1	38	12.0	33
Garfield Co., Logan Wash LW-106, 952-953' 15.0 gal/ton	4.89	7.6	1.42	1.4	3.0	2.12	0.36	18.9	0.13	29	420	<1	44	5.3	27
Garfield Co., Logan Wash LW-106, 997-998' 41.6 gal/ton	3.16	8.7	2.21	2.3	4.0	0.88	1.30	11.6	0.16	43	500	<1	35	11.4	30
Garfield Co., Logan Wash Sample of Oxy Mine Drift "Lean"	3.84	10.1	1.63	2.6	6.8	0.58	<0.2	15.1	0.21	13	430	<1	39	5.3	32

Table 4.3. Elemental Abundance of Colorado Oil Shale Core Samples (continued)

Core Sample	Trace Elements (ppm)														
	Cs	Cu	Dy	Eu	Ga	Hf	Hg	La	Lu	Mn	Mo	Nb	Nd	Ni	Pb
Rio Blanco Co., Tract C-b Core 33X-1, 1352.6-1352.8' 51.9 gal/ton[a]	4.7	69	1.8	0.52	8.9	1.7	0.18	20.3	0.16	270	35	6.0	19	33	65
Rio Blanco Co., Tract C-b Core 33X-1, 1189.0-1189.2' 15.1 gal/ton[b]	5.7	24	1.6	0.39	7.0	1.4	0.055	13.4	0.11	330	6.8	3.3	12	19	11
Rio Blanco Co., Tract C-b Core 32X-12, 1891.8-1892.2' "Lean"	1.4	44	2.4	0.60	13	1.8	0.078	21.7	0.19	290	18	8.1	15	33	27
Rio Blanco Co., Tract C-b Core 32X-12, 1452.6-1452.8' "Rich"	5.3	74	1.8	0.57	9.1	1.4	0.11	19.5	0.25	240	47	4.3	19	37	32
Garfield Co., Logan Wash LW-106, 952-953' 15.0 gal/ton	4.3	25	1.7	0.46	12	3.1	0.066	25.4	0.14	250	24	4.9	14	24	26
Garfield Co., Logan Wash LW-106, 997-998' 41.6 gal/ton	3.7	54	1.9	0.46	7.9	1.5	0.12	18.6	0.15	270	35	4.9	14	31	38
Garfield Co., Logan Wash Sample of Oxy Mine Drift "Lean"	3.4	21	2.8	0.55	11	2.5	0.044	19.5	0.19	370	5.9	6.9	16	15	9

Core Sample	Trace Elements (ppm)													
	Rb	Sb	Sc	Se	Sm	Sr	Ta	Tb	Th	U	V	Y	Yb	Zn
Rio Blanco Co., Tract C-b Core 33X-1, 1352.6-1352.8' 51.9 gal/ton[a]	63	4.0	5.4	5.4	2.9	350	0.46	0.32	5.5	7.6	120	10	1.1	107
Rio Blanco Co., Tract C-b Core 33X-1, 1189.0-1189.2' 15.1 gal/ton[b]	41	0.9	3.8	3.0	2.0	1120	0.37	0.27	3.8	2.9	52	7.1	0.8	52
Rio Blanco Co., Tract C-b Core 32X-12, 1891.8-1892.2' "Lean"	65	2.0	6.6	1.8	3.0	460	0.57	0.37	5.1	3.2	110	12	1.3	79
Rio Blanco Co., Tract C-b Core 32X-12, 1452.6-1452.8' "Rich"	58	3.3	6.3	3.8	2.9	1590	0.48	0.38	6.9	10.5	93	11	1.6	82
Garfield Co., Logan Wash LW-106, 952-953' 15.0 gal/ton	62	1.3	3.4	1.3	2.5	630	0.58	0.28	6.4	4.8	52	9.2	0.9	57
Garfield Co., Logan Wash LW-106, 997-998' 41.6 gal/ton	78	1.5	4.6	2.3	2.7	740	0.46	0.32	5.5	6.5	98	8.3	1.0	67
Garfield Co., Logan Wash Sample of Oxy Mine Drift "Lean"	88	1.0	6.2	1.0	2.9	610	0.64	0.41	4.6	4.1	80	12	1.3	56

[a]Fischer Assay of 1352-1354' Interval
[b]Fischer Assay of 1188-1190' Interval

in "rich" oil shales represent a larger potential environmental impact per ton of shale retorted; however, impacts assessed on a per barrel of oil basis are not expected to be significantly different with respect to location.

Fossil Fuel Research Materials

J. S. Fruchter

The purpose of the fossil fuel research materials program is to obtain, store, prepare, and distribute homogeneous and chemically analyzed synthetic fossil fuel samples for characterization, environmental, and health effects studies. A number of samples from oil shale retorts and coal conversion processes that are available in our refrigerated repository were listed in last year's Pacific Northwest Laboratory (PNL) annual report. These, plus those added in this year's work, are listed in Table 4.4. The major new additions to the repository during this past year include both raw and spent shale cores from Occidental's Oil Shale Logan Wash Retort 3E, at Logan Wash, Colorado, and a variety of materials from both the solvent refined coal (SRC) II and I processes. The samples from the Occidental Oil Shale Logan Wash site include two spent shale cores

Table 4.4. Currently Available Fossil Fuel Reference Materials

1. Solvent Refined Coal Process-I
   a. Solvent refined coal
   b. Mineral residue
   c. Light oil (naphtha)
   d. Recycle solvent
   e. Wash solvent
2. Lawrence Livermore 125-kg Retort
   a. Mahogany Zone raw shale (24 gal/ton)
   b. Spent shale (Run S-11)
3. Lawrence Livermore 7-T Retort
   a. Spent shale (Run L-1)
   b. Crude shale oil (Run L-1)
   c. Process water (Run L-1)
4. Vernal, Utah In Situ
   a. Process water
   b. Crude shale oil
5. Crude Petroleums
   a. Wilmington (high N)
   b. Gato Ridge (high metals, high N, high S)
   c. Prudhoe Bay
6. Paraho Semiworks Retort[a]
   a. Raw shale
   b. Retorted shale
   c. Crude shale
   d. Product water
   e. Raw shale crushing fines from filter baghouse
   f. Retorted shale fines from filter baghouse
7. CO_2 Acceptor
   a. Ash
   b. Spent acceptor
8. Solvent Refined Coal Process-II
   a. Light distillate
   b. Middle distillate
   c. Heavy distillate (product)
   d. Vacuum bottoms
9. Paraho Refined Fuels
   a. Hydrotreated shale oil
   b. JP-5 (jet)
   c. JP-8 (jet)
   d. DFM (diesel)
   e. Acid sludge
10. Conventional Petroleum Fuels
    a. JP-5 (jet)
    b. JP-8 (jet)
    c. DFM (diesel)
11. Occidental In Situ Retort[b]
    a. Crude shale oil
    b. Retort water (Room 6)
    c. Boiler blowdown
    d. Leach water from old retorts (Rooms 1-5)

(a) Use of any materials from Paraho requires approval from Development Engineering, Inc. (operators of Paraho retort) on a case-by-case basis.

(b) Use of any materials from Occidental requires coordination through the DOE-ASEV Modified In Situ Task Force - W. Chappell, University of Colorado, Chairman.

especially drilled for the ASEV Oil Shale Task Force in Retort 3E. In addition, samples were obtained of a raw shale core drilled between the locations of the future retorts 7 and 8. The spent shale core samples were crushed, sieved, and split. They were then distributed to members of the oil shale task force as well as used for our own analyses. Unused portions of the samples are retained in the PNL refrigerated repository for future work. Current studies on these materials include chemical characterization, mineralogical characterization, and leaching. In addition, half of the samples were returned to Occidental Research for their characterization studies.

During the past year, samples were obtained from both the SRC II and I processes. The SRC II samples listed in Table 4.4 were obtained during a special run for environmental and biotesting conducted in June. In addition, three solvent fractions and a gasified fly ash were obtained from the SRC I process. Studies to be conducted on these samples include organic analyses, chemical fractionation in support of biological studies, Ames mutagenicity assays, and various cell assays and skin painting tests.

Organic Characterization and Mutagenicity of Shale Oils

D. S. Sklarew, A. P. Toste, R. A. Pelroy and D. M. Schoengold

The basic objectives of this program are to identify and compare potential environmental pollutants resulting from production of shale oils by different processes. Four shale oils have been compared--Paraho, Livermore, Vernal (Utah), and Occidental--as well as a crude petroleum (Prudhoe Bay) and two coal liquids [solvent refined coal (SRC) II heavy distillate and distillate blend].

In the first phase of this work, results from two different fractionation methods were compared for their effectiveness in providing fossil fuel materials suitable for mutagenesis bioassay. The first method used solvent extraction to separate components into organic acids, bases, and neutral materials. Seven materials resulted: acid, basic, neutral, acid tar, basic tar, neutral tar, and polycyclic aromatic hydrocarbon (PAH)(Fruchter, Petersen and Laul 1979). The second method (Jones, Guerin and Clark 1977), based on Sephadex LH-20 partition chromatography, depended primarily on separation of chemical classes by differences in polarity. Three solvents were used and three fractions generated: hexane, toluene/hexane, and methanol. In the second phase, the LH-20 fractions for Paraho and the distillate blend were further subdivided by high-performance liquid chromatography (HPLC) using a semipreparative normal phase amine column. Solvent gradients with hexane, methylene chloride, and isopropanol were used to elute the samples resulting in three major ultraviolet (UV) absorbance areas: a nonpolar, a moderately polar, and a polar peak.

The chemical fractions from the first phase were tested for mutagenicity in the Ames assay using Salmonella typhimurium TA98. Results for both the acid-base fractions (Figure 4.4) and the LH-20 fractions (Figure 4.5) as well as for the crude unfractionated materials (Figure 4.6) indicated the same trends. The mutagenicities of the four shale oils ranged over nearly one order of magnitude, with higher values obtained for Paraho and Livermore, and lower values for Vernal and Occidental. It is not clear at this time whether these differences are attributable to the differences in the processes involved, to the reaction conditions used or possibly to differences in composition of the original oil shales. One chemical difference among the shale oils can be noted here: the nitrogen content of the Paraho and Livermore (~2-2.6%) shale oils is higher than that of Occidental and Vernal (~1.5%).

The SRC II distillate blend was about four times as active and the heavy distillate about ten times as active as the most active shale oil. The Prudhoe Bay petroleum exhibited no mutagenic activity against TA98. However, at least one petroleum, Louisiana sweet crude, has been shown to be mutagenic (Epler et al. 1978).

Fractions which are not shown in Figures 4.4 to 4.6 were inactive against TA98. In the acid-base extraction scheme, mutagenic activity was concentrated in the basic, neutral tar, and basic tar fractions which comprise 20 to 30% of the mass of the crude. In the LH-20 procedure, nearly all of the activity was obtained in a single fraction (methanol) which constitutes 3 to 11% of the mass of the starting material. Recovery of mutagenic activity, however, is greater in the acid-base fractions (43 to 124%) than in the LH-20 fractions (21 to 62%) at this phase of the fractionation (Figure 4.6).

In the second phase of this work, the Ames assay was used to ascertain the mutagenic potency of the HPLC fractions

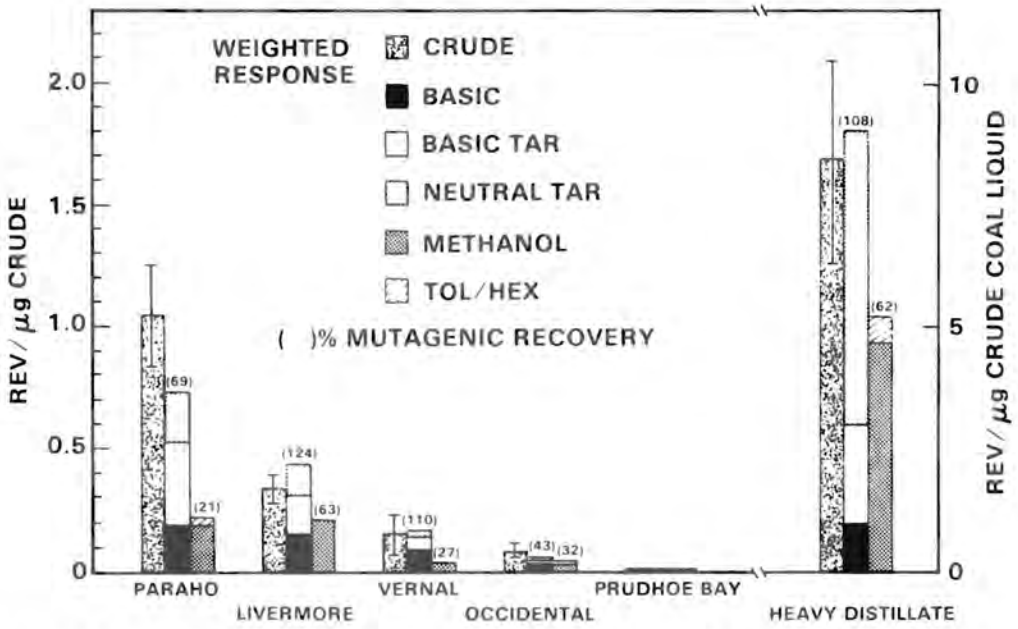

Figure 4.4. Specific Mutagenic Activity Against TA98 of Fractions from the Acid-base Extraction Scheme

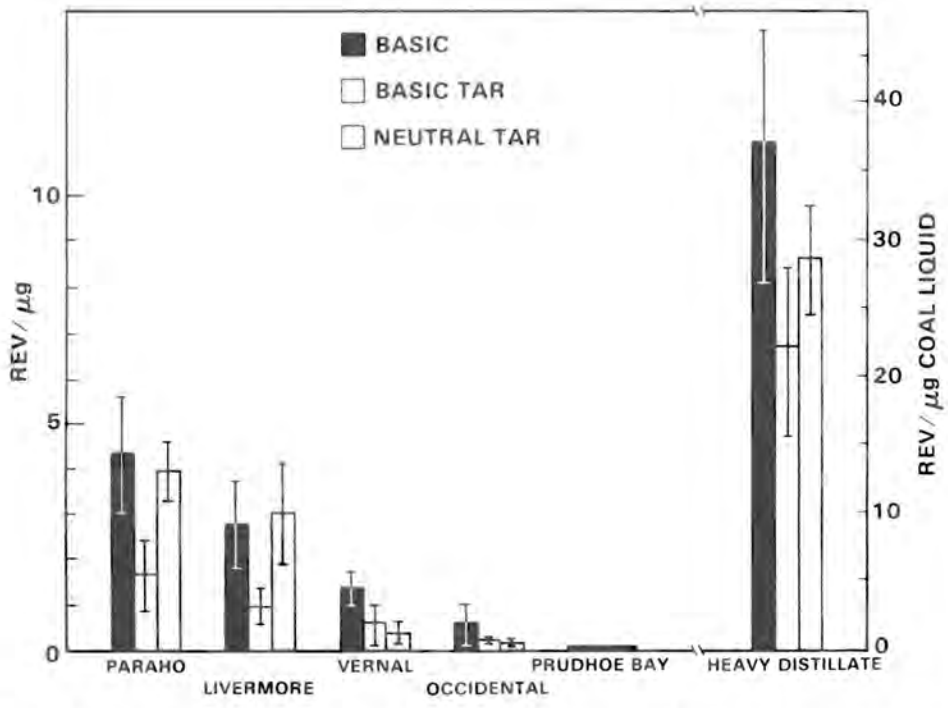

Figure 4.5. Specific Mutagenic Activity Against TA98 of Fractions from the LH-20 Partition Scheme

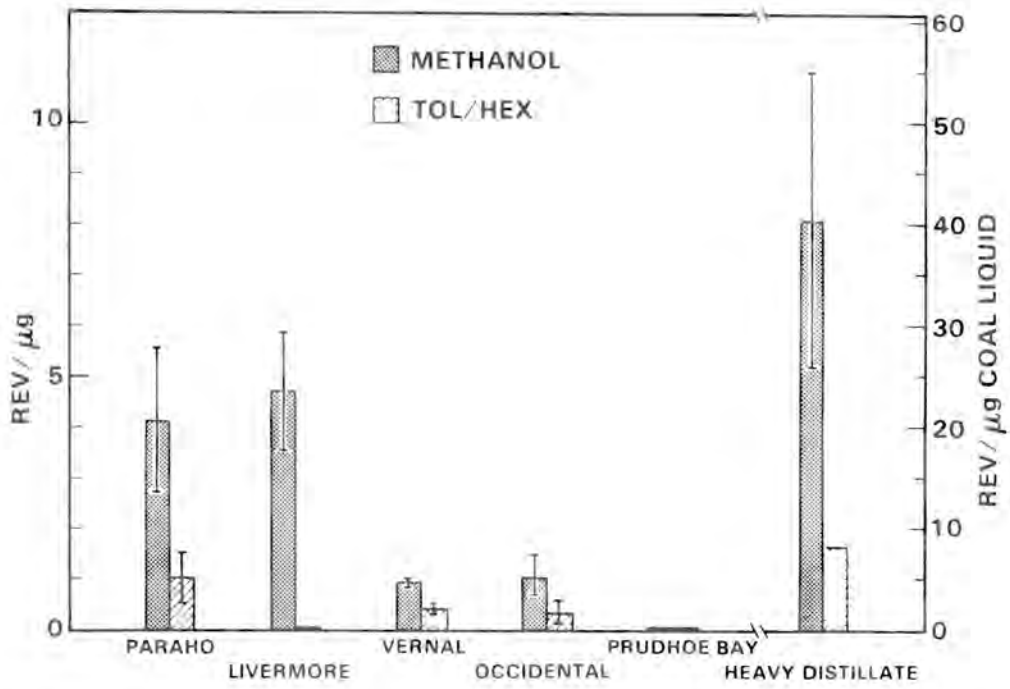

Figure 4.6. Mutagenic Activity of Crude Materials and Mutagenic Recovery of Fractions from the Acid-base and LH-20 Fractionation Schemes. [% mutagenic recovery = Σ (spec. activity x weight percent of fractions)]

generated from the LH-20 fractions of Paraho and the SRC II distillate blend. The mutagenically inactive Paraho hexane fraction remained inactive in contrast to the distillate blend. In the latter, the inactive LH-20 hexane fraction yielded mutagenic subfractions enriched in the non-polar and moderately polar compounds. The activity of the Paraho LH-20 methanol fraction appears to be attributable to several types of components as seen by the wide distribution of mutagens in both moderately polar (fractions 3 and 4) and strongly polar (fractions 7 and 8) HPLC subfractions (Figure 4.7). This contrasts with the HPLC results obtained from the analogous fraction of the distillate blend in which most of the activity was located in the moderately polar fraction with only minor contributions in the more polar fractions. Thus, the HPLC Ames data suggest a greater contribution of polar mutagens to total mutagenic activity in Paraho shale oil than in the coal liquid distillate blend.

Chemical characterization of a number of these fractions has been undertaken. Total ion current traces of gas chromatographic/mass spectroscopic (GC/MS) data from the four shale oils show a remarkable similarity in their gross composition (Figure 4.8). The peaks correspond to several series: phenol, C_1- to C_7-alkyl-and/or alkenylphenols, naphthol, C_1 and C_2-alkylnaphthols, C_3- to C_6-pyridines, indole, C_1- to C_5- alkylindoles, carbazole, C_1- to C_4-alkylcarbazoles, quinolines (minor), C_1- and C_2-alkylquinolines (minor), and some acids. None of these major components is mutagenic in the Ames assay. Single ion reconstructs and GC retention time data have been used to search for the known mutagens--aromatic amines. Strong evidence for these compounds is found in the SRC-II heavy distillate and the distillate blend; however, the single ion reconstructs of the shale oils do not show any evidence of the 2- to 4-ring aromatic amines, except for the possible suggestion of aminopyrene. It is, nevertheless, possible that the shale oils do contain aromatic amines; in fact, the HPLC Ames data suggest their presence in the moderately polar fraction. Further separation will be necessary to reveal the possible presence of low levels of aromatic amines.

Sulfur Gas Analysis

D. S. Sklarew and M. R. Petersen

The on-line analysis of sulfur gases in the product gas from an oil shale retort is a valuable way to determine necessary

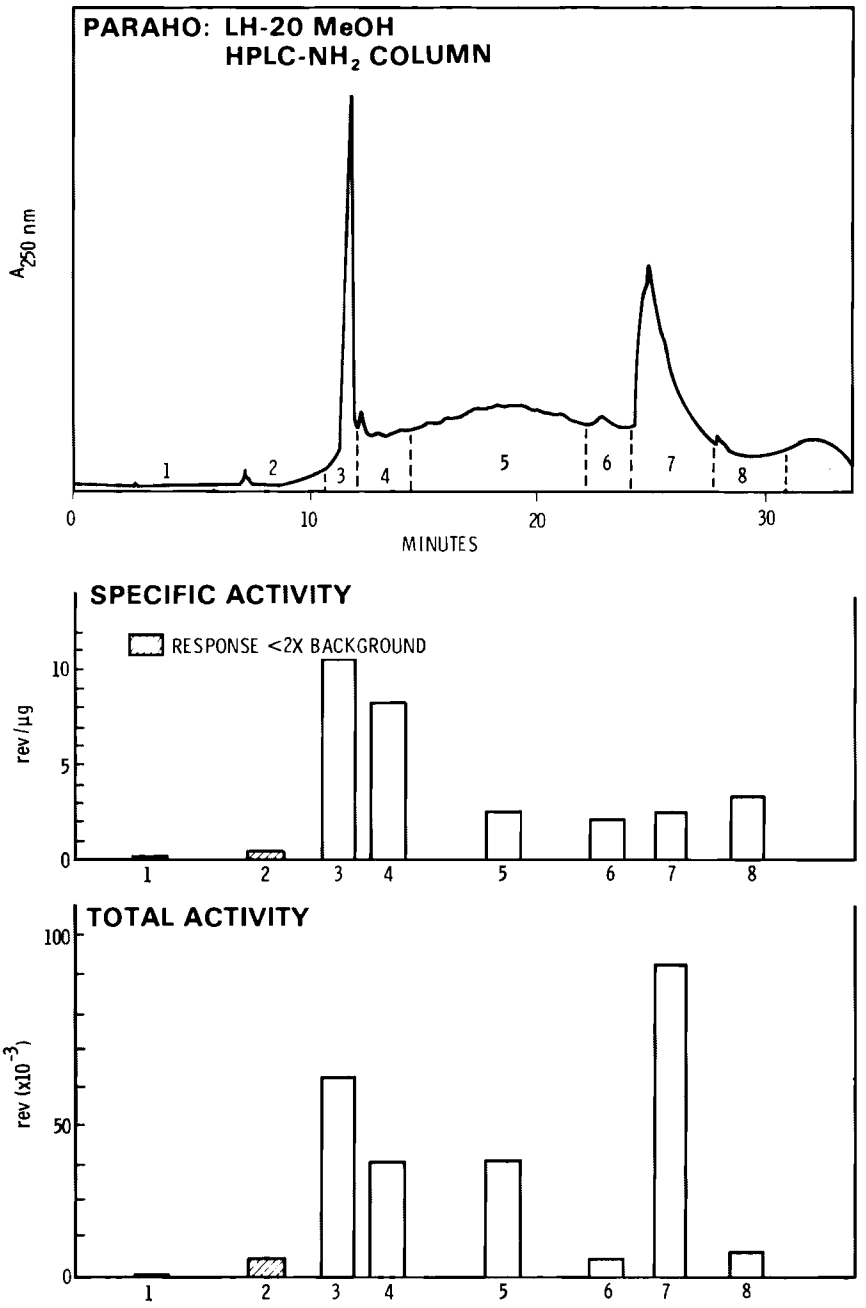

Figure 4.7. Specific and Total Mutagenic Activity Against TA98 of Fractions from HPLC of Paraho LH-20 Methanol Fraction

pollution control methods. On-site measurement appears to be important because of the possible instability of some of these gases. Methods were developed at a Paraho aboveground retort burn of Green River oil shale and utilized at the Rio Blanco modified in situ burn at "retort O." Samples at Rio Blanco were taken at about one week after the start of the burn. At Paraho, the recycle gas was accessed after the electrostatic precipitator.

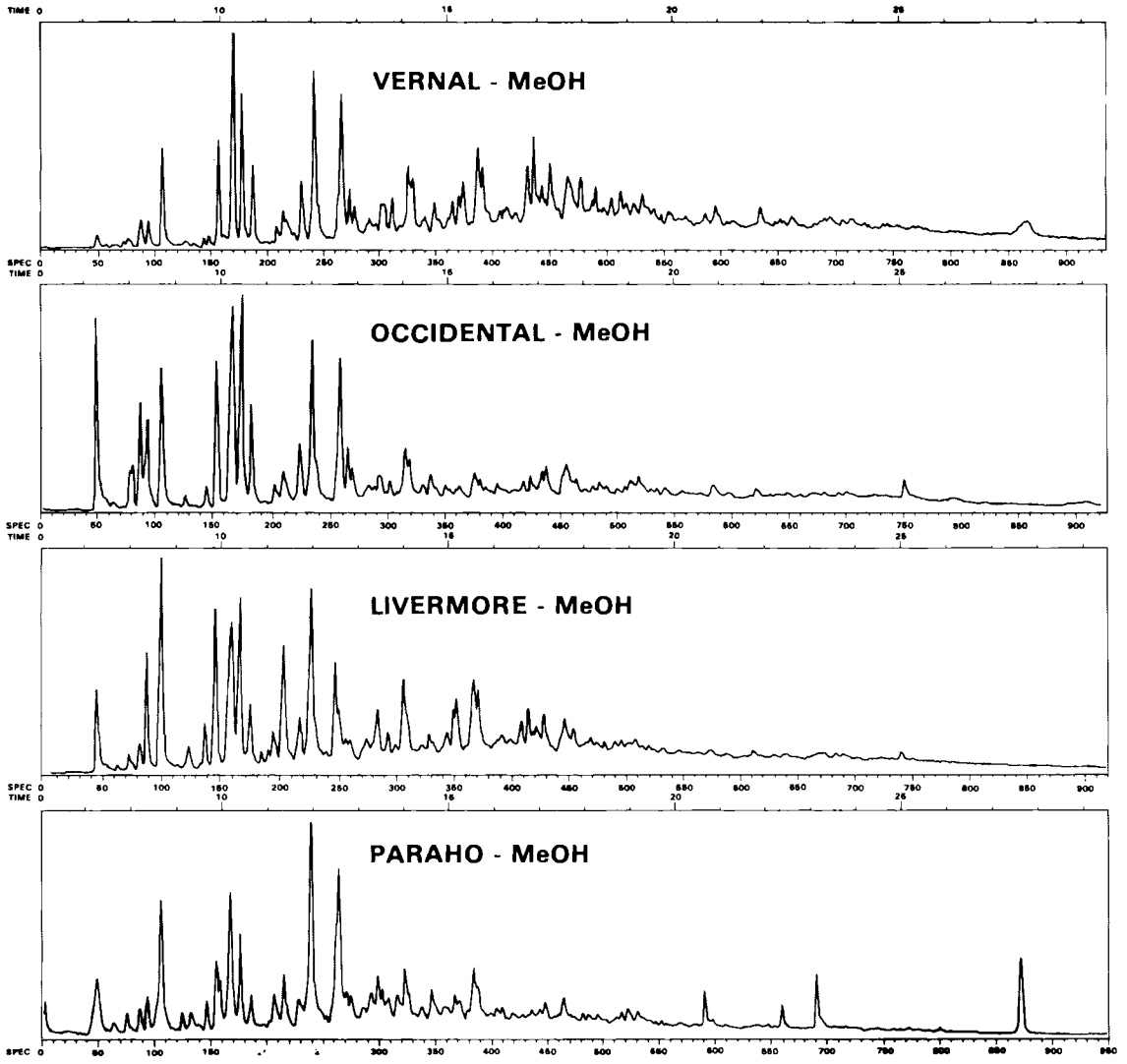

Figure 4.8. Total Ion Current Chromatograms of the LH-20 Methanol Fractions of Four Shale Oils: Paraho, Livermore, Vernal, and Occidental

Teflon® lines were used to sample the gas which was at a temperature of ~160°F. At Rio Blanco, the retort gas was accessed after the knockout drum using a combination of stainless steel and Teflon lines. The tubing was probably equilibrated with the gas; therefore, the use of stainless steel was not thought to present a problem. The length of unheated line at Rio Blanco (~100 yds) (compared to ~6 ft at Paraho) could pose a problem for condensable sulfur gases such as CS_2 or thiophene. The samples were taken before the retort gas passed to the incinerator/scrubber which was used to convert the sulfur species to SO_2; SO_2 was then scrubbed prior to release of flue gases to the atmosphere.

A gas chromatograph (GC) equipped with flame photometric (FPD) and flame ionization detectors (FID) and a Teflon-lined gas sampling valve was used to analyze the sulfur gases. Since hydrocarbon gases have a major quenching effect on the FPD, it is essential to separate them chromatographically from the sulfur gases to obtain quantitative information about the latter. A 6 ft x 1/8 in. glass column packed with

® Registered Trademark of E. I. du Pont deNemours and Co.

Porapak QS® provided the best separations for most of the gases. For selected gases, a Chromosorb® 107 column was also used. Because of the high concentrations of several gases, a dilution apparatus consisting of two rotameters and a glass mixing chamber was needed to obtain measurements within the dynamic range of the FPD.

Three sulfur gases were identified at Rio Blanco by comparison of retention times with standards on two GC columns (Figures 4.9 and 4.10): H_2S, COS, and CS_2. CH_3SH was identified on the Porapak QS GC column and a small SO_2 peak was also tentatively identified on the Chromosorb 107 GC column. Three additional peaks on the FPD did not correlate with any of the sulfur standards available on site. A grab sample was taken in a Teflon-lined stainless steel bomb for analysis by gas chromatography/mass spectroscopy (GC/MS) in the laboratory. Gas chromatographic/mass spectrometric analysis confirmed the presence of COS and CS_2, and revealed the presence of thiophene and methylthiophene. The latter appear to correspond to the unknown peaks (1 and 2), but identification is not yet positive.

Quantitation of COS, CH_3SH, and CS_2 was accomplished by comparison of the sample with known standards--certified Matheson standards in the case of COS and CH_3SH, and a hexane solution in the case of CS_2. Because of the nonlinearity of the flame photometric detector and the high concentration of sulfur species in the retort gas, it was considered best to dilute the sample until the area of a given sample peak approximately matched that of the standard. Numerous H_2S measurements were available from other on-site monitors; therefore, quantitation of H_2S was not done because of the extremely large dilutions necessary to bring this component within the dynamic range of the FPD. The presumed thiophene, methylthiophene, and SO_2 peaks, as well as the unknown, were determined semiquantitatively; i.e., the areas of these peaks were not matched quite so closely with the areas of standards. The thiophene and methylthiophene peaks were calibrated against the methyl mercaptan standard since the identities of the peaks were unknown at the time. The unknown was calibrated against both a one

® Registered Trademark of Waters Associate, Inc.
® Registered Trademark of Johns Manville.

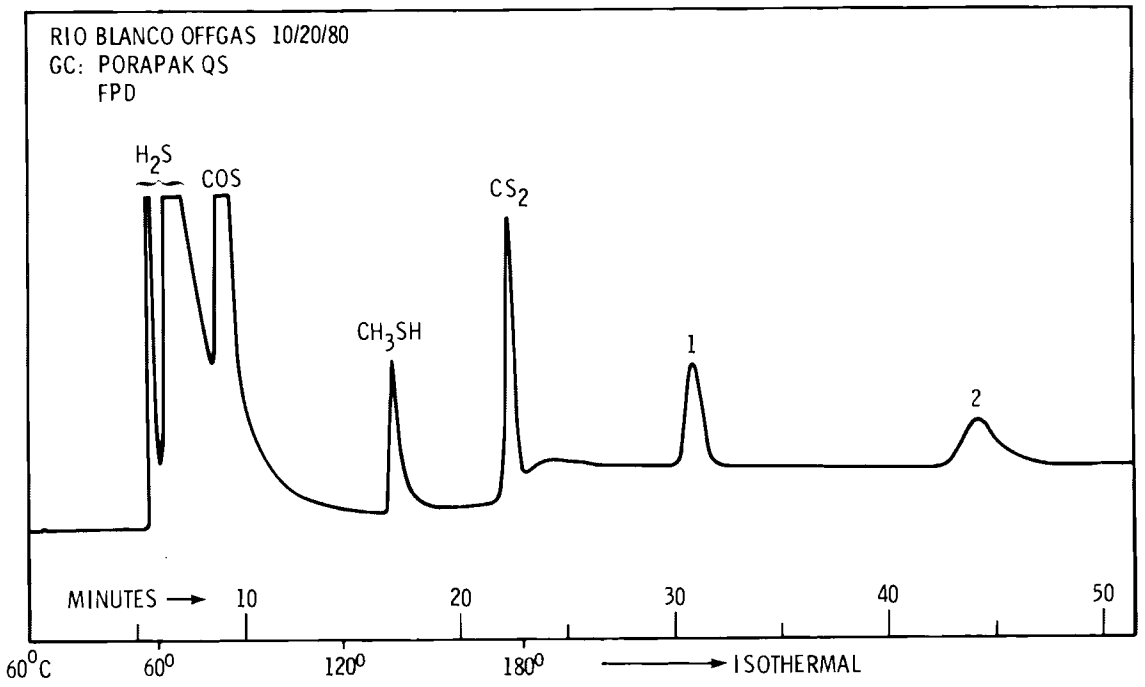

Figure 4.9. Gas Chromatogram of Sulfur Gases from a Rio Blanco Offgas—Porapak QS, 6 ft x ⅛ in. Glass, Flame Photometric Detector

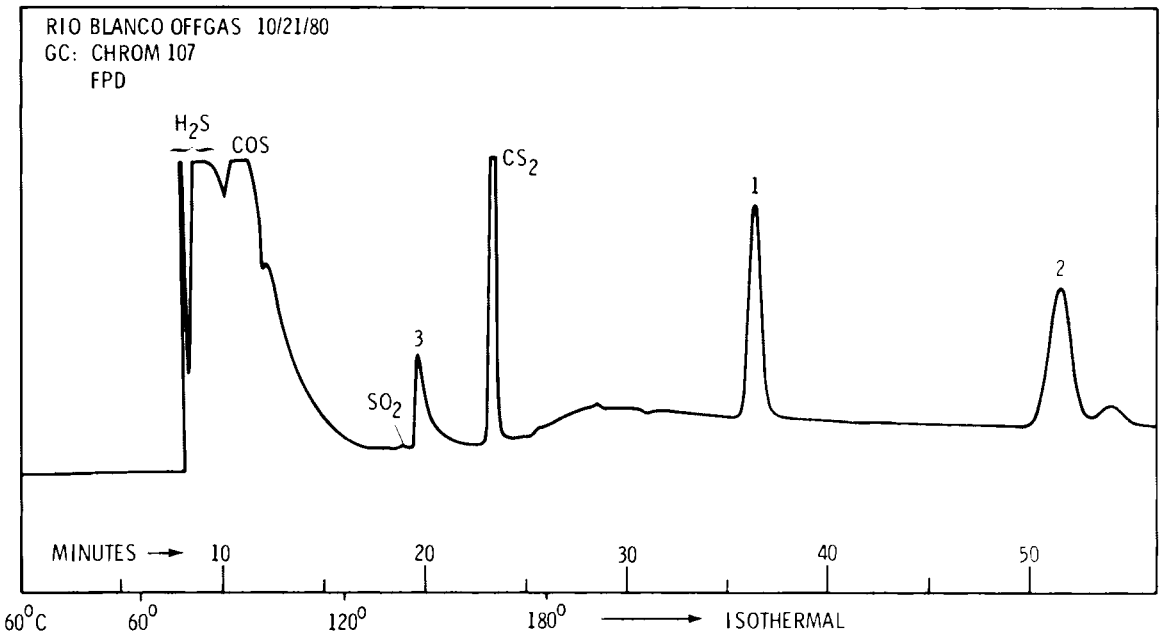

Figure 4.10. Gas Chromatogram of Sulfur Gases from a Rio Blanco Offgas—Chromosorb 107, 6 ft x ⅛ in. Glass, Flame Photometric Detector

sulfur atom (SO_2) and a two sulfur atom (CS_2) standard since its stoichiometry is unknown. The results are summarized in Table 4.5. The numers for COS, CH_3SH, and CS_2 have a precision of ~5% at a given sampling time.

Hydrocarbon gases from C_1 through C_7 were also detected at Rio Blanco on the GC columns used. These included saturated, singly saturated, and doubly unsaturated hydrocarbons. Benzene and toluene were also identified by GC/MS.

Qualitative analyses of bulk gas from another retort--Occidental--were also performed using GC/MS. The sample was collected and stored in stainless steel bombs. Components present include a series of alkanes and unsaturated aliphatic hydrocarbons ranging from C_2 through C_{10}, and aromatic hydrocarbons ranging from benzene through C_4-alkylbenzenes, SO_2, and COS.

Table 4.5. Sulfur Gases in Rio Blanco Retort "O," Week 1.

COS	500 ppm
CH_3SH	85 ppm
CS_2	25 ppm
SO_2	~7 ppm
Peak 1 (thiophene?)	~115 ppm (based on CH_3SH)
Peak 2 (methylthiophene?)	~110 ppm (based on CH_3SH)
Peak 3 (unknown)	~60 ppm (based on SO_2)

REFERENCES

Epler, J., J. Young, A. Hardigree, T. Rao, M. Guerin, I. Rubin, C. Ho, and B. Clark. 1978. "Analytical and biological analysis of test materials from the synthetic fuel technologies. I. Mutagenicity of crude oils determined by the Salmonella typhimurium microsomal activation system." Mutation Res. 57:265-276.

Fruchter, J. S., M. R. Petersen, and J. C. Laul. 1977. "Characterization of products, effluents, and wastes from oil shale retort pilot plants." In Part 4 Pacific Northwest Laboratory Annual Report for 1976 to the ERDA Assistant Secretary for Environment. PNL-2100, PT4, Pacific Northwest Laboratory, Richland, Washington.

Jones, A. R., M. R. Guerin, and B. R. Clark. 1977. "Preparative-scale liquid chromatographic fractionation of crude oils derived from coal and shale." Anal. Chem. 49:1766-71.

5 Multitechnology

• Environmental Pollutant Characterization by Direct-Inlet Mass Spectrometry

The utility of direct-inlet mass spectrometry (DIMS) for the detection, characterization and monitoring of toxic airborne particulate pollutants is being experimentally determined. The response of the entire DIMS to artificially generated aerosols of $CsNO_3$ has been characterized as a function of surface ionization filament temperature and particle size.

Environmental Pollutant Characterization by Direct-Inlet Mass Spectrometry

C. R. Lagergren, R. L. Gordon, and J. J. Stoffels

The purpose of this task is to experimentally determine the utility of direct-inlet mass spectrometry (DIMS) as an analytical technique for the detection, characterization and monitoring of specific toxic particulate airborne pollutants that enter the environment as by-products of energy generation or other industrial activities.

The DIMS technique is essentially a method by which particles in air are transported directly to the hot ionizing filament of a surface ionization mass spectrometer without the need for any collection, manipulation or processing procedures. Individual particles striking the hot filament form bursts of ions which are then mass analyzed and measured. Burst rates are related to particle concentration in sampled air while the total charge per burst is a measure of particle size. Mass analysis of the ions provides a means of selectivity for a specific particle material and potentially the identification of its chemical composition. Ionization efficiencies by surface ionization for a wide range of elements are high enough that submicrometer-size particles of such elements and their compounds can be detected and measured.

To determine the utility of DIMS as a sensitive, species-selective, and real-time analytical technique for measuring airborne pollutants, the nature of the ionization produced by surface ionization of specific pollutant materials must be established. The ionization efficiency, cracking pattern (ion mass spectrum), and time characteristics of the signals that are produced depend on the chemical and physical properties of the pollutant material and the nature and temperature of the filament surface. These quantities and relationships are unknown and need to be determined in order to assess the utility of the technique.

The first major part of this task, after the development of suitable instrumentation, is the determination of the response of the entire DIMS system to a nontoxic aerosol, cesium nitrate, in the submicrometer size range. Earlier experiments, previously reported, suggested that the number of ions produced in a burst from a particle was related to the second rather than the third power of the particle diameter. This was based on a comparison of the distribution of measured total ion charge per burst with the distribution of diameters measured on collected particles. Uncertainties in particle collection efficiency and in the size measurement process, together with unstable performance of the aerosol generator, made the comparison ambiguous. Estimates of ionization efficiency were correspondingly suspect.

In order to provide sample particles of defined and controlled size an Electrostatic Classifier® was obtained. This device, based on the size dependence of a particle's mobility in air, serves as a variable particle size filter to select a nearly mono-disperse portion of the polydisperse output of the aerosol generator.

® Registered trademark of Thermo-Systems, Inc.

Figures 5.1, 5.2, and 5.3 show the distributions of the number of Cs^+ ions produced per particle for a filament temperature of 960°C and selected particle diameters of 0.076, 0.113, and 0.144 μm, respectively. Since the driving force for mobility selection is provided electrostatically, a doubly charged particle, having half of the mobility of the selected singly charged particle, will be passed also and appears as the secondary peaks indicated at 0.113 μm in Figure 5.1 and 0.173 μm in Figure 5.2. A plot of the centroid of each peak as a function of the square of the selected diameter is shown in Figure 5.4. These measurements unambiguously show that the number of Cs^+ ions produced per particle is proportional to the square of the diameter. The number of Cs^+ ions measured per 0.076 μm particle at a filament temperature of 960°C corresponds to 13% of the cesium atoms contained in the particle. Since the efficiency of transmission of ions from the ionizing filament to the ion detector in the mass spectrometer is not known, the ionization efficiency for this case can be determined only as greater than or equal to 13%.

In a different kind of experiment with the direct inlet connected to an aerosol chamber in which a steady concentration of submicrometer cesium nitrate particles was maintained, the relative equilibrium ion yield was measured as a function of filament temperature. The results plotted in Figure 5.5 show that the ion yield increases rapidly with temperatures above the melting point of $CsNO_3$, up to about 525°C. Above 550°C, the ion yield decreases fairly rapidly with increasing temperature. This decrease in yield is much greater than could be accounted for by any reasonable drop in filament surface work function and is believed to be the result of evaporation and probably dissociation of $CsNO_3$ molecules from the particle itself without ever touching the filament surface. This process could also account for the dependence of ion yield on the square of the particle diameter.

During the course of the experiments with selected particle sizes it was discovered that the direct-inlet system could alter the size distribution being sampled. As is shown in Figures 5.1 to 5.3, such alterations may result in the appearance of smaller sized particles than those selected. The inlet component and alignment conditions responsible for this are being investigated.

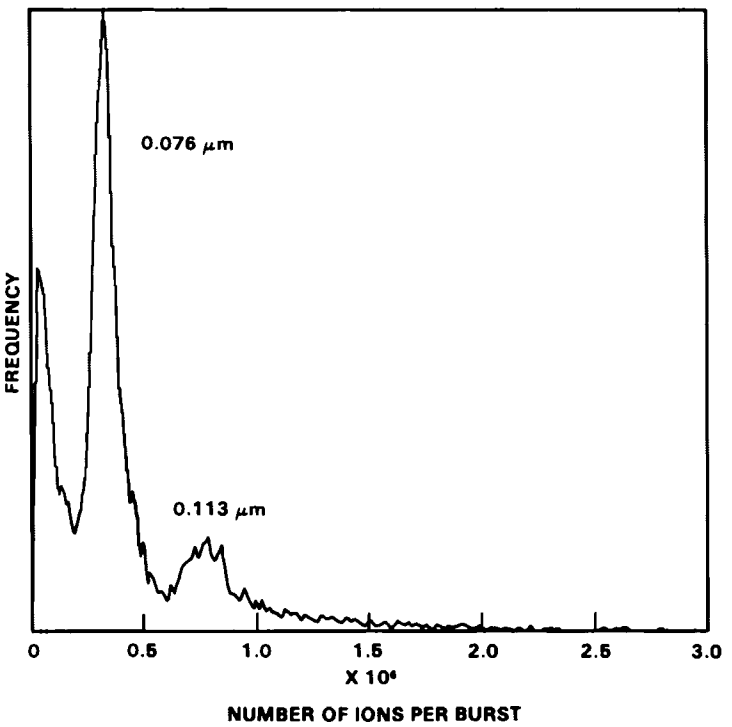

Figure 5.1. Distribution of the Number of Cs^+ Ions Produced from 0.76 μm Selected Size $CsNO_3$ Particles at T_f = 960°C

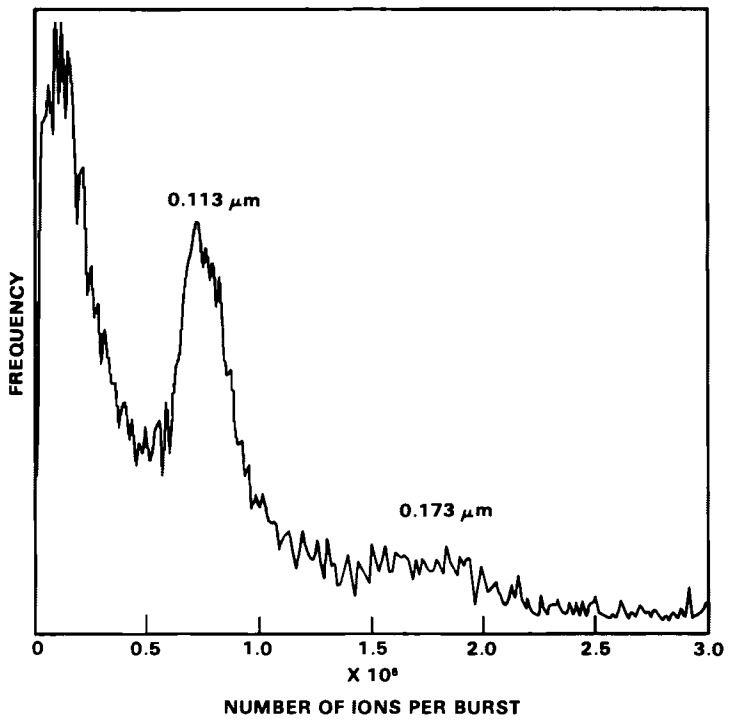

Figure 5.2. Distribution of the Number of Cs^+ Ions Produced from 0.113 μm Selected Size $CsNO_3$ Particles at T_f = 960°C

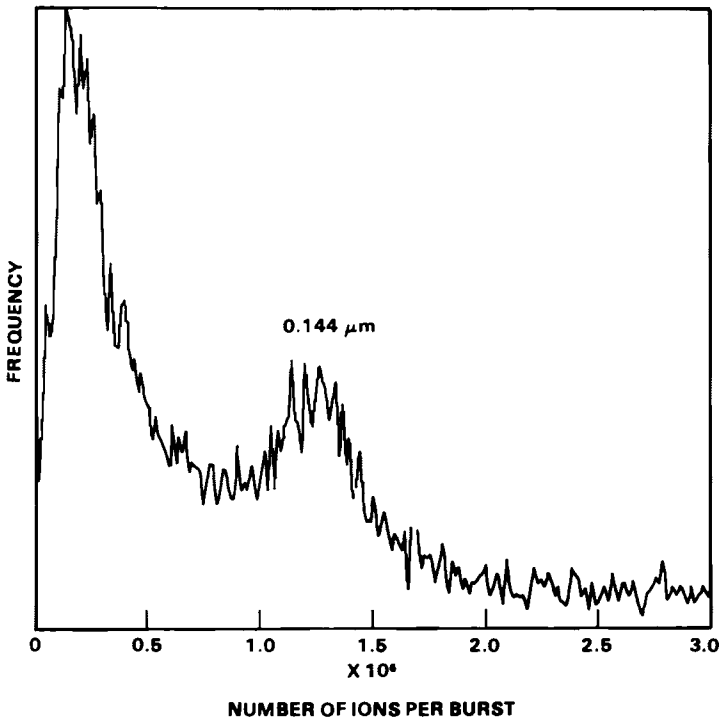

Figure 5.3. Distribution of the Number of Cs^+ Ions Produced from 0.144 μm Selected Size $CsNO_3$ Particles at T_f = 960°C

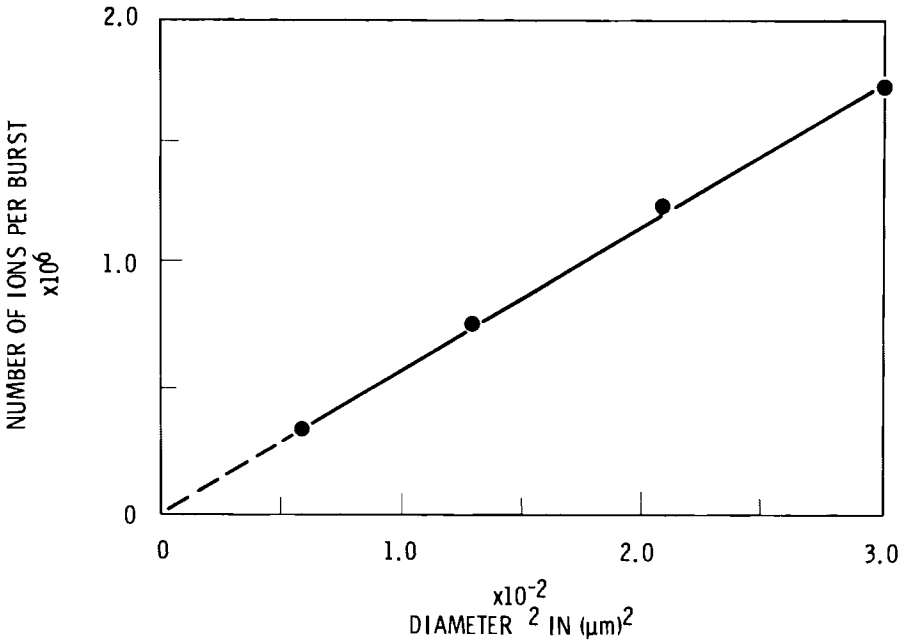

Figure 5.4. Plot of the Number of Ions Per Burst as a Function of the Particle Diameter Squared

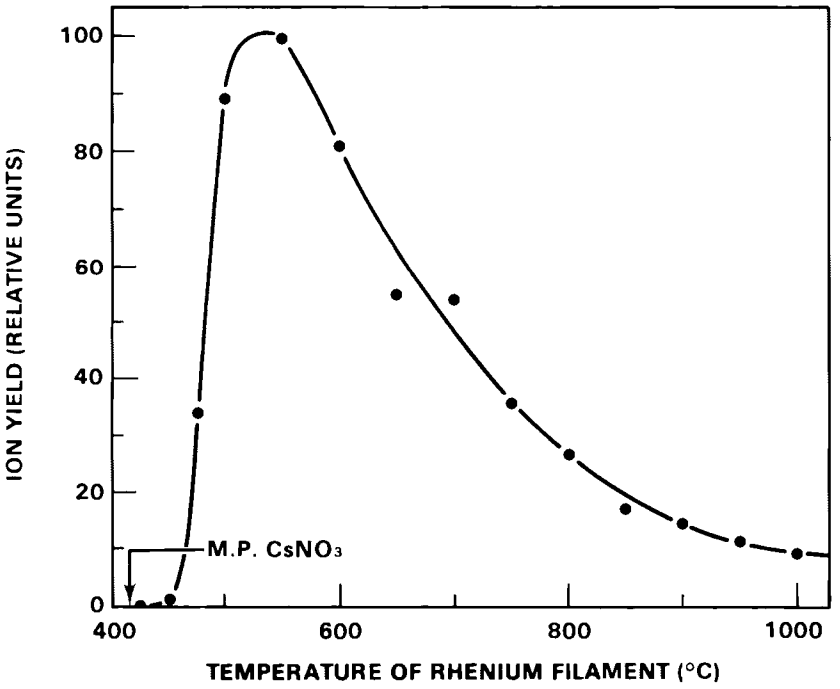

Figure 5.5. Ion Yield as a Function of Filament Temperature

• Trace Analysis by Laser Excitation

This program is designed to research methods of trace analysis using lasers. The principal thrust has been to explore techniques using resonance ionization in the detection of atomic and molecular species. Among the accomplishments in the past year are the development of a technique that reduces the laser power requirements for resonance ionization experiments, the first demonstration of isotopically selective excitation of noble gases from the ground state, and initial development of a simple field instrument for the detection of airborne aromatic hydrocarbons.

Collisionally-Induced Ionization Techniques

T. J. Whitaker and B. A. Bushaw

Single atom detection by resonance ionization spectroscopy (RIS) has provided the ultimate in analytical sensitivity. However, these methods require the use of high power flashlamp-pumped dye-lasers which are not desirable instruments for routine and analytical procedures. They suffer from low duty cycle, high dye consumption, and low reliability. We have devised a variation of RIS which reduces laser power requirements by more than two orders of magnitude. Thus, a nitrogen laser-pumped dye-laser, which will run at high repetition rates for extended periods without maintenance, can be used as the excitation source for single atom detection experiments.

The process relies upon two resonant excitation steps to populate high lying Rydberg states followed by collisional ionization. The cross section of the resonant excitation in the second step is larger than direct photoionization cross sections by several orders of magnitude. Therefore, optical saturation is accomplished using much lower power laser intensities. Since RIS depends on the detection of ions, we had to demonstrate that the efficiency of collisional ionization of the Rydberg state was near unity. This was accomplished by comparison of ion production in this process with that obtained in a normal saturated photoionization process. Figure 5.6 shows the resonantly enhanced ionization spectrum of rubidium in several torr of krypton buffer gas as the laser frequency for the second step is scanned over the Rydberg region.

Doppler-Free Multiphoton Ionization of Noble Gases

T. J. Whitaker and B. A. Bushaw

The isotopically-selective detection of noble gases finds applications in a number of fields including environmental monitoring, isotope ratio measurements for fuel-pin leak tagging and material origin studies, detection of solar neutrinos and double "beta" decay events. Yet, the direct detection of noble gases is an extremely difficult analytical problem because of their lack of chemical activity and the fact that the lowest lying states require optical excitation energies in the vacuum ultraviolet region of the spectrum. These difficulties are further compounded by the requirement of isotopic selectivity.

We have developed a high-resolution three-photon ionization scheme which is capable of low-level, real-time detection of xenon and krypton isotopes. The process involves a Doppler-free, two-photon excitation of a bound intermediate state followed by absorption of a third photon, raising the atom above the ionization limit. The ion pair produced is detected with conventional ion detection electronics. Isotopic selectivity is derived from the hyperfine level splitting in the intermediate state and the use of a very high resolution pulse-amplified, cw dye laser in the Doppler-free excitation. Figure 5.7 shows the spectrum of the 6P(5/2),2 state of xenon recorded using this technique. The peaks due to ^{131}Xe and ^{129}Xe are well resolved, thus demonstrating the isotopic selectivity of the excitation. The analogous 5P(5/2),2 state in krypton and a number of other two-photon allowed states in xenon have also been observed.

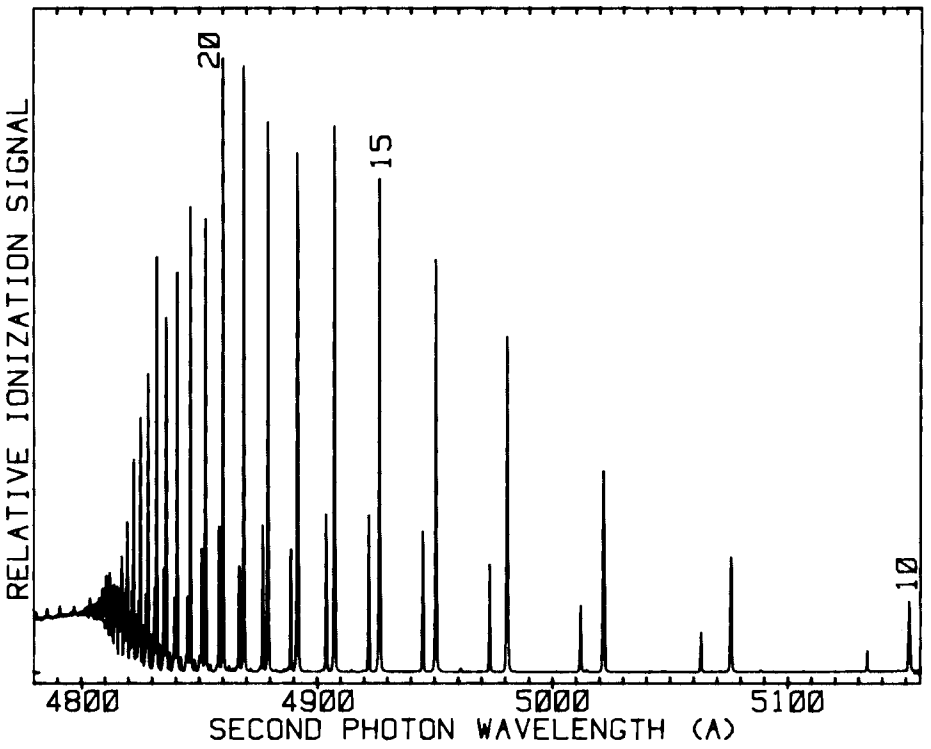

Figure 5.6. Dual Resonance, Collisional Ionization Spectrum of Rubidium

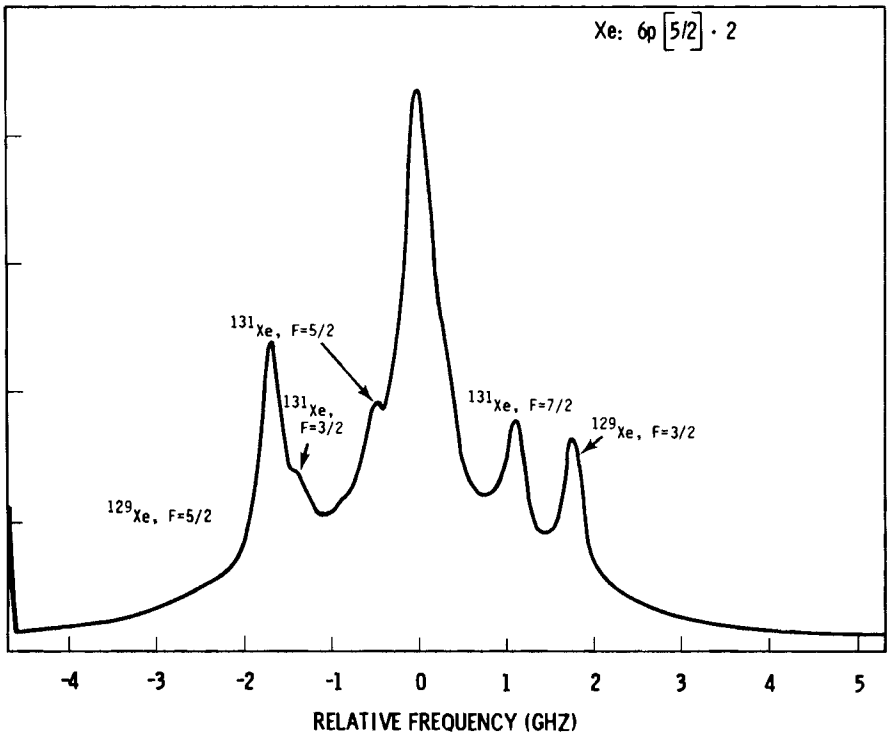

Figure 5.7. Two-photon Resonant, Three-photon Ionization Spectrum of the 6P(5/2),2 State of Xenon

Field Instrument for PAH Detection

T. J. Whitaker and B. A. Bushaw

Initial tests have begun to determine the feasibility of a portable field instrument for monitoring polycylic aromatic hydrocarbons (PAH) under ambient conditions. The instrument would rely on nitrogen laser excitation of the molecules followed by detection of the ensuing fluorescence. Because of atmospheric quenching, further tests must be conducted to determine whether the system is practical.

• Applications of Holography

The nature and distribution of aerosols and particulate matter in the atmosphere and of particulates and microscopic-sized organisms in water are of interest and concern in characterizing our environment. Holograms are in some respects an ideal way to record the information needed. A hologram provides a static image of a selected volume of air or water at a chosen instant without disturbing the disposition of the particles in any way. Using this image, the position, size and shape of every particle in the volume can be individually determined. When the laser used to record the hologram is double or triple pulsed, information is recorded from which velocities and accelerations can be calculated. Semiautomatic methods of hologram image analysis have been developed to increase the speed and efficiency of determining size distributions, volume fractions, velocity distributions and shape factors.

Applications of Holography to Environmental Studies

B. B. Brenden

Pulsed ruby lasers have been used for aerosol and particulate studies since 1964. The aim of our work has been to reduce the size and increase the portability of the pulsed-laser holocamera so that it can be used in a much broader range of applications. A miniature holocamera has been developed which utilizes cantilever beam vibrations of a ruby rod as a Q-switch mechanism. Up to three Q-switched pulses are obtained per pumping cycle. Triple-pulsed holograms provide data from which particle sizes, velocities and accelerations are directly measured. The holographic record of a 100 cm^3 volume is made with each firing of the laser. The holocamera, together with its battery-based power supply and timing circuitry, is packaged in a 20-pound unit about one square foot in cross-sectional area and two feet long. When the unit is switched on and set for a one-minute time interval, the laser fires once per minute and the film holder automatically advances the film for the next shot. The firing continues at one-minute intervals until the preset number of exposures has been made. Each time the laser fires, three uniformly separated pulses of light are generated so that if a particle is moving, it is seen in three different positions in the image. Each laser pulse is 4 μsec long and separated from the neighboring pulses by 0.5 msec.

The holocamera has been used to study powder dispersements in small room-sized experimental chambers. It is compact enough to be packaged for underwater use.

The holograms resulting from the use of this camera contain a wealth of detail. Semiautomatic equipment for hologram image analysis has been built up to make data retrieval a manageable task. A hologram image display unit has been assembled which scans stepwise through the image volume and couples to a video-based image analysis system. A magnified image of a small volume within the field is displayed on the video monitor. After the operator edits the image, the analyzer computer determines coordinate positions of particles and measures diameters and areas. A programmable calculator then calculates volumes, void fractions, distributions, or such other information as provided for by the software. Plots of the calculated distributions are printed out or accumulated, and the X, Y, Z scanner automatically moves to the next volume element to be addressed.

Experience using the holocamera has shown that it performs excellently for particles five microns in diameter and larger. Fields of particles less than five microns in diameter are recorded but the holocamera has difficulty distinguishing particle images from noise. Further work with the holocamera and with data readout may reduce the noise level. It seems likely that the holocamera could also be improved by the addition of an optical amplifier. This addition would result in a somewhat larger but still very portable camera yielding a more uniform background in the image and better resolution by reducing background noise.

Publications and Presentations

PUBLICATIONS

Ballou, J. E., and N. A. Wogman. 1980. "The Disposition of ^{232}U Daughters Following Inhalation of $^{232}UO_2(NO_3)^2$ Aerosols." In Proceedings of the Health Physics Society Annual Meeting, July 20-25, 1980, Seattle, Washington.

Bean, R. M., C. D. Becker, J. R. Skalski, W. E. Fallon, A. J. Scott, K. Shiosaki and B. W. Wilson. 1980. "Aqueous Suspensions of Solvent Refined Coal Liquids: Effects of Preparation Procedure on Resulting Chemical Composition and Toxicity." In Proceedings of 20th Hanford Science Symposium, eds. W. D. Felix and D. D. Mahlum, Richland, Washington.

Bean, R. M., D. C. Mann, B. W. Wilson, R. G. Riley, E. W. Lusty and T. O. Thatcher. 1980. "Organohalogen Production from Chlorination of Natural Waters Under Simulated Biofouling Control Conditions." In Water Chlorination Environmental Impact and Health Effects, Vol. 3, eds. R. L. Jolley, W. A. Brungs, R. B. Cumming and V. A. Jacobs. Ann Arbor Science Publishers, Inc., Ann Arbor, Michigan.

Braby, L. A., J. M. Nelson and W. C. Roesch. 1980. "Comparison of Repair Rates Determined by Split-Dose Rate Methods." Radiation Research 82:211-215.

Brenden, B. B., J. S. Hartman and F. R. Reich. 1980. "Measuring Transient High Temperature Thermal Phenomena in Hostile Environment." In Proceedings of the Society of Photo-Optical Instrumentation Engineers, Vol. 216, pp. 221-228, Bellingham, Washington.

Brodzinski, R. L. 1980. "In-Situ Radiation Measurements and Instrumentation for Monitoring Nuclear Waste Storage Facilities." IEEE Transactions on Nuclear Science NS-27:1277-1279.

Brodzinski, R. L. 1980. "Monitoring Transuranics in Sediments by Neutron Activation of Metals." PNL-3394, Pacific Northwest Laboratory, Richland, Washington.

Brodzinkski, R. L., and H. L. Nielson. 1980. "A Well Logging Technique for the In-Situ Determination of ^{90}Sr." Nuclear Instruments and Methods 173:299-301.

Fruchter, J. S., J. C. Evans, C. L. Wilkerson and R. W. Sanders. 1980. "Analysis of Oil Shale Products and Effluents Using a Multitechnique Approach." In Proceedings of American Nuclear Society/ American Chemical Society/ DOE Topical Conference on Atomic and Nuclear Methods in Fossil Energy Research, Mayaguez, Puerto Rico.

Fruchter, J. S., and M. R. Petersen. 1979. "Environmental Characterization of Products and Effluents from Coal Conversion Processes." Analytical Methods for Coal and Coal Products, Vol. III, pp. 247-275.

Fruchter, J. S., J. W. Shade, et al. 1980. "Mount St. Helens Ash from the 18 May 1980 Eruption: Chemical, Physical, Mineralogical, and Biological Properties." Science 209:1116-1125.

Fruchter, J. S., and C. L. Wilkerson. 1980. "Characterization of Oil Shale Effluents." In Proceedings of Oil Shale: The Environmental Challenges, Vail, Colorado.

Fruchter, J. S., and C. L. Wilkerson. 1980. "Elemental Partitioning in an Aboveground Oil Shale Retort Pilot Plant." Environmental Science and Technology, November 1980.

Germani, M. S., I. Gokmen, A. C. Sigleon, G. S. Kowalczyk, I. Olmez, A. Small, D. L. Anderson, M. P. Failey, M. C. Gulovali, C. E. Choquette, E. A. Lepel, G. E. Gordon, and W. H. Zoller. 1980. "Concentrations of Elements in the National Bureau of Standards' Bituminous and Sub-bituminous Coal Standard Reference Materials." Anal. Chem. 52:240-245.

Goles, R. W., and F. P. Brauer. 1980. "An Automated ^{85}Kr Gamma-Ray Stack Monitor." In Proceedings of the 1980 Nuclear Science Symposium, Orlando, Florida.

Goles, R. W., and F. P. Brauer. 1980. "Differential Monitoring of Tritium and Carbon-14 Compounds." In Proceedings of the ANS Topical Meeting, Conf-800427, pp. 182-185.

Goles, R. W., R. C. Fukuda, M. W. Cole and F. P. Brauer. 1980. "Fluorescent Detection of Iodine-129." PNL-3327, Pacific Northwest Laboratory, Richland, Washington.

Gordon, R. L., and P. G. Pallmer, Jr. 1980. "The Work Function of Carburized Rhenium." Journal of Applied Physics 51:3776-3779.

Hartman, J. S., R. L. Gordon and D. L. Lessor. 1980. "Development of Nomarski Microscopy of Quantitative Determination of Surface Topography." In Proceedings of the Society of Photo-Optical Instrumentation Engineers, Vol. 192, Interferometry, pp. 223-230, San Diego, California.

Hartman, J. S., R. L. Gordon and D. L. Lessor. 1980. "Quantitative Surface Topography Determination by Nomarski Reflection Microscopy. II. Microscope Modification Calibration and Planar Sample Experiments." Optical Society of America 19:2998-3009.

Kalkwarf, D. R., and J. C. Langford. 1980. "Response of Agarose Solutions to Magnetic Fields." In Proceedings of the 18th Hanford Life Science Symposium--Biological Effects of Extremely Low Frequency Electromagnetic Fields, pp. 408-416.

Kaye, J. H., F. P. Brauer and R. S. Strebin, Jr. 1980. "Tellurium Interference in ^{129}I Activation Analysis." Jr. Radioelement Analysis Progress and Problems, Chapter 19, pp. 165-174.

Lagergren, C. R. 1980. "Characterization of Low Activities by Mass Spectrometry." In Proceedings of the Second International Conference on Low Level Counting, Low Radioactivities '80, Strbske Pleso, Czechoslovakia, PNL-SA-8912.

Laul, J. C., C. L. Wilkerson and V. L. Crow. 1979. "Computer Methodology and Its Applications to Geological and Environmental Matrices." In Proceedings of Computers in Activation Analysis and Gamma-Ray Spectroscopy, pp. 840-856.

Lepel, E. A., J. C. Laul, L. A. Rancitelli and R. L. McKeever. 1980. "Background Air Particulate Chemistry Near Colstrip, Montana." Environmental Science and Technology 14(4):422-428.

Ludwick, J. D., D. B. Weber, K. B. Olsen and S. R. Garcia. 1980. "Air Quality Measurements in the Coal Fired Power Plant Environment of Colstrip, Montana." Atmospheric Environment 14:523-532.

Nelson, J. M., L. A. Braby, and W. C. Roesch. 1980. "Rapid Repair of Ionizing Radiation Injury in Chlamydomonas reinhardi." Radiation Research 83:279-289.

Pallmer, P. G., Jr. and R. L. Gordon. 1980. "The Emissivity of Carburized Rhenium." Applied Physics 51(3):1798-1801.

Pallmer, P. G., Jr. and R. L. Gordon. 1980. "The Work Function of Carburized Rhenium." Journal of Applied Physics 51:3776-3779.

Pelroy, R. A., and B. A. Wilson. 1980. "Relative Concentrations of Polyaromatic Primary Amines and Azarenes in Mutagenically Active Nitrogen Fractions from Coal Liquid." Submitted for publication to Mutation Research.

Reeder, P. L., and R. A. Warner. 1980. "Measurement of Average Neutron Energies by a Counting Rate Ratio Technique." Submitted for publication in Nuclear Instruments and Methods, PNL-SA-7536.

Reeder, P. L., L. J. Alquist, R. L. Kiefer, F. H. Ruddy and R. A. Warner. 1980. "Energy Spectra of Delayed Neutrons from the Separated Precursors Rubidium-93, -94, -95, and Cesium-143." Nuclear Science and Engineering 75:140-150.

Reeder, P. L., and R. A. Warner. 1980. "Photoneutron Energy Spectra from ^{24}Na-Be and ^{24}Na-D." Submitted to Nuclear Instruments and Methods, PNL-SA-8444.

Smith, R. D. 1980. "Modulated Molecular Beam Mass Spectrometric Studies of the High Temperature Pyrolysis of Hydro- carbons." Advances in Mass Spectrometry 8A:961, Heyden and Son, London.

Smith, R. D. 1980. "The Trace Element Chemistry of Coal During Combustion and the Emissions from Coal Fired Plants." Progress in Energy and Combustion Science 6(1):53-119.

Smith, R. D., J. A. Campbell and K. K. Nielson. 1980. "Volatility of Fly Ash and Coal." Fuel 59:661.

Stoffels, J. J. 1980. Real-Time Measurement of Plutonium in Air by Direct-Inlet

Surface Ionization Mass Spectrometry - Status Report. PNL-3368, Pacific Northwest Laboratory, Richland, Washington.

Tenny, H. 1979. "Single Particle Powder Patterns." Microchemical Journal, Dec. 1979, pp. 522-525.

Toburen, L. H., W. E. Wilson and R. J. Popowich. 1980. "Secondary Electron Emission from Ionization of Water Vapor by 0.3 to 2.0 MeV He^+ and He^{2+} Ions." Radiation Research 82:27-43.

Weber, D. B., K. B. Olsen and J. D. Ludwick. 1980. "Field Experience with Ambient Level Flame Photometric Sulphur Detectors." Talanta 27:665-668.

Wehner, A. P., C. L. Wilkerson, J. A. Mahaffey and E. M. Milliman. 1980. "Fate of Inhaled Fly Ash in Hamsters." Environmental Research 22:485-498.

Weimer, W. C., J. C. Laul and J. C. Kutt. 1980. "Prediction of the Ultimate Biological Availability of Transuranium Elements in the Environment." Contaminants and Sediments 2:465-484.

Weimer, W. C., B. W. Wilson, R. A. Pelroy and J. C. Craun. 1980. Initial Chemical and Biological Characterization of Hydrotreated Solvent Refined Coal (SRC-II) Liquids: A Status Report. PNL-3464, Pacific Northwest Laboratory, Richland, Washington.

West, M. L., and J. H. Miller. 1980. "Radiation Quality Effects in Quenching of Benzene Fluorescence in Pulsed Proton and Alpha Particle Irradiation." Chemical Physics Letters 71(1):110-112.

Wilson, B. W., et al. 1980. "Effect of 60 Hz Electric Fields on Pineal Melatonin Rhythms in Exposed Rats." In Melatonin: Current Status and Perspectives, eds. Birau and Schloot, Pergammon Press, London.

Wilson, B. W., et al. 1980. "GC/MS Analysis of Coal Liquid and Its Catalytically Hydrogenated Products." In Proceedings of 28th Annual Conference on Mass Spectrometry and Allied Topics, New York, May 25-30.

Wilson, B. W., et al. 1980. "Pineal Gland Function in Rats Exposed to 60 Hz Electric Fields." Bioelectromagnetics 1:236.

Wilson, B. W., et al. 1980. "Strategies for Characterizing the Fate of Bioactive Materials During Coal Liquefaction Product Upgrading." In Proceedings of Second U.S. DOE Symposium on Environmental Control, Reston, Virginia, March.

Wilson, B. W., C. E. Costello, S. A. Carr, K. Biemann, C. Orvig, A. Davison and A. G. Jones. 1979. "Field Desorption Mass Spectrometry of Complex Anions Containing Rhenium and Technetium." Analytical Letters 12(A3):303-311.

Wilson, B. W., and R. A. Pelroy. 1980. "Effects of Catalytic Hydrogenation on Coal Liquids Which Exhibit Microbial Mutagenic Activity." Environmental Analytical Chemistry (in press).

Wilson, B. E., R. A. Pelroy and J. T. Cresto. 1980. "Gas Chromatographic-Mass Spectral Analysis and In Vitro Assay for Mutagenic Activity of Coal Liquefaction Material and the Fuel Products Resulting from Its Hydrogenation." Fuel (in press).

Wilson, B. W., and R. A. Pelroy. 1980. "High Resolution and Metastable Ion Analysis of Heavier Nitrogen Compounds in SRC-II Liquids." In Proceedings of Second Symposium on Environmental Analytical Chemistry, Provo, Utah, June 18-20.

Wilson, B. W., R. A. Pelroy and J. T. Cresto. 1980. "Identification of Primary Aromatic Amines in Mutagenically Active Subfractions from Coal Liquefaction Materials." Mutation Research 79:193-202.

Wilson, B. W., and W. Snedden. 1979. "Capillary Column GC/MS Detection of 5-Methoxytryotamine in Human Plasma Using Selected Ion Monitoring." Journal of Neurochemistry 33:939-941.

Wilson, B. W., A. P. Toste and R. A. Pelroy. 1980. "Accurate Mass/Metastable Ion Analysis of Higher Molecular Weight Nitrogen Compounds in Coal Liquids." In Proceedings of 20th Hanford Life Science Symposium, eds. W. D. Felix and D. D. Mahlum, Richland, Washington. PNL-SA-8852.

Wilson, W. E., and H. G. Paretzke. 1980. "Calculation of Ionization Frequency Distribution in Small Sites." Radiation Research 81:326-335.

Wogman, N. A. 1980. "Natural Contamination in Radionuclide Detection Systems." In Proceedings of the 1980 IEEE Nuclear Science Symposium, Orlando, Florida, PNL-8989 (in press).

Wogman, N. A. 1980. "Nuclear Techniques Applicable to Studies of Pollutants in Groundwater." In Proceedings of an Advisory Group Meeting Organized by the International Atomic Energy Agency, pp. 127-153.

Wogman, N. A., R. L. Brodzinski and D. P. Brown. 1980. "Evaluation of a Phoswich Detector for the In Situ Analysis of ^{90}Sr." IEEE Transactions in Nuclear Science 27(1):733-741.

Wogman, N. A., D. P. Brown, H. G. Rieck, Jr. and J. C. Laul. 1979. "Computer-Controlled Cyclic Activation Analysis with a ^{252}Cf-^{235}U Subcritical Multiplier." In Proceedings of Computers in Activation Analysis and Gamma-Ray Spectroscopy, pp. 728-783.

Wogman, N. A., and K. K. Nielson. 1980. "Development and Application of an In-Situ X-ray Fluorescence Spectrometer for Underwater Sediment Analysis." Accepted for publication in Environmental Science and Technology.

PRESENTATIONS

Abel, K. H. and E. A. Crecelius. 1980. "Determination of Elemental Solubilities from Atmospheric Aerosols Using Instrumental Neutron Activation Analysis and Seawater Leaching." Presented at the 10th Annual Symposium on the Analytical Chemistry of Pollutants, May 28-30, 1980, Dortmund, West Germany.

Ballou, J. E. and N. A. Wogman. 1980. "The Disposition of ^{232}U Daughters Following Inhalation of $^{232}UO_2(NO_3)_2$ Aerosols." Presented at the Health Physics Society Annual Meeting, July 20-25, 1980, Seattle, Washington.

Bean, R. M., et al. 1980. "Aqueous Suspensions of Solvent Refined Coal Liquids: Effects of Preparation Procedure on Resulting Chemical Composition and Toxicity." Presented at the 20th Hanford Science Symposium, October 20, 1980, Richland, Washington.

Braby, L. A., J. M. Nelson, and W. C. Roesch. 1980. "Survival of Cells Irradiated at Dose Rates from 10^2 to 10^6 rad/sec." Presented at the Radiation Research Society Meeting, June 1-5, 1980, New Orleans, Louisiana.

Brenden, B. B., J. S. Hartman, and F. R. Reich. 1980. "Measuring Transient High Temperature Thermal Phenomena in Hostile Environment." Presented at the Society of Photo-Optical Instrumentation Engineers, Bellingham, Washington.

Brodzinski, R. L. 1980. "In Situ Radiation Measurements and Instruments for Monitoring Nuclear Waste Storage Facilities." Presented at IEEE Short Course on Introduction to Nuclear Waste Management and Storage, October 20, 1980, San Francisco, California.

Burger, J. E. 1980. "Chemical Group Separation of SRC-II Material Utilizing Ternary Gradient HPLC." Presented at Environmental Analytical Chemistry Symposium, June 18-20, 1980, Provo, Utah.

Felix, W. D., et al. 1980. "Chemical/Biological Characterization of SRC-II Product and By-Products." Presented at the Symposium on Environmental Aspects of Fuel Conversion Technology V, September 16-19, 1980, St. Louis, Missouri.

Fruchter, J. S., J. C. Evans, C. L. Wilkerson, and R. W. Sanders. 1980. "Analysis of Oil Shale Products and Effluents Using a Multitechnique Approach." Presented at the Meeting of the American Nuclear Society/American Chemical Society/DOE Topical Conference on Atomic and Nuclear Methods in Fossil Energy Research, December 1-4, 1980, Mayaguez, Puerto Rico.

Fruchter, J. S. and C. L. Wilkerson. 1980. "Characterization of Oil Shale Effluents." Presented at Oil Shale: The Environmental Challenges Conference, August 11-14, 1980, Vail, Colorado.

Goles, R. W. and F. P. Brauer. 1980. "An Automated ^{85}Kr Gamma-Ray Stack Monitor." PNL-SA-8642. Presented at the 1980 Nuclear Science Symposium, November 5-7, 1980, Orlando, Florida.

Goles, R. W. and F. P. Brauer. 1980. "Differential Monitoring of Tritium and Carbon-14 Compounds." Presented at the American Nuclear Society Topical Meeting, April 29-May 1, 1980, Dayton, Ohio.

Johnson, A. L. and R. D. Smith. 1980. "The Application of Pyrolysis Mass Spectrometry to Complex Samples and Model Compounds." Presented at the 180th National American Chemical Society Meeting, August 24-29, 1980, Las Vegas, Nevada.

Kalkwarf, D. R. 1980. "High-Performance Thin-Layer Chromatography of Sulfonated Polycyclic Aromatic Compounds." Presented at the 2nd Symposium on Environmental Analytical Chemistry, June 18-20, 1980, Provo, Utah.

Kalkwarf, D. R. 1980. "Photochemical Reactions of Polycyclic Aromatic

Hydrocarbons with SO_2 Gas." Presented at the 35th Regional Meeting, American Chemical Society, June 12-14, 1980, Salt Lake City, Utah.

Kalkwarf, D. R. and S. R. Garcia. 1980. "A Search for PAH-Transformation Products in Coal-Fired Power-Plants Plumes." Presented at the Physics and Chemistry of Energy-Related Atmospheric Pollution Conference, May 28-30, 1980, Harpers Ferry, West Virginia.

Kalkwarf, D. R. and S. R. Garcia. 1980. "Sublimation of Polycyclic Aromatic Hydrocarbons from Coal Fly Ash." Presented at the American Chemical Society Meeting, March 23-28, 1980, Houston, Texas.

Lagergren, C. R. 1980. "Characterization of Low Activities by Mass Spectrometry." PNL-SA-8912. Presented at the Second International Conference on Low Level Counting, Low Activities '80, November 24-28, 1980, Stroske Pleso, Czechoslovakia.

Lagergren, C. R. 1980. "Direct-Inlet Mass Spectrometry." Presented at the DOE-sponsored Workshop to Evaluate Present and Future Research Needs in Mass Spectrometry, January 3-4, 1980, Seattle, Washington.

Lagergren, C. R. 1980. "Investigations into the Mechanisms of Surface Ionization." Presented at the DOE-sponsored Workshop to Evaluate Present and Future Research Needs in Mass Spectrometry, January 3-4, 1980, Seattle, Washington.

Lagergren, C. R. 1980. "The Ion Optics of a Split-Pole Mass Spectrometer." Presented at the American Society for Mass Spectrometry Conference, May 25-30, 1980, New York, New York.

Miller, J. H., L. H. Toburen, and S. T. Manson. 1980. "Bethe-Born Approximation for the Energy Distribution of Electrons Ejected from Neon by Proton Impact." Presented at the DEAP Meeting, December, 1980, Los Angeles, California.

Nelson, J. M., L. A. Braby, and W. C. Roesch. 1980. "Rapid Repair of Sublethal Damage in Irradiated Cells." Presented at the 7th Symposium on Microdosimetry, Commission of European Communities, September 8-12, 1980, Oxford, England.

Nelson, J. M., L. A. Braby, and W. C. Roesch. 1980. "Repair of Sublethal Radiation Damage in Stationary Phase CHO Cells." Presented at the Radiation Research Society Meeting, June 1-5, 1980, New Orleans, Louisiana.

Olsen, K. B. 1980. "A Computer Controlled Scanning Echelle Monochromator System." Presented at the 5th National Conference of Spectrochemical Excitation and Analysis, September 8, 1980, Boston, Massachusetts.

Olsen, K. B. 1980. "The Eruption of Mount St. Helens." Presented at the 5th National Conference of Spectrochemical Excitation and Analysis, September 8, 1980, Boston, Massachusetts.

Roesch, W. C., L. A. Braby, and J. M. Nelson. 1980. "Modeling the Radiation Response of Chlamydomonas reinhardi." Presented at the Radiation Research Society Meeting, June 1-5, 1980, New Orleans, Louisiana.

Roesch, W. C. and D. R. Fisher. 1980. "Microdosimetry of Alpha Particles in the Lung." Presented at the Radiation and Research Society Meeting, June 1-5, 1980, New Orleans, Louisiana.

Sklarew, D. S., et al. 1980. "Characterization and Mutagenicity of Shale Oil Fractions." Presented at the American Chemical Society Meeting, March 23-28, 1980, Houston, Texas.

Smith, R. D. 1980. "An LC-MS Using SIMS and Laser Desorption." Presented at the DOE-sponsored Workshop to Evaluate Present and Future Research Needs in Mass Spectrometry, January 3-4, 1980, Seattle, Washington.

Smith, R. D. 1980. "Direct High Temperature Pyrolysis Mass Spectrometry." Presented at the Pittsburgh Conference on Analytical Chemistry, March 10-15, 1980, Atlantic City, New Jersey.

Smith, R. D. 1980. "Kinetics and Mechanisms for the Formation of Organic Pollutants During Pyrolysis and Combustion." Presented at the Atmospheric Chemistry Conference, May 28-30, 1980, Harpers Ferry, West Virginia.

Smith, R. D. and J. E. Burger. 1980. "An LC-MS Using Ion Impact." Presented at the American Society for Mass Spectrometry Conference, May 25-30, 1980, New York, New York.

Smith, R. D. and J. E. Burger. 1980. "Liquid Chromatography-Mass Spectrometry of Thermally Unstable Compounds Using Secondary Ion Emission." Presented at the 180th National American Chemical Society Meeting, August 24-29, 1980, Las Vegas, Nevada.

Stoffels, J. J. and C. R. Lagergren. 1980. "On the Real-Time Measurement of Particles in Air by Direct-Inlet Surface Ionization Mass Spectrometry." Presented at the American Society for Mass Spectrometry, May 25-30, 1980, New York, New York.

Toste, A. P. 1980. "Bacterial Mediation of Short-Term Sterol Diagenesis." Presented at the 180th National American Chemical Society Meeting, August 24-29, 1980, Las Vegas, Nevada.

Toste, A. P. and M. Calvin. 1980. "Bacterial Mediation of Short-Term Sterol Diagenesis." Presented at the Second Chemical Congress of the North American Continent, August 28, 1980, Las Vegas, Nevada.

Toste, A. P., et al. 1980. "Comparison of Chemical and Mutagenic Properties of a Coal Liquid and a Shale Oil." Presented at the 20th Hanford Science Symposium, October 20, 1980, Richland, Washington.

Warner, R. A. and P. L. Reeder. 1980. "Comparisons of Delayed Neutron Energy Spectra." Presented at the American Chemical Society Meeting, March 23-28, 1980, Houston, Texas.

Weimer, W. C., et al. 1980. "Chemical Fractionation of Complex Materials for Biological Testing Purposes: A Comparison of Five Methodologies." Presented at the Environmental Analytical Chemistry Symposium, June 18-20, 1980, Provo, Utah.

Weimer, W. C., B. W. Wilson, R. A. Pelroy, and M. R. Petersen. 1980. "Analysis of Coal Liquids Which Exhibit Microbial Mutagenic Activity." Presented at the Second Annual Symposium on Process Measurement for Environmental Assessment, February 25-27, 1980, Atlanta, Georgia.

Whitaker, T. J. and B. A. Bushaw. 1980. "Doppler-Cancelled Two Photon Resonant Ionization Spectroscopy." Presented at the International Quantum Electronics Conference, June 23-26, 1980, Boston, Massachusetts.

Wilkerson, C. L. and J. S. Fruchter. 1980. "Comparison and Contrast of Trace Elements in Crude Shale Oils and Petroleum." Presented at the American Chemical Society Meeting, March 24-28, 1980, Houston, Texas.

Wilson, B. W., et al. 1980. "Strategies for Characterizing the Fate of Bioactive Materials During Coal Liquefaction Product Upgrading." Presented at the Second U.S. DOE Symposium on Environmental Control, March, 1980, Reston, Virginia.

Wilson, W. E. and H. G. Paretzke. 1980. "Microscopic Track Structure for 0.25 to 3 MeV Protons." Presented at the Radiation Research Society Meeting, June 1-5, 1980, New Orleans, Louisiana.

Wilson, B. W., R. A. Pelroy, M. R. Petersen, and W. C. Weimer. 1980. "Analysis of Coal Liquid Subfractions Which Exhibit Microbial Mutagenic Activity." Presented at the Process Measurements for Environmental Assessment Symposium, February 25-27, 1980, Atlanta, Georgia.

Wilson, B. W., D. M. Schoengold, M. R. Petersen, and R. A. Pelroy. 1980. "GCMS Analysis of Coal Liquid and Its Catalytically Hydrogenated Products." Presented at the 28th Annual Conference on Mass Spectrometry and Allied Topics, May 25-30, 1980, New York, New York.

Wilson, B. W., T. A. Toste, and R. A. Pelroy. 1980. "Accurate Mass/Metastable Ion Analysis of Higher Molecular Weight Nitrogen Compounds in Coal Liquids." Presented at the Proceedings of the 20th Hanford Science Symposium, October 20, 1980, Richland, Washington.

Wilson, B. W., B. A. Vieux, and R. A. Pelroy. 1980. "High Resolution and Metastable Ion Mass Spectral Analysis of Higher Molecular Weight Nitrogen Compounds in Coal Liquids." Presented at the Environmental Analytical Chemistry Symposium, June 18-20, 1980, Provo, Utah.

Wogman, N. A. 1980. "Natural Contamination in Radionuclide Detection Systems." Presented at the 1980 IEEE Nuclear Science Symposium, November 5-7, 1980, Orlando, Florida.

Wogman, N. A. 1980. "Nuclear Techniques Applicable to Studies of Pollutants in Groundwater." Presented at the IAEA Meeting on Use of Nuclear Techniques in Sea-Bed Mineral Exploration, November, 1980, Vienna, Austria.

Wogman, N. A., R. L. Brodzinski, and D. P. Brown. 1979. "Evaluation of a Phoswich Detector for the In-Situ Analysis of ^{90}Sr." Presented at the IEEE San Francisco Meeting, November, 1979, San Francisco, California.

Author Index

AUTHOR INDEX

Organization Charts Distribution

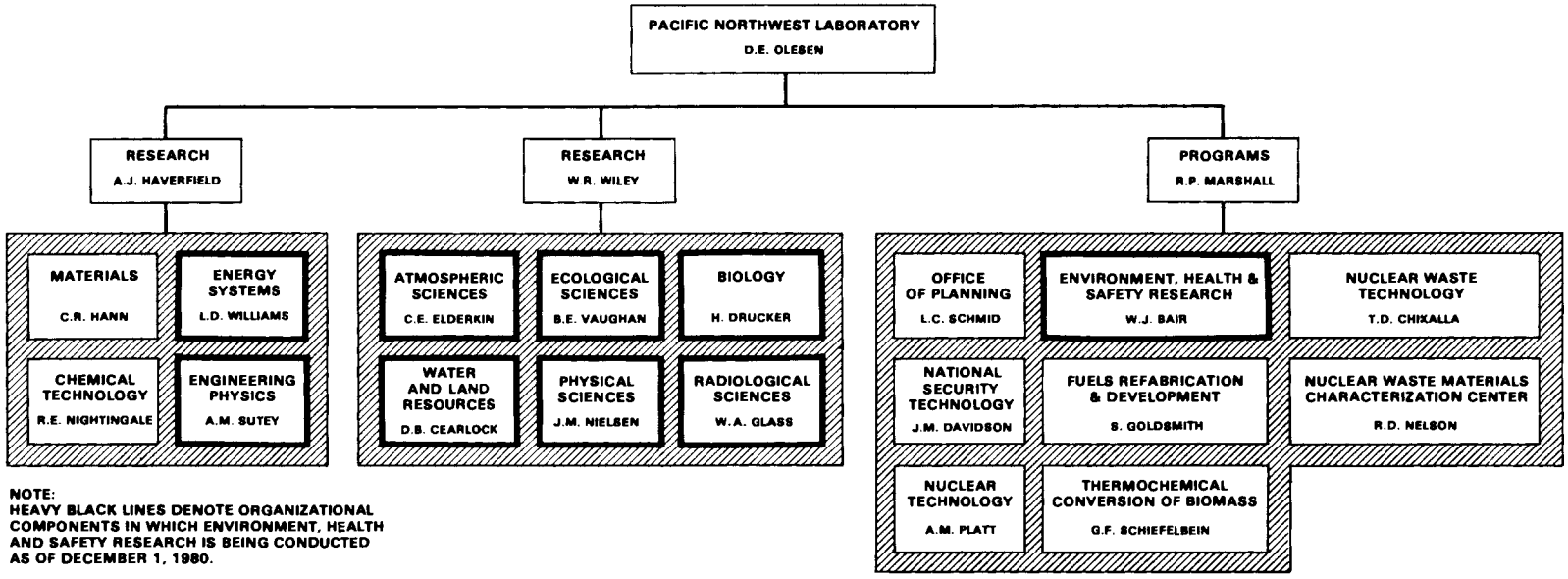

NOTE:
HEAVY BLACK LINES DENOTE ORGANIZATIONAL COMPONENTS IN WHICH ENVIRONMENT, HEALTH AND SAFETY RESEARCH IS BEING CONDUCTED AS OF DECEMBER 1, 1980.

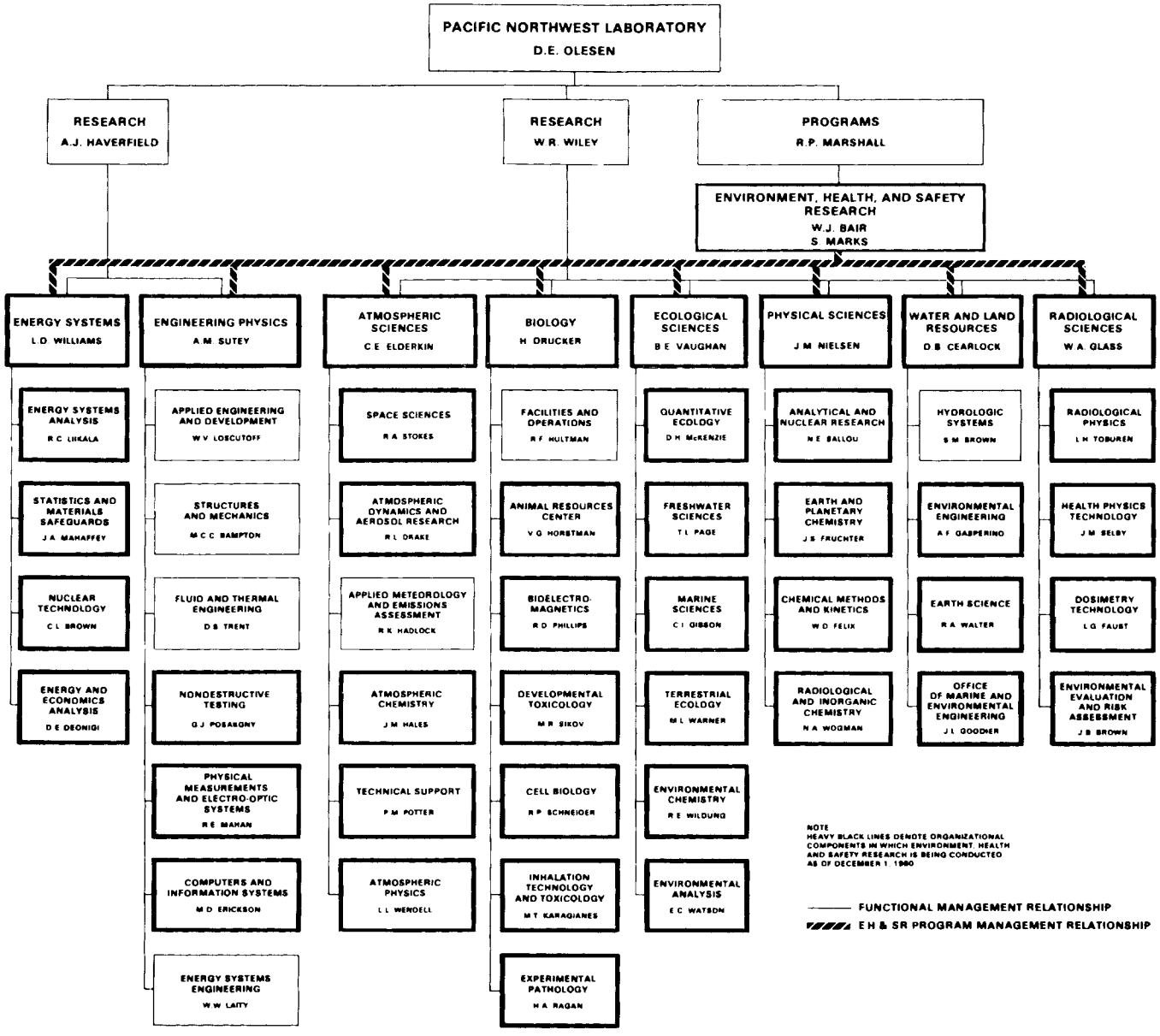
PACIFIC NORTHWEST LABORATORY
D.E. OLESEN
RESEARCH
A.J. HAVERFIELD
RESEARCH
W.R. WILEY
PROGRAMS
R.P. MARSHALL
ENVIRONMENT, HEALTH, AND SAFETY RESEARCH
W.J. BAIR
S. MARKS
ENERGY SYSTEMS
L.D. WILLIAMS
ENERGY SYSTEMS ANALYSIS
R.C. LIKALA
STATISTICS AND MATERIALS SAFEGUARDS
J.A. MAHAFFEY
NUCLEAR TECHNOLOGY
C.L. BROWN
ENERGY AND ECONOMICS ANALYSIS
D.E. DEONIGI
ENGINEERING PHYSICS
A.M. SUTEY
APPLIED ENGINEERING AND DEVELOPMENT
W.V. LOSCUTOFF
STRUCTURES AND MECHANICS
M.C.C. BAMPTON
FLUID AND THERMAL ENGINEERING
D.S. TRENT
NONDESTRUCTIVE TESTING
G.J. POSAKONY
PHYSICAL MEASUREMENTS AND ELECTRO-OPTIC SYSTEMS
R.E. MAHAN
COMPUTERS AND INFORMATION SYSTEMS
M.D. ERICKSON
ENERGY SYSTEMS ENGINEERING
W.W. LAITY
ATMOSPHERIC SCIENCES
C.E. ELDERKIN
SPACE SCIENCES
R.A. STOKES
ATMOSPHERIC DYNAMICS AND AEROSOL RESEARCH
R.L. DRAKE
APPLIED METEOROLOGY AND EMISSIONS ASSESSMENT
R.K. HADLOCK
ATMOSPHERIC CHEMISTRY
J.M. HALES
TECHNICAL SUPPORT
P.M. POTTER
ATMOSPHERIC PHYSICS
L.L. WENDELL
BIOLOGY
H. DRUCKER
FACILITIES AND OPERATIONS
R.F. HULTMAN
ANIMAL RESOURCES CENTER
V.G. HORSTMAN
BIOELECTRO-MAGNETICS
R.D. PHILLIPS
DEVELOPMENTAL TOXICOLOGY
M.R. SIKOV
CELL BIOLOGY
R.P. SCHNEIDER
INHALATION TECHNOLOGY AND TOXICOLOGY
M.T. KARAGIANES
EXPERIMENTAL PATHOLOGY
H.A. RAGAN
ECOLOGICAL SCIENCES
B.E. VAUGHAN
QUANTITATIVE ECOLOGY
D.H. McKENZIE
FRESHWATER SCIENCES
T.L. PAGE
MARINE SCIENCES
C.I. GIBSON
TERRESTRIAL ECOLOGY
M.L. WARNER
ENVIRONMENTAL CHEMISTRY
R.E. WILDUNG
ENVIRONMENTAL ANALYSIS
E.C. WATSON
PHYSICAL SCIENCES
J.M. NIELSEN
ANALYTICAL AND NUCLEAR RESEARCH
N.E. BALLOU
EARTH AND PLANETARY CHEMISTRY
J.S. FRUCHTER
CHEMICAL METHODS AND KINETICS
W.D. FELIX
RADIOLOGICAL AND INORGANIC CHEMISTRY
N.A. WOGMAN
WATER AND LAND RESOURCES
D.B. CEARLOCK
HYDROLOGIC SYSTEMS
S.M. BROWN
ENVIRONMENTAL ENGINEERING
A.F. GASPERINO
EARTH SCIENCE
R.A. WALTER
OFFICE OF MARINE AND ENVIRONMENTAL ENGINEERING
J.L. GOODIER
RADIOLOGICAL SCIENCES
W.A. GLASS
RADIOLOGICAL PHYSICS
L.H. TOBUREN
HEALTH PHYSICS TECHNOLOGY
J.M. SELBY
DOSIMETRY TECHNOLOGY
L.G. FAUST
ENVIRONMENTAL EVALUATION AND RISK ASSESSMENT
J.B. BROWN
NOTE
HEAVY BLACK LINES DENOTE ORGANIZATIONAL COMPONENTS IN WHICH ENVIRONMENT, HEALTH AND SAFETY RESEARCH IS BEING CONDUCTED AS OF DECEMBER 1, 1980
FUNCTIONAL MANAGEMENT RELATIONSHIP
E H & SR PROGRAM MANAGEMENT RELATIONSHIP

DISTRIBUTION

No. of Copies

A. A. Churm, Director
Patent Division
DOE - Chicago Operations
9800 S. Cass Avenue
Argonne, IL 60439

27 DOE Technical Information Center

R. C. Clusen
Department of Energy
Office of the Asst. Sec. for Environment
Washington, DC 20545

W. R. Albers
Department of Energy
Office of the Asst. Sec. for Environment
Washington, DC 20545

D. S. Ballantine
Department of Energy
Office of the Asst. Sec. for Environment
Washington, DC 20545

R. W. Barber
Department of Energy
Office of the Asst. Sec. for Environment
Washington, DC 20545

N. F. Barr
Department of Energy
Office of the Asst. Sec. for Environment
Washington, DC 20545

R. W. Beadle
Department of Energy
Office of the Asst. Sec. for Environment
Washington, DC 20545

R. P. Berube
Department of Energy
Office of the Asst. Sec. for Environment
Washington, DC 20545

No. of Copies

J. R. Bair
Department of Energy
Office of the Asst. Sec. for Environment
Washington, DC 20545

R. P. Blaunstein
Department of Energy
Office of Health and Environmental Research
Washington, DC 20545

C. M. Borgstrom
Department of Energy
Office of the Asst. Sec. for Environment
Washington, DC 20545

L. Brothers
Department of Energy
Office of the Asst. Sec. for Environment
Washington, DC 20545

S. H. Bryan
Department of Energy
Office of the Asst. Sec. for Environment
Washington, DC 20545

W. W. Burr, Jr.
Department of Energy
Deputy Asst. Sec. for Research
Washington, DC 20545

R. L. Butenhoff
Department of Energy
Office of Health and Environmental Research
Washington, DC 20545

P. Cho
Department of Energy
Office of the Asst. Sec. for Environment
Washington, DC 20545

No. of Copies

J. A. Coleman
Department of Energy
Office of the Asst. Sec. for Environment
Washington, DC 20545

L. J. Deal
Department of Energy
Office of the Asst. Sec. for Environment
Washington, DC 20545

C. Dougherty
Department of Energy
Office of the Asst. Sec. for Environment
Washington, DC 20545

A. P. Duhamel
Department of Energy
Office of the Asst. Sec. for Environment
Washington, DC 20545

C. W. Edington
Department of Energy
Office of the Asst. Sec. for Environment
Washington, DC 20545

C. Eifert
Department of Energy
Office of the Asst. Sec. for Environment
Washington, DC 20545

H. C. Field
Department of Energy
Office of the Asst. Sec. for Environment
Washington, DC 20545

T. G. Frangos
Department of Energy
Office of the Asst. Sec. for Environment
Washington, DC 20545

No. of Copies

R. E. Franklin
Department of Energy
Office of the Asst. Sec.
for Environment
Washington, DC 20545

G. Goldstein
Department of Energy
Office of the Asst. Sec.
for Environment
Washington, DC 20545

M. Gottlieb
Department of Energy
Office of the Asst. Sec.
for Environment
Washington, DC 20545

E. B. Harvey
Department of Energy
Office of the Asst. Sec.
for Environment
Washington, DC 20545

H. L. Hollister
Department of Energy
Office of the Asst. Sec.
for Environment
Washington, DC 20545

P. W. House
Department of Energy
Office of the Asst. Sec.
for Environment
Washington, DC 20545

F. P. Hudson
Department of Energy
Office of the Asst. Sec.
for Environment
Washington, DC 20545

C. A. Jolly
Department of Energy
Office of the Asst. Sec.
for Environment
Washington, DC 20545

J. S. Kane
Department of Energy
Office of the Asst. Sec.
for Energy Research
Washington, DC 20545

W. J. Little, Jr.
Department of Energy
Office of the Asst Sec.
for Environment
Washington, DC 20545

No. of Copies

J. N. Maddox
Department of Energy
Office of the Asst Sec.
for Environment
Washington, DC 20545

D. D. Mayhew
Department of Energy
Office of the Asst. Sec.
for Environment
Washington, DC 20545

H. M. McCammon
Department of Energy
Office of the Asst. Sec.
for Environment
Washington, DC 20545

T. McCraw
Department of Energy
Office of the Asst. Sec.
for Environment
Washington, DC 20545

C. E. Miller, Jr.
Department of Energy
Office of the Asst. Sec.
for Environment
Washington, DC 20545

M. L. Minthorn, Jr.
Department of Energy
Office of the Asst. Sec.
for Environment
Washington, DC 20545

D. R. Monti
Department of Energy
Office of the Asst. Sec.
for Environment
Washington, DC 20545

W. E. Mott
Department of Energy
Office of the Asst. Sec.
for Environment
Washington, DC 20545

W. A. Neustadt
Department of Energy
Office of the Asst. Sec.
for Environment
Washington, DC 20545

D. E. Patterson
Department of Energy
Office of the Asst. Sec.
for Environment
Washington, DC 20545

No. of Copies

R. P. Prichard
Department of Energy
Office of the Asst. Sec.
for Environment
Washington, DC 20545

R. E. Ramsburg
Department of Energy
Office of the Asst. Sec.
for Environment
Washington, DC 20545

S. L. Rose
Department of Energy
Office of the Asst. Sec.
for Environment
Washington, DC 20545

D. M. Ross
Department of Energy
Office of the Asst. Sec.
for Environment
Washington, DC 20545

R. D. Shull
Department of Energy
Office of the Asst. Sec.
for Environment
Washington, DC 20545

D. H. Slade
Department of Energy
Office of the Asst. Sec.
for Environment
Washington, DC 20545

J. Snyder
Department of Energy
Office of the Asst. Sec.
for Environment
Washington, DC 20545

R. J. Stern
Department of Energy
Office of the Asst. Sec.
for Environment
Washington, DC 20545

J. Swinebroad
Department of Energy
Office of the Asst. Sec.
for Environment
Washington, DC 20545

J. W. Thiessen
Department of Energy
Office of the Asst. Sec.
for Environment
Washington, DC 20545

No. of Copies

A. R. Vincent
Department of Energy
Office of the Asst. Sec. for Environment
Washington, DC 20545

R. Von Saunder
Department of Energy
Office of the Asst. Sec. for Environment
Washington, DC 20545

B. W. Wachholz
Department of Energy
Office of the Asst. Sec. for Environment
Washington, DC 20545

R. L. Watters
Department of Energy
Office of the Asst. Sec. for Environment
Washington, DC 20545

J. C. Whitnah
Department of Energy
Office of the Asst. Sec. for Environment
Washington, DC 20545

E. R. Williams
Department of Energy
Office of the Asst. Sec. for Environment
Washington, DC 20545

R. W. Wood
Department of Energy
Office of the Asst. Sec. for Environment
Washington, DC 20545

C. W. Duncan
Department of Energy
Sec. for the Department of Energy
Washington, DC 20545

M. Adams
Department of Energy
Office of the Asst. Sec. for Fossil Energy
Washington, DC 20545

G. W. Cunningham
Department of Energy
Office of the Asst. Sec. for Nuclear Energy
Washington, DC 20545

No. of Copies

E. Frieman
Department of Energy
Office of the Director of Energy Research
Washington, DC 20585

G. Fumich
Department of Energy
Office of the Asst. Sec. for Fossil Energy
Washington, DC 20545

F. Koomanoff
Department of Energy
Office of the Director of Energy Research
Washington, DC 20585

A. Liccardi
Department of Energy
Office of the Asst. Sec. for Fossil Energy
Washington, DC 20545

A. H. Linden
Department of Energy
Office of the Administrator, Energy Information Administration
Washington, DC 20461

R. Rabson
Department of Energy
Office of the Director of Energy Research
Washington, DC 20545

R. G. Rader
Department of Energy
Office of the Director of Energy Research
Washington, DC 20545

T. E. Stelson
Department of Energy
Office of the Asst. Sec. for Conservation and Solar Energy
Washington, DC 20545

R. J. Roeder
DOE - Albuquerque Operations Office
P.O. Box 5400
Albuquerque, NM 87115

No. of Copies

J. F. Stevens
Dayton Area Office
DOE - Albuquerque Operations Office
P.O. Box 66
Miamisburg, OH 45342

E. W. Bean
Rocky Flats Area Office
DOE - Albuquerque Operations Office
P.O. Box 928
Golden, CO 80401

D. M. Gardiner
DOE - Chicago Operations Office
9800 S. Cass Avenue
Argonne, IL 60439

J. H. Spickard
DOE - Idaho Operations Commission
550 Second Street
Idaho Falls, ID 83401

M. M. Williamson
DOE - Idaho Operations Commission
550 Second Street
Idaho Falls, ID 83401

P. B. Dunnaway
DOE - Nevada Operations Office
P.O. Box 14100
Las Vegas, NV 89114

M. E. Gates
DOE - Nevada Operations Office
P.O. Box 14100
Las Vegas, NV 89114

R. Ray
DOE - Nevada Operations Office
P.O. Box 14100
Las Vegas, NV 89114

J. A. Lenhard
DOE - Oak Ridge Operations Office
P.O. Box E
Oak Ridge, TN 37830

J. Robertson, Director
DOE - Region X Office
1992 Federal Building
915 Second Avenue
Seattle, WA 98174

No. of Copies

C. Jackson
DOE - San Francisco Operations Office
133 Broadway
Wells Fargo Building
Oakland, CA 94616

B. Morgan
DOE - Savannah River Operations Office
P.O. Box A
Aiken, SC 29801

W. Reese
DOE - Savannah River Operations Office
P.O. Box A
Aiken, SC 29801

J. S. Ball
Bartlesville Energy Research Center
Department of Energy
P.O. Box 1398
Bartlesville, OK 74003

G. H. Gronhovd
Grand Forks Energy Research Center
Department of Energy
Box 8213, University Station
Grand Forks, ND 58202

A. W. Decora
Laramie Energy Research Center
Department of Energy
P.O. Box 3395
University Station
Laramie, WY 83071

A. A. Pitrolo
Morgantown Energy Research Center
Department of Energy
P.O. Box 880
Morgantown, WV 26505

I. Wender
Pittsburgh Energy Research Center
4800 Forbes Avenue
Pittsburgh, PA 15213

B. M. Erickson
DOE - Schnectady Naval Reactors Office
P.O. Box 1069
Schenectady, NY 12301

No. of Copies

T. M. Schoenberg
DOE - Schnectady Naval Reactors Office
P.O. Box 1069
Schenectady, NY 12301

U.S. Nuclear Regulatory Commission
Advisory Committee on Reactor Safeguards
Washington, DC 20555

R. Alexander
U.S. Nuclear Regulatory Commission
Washington, DC 20545

W. Cool
U.S. Nuclear Regulatory Commission
Washington, DC 20545

E. E. Held
Office of Standards Development
U.S. Nuclear Regulatory Commission
Washington, DC 20555

Frank Swanberg
U.S. Nuclear Regulatory Commission
Washington, DC 20545

J. J. Davis
Asst. Director of Research
U.S. Nuclear Regulatory Commission
Washington, DC 20545

R. A. Scarano
U.S. Nuclear Regulatory Commission
Mill Licensing Section
Washington, DC 20545

J. R. DeVoe
National Bureau of Standards
A121, Building 222
Washington, DC 20234

P. LaFluer
Nuclear Reactor Laboratory
National Bureau of Standards
Gaithersburg, MD 20760

No. of Copies

W. R. Ney
Executive Director
National Council on Radiation Protection and Measurement
7910 Woodmont Avenue
Suite 1061
Washington, DC 20014

H. L. Volchok
Environmental Measurements Laboratory
376 Hudson St.
New York, NY 10014

W. Mills
U.S. Environmental Protection Agency
Washington, DC 20460

D. Smith
U.S. Environmental Protection Agency
Washington, DC 20460

P. F. Gustafson
Argonne National Laboratory
9700 S. Cass Avenue
Argonne, IL 60439

J. Sedlet
Argonne National Laboratory
9700 S. Cass Avenue
Argonne, IL 60439

W. K. Sinclair
Argonne National Laboratory
9700 S. Cass Avenue
Argonne, IL 60439

V. P. Bond
Brookhaven National Laboratory
Upton, Long Island, NY 11973

Librarian
Research Library, Reference
Brookhaven National Laboratory
Upton, Long Island, NY 11973

No. of Copies

C. B. Meinhold
Brookhaven National Laboratory
Upton, Long Island, NY 11973

G. M. Woodwell
Brookhaven National Laboratory
Research Library
Reference Section
Information Division
Upton, Long Island, NY 11973

S. I. Auerbach
Oak Ridge National Laboratory
Oak Ridge Operations Office
P.O. Box X
Oak Ridge, TN 37830

J. A. Auxier
Oak Ridge National Laboratory
P.O. Box X
Oak Ridge, TN 37830

C. R. Richmond
Oak Ridge National Laboratory
P.O. Box X
Oak Ridge, TN 37830

R. M. Jefferson
Sandia Laboratories
P.O. Box 5800
Albuquerque, NM 87187

K. A. Smith
Sandia Laboratories
P.O. Box 5800
Albuquerque, NM 87187

A. R. Boulogne
Technical Information Service
Room 773A
Savannah River Laboratory
E. I. DuPont de Nemours & Co.
Aiken, SC 29801

No. of Copies

E. L. Alpen
Lawrence Berkeley Laboratory
University of California
Building 90, Room 2056
No. 1 Cyclotron Road
Berkeley, CA 94720

Librarian
Lawrence Radiation Laboratory
University of California
Technical Information Dept., L-3
P.O. Box 808
Livermore, CA 94550

M. L. Mendelsohn
University of California
Lawrence Livermore Laboratory
P.O. Box 808
Livermore, CA 94550

P. Phelps
Lawrence Radiation Laboratory
University of California
Lawrence Livermore Laboratory
Technical Information Dept., L-3
P.O. Box 808
Livermore, CA 94550

J. W. Healy
Los Alamos Scientific Laboratory
University of California
P.O. Box 1663
Los Alamos, NM 87545

Librarian
Los Alamos Scientific Laboratory
P.O. Box 1663
Los Alamos, NM 87545

S. D. Nielsen
Los Alamos Scientific Laboratory
University of California
P.O. Box 1663
Los Alamos, NM 87545

D. F. Petersen
University of California
Los Alamos Scientific Laboratory
P.O. Box 1663
Los Alamos, NM 87545

No. of Copies

G. L. Voelz
University of California
Los Alamos Scientific Laboratory
P.O. Box 1663
Los Alamos, NM 87545

B. W. Von Zellen
Department of Biological Sciences
Northern Illinois University
Dekalb, IL 60115

R. O. McClellan
Inhalation Toxicology Research Institute
Lovelace Foundation for Medical Education and Research
P.O. Box 5890
Albuquerque, NM 87115

D. Rall, Director
NIEHS
P.O. Box 12233
Research Triangle Park, NC 27709

D. Beirman
Chief, Document Service Branch
Central Intelligence Agency
Attn: CRS/DPSD/DSB/IAS/409779/DB
Washington, DC 20505

Council on Environmental Quality
72 Jackson Place, NW
Washington, DC 20006

W. E. Lotz
Electric Power Research Institute
1800 Massachusetts Ave., NW
Suite 7000
Washington, DC 20036

W. Weyzen
Electric Power Research Institute
3412 Hillview Ave
Palo Alto, CA 92665

J. W. McCaslin
INEL, Aerojet Nuclear
550 Second Street
Idaho Falls, ID 83401

No. of Copies

R. E. Yoder
Rockwell International
Rocky Flats Plant
P.O. Box 464
Golden, CO 80401

J. F. Johnson
Kenworth Trucking
P.O. Box 1000
Kirkland, WA 98033

Leo Bustad, Dean
College of Veterinary Medicine
Washington State University
Pullman, WA 99163

Librarian
Joint Center for Graduate Study
100 Sprout Road
Richland, WA 99352

J. R. Arnold
Chemistry Department
University of California
San Diego
La Jolla, CA 92037

W. Singlevich
Air Force Technical Applications Center/TD-4
Patrick AFB, FL 32925

Director
Commonwealth Scientific and Industrial Research Organization
Aspendal, Victoria 3195
AUSTRALIA

Librarian
Australian AEC
Riverina Laboratory
P.O. Box 226
Deniliquin
New South Wales
AUSTRALIA 2710

Librarian
Commonweath Scientific and Industrial Research Organization
314 Albert Street
P.O. Box 89
East Melbourne, Victoria
AUSTRALIA

No. of Copies

H. Daw
Director, Division of Health, Safety and Waste Management
International Atomic Energy Agency
Vienna, 1, Kaerntenerring 11,
AUSTRIA

J. Z. Minczewski
International Atomic Energy Agency
Vienna, 1, Kaerntenerring 11,
AUSTRIA

V. Lyscov
Vienna International Center
P.O. Box 500
1400 Vienna,
AUSTRIA

A. M. Marko, Director
Atomic Energy of Canada, Ltd.
Biology and Health Physics Division
Chalk River Nuclear Laboratories
Chalk River
Ontario KOJ IJO
CANADA

M. Anderson
Library, Department of National Health and Welfare
Ottawa, Ontario
CANADA

M. J. Suess
Regional Officer for Environmental Hazards
World Health Organization
8, Scherfigsvej
DK-2100
Copenhagen, DENMARK

Andrew McLean
National Radiological Protection Board
Harwell, Didcot
Oxfordshire OXII ORQ
ENGLAND

Librarian, Building 465
Atomic Energy Research Establishment
Harwell, Didcot
OXON OXII ORQ
ENGLAND

No. of Copies

D. H. Perison
Atomic Energy Research Establishment
Health Physics and Medical Division
B. 364
Harwell, Didcot, Berkshire
ENGLAND

F. D. Sowby
International Commission on Radiological Protection
Clifton Avenue
Sutton, Surrey
ENGLAND

A. R. Gopal-Ayengar
Inst. fur Biophysik
Herrenhauser Str. 2
3000 Hannover, 21
FEDERAL REPUBLIC OF GERMANY

L. Feinendegen, Director
Institut fur Medizin
Kernforschung
Sanlage Julich
Postfach 1913
517 Julich
FEDERAL REPUBLIC OF GERMANY

W. Jacobi
Institut fur Strahlenschutz
D-8042 Neuherberg
Ingolstadter Landstrasse 1
FEDERAL REPUBLIC OF GERMANY

J. K. Miettinen
University of Helsinki
Department of Radiochemistry
Unionkatu 35, Helsinki
FINLAND

Director
Commissariat a l'Energie Atomique
Centre d'Etudes Nucleaires de Fontenay-aux-Roses (Seine)
FRANCE

No. of Copies

Librarian
Centre d'Etudes Nucleaires de Saclay
P.O. Box 2, Saclay
Fig-sur-Yvette (S&O)
FRANCE

A. Barbreau
Centre d'Etudes Nucleaires de Saclay
P.O. Box 2, Saclay
Fig-sur-Yvette (S&O)
FRANCE

J. C. Nenot
Comite de Radioprotection
69, rue de Micromesnil
75008 Paris,
FRANCE

M. Rzekiecki
Commissariat a l'Energie Atomique
Centre d'Etudes Nucleaires de Cadarache
BP n 13-St. Paul
Les Durance
FRANCE

E. Wallauschek
ENEA (OECD) Health and Safety Office
38, Blvd. Sucket
Paris, /v/
FRANCE

T. Kumatori
Director
National Institute of Radiological Science
4-9-1, Anagawa
Chiba-shi, JAPAN

Z. M. Beekman
President of IRPA
Rooseveltlaan 197
1079 AP Amsterdam
THE NETHERLANDS

J. K. Basson
Vice-President
Raad Op Atomic
Atoomkrag Energy Board
Privaatsak X 256
Pretoria 001
REPUBLIC OF SOUTH AFRICA

No. of Copies

B. C. Winkler
Director, Licensing (Standards)
Raad Op Atoomkrag/Atomic Energy Board
Privaatsak X 256/ Private Bag X 256
Pretoria 001
REPUBLIC OF SOUTH AFRICA

A. Brink
Sasol-One Limited
P.O. Box 1
Sasolburg 9570
REPUBLIC OF SOUTH AFRICA

K. E. Lennart Johansson
National Defense Research Institute
FOA 45 1
S-901-82
Umea, SWEDEN

E. Komorov
HCS/EHE
World Health Organization
Geneva, SWITZERLAND

D. Djuric
Institute of Occupational & Radiological Health
11000 Beograd
Deligradska 29,
YUGOSLAVIA

ONSITE

7 DOE Richland Operations Office

T. E. Austin
P. F. Dunigan
R. W. Newlin
H. E. Ransom
F. R. Standerfer
M. W. Tiernan
M. G. White

Rockwell Hanford Operations

P. G. Lorenzini

UNC Nuclear Industries

T. E. Dabrowski

No. of Copies

2 Westinghouse Hanford Company

R. O. Budd
D. E. Simpson

2 Hanford Environmental Health Foundation

B. D. Breitenstein
B. D. Reinert

8 Battelle-Seattle

S. M. Nealey
E. B. Perrin
J. E. Rasmussen
A. H. Schilling
C. R. Schuller
R. Shikiar
M. E. Walsh
M. T. Wood

7 Battelle Memorial Institute

N. E. Carter
L. L. German
R. S. Paul
L. A. Rancitelli
D. B. Shipler
C. R. Vest
Librarian

4 Battelle Columbus

A. H. Adelman
A. D. Barker
F. J. Milford
R. H. Poirier

3 Battelle-Washington DC Office

G. Johnson
S. Stryker
C. Vest

142 Pacific Northwest Laboratory

J. L. Baer
W. J. Bair (20)
N. E. Ballou (5)
D. B. Cearlock
J. P. Corley
J. M. Davidson
H. Drucker
C. E. Elderkin
S. J. Farmer

No. of Copies

W. D. Felix (10)
J. W. Finnigan
J. C. Fox (5)
J. S. Fruchter (10)
J. J. Fuquay
C. I. Gibson
W. A. Glass (10)
A. J. Haverfield (5)
D. L. Hessel
V. G. Horstman
I. D. Hays

No. of Copies

H. V. Larson
R. C. Liikala
S. Marks
R. P. Marshall
I. C. Nelson (5)
J. M. Nielsen (10)
R. E. Nightingale
D. E. Olesen
J. F. Park
R. W. Perkins (5)
S. R. Roush

No. of Copies

C. L. Simpson
W. H. Swift
W. L. Templeton
L. H. Toburen (12)
C. M. Unruh
B. E. Vaughan
W. R. Wiley
N. A. Wogman (10)
Biology Library (2)
Technical Information (5)
Publishing Coordination (2)